

The Short-Timescale Behavior of Glacial Ice

Thesis by
Jeffrey Muir Thompson

In Partial Fulfillment of the Requirements for the
degree of
Doctorate of Philosophy in Geophysics



CALIFORNIA INSTITUTE OF TECHNOLOGY
Pasadena, California
2013
(Defended May 30th, 2013)

© 2013

Jeffrey Muir Thompson

All Rights Reserved

This thesis is dedicated to William (Bill) Bing and Dr. Jennifer Howes. Without their unending support I would never have completed this doctorate.

ACKNOWLEDGEMENTS

I have quite a few people I would like to acknowledge, so I apologize in advance for the length of this section. First, I have to thank my advisor, Mark Simons, for allowing me to make the transition from being a field geologist to becoming a finite element modeler and glaciologist. Your support has been greatly appreciated over the years. I would also like to thank Victor Tsai for giving me the opportunity to work with him on the project related to supraglacial lake drainage. Next is my thesis advisory committee, which includes Mark and Victor as well as Jennifer Jackson and Andy Thompson. Thank you for your input and for being willing to sit through my thesis defense. I would also like to thank Tom Heaton, for being both a member of my thesis advisory committee, and for encouraging me to get a minor in civil engineering. I've learned a lot and hopefully that'll help me get a job. To finish my round-up of Caltech faculty, I'd like to thank Brian Wernicke, John Eiler, and Paul Asimow. Brian and John, thank you for the chance to spend a year and some change doing clumped isotope work as one of my first year propositions. Paul, thank you for being my first year academic advisor and just generally for being an awesome addition to the concert band.

Now I should thank the people responsible for getting me excited about research and ultimately into Caltech. First on that list are Scott Paterson and Lawford Anderson, who helped turn me from a geology student into a field geologist. The two years I spent working with you with the Team Research group is among my favorite science-related memories. In addition, thanks go out to Vali Memeti, Frances Cooper, and Geoff Pignotta for being awesome graduate students and teaching assistants. Hopefully I lived/live up to the excellent example that you all provided me. Finally, but not least, I would like to thank my dear friends Austin Elliott and Bradford Foley for pushing me to be better by always telling me I was wrong (even if I was right). Your friendship and love of science is a big part of why I ended up at Caltech.

It is no stretch of the imagination to say that I should have earned a music degree while here at Caltech. I want to thank Bill Bing for his wonderful dedication to the Caltech music

program and for helping to foster an enclave of musicians in the middle of a bunch of scientists. Whenever I came close to giving up and packing my bags, the music department kept me tethered to Caltech more than anything else, and you deserve all my thanks and more for that. Additionally, thanks for letting me do crazy things like run a trombone choir and create the Caltech Pep Band, all while being a member of three ensembles and trying to finish my thesis. I would also like to thank Allen Gross for my five wonderful years in the Caltech-Oxy Orchestra. We made some beautiful music and I'm very grateful to have had the chance to be part of it.

I would be utterly remiss if I did not thank all the trombone players in my life. From USC, my wonderful group of friends, who always kept me honest by never cutting me any slack: Gwen, Austin, Holly, Chris, Jon, Craig, Dan, Anthony, Kathryn, Mark, Jason, Colin, Nathan, Ashwin, Dave, and Dave, you guys make my day. A special thanks to Gwen for both making the weekly commute up to Caltech for trombone choir (clearly an important part of my thesis) and for utterly refusing to call me doctor ever. From Caltech: Jeremy, Jill, Andy, Conrad, Catherine, Zeke, Elaine, Jeff, Chris, Chris, Sarah, and Ben...I'm proud to be your pep pep and you've truly made my experience at Caltech great.

An important thank you to Dr. Jennifer Howes of the Caltech counseling center. You helped me come to grips with my decision to finish out my degree, and I really do want to thank you for spending many, many hours listening to me struggle through the issues that I was having. You really did help me.

My time at Caltech would have been completely unbearable if not for my fellow students. While there are too many of you to name specifically, I'm going to try. First up has to be Dr. Professor Konstantin Batygin and his better 2/3 Olga. You guys were and are amongst the best friends any one person could ever ask for. Next up has to be Mike, you really made graduate school feel like undergrad most of the time, and we had some great moments. The ChEESE(G)PSers: Christine, Lindsay, Anne, Mike, Ajay, Joey, Mandy, Da, Jill...I was happy to be the silent G. My first year officemates: Isaac, June, Claire, Kristen,

Katie, and Marion...I wish you all the best in all the wonderful things I'm sure you'll all accomplish.

I would not be where I am today without my amazing family. Mom and Dad, you have been incredibly supportive and encouraging my entire life, but especially through my life as a graduate student. Dad, thanks for the years of Tuesday lunches...I'll get around to paying you back sometime. And Mom, I'd especially like to thank you for the hours of proofreading this thesis you've done. Jessica and Andrew, you guys are the best siblings I could ask for. I hope my thesis talk did not put you guys to sleep too quickly. Philip and Yuki, you guys are the best brothers-from-another-mother I could ask for. Thank you for all the years of good times we'll all had.

And last, but not least, thanks to my wonderful amazing girlfriend Kacy. You not only had to put up with me working late (and early) hours, but you also managed to give me the princess treatment while I was doing so. Thank you, thank you, thank you!

ABSTRACT

Glaciers are often assumed to deform only at slow (i.e., glacial) rates. However, with the advent of high rate geodetic observations of ice motion, many of the intricacies of glacial deformation on hourly and daily timescales have been observed and quantified. This thesis explores two such short timescale processes: the tidal perturbation of ice stream motion and the catastrophic drainage of supraglacial meltwater lakes. Our investigation into the transmission length-scale of a tidal load represents the first study to explore the daily tidal influence on ice stream motion using three-dimensional models. Our results demonstrate both that the implicit assumptions made in the standard two-dimensional flow-line models are inherently incorrect for many ice streams, and that the anomalously large spatial extent of the tidal influence seen on the motion of some glaciers cannot be explained, as previously thought, through the elastic or viscoelastic transmission of tidal loads through the bulk of the ice stream. We then discuss how the phase delay between a tidal forcing and the ice stream's displacement response can be used to constrain *in situ* viscoelastic properties of glacial ice. Lastly, for the problem of supraglacial lake drainage, we present a methodology for implementing linear viscoelasticity into an existing model for lake drainage. Our work finds that viscoelasticity is a second-order effect when trying to model the deformation of ice in response to a meltwater lake draining to a glacier's bed. The research in this thesis demonstrates that the first-order understanding of the short-timescale behavior of naturally occurring ice is incomplete, and works towards improving our fundamental understanding of ice behavior over the range of hours to days.

TABLE OF CONTENTS

| | |
|--|------|
| Dedication | iii |
| Acknowledgements | iv |
| Abstract | vii |
| Table of Contents | viii |
| List of Figures | xii |
| List of Tables | xv |
| Chapter 1: Introduction..... | 1 |
| 1.1 The Cryosphere | 2 |
| 1.2 Ice Stream Dynamics | 5 |
| 1.3 Tidal Interaction with Grounded Ice..... | 9 |
| 1.3.1 Antarctic Tidal Interactions | 10 |
| 1.3.2 Greenland Tidal Interactions | 16 |
| 1.3.3 Observation Summary | 19 |
| 1.4 General Finite Element Methods | 20 |
| 1.5 Thesis Outline..... | 23 |
| Chapter 2 | 33 |
| 2.1 Introduction | 34 |
| 2.2 Methodology..... | 36 |
| 2.2.1 Model Descriptions | 37 |
| 2.2.2 Model Construction..... | 37 |
| 2.3 Results..... | 39 |
| 2.3.1 Two-Dimensional Results..... | 40 |
| 2.3.2 Three-Dimensional Results | 42 |
| 2.4 Transmission of Tidal Stresses | 43 |
| 2.5 Discussion..... | 46 |
| 2.5.1 Comparison to Previous Models..... | 46 |
| 2.5.2 Model Shortcomings..... | 48 |

| | |
|--|-----|
| 2.6 Summary and Conclusions..... | 51 |
| Appendix 2A: Importance of the Ice Shelf..... | 69 |
| Appendix 2B: Flotation Condition for a One-Dimensional Ice Shelf | 71 |
| Appendix 2C: Two-Dimensional Model Results | 76 |
| Appendix 2D: Three-Dimensional Model Results | 83 |
| Chapter 3 | 97 |
| 3.1 Introduction | 98 |
| 3.1.1 Elastic Rheological Effects | 98 |
| 3.1.2 Appropriateness of Viscoelasticity..... | 103 |
| 3.2 Strain-Weakening in the Shear Margins..... | 108 |
| 3.2.1 Continuum Damage Mechanics Formulation | 109 |
| 3.2.2 Continuous Margin Results | 112 |
| 3.2.3 Discrete Margin Results..... | 113 |
| 3.2.4 Strain-Weakening Discussion..... | 115 |
| 3.3 Viscoelasticity | 118 |
| 3.3.1 Viscoelastic Model Considerations | 119 |
| 3.3.2 Homogeneous Viscoelastic Modeling Results..... | 127 |
| 3.3.3 Temperature-Dependent Viscosity Results..... | 129 |
| 3.3.4 Viscoelasticity Discussion | 130 |
| 3.4 Summary and Conclusions..... | 133 |
| Appendix 3A: Full Tidal Loading vs. Partial Tidal Loading | 163 |
| Chapter 4 | 169 |
| 4.1 Introduction | 169 |
| 4.2 Phase Shift in Analytic Models..... | 172 |
| 4.2.1 One-Dimensional Phase Shift..... | 173 |
| 4.2.1Phase Shift for a Nonlinear Maxwell Material..... | 174 |
| 4.3 Two-Dimensional Finite Element Models | 176 |
| 4.3.1 Methodology | 177 |
| 4.3.2 Numerical Results | 177 |
| 4.3.3 Application to Helheim Glacier Data | 180 |

| | |
|--|-----|
| 4.4 Discussion..... | 181 |
| 4.4.1 Data Constraints and Accuracy | 182 |
| 4.4.2 Survey Requirements | 183 |
| 4.4.3 Ideal Survey Targets | 186 |
| 4.5 Summary and Conclusions..... | 190 |
| Appendix 4A: Spatial Distribution of Phase Shift | 206 |
| Chapter 5 | 217 |
| 5.1 Introduction | 218 |
| 5.2 Model Methodology | 221 |
| 5.2.1 General Model for Turbulent Hydraulic Fracture..... | 222 |
| 5.2.2 Solution Method..... | 224 |
| 5.2.3 Nonlinear Viscoelasticity and Finite Element Implement. | 226 |
| 5.3 Model Solutions..... | 228 |
| 5.3.1 Linear Viscoelastic Results..... | 228 |
| 5.3.2 Nonlinear Viscoelastic Results | 230 |
| 5.3.3 “Pseudo-Nonlinear” Viscoelastic Results | 237 |
| 5.4 Comparison to Observations | 238 |
| 5.4.1 Lake Drainage | 239 |
| 5.4.2 Surface Deformation | 244 |
| 5.5 Discussion..... | 247 |
| 5.5.1 Re-Evaluating Lake Drainage Timing | 247 |
| 5.5.2 Influence of Viscoelasticity | 250 |
| 5.6 Summary and Conclusions..... | 253 |
| Appendix 5A: Effective Stress Formulation..... | 275 |
| Appendix 5B: Inhomogeneous Bernoulli-Euler Beam | 289 |
| Appendix 5C: Spatial Variability of Effective Viscosity | 295 |
| Appendix 5D: Conduit Size | 301 |
| Appendix 5E: Surface Deformation Caused by Crack Opening | 307 |
| Chapter 6 | 315 |
| 6.1 Synopsis..... | 315 |

6.2 The Importance of Ice Viscoelasticity 317

6.3 Closing Thoughts 320

References 321

LIST OF FIGURES

| <i>Number</i> | <i>Page</i> |
|---|-------------|
| 1.1 Location Map..... | 26 |
| 1.2 Ice Sheet Cross Section | 27 |
| 1.3 Satellite Imagery of Glaciers | 28 |
| 1.4 Tides and Seismicity of Kamb Ice Stream..... | 29 |
| 1.5 GPS Data from Whillans Ice Plain..... | 30 |
| 1.6 Tidal Displacements, Rutford and Bindschadler Ice Streams | 31 |
| 2.1 Model Schematics..... | 53 |
| 2.2 Frozen Bed Results | 54 |
| 2.3 Free Sliding Results..... | 55 |
| 2.4 Two- Dimensional Displacements..... | 56 |
| 2.5 L_{tr} Demonstration | 57 |
| 2.6 Three-Dimensional Stress State..... | 58 |
| 2.7 Three-Dimensional Displacements..... | 59 |
| 2.8 Parameter Variations, Two Dimensions | 60 |
| 2.9 Parameter Variations, Three Dimensions..... | 61 |
| 2.10 Model Geometry Comparison | 62 |
| 2.11 Model Displacement Decay..... | 63 |
| 2.12 Whillans Ice Plain Model..... | 64 |
| 2B.1 Beam Model Output | 73 |
| 2C.1–2C.8 Two-Dimensional Results | 75–82 |
| 2D.1–2D.13 Three-Dimensional Results..... | 84–96 |
| 3.1 Simple Viscoelastic Models..... | 138 |
| 3.2 Maxwell and Burgers Model Behavior | 139 |
| 3.3 Damage Formulation..... | 140 |
| 3.4 Ice Margin Models | 141 |
| 3.5 Continuous Margin Model Stress State | 142 |
| 3.6 L_{tr} and Elasticity | 143 |
| 3.7 Discrete Margin Model Stress State | 144 |
| 3.8 Discrete Margin Behavior..... | 145 |

| | |
|---|---------|
| 3.9 Margins Effect on L_{tr} | 146 |
| 3.10 Viscoelastic Model Schematics | 147 |
| 3.11 Tide Comparison | 148 |
| 3.12 Viscoelastic Model Stress State | 149 |
| 3.13 Homogenous Model, Semidiurnal Tide | 150 |
| 3.14 Homogenous Model, Diurnal Tide..... | 151 |
| 3.15 Homogenous Model, Fortnightly Tide..... | 152 |
| 3.16 Fitted Tidal Response..... | 153 |
| 3.17 Temperature Dependent Model, Semidiurnal Tide..... | 154 |
| 3.18 Temperature Dependent Model, Diurnal Tide | 155 |
| 3.19 Temperature Dependent Model, Fortnightly Tide | 156 |
| 3.20 Effective Viscosity | 157 |
| 3.21 Displacement Decay..... | 158 |
| 3.22 Hydrology Model | 159 |
| 3A.1 Tide Schematics | 167 |
| 3A.2 Effects of Full Tide..... | 168 |
| 4.1 One-Dimensional Linear Phase | 193 |
| 4.2 One-Dimensional Nonlinear Phase..... | 194 |
| 4.3 Phase Model Schematics..... | 195 |
| 4.4 Phase Results, Basal Model | 196 |
| 4.5 Phase Results, Side Wall Model | 197 |
| 4.6 Distance-Dependence, Basal Model..... | 198 |
| 4.7 Distance-Dependence, Side Wall Model..... | 199 |
| 4.8 Helheim Data Fit | 200 |
| 4A.1–4A.9 Spatial Variation in Phase Shift | 207–215 |
| 5.1 Drainage Model Schematics | 257 |
| 5.2 Pressure and Crack Opening Results..... | 258 |
| 5.3 Crack Opening Evolution..... | 259 |
| 5.4 Scaled Velocity..... | 260 |
| 5.5 Nonlinear Model Opening | 261 |
| 5.6 Normalized Opening and Effective Viscosity Profiles | 262 |
| 5.7 Crack Regimes | 263 |
| 5.8 Pseudo-Nonlinear Model Calibration | 284 |

| | |
|--|---------|
| 5.9 Lake Drainage Schematic | 265 |
| 5.10 Drainage Results, No Fluid Drag..... | 266 |
| 5.11 Drainage Results, Fluid Drag..... | 267 |
| 5.12 Model and Observed Surface Displacements..... | 268 |
| 5.13 Projected Model Surface Displacements | 269 |
| 5.14 Lake Drainage Time..... | 270 |
| 5.15 Conduit Opening Schematics..... | 271 |
| 5.16 Lake Bathymetric Effect | 272 |
| 5A.1 Effective Stress Formulation..... | 288 |
| 5B.1 Inhomogeneous Beam Deflection..... | 292 |
| 5B.2 Fit to Linear Beam..... | 293 |
| 5C.1–5C.5 Effective Viscosity Profiles | 296–300 |
| 5D.1 χ Behavior with Conduit Size..... | 304 |
| 5D.2 Crack Tip Velocity with Conduit Size..... | 305 |
| 5D.3 Drainage Parameters with Conduit Size | 306 |
| 5E.1 Surface Displacement Mesh Configuration | 309 |
| 5E.2 Conduit Condition Comparison, Elastic Model..... | 310 |
| 5E.3 Conduit Condition Comparison, Viscoelastic Model..... | 311 |
| 5E.4 Displacement Field, Elastic Model | 312 |
| 5E.5 Displacement Field, Viscoelastic Model..... | 313 |

LIST OF TABLES

| <i>Number</i> | <i>Page</i> |
|--|-------------|
| 1.1 Observations of Tidal Influence | 32 |
| 2.1 Material Properties..... | 65 |
| 2.2 L_{tr} Components | 66 |
| 2.3 Two-Dimensional Results | 67 |
| 2.4 Three-Dimensional Results | 68 |
| 3.1 Transitional Stresses | 173 |
| 3.2 Tidal Constituents..... | 174 |
| 3.3 Tidal Model Results | 175 |
| 4.1 Simple Viscoelastic Model Parameters | 201 |
| 4.2 Combined Tide De Values | 202 |
| 4.3 Helheim Viscosity Estimates | 203 |
| 4.4 Target Ice Stream Profiles..... | 204 |
| 5.1 Non-Dimensionalization Relationships | 273 |
| 5.2 Model Results, Drainage Parameters | 274 |
| 5B.1 Beam Model Parameters..... | 294 |

Chapter 1

Thesis Introduction

Sea level rise. Tipping points. Global warming. Today, the field of glaciology is irrevocably linked to the study of climate change, from the ivory tower to the network news. However, beyond attempts to quantify ice melting rates and predictions of the lifespans of dwindling glaciers, many aspects of the fundamental physics underlying the deformation of glaciers are poorly understood. Computational modeling of the response of glaciers in Greenland and Antarctica to hydrologic forcing over a timescale shorter than one month is the focus of this thesis. The results presented here are almost completely based on computational modeling but the goal is to explain several field observations of outlet glaciers and ice streams in the published literature. The interaction between ocean tides and ice stream motion (chapters 2, 3, and 4) and the rapid drainage of supraglacial meltwater lakes are the two glacial processes on which this thesis focuses.

The introductory section describes the Earth's cryosphere, focusing on the current scientific interest in glacier dynamics. The next section outlines the classical treatment of ice dynamics—both for general ice masses and the specific case of ice streams. The introduction then summarizes the current understanding of the interaction between the ocean tides and outlet glaciers, specifically over timescales shorter than a month. The next section discusses observations of the tidal influence on outlet glaciers from Antarctica and Greenland. The penultimate introductory section is a brief synopsis of the

finite element modeling methods used throughout this thesis. Last is a short outline of the remainder of this thesis.

1.1 The Cryosphere

The term *cryosphere* refers to all frozen water on planet Earth. While sea ice, river and lake ice, snow, and permafrost all belong to the cryosphere, glacial ice dominates the system. A *glacier* refers to any mass of crystalline ice that both persists over the course of an entire year and is large enough to flow under its own weight. The largest glaciers on the planet are the Antarctic and Greenland Ice Sheets, which together contain nearly 85% of all the freshwater on the planet (e.g., SMIC Report, 1971; L'vovich, 1979; IPCC, 1990; 1996; Van der Veen, 1999).

In the past few decades, the specter of global climate change has driven a renewed interest in the cryosphere, focusing on the fact that water in the cryosphere, primarily in the Greenland and Antarctic Ice Sheets, is equivalent to about 65 meters of sea level equivalent height (e.g., Cuffey and Paterson, 2010; Lythe et al., 2001; Bamber et al., 2001; Meier et al., 2007; Dyurgerov and Meier, 2005). As highlighted by the International Panel on Climate Change's (IPCC's) Fourth Assessment Report (2007), the lack of understanding of the interaction between the cryosphere and hydrosphere (i.e., ice sheets and the ocean) is a key piece of missing information that limits the believability of forward, predictive climate modeling. Upwards of 60% of the ice leaving the Greenland Ice Sheet and upwards of 90% of the ice leaving the Antarctic Ice Sheet is carried through a limited number of fast moving outlet glaciers, thus understanding the dynamics of these outlet glaciers is critical to predicting future ice levels (e.g., Cuffey and Paterson, 2010; Morgan et al., 1982; Bauer, 1961; Rignot and Kanagaratnam, 2006). The focus of

the first two research chapters is the interaction of these outlet glaciers and the short-term ocean tides.

We use Cuffey and Paterson (2010) as the reference for defining the characteristics of outlet glaciers. The technical definition of an *outlet glacier* is a fast-moving region of ice bounded by visible rock; an *ice stream* is a fast-moving region of ice bounded only by slower-moving ice. However following the convention of Cuffey and Paterson (2010), these terms are used interchangeably. The distinction between outlet glaciers and ice streams is generally too strict for practical use as many glaciers transition between ice-ice and ice-rock boundaries over their lengths. Note that while ice streams and outlet glaciers almost always flow into the ocean, the presence of a floating ice shelf or ice tongue is not a defining characteristic. Figure 1.1 shows the locations of all the ice streams discussed in this thesis.

As mentioned earlier, the majority of ice leaving the Greenland and Antarctic Ice Sheets travels through outlet glaciers. Direct calving of icebergs and basal melt are two of the primary mechanisms for removal of ice mass (e.g., Jacobs et al, 1992; Vaughan and Doake, 1996; Reeh et al., 1999; Mote, 2003; Wild et al., 2003; Hanna et al., 2005; Box et al., 2006; Krinner et al., 2006; Rignot et al., 2008; Cuffey and Paterson, 2010). Calving occurs when fractures propagate through the ice thickness at the edge of a glacier, resulting in blocks of ice shearing off the main ice body. Usually these new icebergs are carried out to sea, where they eventually melt. Basal melting occurs due to frictional heating along the base of grounded ice, melting due to geothermal heat along the base (e.g., subglacial volcanism, such as in Iceland), and the melting of floating ice shelves due to warmer ocean water reaching the ice's base.

Over long timescales, changes in the climate system can dramatically impact the response of ice streams to the conditions of the ocean. Increased melting, both on-land and at the grounding line due to higher ocean temperatures, reduces ice in the ice stream system and lubricates the ice stream's base, further increasing flow speeds. The combination of increased flow speeds and increased basal melt can thin ice streams to the point that any attached ice shelf breaks up. Ice shelf breakup in turn causes increased ice stream speeds due to the removal of the buttressing stress of the ice shelf, as was observed in the 1995 breakup of the Larsen A Ice Shelf and the 2002 breakup of the Larsen B Ice Shelf in Antarctica (Rott et al., 2002; De Angelis and Skvarca, 2003; Rignot et al., 2004, Scambos et al., 2004). Thus, the long-term behavior (and future) of ice shelves is linked to the interaction, and potential feedback, between the cryosphere and the earth's oceans.

However, the loss of ice through outlet glaciers is not the only mechanism for removing mass from the Greenland and Antarctic Ice Sheets on yearly timescales. Surface melt accounts for about 40% of the ice lost from Greenland and about 10% of the ice lost from Antarctica each year (e.g., Box et al., 2006; Krinner et al., 2006; Cuffey and Paterson, 2010). While this mass loss alone is significant, there is evidence from Greenland that supraglacial meltwater, should it reach the glacier's bed, can increase ice flow rates (e.g., Zwally et al., 2002; Joughin et al., 2008). The potential for such a feedback to cause a dramatic increase in the loss of ice mass with increasing temperatures (and thus melt rates) is not fully established, but modeling suggests that the effect can increase the mass-loss by upwards of a factor of two (Parizek and Alley, 2004).

Ultimately, while this thesis is not a direct study of the interaction of the cryosphere and the global climate system, that connection is the background motivation of this work. The hope is that the research presented here helps to elucidate some of the fundamentals of the response of ice to short timescale forcing. Understanding the hourly and daily dynamics of outlet glaciers requires more study. Through the investigation of tidal forcing of ice streams (chapters 2 to 4) and rapid drainage of supraglacial lakes (chapter 5), this thesis demonstrates some of the modeling concerns of processes that span the gap between very rapid (elastic) response on the order of days and more measured (viscous) response of ice streams on the order of years. The remainder of this introduction focuses on background information related to tidal forcing of ice streams, while the introductory material for the lake drainage problem is deferred to chapter 5 as that background material is unrelated to the remainder of this thesis.

1.2 Ice Stream Dynamics

This section provides a brief summary of ice stream dynamics. Information is presented from the introductory textbooks on glaciology by Van der Veen (1999) and Cuffey and Paterson (2010). A discussion of the general deformation of ice sheets and other non-streaming glaciers illustrates the unique nature of ice stream behavior. A description of the general physics in the extreme cases of ice stream geometry follows.

Consider a cross-sectional view of an ice sheet, as is shown in figure 1.2. The surface deformation at the location of a longitudinal cross section can be approximated by:

$$\vec{u} = \vec{u}_d + \vec{u}_b \quad (1.1)$$

where the total velocity vector \vec{u} is the additive sum of the internal deformation \vec{u}_d and the basal sliding \vec{u}_b .

In terms of internal deformation, we assume that glacier flow is driven by the weight of the ice itself, where the basal driving stress τ_b for a vertical profile of the ice is:

$$\tau_b = \rho_i g H \sin(\alpha) \quad (1.2)$$

where ρ_i is the ice density, g is gravitational acceleration, H is the ice thickness, and α is the surface slope. Assuming that ice deforms viscously over most timescales, that viscous deformation can be expressed using a canonical Glen-style flow law (Glen, 1955; 1958), and that glacier flow is laminar, we find that:

$$\vec{u}_d = \frac{2A_D}{n+1} (\tau_b)^n H \quad (1.3)$$

The value for the stress exponent n is traditionally chosen to be equal to three based on laboratory stress-strain curves (e.g., Glen, 1955; 1958).

To approximate basal sliding, we use the Weertman sliding law (Weertman, 1957; 1964), which assumes that the ice/bed interface is smooth and lubricated, save for a set of cubic bumps located at a regular interval. The resulting form of the sliding law, lumping many model parameters into the value A_W , is:

$$\vec{u}_b = A_W \tau_b^{\frac{n+1}{2}} \quad (1.4)$$

Such a sliding law is only applicable to glaciers that have a hard (i.e., rock) bed, as a soft, deformable till layer will behave differently. Observationally, most ice sheets are both slow moving and poorly lubricated at their bed, and thus are dominated by the internal deformation of the ice body (Cuffey and Paterson, 2010).

We are now equipped to comment on the dynamics of ice streams. Unlike ice sheets proper, ice streams are characterized by rapid velocities (e.g., Mae, 1979; Alley et

al., 1986; Bindschadler et al, 1986; Blankenship et al., 1986; Bindschadler et al, 1987; Shabtaie and Bentley 1987; 1988; Engelhardt et al., 1990; Engelhardt and Harrison, 1990; Alley and Whillans, 1991; Echelmeyer et al., 1991; Kamb, 1991; Echelmeyer et al., 1992; Iken et al., 1993; Funk et al., 1994; Clarke and Echelmeyer, 1996; Whillans and van der Veen, 1997; Sohn et al., 1998; van der Veen, 1999; Joughin et al, 2001; Kamb, 2001; Raymond et al., 2001; Lüthi et al., 2002; Thomas et al., 2003; Thomas, 2004; Joughin et al., 2004a/b; Cuffey and Paterson, 2010; many others). Apart from their rapid motions, ice streams can be quite diverse in character. On one end of the spectrum are the ice streams of the Siple Coast, Antarctica, or Rutford Ice Stream, which are characterized by very low surface slopes (and thus low driving stresses), heavily crevassed ice-ice lateral margins and a deformable till base. These ice streams are also extraordinarily long, reaching lengths of at least a few hundred kilometers in some cases. On the other end of the ice stream spectrum are the outlet glaciers found in Greenland, such as Helheim and Jakobshavn Isbrae. These ice streams are short, steep (high driving stress), and bounded by ice-rock margins along the confining fjords through which these outlet glaciers flow. Figure 1.3 shows satellite imagery of the Siple Coast, Rutford Ice Stream and Helheim Glacier. We discuss the dynamics of each separately as end-member possibilities.

The low driving stresses on the West Antarctica ice streams of the Siple Coast, as small as 20 kPa (Alley and Whillans, 1991), necessarily implies essentially zero basal tractions on these ice streams. From equations 1.3 and 1.4, we see this means very small amounts of internal deformation and very little sliding along the ice-bed interface (assuming a Weertman sliding law). Therefore, the observed rapid ice velocities must be

accounted for through deformation of the substrate beneath the ice streams. Numerous studies suggest that there is both a well-hydrated till layer beneath the Siple Coast ice streams, and that this till layer readily deforms plastically (e.g., Alley et al., 1986; Engelhardt et al., 1990; Kamb, 1991; Engelhardt and Kamb, 1998; Tulaczyk et al., 1998; 2000a/b; Kamb, 2001). In this configuration, the primary resistance to the ice stream's motion comes from the lateral margins of the ice streams, where the ice velocity rapidly falls by several orders of magnitude in the highly crevassed shear margins (Whillans et al., 1987; 1993; Whillans and van der Veen, 1993a/b).

Additionally, the ice streams of the Siple Coast are not flowing in a steady-state regime, as preserved paleo-glaciological features indicate different flow directions and orientations over the ice streams' existences (e.g., Conway et al., 2002; Retzlaff and Bentley, 1993; Clarke et al., 2000; Fahnestock et al., 2000; Gades et al., 2000; Joughin et al., 2004c). Furthermore, the velocity of ice streams can vary strongly over periods of centuries (Joughin et al., 2005). Cuffey and Paterson (2010) describes three hypotheses for the mechanism behind these long-timescale flow variations as: changes in ice stream geometry (e.g., Jacobson and Raymond, 1998), variations in basal water pressure (e.g., Raymond, 2000), and basal freeze-on resulting in stream stagnation (e.g., Alley et al., 1994; Tulaczyk et al., 2000b; Joughin et al., 2004b).

The fjord-constrained ice streams of Greenland are altogether different, primarily as the basal driving stress can reach values of 300–420 kPa due to the steep surface slopes (e.g., Clarke and Echelmeyer, 1996; Echelmeyer et al., 1991; 1992; Cuffey and Paterson, 2010). Estimates of Clarke and Echelmeyer (1996) suggest that frictional stress from the lateral margins balances between 10% and 50% of this driving stress, meaning

that the bed must support the remaining stress. Furthermore, these glaciers are assumed to lack the soft till beds that are found beneath Antarctic ice streams due to these large basal driving stresses, flowing instead along the hard rock bases of fjords. As there is no till layer to accommodate the driving stress, this stress partitioning necessary leads to internal deformation being more important to ice motion than basal sliding (compare equations 1.3 and 1.4 with a value of $n=3$). This situation matches the modeling of Echelmeyer et al. (1991; 1992), which suggests that the internal deformation of Jakobshavn Isbrae is sufficiently large to explain the rapid ice velocity over most of the glacier, with basal sliding only necessary at the foot of the glacier where the driving stress drops due to shallower surface slopes. Thus, unlike the case of the Antarctic ice streams, the base of outlet glaciers in Greenland is thought to provide the primary resistance to flow.

1.3 Tidal Interaction with Grounded Ice

Section 1.1 described how the long-term variability in the interaction between outlet glaciers and ocean tides can impact the motion of the ice streams. Of course, the tides act on the solid earth in addition to the world's oceans. However, several factors argue against the importance of the *earth tides* in determining the tidal behavior of ice streams and outlet glaciers. First, the amplitude of the semidiurnal and diurnal earth tides are small at high and low latitudes, theoretically reaching a value of zero at the north and south poles for an idealized spherical earth. While such a simplification clearly does not hold for the real earth, studies of ocean and earth tides in Greenland and Antarctica suggest that the magnitude of the earth tide is at least an order of magnitude smaller than that of the ocean tides for these regions (e.g., Thiel et al., 1960; Zwally et al., 1983).

Second, the phase variation in the tidal response of many ice streams (as discussed below, e.g., Gudmundsson, 2006; 2007; de Juan, 2009; 2010a/b; de Juan Verger, 2011) suggests that the response is not caused by the earth tides, which acts roughly uniformly over the length-scales studied here (a few hundred kilometers). Thus, from this point forward, any reference to the tides will implicitly mean the ocean tides, unless otherwise specified.

Ocean tides obviously vary over timescales far shorter than those of sea level change, with the most relevant ocean tides being the semidiurnal, diurnal, and fortnightly tides. These short-period ocean tides directly control the motion of ice streams, foremost through the flexing of the ice stream due to the rising and falling of an attached ice shelf with the ocean tide. From surface observations, the spatial extent of ice flexure is limited to the first five to ten ice-thicknesses inland of the *grounding line*—the position where the ice stream transitions from floating to grounded ice (e.g., Rignot 1998a). Tidal flexure has been used primarily to constrain rheological parameters of *in situ* ice (assuming elasticity and, more recently, linear viscoelasticity). Such work derives values of Young modulus that are between three and ten times smaller from ice flexure than from laboratory experiments (e.g., Holdsworth, 1969; 1977; Lingle et al., 1981; Stephenson, 1984; Vaughan, 1994; 1995; Rignot 1996; 1998a/b; Reeh et al., 2000; 2003 compared against Petrenko and Whitworth, 1999). While useful for approximating rheological parameters, these flexure studies are essentially independent of the ocean tidal frequency, as these studies all focus on fitting the maximum tidal flexure amplitude and transmission.

A consequence of ice flexure during a tidal cycle is that the grounding line of an ice stream will necessarily move with the ocean tides, traveling further inland during high

tides and further seaward during low tides. As the exact amount of such a motion is dependent upon the slope and character of the ground beneath the ice stream, such behavior is inherently difficult to model. Observations from Antarctica (e.g., Rignot 1998a) suggest that the extent of this *grounding line zone* is approximately five kilometers—a distance equivalent to the flexural wavelength of an ice stream.

However, a more subtle interaction between the ocean tides and ice stream motion exists. Over the past two decades, glaciologists have accumulated a critical mass of tidally relevant observations such that the character of the tidal interaction with the flow of ice streams, especially at different frequencies, can now be broadly characterized. The next two subsections summarize such observational data, first from Antarctic ice streams and second from Greenland outlet glaciers.

1.3.1 Antarctic Tidal Interactions

Observations from Antarctica show tidally modulated surface displacements on some ice streams extend many tens of kilometers inland of the grounding line (see table 1.1 and associated references). Three classes of observations probe the interaction between ocean tides and the motion of ice streams: 1) surface tilt of the ice stream as estimated by tiltmeters, interferometric synthetic aperture radar (InSAR) and altimetric surveys; 2) surface recordings of basal seismicity beneath ice streams; 3) surface motion of ice streams from global position system (GPS) surveys. These observations can be used to identify which portion of an ice stream may be sensitive to tidal forcing (see table 1.1). Next is a summary of observations where the ocean tides do not have an impact on the motion of an ice stream far inland of the grounding line. While this thesis focuses on the observations of long distance transmission of tidal stresses, the usual tidal response of ice

streams is that the ocean tides only influence the motion of ice close to the grounding line.

Surface Tilt

Surface tilt surveys quantify the maximum extent of tidal flexure of an ice body. The location of the change in curvature in ice surface due to the flexure of the ice stream is defined as the hinge line. The hinge line is found between five and ten kilometers inland for all ice streams in table 1.1 regardless of the specific method of determining hinge line location. For comparison, the hinge line is farther inland than the physical ungrounding of the ice stream due to increased flotation at high tide, which extends about five kilometers as an upper boundary for stable tidal modulation (e.g., Rignot, 1998a).

Seismicity

Seismic studies on several Siple Coast ice streams correlate fluctuations in basal seismicity to the semidiurnal and/or fortnightly ocean tides. As these seismic triggers have been located at the base of the ice stream, there is probable cause to search for a link between the ocean tidal loading and the basal stress state in these ice streams. The rationale is as follows: ice slides frictionally over its bed, triggering seismicity due to asperities at the ice-bed interface. Changes in ocean tides can perturb the stress balance at the base of the ice stream by modifying the basal shear stress (e.g., Anandakrishnan et al., 1997; Bindschadler et al., 2003; Cuffey and Paterson, 2010). The rate of seismicity should correlate positively with the rate of motion, meaning that as basal shear stress increases, so too should the ice velocity, and thus the seismicity at the ice-bed interface.

The first suggestion of possible tidal variation in the observed seismicity beneath an ice stream came from Harrison et al. (1993). Harrison et al. suggests that ocean tides

may influence seismicity on Whillans Ice Stream at a single station 300 kilometers away from the nearest grounding line through the subglacial hydrologic network. This locale is somewhat anomalous in the observations of ocean tidal influence on ice streams due to its extreme distance inland of the grounding line. We are hesitant to use this site as a robust marker of tidal influence for three reasons. First, the authors note that the strain amplitudes are independent of the tidal amplitudes, a result unexpected for true tidal influence. Second, the authors also point out that the tidally variable strain appears and disappears seasonally whereas the ocean tides obviously do not. Third, the distance inland of this data point is in direct opposition to a limit set by the constraint provided by the geodetic survey of Winberry et al. (2009) described in section 2.2.3. As a result, we note the potential for tidal signal described in Harrison et al. (1993) for completeness, but we do not use it as an observational constraint for the purposes of ground-truthing our model results.

Observations from a three station seismic survey described in Anandkrishnan et al. (1997) limit the spatial extent of tidal sensitivity on Kamb Ice Stream to between 86 kilometers and 126 kilometers inland from the grounding line. The authors find that the frequency of subglacial seismic events correlates temporally with low tides within the nearby Ross Sea. Figure 1.4 shows an adaptation of figure 4 of Anandkrishnan et al. (1997) for the purpose of describing the observation. This figure shows the seismicity at a station 10 kilometers inland of the grounding line. While the seismicity peaks do not correspond one-to-one with the diurnal low tides, all the spikes in seismicity fall at these times. Of note is that the signal seems to be independent of the fortnightly variability in the tidal amplitude. Finally, the authors note that the Kamb Ice Stream is likely devoid of

subglacial water in the region of tidal modulated icequakes (based on Rose, 1979; Atre and Bentley, 1993; Anandakrishnan and Alley, 1994), implying that the connection between the ocean tides and the basal seismicity is carried through the bulk of the ice stream rather than through the subglacial hydrologic network.

Bindschadler et al. (2003) observed stick-slip generated seismicity on Whillans Ice Plain, a fact corroborated by the later studies of Wiens and other (2008) and Walter et al. (2011). These latter two studies disagree on the location of the nucleation of the observed stick-slip events, locating the seismicity either 10 or 50 kilometers inland of the grounding line of Whillans Ice Plain. In either case, stick-slip motion begins at an assumed asperity at the nucleation point and then propagates radially inland from there.

Geodesy

Temporally continuous GPS (CGPS) surveys on some Antarctic ice streams find surface velocities modulating at a variety of tidal frequencies. Here, we review data from Rutford Ice Stream (Gudmundsson, 2006; 2007), Bindschadler Ice Stream (Anandakrishnan et al., 2003), and the Whillans Ice Plain/Ice Stream (Wiens et al., 2008; Winberry et al., 2009). For Rutford and Bindschadler Ice Streams, the tidal influence manifests itself as a variable tidal displacement in the flow direction when the GPS signal is de-trended for the linear motion of the ice towards the grounding line. On the Whillans Ice Plain and Ice Stream, the ocean tides modulate the timing of the onset of stick-slip motion, roughly in phase with the maxima and minima of the tides.

As the CGPS surveys are the most temporally-refined method of observing the tidally-induced motion of these ice streams, we focus on these data as our primary constraints. As the ice streams are rapidly flowing, the GPS signal has a strong linear

trend associated with the background flow velocity, which over the timescales studied here is roughly constant. By subtracting the background flow rate (i.e., the displacement due to the average ice flow), any remaining displacement signal must be due to other processes, the foremost of which is the influence of ocean tides. Figure 1.5 shows such a process for a few selected GPS stations from the Whillans Ice Stream as a representative case (data provided by S. Anandakrishnan and H. Gudmundsson).

All the studies discussed here involve GPS surveys with stations either placed linearly along the flow line of the ice stream (Rutford, Bindschadler, and Whillans Ice Streams) or in a grid across the ice stream (Whillans Ice Plain). Thus, the relative amplitude of displacement due to the tidal load as a function of distance is fairly well constrained. All the surface displacements corresponding to the tidal modulated motion decay with distance inland from the grounding line with decay length-scales (for an order of magnitude drop) on the range of 35 to 75 kilometers, as shown in figure 1.6 (data from Anandakrishnan et al., 2003; Gudmundsson, 2006; 2007). For the ice streams in question, the maximum inland distances where a discernible tidal signal in the surface displacement is seen are: 40 kilometers inland of the grounding line for Rutford Ice Stream, 80 kilometers inland of the grounding line for Bindschadler Ice Stream, and from the spatial distribution of tidal-frequency stick-slip events, at least 100 kilometers inland of the nearest grounding line for the Whillans Ice Plain.

An additional major constraint on the tidally-induced surface motion of these ice streams is the phase lag between the observed tidal displacement signal and the peak tidal amplitude. As part of the aforementioned studies, at least one GPS station was placed on floating ice. In each study, the vertical displacement of this floating station functionally

became the tidal record. When the GPS records at the inland sites are de-trended to remove the background flow, we can measure an apparent phase-shift between the tidal frequencies seen in the floating tidal signal and the grounded surface displacement records.

For Rutford Ice Stream, Gudmundsson (2006; 2007) demonstrates that there is a distance dependent phase lag in the signal, such that the phase of all tides (semidiurnal, diurnal, and fortnightly) increases with inland distance. For reference, these studies define a zero-phase ice response as having the peak outboard de-trended ice motion contemporaneous with the high tide from the tide model T_Tides (Pawlowicz et al., 2002). Additionally, the phase is between 45 and 270 degrees behind the tidal signal, suggesting that the high tide corresponds roughly with the maximum (de-trended) inland displacement in the GPS records. Additionally, a non-zero phase is seen even on the floating ice shelf, meaning that the motion of the glacier is never in-phase with the ocean tides. From GPS data on Bindschadler Ice Stream, Anandakrishnan et al. (2003) found that the relative phase lag in the ice response to the diurnal tide grows from 1.1 ± 2 hrs (16.5 ± 30 degrees) at 40 kilometers inland to 3.1 ± 2 hrs (46.5 ± 30 degrees) at 80 kilometers inland, similarly showing a distance dependence to the phase lag. For the Whillans Ice Stream and Plane, the stick-slip motion of the ice makes determining a phase lag in the displacement signal untenable.

Contrary Observations

Not all Antarctic ice streams show measurable tidal modulation of surface displacements upstream of their hinge lines. CGPS observations on Pine Island Glacier, for example, show no tidal variability in surface motion at stations 55, 111, 169, and 171 kilometers

inland of the grounding line (Scott et al., 2009). Ekstrom Ice Shelf has an even tighter constraint on the spatial extent of tidal perturbations: CGPS recordings only one kilometer inland of the grounding line possess no measurable component of motion at tidal frequencies (Riedel et al., 1999; Heinert and Riedel, 2007). As will be discussed in the next section the spatially-limited transmission of a tidal signal on these Antarctic ice streams is similar to outlet glaciers in Greenland.

1.3.2 Greenland Tidal Interactions

Direct observations of short-timescale tidal influence on the behavior of outlet glaciers in Greenland are more limited than those from Antarctica. GPS studies investigating the floating portion of Kangerdlugssuaq and Helheim Glaciers reveal flow velocities that fluctuate with ocean tides (Hamilton et al., 2006; Davis et al., 2007; de Juan et al., 2009; 2010a/b; de Juan Verger, 2011). Of this work, the largest single GPS survey is the geodetic survey of Helheim Glacier from 2006–2009, comprised of 23 GPS stations arrayed over the length of Helheim Glacier (de Juan, 2009; 2010a/b; de Juan Verger, 2011).

From the aforementioned geodetic survey, de Juan Verger (2011) was able to characterize the tidal interaction of Helheim glacier based on the admittance amplitude (relative magnitude of tidally-induced glacier displacement to the ocean tidal amplitude) and the phase lag between the GPS receivers on the lower portion of Helheim glacier and a tidal record from within the Sermilik Fjord (into which Helheim Glacier flows). The admittance amplitude decays exponentially with distance inland from the glacier's calving front with a phase lag of 0–4 hours (0–120 degrees). For the purposes of this summary, we divide the survey into two portions: first, the 2006 records, where Helheim

Glacier had a floating ice tongue; and second, the 2007-2008 survey, where Helheim Glacier has no floating ice tongue.

During the 2006 survey when Helheim Glacier had a floating ice tongue, de Juan Verger (2011) reports that there is a tidal signal in the along-glacier, cross-glacier, and vertical directions. In all cases, the signal decays exponentially with distance away from the glacier's edge, with the cross-glacier and vertical components decaying over an e-folding length of about 1.0 kilometers, while the along-glacier length-scale is about 2.3 kilometers. These distances translate to an order of magnitude drop in stress over a length of 3.7 kilometers and 8.5 kilometers, respectively. For reference, the thickness of Helheim Glacier was approximately 750 meters during these surveys (de Juan Verger, 2011). The de-trended response of Helheim Glacier to the semidiurnal ocean tides is out of phase, such that at high tide the de-trended position of Helheim Glacier is farther inland than at low tide. However, there is additional lag between this response and the semidiurnal ocean tides, such that the peak glacier motion is delayed relative to the peak tidal amplitudes. The best fit phase lag between the response of the along-glacier displacement and the tide gauge ranges between about 1 hour and 2 hours (30-60 degrees), though a large error on some data points allows for a range that may extend between 0 and 4 hours (0-120 degrees). The best fit values suggest an increase in phase lag with distance inland, but such a trend is dubious at best as the magnitude of the distance-variation falls below the errors of the fits.

For the grounded glacier surveys during 2007-2008, de Juan Verger (2011) reports that there is essentially no tidal signal in the cross-glacier and vertical directions, while the e-folding length-scale for the along-glacier admittance amplitude is around 4.2

kilometers for the two years. This decay rate translates to an order of magnitude drop in amplitude over a distance of around 15.3 kilometers. As in the 2006 survey, the response of Helheim Glacier is out of phase with the semidiurnal ocean tide, with the best fit phase lags falling between 2 and 3 hours (60–90 degrees) with errors ranging from 0 to 4 hours (0–120 degrees). Similarly between surveys, there is a slight trend for increasing phase with the best fit phase values, but that this trend is well within the error of the observations. However, the mean values of the best fit do seem to indicate that the grounded ice may have an increased phase lag compared to the floating ice.

Apart from this work, the only other major observations of tidal forcing of Greenland outlet glaciers come from Jakobshavn Isbrae. On Jakobshavn Isbrae, the lowest reaches of the ice stream are found to have a variable velocity at tidal frequencies (up to 35%, Echemeyer and Harrison, 1990; 1991), but that the tidal amplitude of this signal decays rapidly inland of the ice stream terminus, with a characteristic length-scale of a few ice-thicknesses (Podrasky et al., 2002; 2012). Inland of this tidal signal there are variations in ice stream velocity, but Podrasky et al. (2012) accounts for these variations through seasonal melt rather than ocean tidal loading. There is no discussion of the relative phase of the glacial motion compared to the ocean tidal signal for Jakobshavn Isbrae within these works.

1.3.3 Observation Summary

To close our discussion of the observations of tidal influence on ice stream motion, we summarize the salient features of these tidal observations as:

- 1) Not all ice streams exhibit tidally modulated surface motion far from the grounding line. For example, Helheim Glacier has a tidal signal that is essentially

unseen beyond 14 kilometers inland of the calving front. However, some Antarctic ice streams transmit tidal signals many 10's of kilometers inland of the grounding line.

- 2) Tidal influence on ice motion happens over multiple timescales, often at semidiurnal, diurnal, and fortnightly periods. The ice stream seems to filter some of the tidal frequencies such that the de-trended GPS records do not exhibit many of the beat frequencies seen from the vertical component of GPS stations on floating ice.
- 3) The time-domain phase of the ice stream response can vary with distance inland of the ice stream's grounding line. Such temporal lag likely provides information about the rheology of the material transmitting the tidal stress inland. Furthermore, the phase lag is different over the various tidal frequencies.
- 4) Indirect measurement of ice stream motion, such as seismicity located at the ice stream's bed, indicate that basal processes are important to determining the motion of a given ice stream. However, the variability in seismicity on tidal periods implies that there is some connection between the tidal forcing on the ice stream and the frictional processes at the bed-ice interface.

1.4 General Finite Element Methods

Because we use finite element modeling throughout this thesis, we now depart from glaciology briefly to present a summary of the computational finite element methods here. In the later chapters, we will discuss project-specific modeling finite element formulation and model configurations. All of our finite element methods use the finite element analysis software *PyLith* (Williams et al., 2005; Williams, 2006; Aagaard et al.,

2007; 2008; 2011). This open-source Lagrangian FEM code has been developed and extensively benchmarked in the crustal deformation community (available at www.geodynamics.org/pylith).

PyLith solves the conservation of momentum equations with an associated rheological model. As we assume a quasi-static formulation (i.e., all inertial terms are dropped), the governing equations are:

$$\begin{aligned}\sigma_{ij,j} &= f_i \text{ in } V \\ \sigma_{ij}n_j &= T_i \text{ on } S_T \\ u_i &= u_i^0 \text{ on } S_U\end{aligned}\tag{1.5}$$

where V is an arbitrary body with boundary condition surfaces S_T and S_U . On S_T , the traction $\sigma_{ij}n_j$ equals the applied Neumann boundary condition T_i . On S_U , the displacement u_i is set equal to the applied Dirichlet boundary condition u_j^0 .

PyLith solves these equations using a Galerkin formulation of the spatial equation and an unconditionally stable method of implicit timestepping (following the form of Bathe, 1995). For model convergence, we select convergence tolerances in absolute and relative residual of the iterative solver from the *PETSc* library (Balay et. al, 1997; 2012a/b) such that our model results are independent of the convergence tolerances to a factor of less than 1/1000%. Such convergence tolerances are determined through trial-and-error with our model accuracy criterion chosen to provide reliable results while minimizing the computational time of any given model.

We construct our FEM meshes using the software *Cubit* (cubit.sandia.gov). For our two-dimensional models, we use linear isoparametric triangular elements, while in our three-dimensional modeling we use linear isoparametric

quadrilateral or tetrahedral elements. We manually refine our meshes near regions of applied stresses, changes in boundary conditions, and material property variations. In such locations our mesh spacing can be as small as 1 meter, resulting in meshes with between 10^5 and 10^6 elements. To ensure that our results are independent of our meshing scheme, we check all our results against meshes that are uniformly refined. We only present results from meshes that have less than a 0.1% change in displacement, 1st strain invariant, and 2nd deviatoric stress invariant upon this refinement in our elastic models and less than 1% in our viscoelastic models. We allow a greater error in our viscoelastic modeling as the computational time necessary for a 0.1% error is restrictively long.

Our final modeling constraint is our choice of material rheology. We begin with a linear, isotropic elastic model for ice in our models that takes the familiar form of Hooke's Law in three dimensions:

$$\mathbf{C}_{ijkl} = \lambda \delta_{ij} \delta_{kl} + \mu (\delta_{ik} \delta_{jl} + \delta_{il} \delta_{jk}) \quad (1.6)$$

The choice of material moduli varies between our models; however, for all our models we assume that the Poisson's ratio is well known for ice (and thus is fixed) when exploring the ranges in values of the other elastic moduli. We also consider a Glen-style Maxwell viscoelastic rheology:

$$\dot{\epsilon} = \frac{\dot{\sigma}}{E} + A \sigma^n \quad (1.7)$$

As we vary the value of the viscosity coefficient A and the power law exponent n in our modeling, the selection of the precise values of these quantities will be discussed in each chapter separately.

1.5 Thesis Outline

This thesis is divided into four sections summarizing the results from three separate research projects undertaken between 2009 and 2013. In chapter 2, we test the common assumption that tidal loads are transmitted elastically through the bulk of ice streams to the long inland distances observed in Antarctica. We find that the geometric constraints of the ice stream itself limit the transmission of a tidal stress to distances far shorter than seen observationally. In chapter 3, we then explore the potential effect that including strain-weakened lateral margins and viscoelasticity in models has on the transmission length-scale.

Chapter 4 outlines a procedure for using geometrically simple finite element models and surface observations of tidally modulated glacier motion to constrain viscoelastic rheological parameters. We also explore the type, quantity, and quality of surface observations needed to provide an accurate constraint on the *in situ* material properties for outlet glaciers. We then provide a test example using GPS data from Helheim Glacier, Greenland.

Chapter 5 discusses our results from investigating the impact of viscoelastic deformation during transient drainage events of supraglacial lakes. We present both semi-analytic linear viscoelastic and finite element nonlinear viscoelastic modeling, using as a constraint observations from a 2006 lake drainage event near Jakobshavn Isbrae, Greenland.

At the end of each chapter, we include a list of all variables specific to that chapter. While many variables are shared between chapters, some variables have multiple definitions between chapters. Following the variable list are the figures and

tables discussed in the main chapter. The final portion of each chapter includes any associated appendices. For appendices with figures and tables, these are presented at the end of that appendix. Lastly, as many of the references are common between chapters, all references for the entire thesis are included at the end of the full document.

| | Variable Names | Units |
|--|---|---------------------------------|
| | A Nonlinear viscosity coefficient | $\text{Pa}^{-n} \text{s}^{-1}$ |
| | A_D Ice deformation coefficient | Pa^{-n} |
| | A_W Basal sliding coefficient | $\text{Pa}^{-(n+1)/2} \text{m}$ |
| | \mathbf{C}_{ijkl} Elasticity tensor | Pa |
| | E Young's modulus | Pa |
| | f_i Force vector | N |
| | g Gravitational acceleration | m s^{-2} |
| | H Ice sheet thickness | km |
| | n Power law exponent | -- |
| | n_i Normal vector | -- |
| | S_T Traction boundary surface | -- |
| | S_U Displacement boundary surface | -- |
| | T_i Applied traction | Pa |
| | \vec{u} Velocity vector | m/s |
| | \vec{u}_b Basal sliding vector | m |
| | \vec{u}_d Internal deformation vector | m |
| | u_i Displacement component | m |
| | u_i^0 Applied displacement | m |
| | V Model volume | m^3 |
| | α Surface slope | $^\circ$ |
| | δ_{ij} Kronecker delta | -- |
| | ε Strain | -- |
| | λ 1 st Lamé constant | Pa |
| | μ 2 nd Lamé constant | Pa |
| | ρ Ice density | kg m^{-3} |
| | σ Stress | Pa |
| | τ_b Basal stress | Pa |

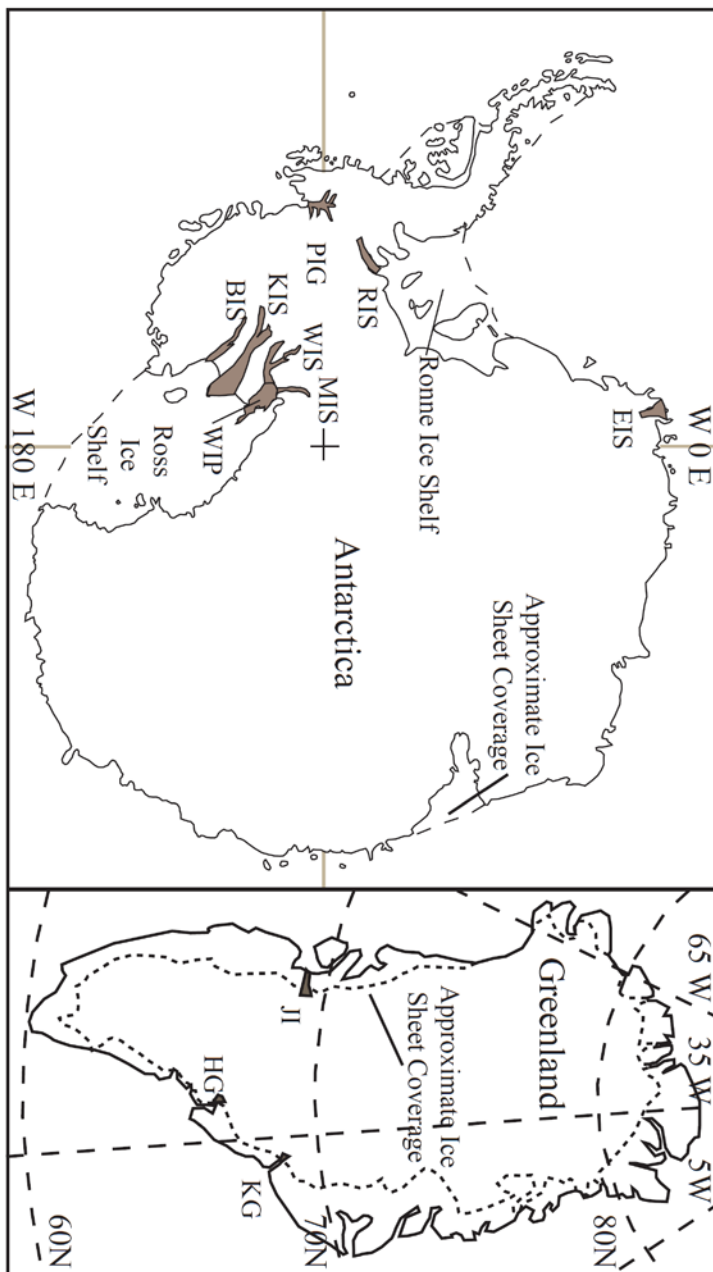


Figure 1.1: Location map of the ice streams discussed in this thesis. Abbreviations are EIS: Ekstrom Ice Shelf; RIS: Rutford Ice Stream; PIG: Pine Island Glacier; MIS: Mercer Ice Stream; WIS: Whillans Ice Stream; WIP: Whillans Ice Plain; KIS: Kamb Ice Stream; BIS: Bindschadler Ice Stream; JI: Jakobshavn Isbrae; HG: Helheim Glacier KG: Kangerdlugssuaq Glacier. Dashed outlines show the extent of glacial ice in both figures.

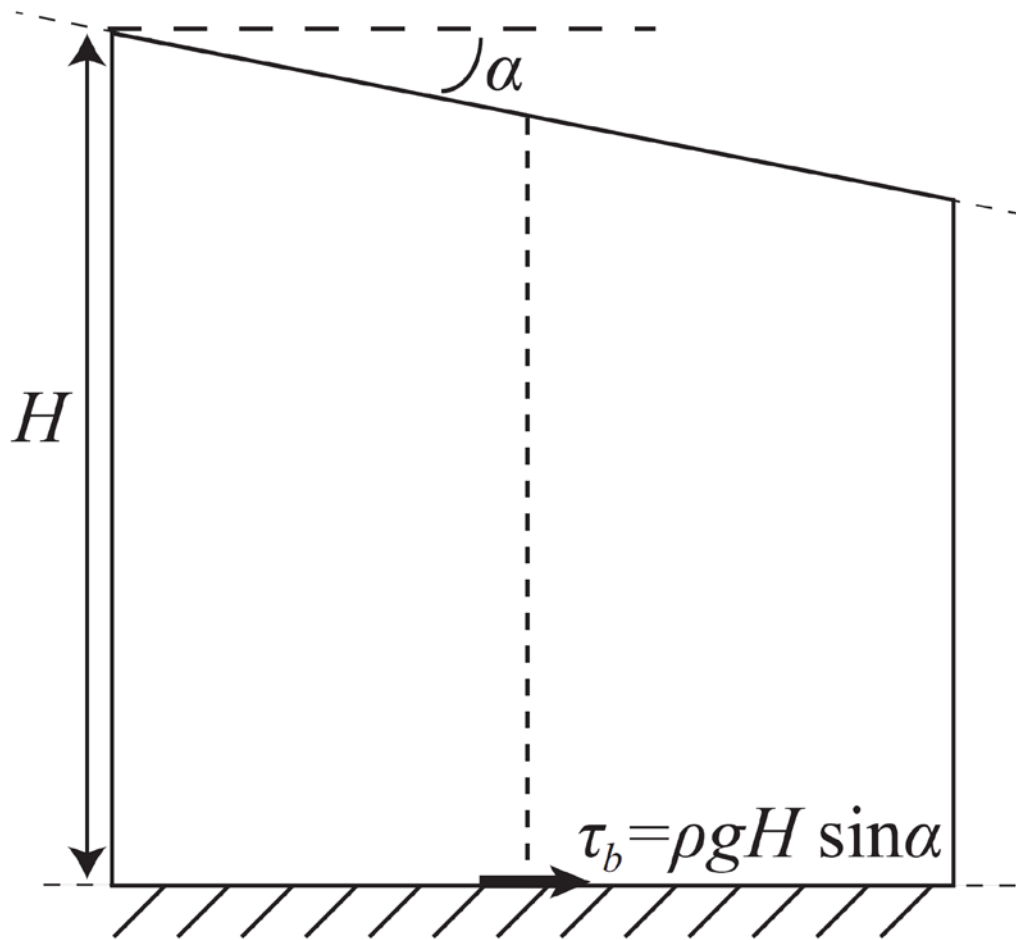


Figure 1.2: Schematic cross section of a simple ice sheet. The surface slope is denoted by α , the ice thickness by H , and the basal driving stress by τ_b . Note that the surface slope is greatly exaggerated in this figure for emphasis. The flow direction of the ice sheet is towards the right.

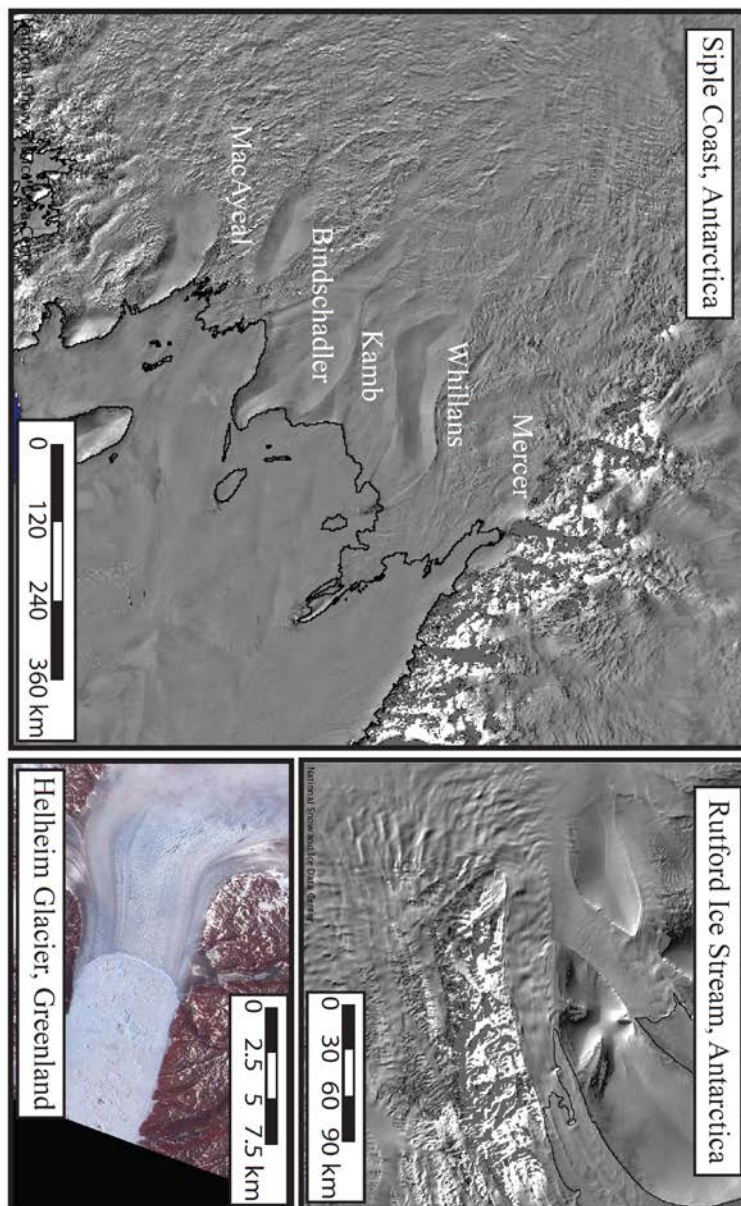


Figure 1.3: Satellite imagery of the specific ice streams discussed in this thesis. Note that the location of each panel is shown in figure 1.1. Imagery from the Siple Coast and Rutford Ice Stream are taken from the Atlas of the Cryosphere, a service provided by the National Snow and Ice Data Center (NSIDC). The satellite image for Helheim Glacier is from the January 20th, 2006 “Picture of the Day” from the NASA Earth Observatory website. The image uses data from Howat et al., 2005.

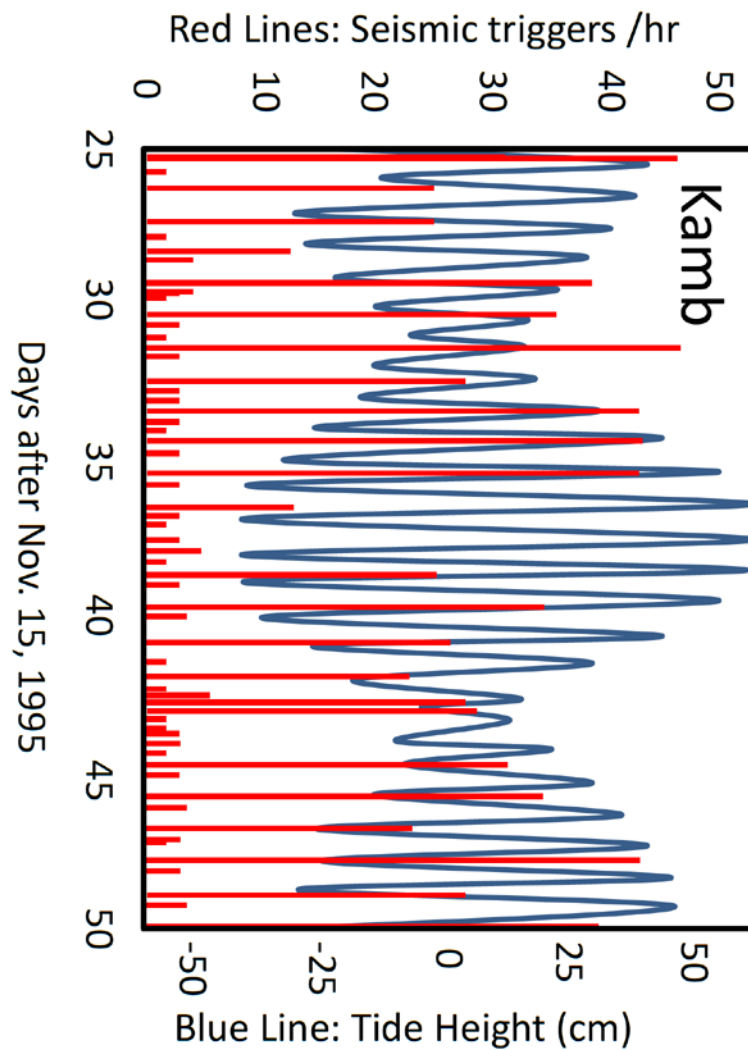


Figure 1.4: Seismicity on the Kamb Ice Stream, adapted from Anandakrishnan et al. (1997). The blue curve in the background shows the tidal signal from a tide meter, with the amplitude shown on the right side of the plot. The red lines show the seismicity rate as a number of triggered events per hour. Note that the peaks in seismic activity correspond to the peak tidal amplitudes.

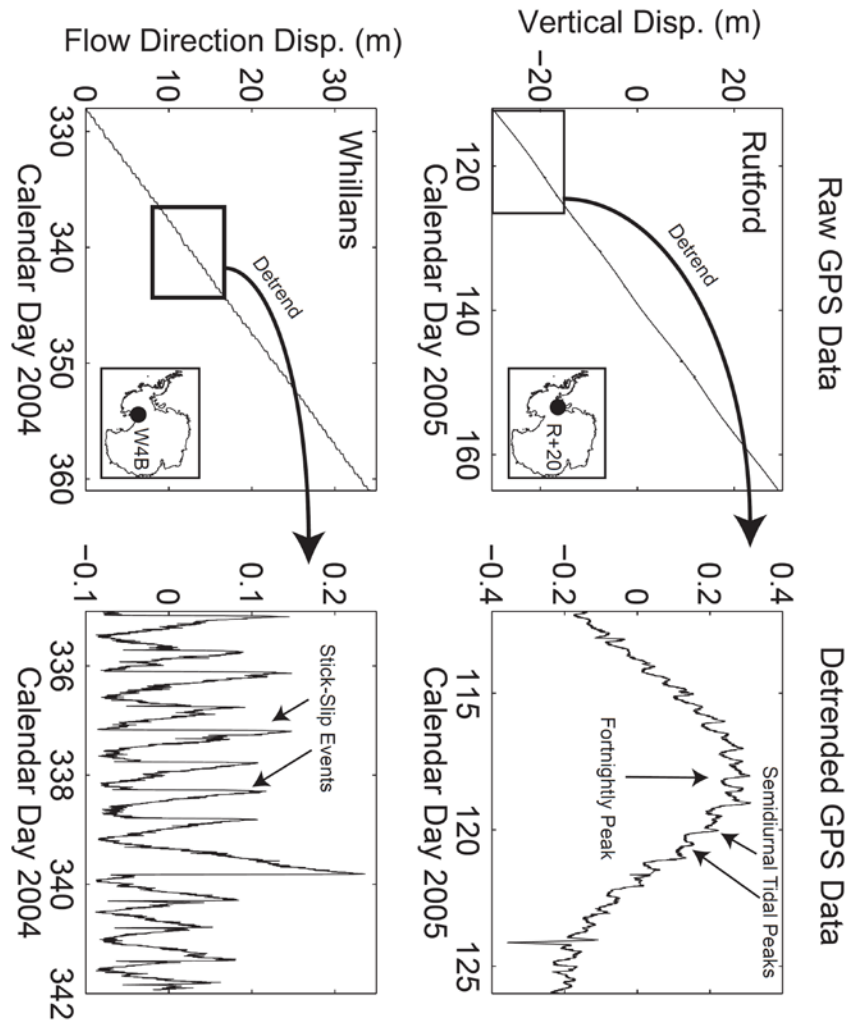


Figure 1.5: Sample GPS records from station R+20 from Rutford Ice Stream (upper figures) and W4B from Whillans Ice Plain (lower figures) for surface displacement rotated into the primary flow direction. The panels on the left show the raw GPS signal; note the strong linear trend in the GPS signal. The GPS records with this linear trend removed are shown in the figures on the right. For the Rutford Ice Stream, the tidal signal is shown as a sinusoidal variation in ice position. For the Whillans Ice Plain, the tidal variability triggers stick-slip events in the displacement record. Data is from H. Gudmundsson (Rutford) and S. Anandakrishnan (Whillans).

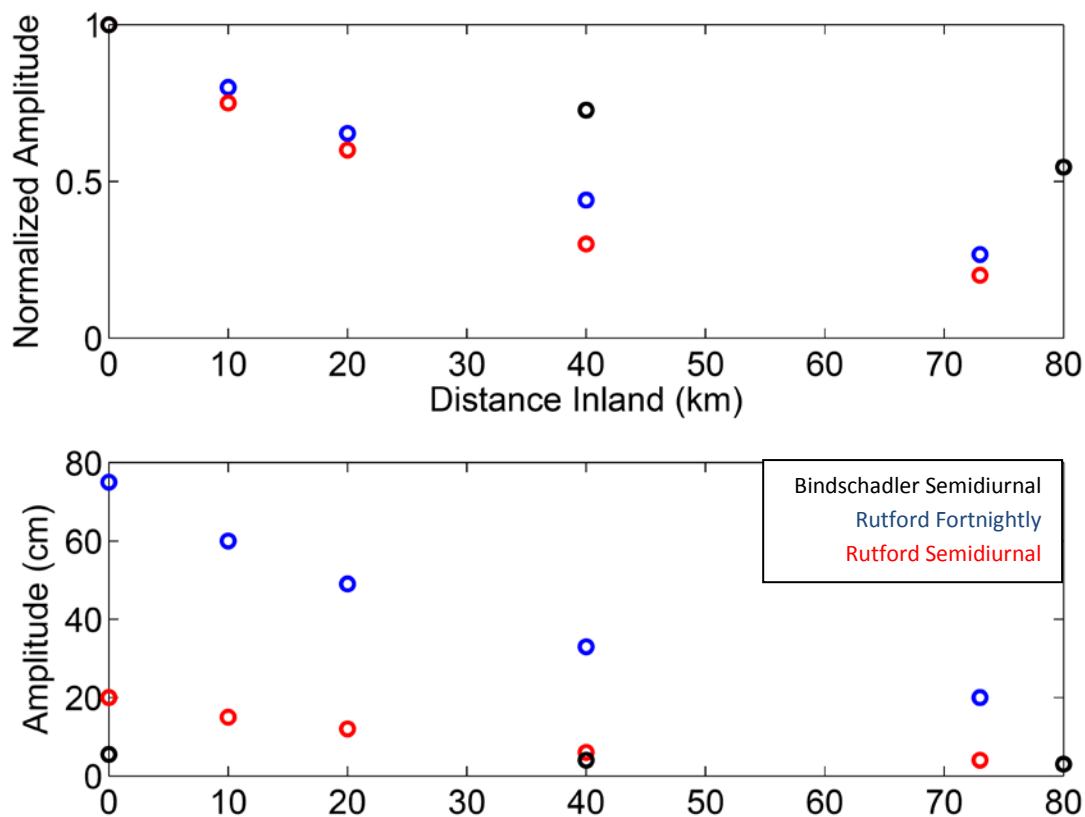


Figure 1.6: Amplitude of the tidal signal present in GPS stations on Rutford and Bindschadler Ice Streams as a function of distance inland from the grounding line. The upper panel shows the normalized amplitudes of the signal, while the lower panel shows the true amplitudes of the three datasets. The colors corresponds to: black-Bindschadler semidiurnal tidal amplitude, blue-Rutford fortnightly tidal amplitude, red-Rutford semidiurnal tidal amplitude.

| <i>Ice Stream</i> | <i>Tidal Stress Transmission</i> | | <i>Ice Flexure</i> | |
|-------------------------|----------------------------------|--|--------------------------------|----------------------------------|
| | <i>Extent</i> (<i>km</i>) | <i>Method</i> | <i>Extent</i> (<i>km</i>) | <i>Method</i> |
| Bindschadler Ice Stream | 80 + | GPS displacement ¹ | ~ 10 | ICESat altimetry ² |
| Ekstrom Ice Shelf | < 3 | GPS displacement ³ | ~ 5 | Tilt ³ |
| Kamb Ice Stream | 85 + | Seismicity ⁴ | ~ 10 | ICESat altimetry ² |
| Pine Island Glacier | < 55 | GPS displacement ⁵ | ~ 5 | SAR ⁶ |
| Rutford Ice Stream | 40 + | GPS disp. ^{7,8} | 5 + | Tilt ⁹ |
| Whillans Ice Plain | ~ 100 | GPS (stick-slip) ^{10,11} Seismicity ^{10,12} | ~ 10 | ICESat altimetry ² |
| Whillans Ice Stream | ~ 300 | Seismicity ¹³ | N/A | ICESat altimetry ² |
| Kangerdlussuaq | ? | N/A | Var. | N/A |
| Helheim | < 10 | GPS disp. ^{14,15,16,17} | Var. | N/A |
| Jakobshavn Isbrae | < 10 | GPS disp. ^{18,19} | Var. | N/A |

Table 1.1: Summary of the spatial extent of tidal stress transmission and ice flexure from ice streams across Antarctica and Greenland. Superscript numbers denote the following references: 1-Anandakrishnan et al. (2003); 2-Brunt et al. (2010); 3-Heinert and Riedel (2007); 4-Anandakrishnan and Alley (1997); 5-Scott et al. (2009); 6-Rignot (1998); 7-Gudmundsson (2006); 8-Gudmundsson (2007); 9-Stephenson (1984); 10-Weins et al. (2008); 11-Winberry et al. (2009); 12-Walter et al. (2011); 13-Harrison et al. (1993); 14-de Juan (2009); 15-de Juan (2010a); 16-de Juan (2010b); 17-de Juan Verger (2011); 18-Podrasky (2002); 19-Podrasky (2012). The flexure of the Greenland outlet glaciers is listed as variable as the flexure depends strongly on the size of the floating ice shelf, which for these glaciers has changed dramatically over the past decade.

Chapter 2

Transmission of Tidal Stresses by Ice Streams

Geodetic surveys suggest that ocean tides can modulate the motion of Antarctic ice streams. Data from Whillans Ice Plain, Rutford Ice Stream, and other Antarctic ice streams show periodicity in flow velocity at periods similar to those of ocean tides at geodetic stations many tens of kilometers inland from the grounding line. These data suggest that ocean tidal stresses can perturb ice stream motion about an order of magnitude farther inland than tidal flexure of the ice stream alone. Recent models exploring the role of tidal perturbations in basal shear stress are all two dimensional e.g., Anandakrishnan and Alley, 1997; Bindshadler et al., 2003; Gudmundsson, 2006, 2007, 2011; Sergienko et al., 2009; Winberry et al., 2009; Walker et al., 2012), with the impact of the ice stream margins either ignored or parameterized. In this chapter, we use two- and three-dimensional finite element modeling to investigate the transmission of tidal stresses in ice streams and the impact of considering more realistic, three-dimensional, ice stream geometries. We demonstrate that the assumption that elastic tidal stresses in ice streams propagate large distances inland fails for channelized glaciers. The resistance at the ice stream margins causes an intrinsic, exponential decay in the tidal stress. This stress decay occurs even with an unrealistic frictionless basal condition beneath the ice stream and even then, does not fit observations from the aforementioned Antarctic ice streams.

2.1 Introduction

All ice streams respond to the daily fluctuations in ocean tidal height. The spatial and temporal extent of this tidal response varies dramatically between ice streams, as demonstrated by surface observations discussed earlier in section 1.3. At one extreme are the outlet glaciers of Greenland and some ice streams of Antarctica, which have only surface movement affected by the ocean tides over horizontal distance inland of the grounding line comparable to a few ice-thicknesses (1 ice-thickness ranges from 600 meters to 2 kilometers for our purposes). In contrast, many of the major ice streams of the Siple Coast (Whillans, Bindschadler, and Kamb Ice Streams) and the Rutford Ice Stream, exhibit surface motion influenced by tides many tens of ice-thicknesses inland of their respective grounding lines. As this latter behavior is anomalous, these ice streams are the focus of this chapter.

Many two-dimensional models are capable of reproducing the seemingly inordinate influence that the ocean tides have on the motion of some Antarctic ice streams (e.g., Anandakrishnan and Alley, 1997; Bindschadler et al., 2003; Gudmundsson, 2006, 2007, 2011; Sergienko et al., 2009; Winberry et al., 2009; Walker et al., 2012). Given that the Maxwell relaxation time (T_{max}) for ice is on the order of hours for tidal loads, these models call on either elastic or viscoelastic transmission of tidal loading stresses through the ice stream to drive the observed ice motions. We discuss several representative published models with the aim of understanding the assumptions made about the upstream transmission of tidal stresses.

A standard approximation for glacial flow is the *flow-line model*. A flow-line model is a two-dimensional representation of a vertical slice along the glacier's flow-

direction, with any resistive forces in the third dimension ignored. The underlying assumption of such a formulation requires that only the conditions at the ice stream's bed determine the sliding and flow behavior of the entire ice stream. Such a model is only appropriate for ice "far" from the lateral margins of the ice stream. The spatially-averaged shear stress formulations of Bindschadler et al. (2003) and Winberry et al. (2009) use flow-line models to investigate the tidally-perturbed surface displacements of Rutford and Whillans Ice Streams. These models assume that tidal stress is uniformly distributed over the entire ice stream and that the stress is completely supported by the ice stream's base. The result is a length-scale for the transmission of stress that depends completely on the length of the ice stream assumed in the problem.

Finite element analysis in two-dimensions allows for flow-line models with increased complexity and realistic geometries. An early example of this approach is the modeling of Anandakrishnan and Alley (1997), which assumes the ice stream behaves as a two-dimensional elastic body (in cross section) riding over a viscous bed. Anandakrishnan and Alley (1997) find that a stress applied at the grounding line decays exponentially with distance inland. The decay of this "tidal" load is controlled primarily by the properties of the viscous till layer in this model, namely the ratio of effective viscosity of the till to the thickness of the till.

Of the published modeling after Anandakrishnan and Alley (1997), the two most applicable models of tidal stress propagation are those of Gudmundsson (2011) and Walker et al. (2012). Both are two-dimensional flow-line models incorporating nonlinear viscoelasticity and a nonlinear basal sliding law. The response of the modeled ice stream is found to relate directly to the basal boundary condition. This result is intuitive as any

resistance due to the lateral margins of the ice is neglected for a flow-line model, and thus the model ice stream's response to a tidal load must be controlled by rheological character of the stream's bed alone. These models do not, however, demonstrate that the lateral resistance in these ice streams is indeed negligible.

Sergienko et al. (2009) approximates an ice stream as a series of masses (blocks) connected elastically (by springs) and restrained laterally (by further springs), under the action of an applied shear along a frictional basal contact. Unlike the flow-line models discussed previously, this spring-block model incorporates the lateral resistance of the ice margins. In this model, Sergienko et al. (2009) note that a "tidal" load applied at one edge diminishes with distance from the loaded block, but this stress decay is not explored in any detail. Intuitively, this transmission distance depends on the stiffness of the springs, both between the masses and as lateral restraints, as well as the magnitude of the basal friction imposed in the model. However, there is no obvious relationship between a physical length-scale and the number of blocks and springs in the model, and it is not clear if the decay of the tidal stress is caused by marginal or basal resistance, or both.

2.2 Methodology

As our brief review of the published literature shows, there is a dearth of three-dimensional ice stream models exploring the transmission of a tidal load inland of the grounding line that account for the resistance of the ice stream's lateral margins. To explore the role of an ice stream's lateral margins, we present results from two- and three-dimensional elastic models that explore and quantify the role that the three-dimensional ice stream geometry plays in controlling transmission of tidal stresses. The opening portion of this methodology section describes the conceptual configuration of

our models, which are shown schematically in figure 2.1. The methods section then closes with a brief description of the finite element modeling necessary to create these models.

2.2.1 Model Descriptions

We begin with a two-dimensional linear elastic flow-line model (figure 2.1A). As with all flow-line models, the underlying assumption is that the ice stream is infinite and uniform in the third dimension, such that there effectively are no lateral margins to the ice stream. These simplified models establish the expected “end-member” behavior of an elastic ice stream with extreme basal conditions of either a fully frozen (no-slip) bed or a freely sliding (no shear traction) bed. Additionally, these two-dimensional models investigate the role played by an ice shelf as the intermediary between the ocean tides and the grounded ice stream (see Appendix 2A).

Based on the insight gained from these two-dimensional models, we then move to our three-dimensional models (figure 2.1B), studying the impact of resistive shearing at the lateral margins of an ice stream on the upstream transmission of the applied tidal load. The ice stream is defined in these models as a block of ice “sliding” over a frictionless basal boundary with lateral margins consisting of two blocks of ice that are “frozen” to their beds. Such models investigate the role that the overall geometry of the ice stream (i.e., ice stream width and thickness) has on the transmission of the stress inland of the grounding line.

2.2.2 Model Construction

We use the finite element software *Pyolith* (Williams et al., 2005; Williams, 2006; Aagaard et al., 2007; 2008; 2011) and meshing software *Cubit* (cubit.sandia.gov)

for our computational modeling. As the general finite element formulation has already been discussed section 1.5, we only describe the mesh geometries and boundary conditions used in our two- and three-dimensional models here.

Our default two-dimensional model is two hundred kilometers long and one kilometer thick. For all our modeling, if the model is long compared to the other dimension, the length is not a controlling parameter. As the bottom corner of the axial forced edge is a location of stress concentration, we refine our mesh near this point to improve our model stability, resulting in a variable element length in the vertical and horizontal directions. In our three-dimensional model, we apply the same mesh-refinement scheme in the vertical and longitudinal direction; in the transverse direction, we refine the elements corresponding to the ice stream and then gradationally increase the element length away from the ice stream margin. The extent of the non-sliding area is chosen to be large enough that changing its width does not impact the behavior of the ice stream proper.

The basal boundary condition is either a Dirichlet condition with zero-displacement in all directions (“frozen”) or a Robin condition with no vertical displacements and zero shear traction (“sliding”). The tidal stress change is a normal force of magnitude equal to the hydrostatic pressure ($\rho g \Delta h$ where Δh is the amplitude of the tide). For the two-dimensional models with an ice shelf, the tidal load acts normal to the base and vertical edge of the ice shelf. For the two-dimensional models with no shelf and the three-dimensional models, the tidal load acts on the vertical edge of the ice stream at the grounding line. In these latter models, neglecting the ice shelf is justifiable as the presence of a shelf only perturbs the stresses in the ice stream near the grounding

line, and our interest is in the stresses far inland of the grounding line. See appendices 2A and 2B for an extended discussion of the impact of the ice shelf on our models. Lastly, in these linear elastic models, it is not necessary to explicitly vary the loading through time, as our solutions must necessarily vary linearly with the magnitude of the applied load.

Table 2.1 lists the default rheological parameters used in our finite element modeling presented in this chapter. Note that while Young’s modulus is varied throughout many of our models, all quantities marked with a “+” are fixed throughout all the simulations. Apart from linear elasticity, our most important rheological assumption is that the Poisson’s ratio, ν , is well constrained by laboratory experiments (e.g., Gammon et al., 1983A; 1983B; Patrenko and Whitford, 2002).

2.3 Results

PyLith calculates the full stress and strain tensors, as well as displacement and velocity vectors, at every node of our model mesh. As we ran close to two dozen models, we show only representative results in the main chapter (figures 2.2 to 2.7). Tables 2.3 and 2.4 list important quantities from all the models, while appendix 2C shows the stress and displacement profiles for all our two-dimensional models and appendix 2D shows the stress field for the three-dimensional models. Note that while we model only physically-representative geometries in our parameter exploration, in order to quantify the dependence of the model on Young’s modulus, we include models with Young’s moduli an order of magnitude larger and smaller than the value from Patrenko and Whitford (2002). While such values may be unrealistic for ice, the wide range of values allows us to easily distinguish the effects of changing the elasticity of each model.

Lastly, to aid in comparing the stress magnitude between models, we define an equivalent stress, τ_{eq} , based on the Von Mises criterion. τ_{eq} is defined in two and three dimensions as:

$$2D: \tau_{eq}^2 = \frac{1}{2} \left[(\sigma_{xx} - \sigma_{yy})^2 + \sigma_{xx}^2 + \sigma_{yy}^2 + 6 * \sigma_{xy}^2 \right] \quad (2.1A)$$

$$3D: \tau_{eq}^2 = \frac{1}{2} \left[(\sigma_{xx} - \sigma_{yy})^2 + (\sigma_{yy} - \sigma_{zz})^2 + (\sigma_{xx} - \sigma_{zz})^2 + 6(\sigma_{xz}^2 + \sigma_{xy}^2 + \sigma_{yz}^2) \right] \quad (2.1B)$$

2.3.1 Two-Dimensional Results

The stress distributions from our two-dimensional models with free-sliding and frozen basal boundary conditions are shown in figures 2.2 and 2.3, respectively. In both panels A and B of these figures, the left column plots the stress results for models including an ice shelf, while the right column plots results for models with only axial forcing. In panel A, the figure shows superimposed longitudinal profiles of τ_{eq} taken at depth intervals of 10 meters. In panel B, the logarithm of the absolute value of the three in-plane stress components is plotted for the entire two-dimensional model domain.

In most models, the magnitude of stress within our body decays exponentially with distance from the grounding line (at $x=0$). Only in the model with a sliding bed and axial forcing (figure 2.2, right column) does the axial stress not decay with inland distance. We define a stress-transmission length-scale, L_{tr} , as the distance inland of the grounding line over which the tidal stress drops by one order of magnitude. Table 2.2 summarizes L_{tr} for all stress components for the four models shown in figures 2.2 and 2.3.

For both basal boundary conditions, the solution for the model with the ice shelf approaches the solution of the shelf-free model after about five ice-thicknesses. For the free-sliding model, the flexural stresses also decay with distance inland of the grounding line, following the expected functional form of a sinusoid multiplied by an exponential function (e.g., Turcotte and Schubert, 2002). The first wavelength of this sinusoid can be seen in figure 2.2A, with a zero crossing approximately two kilometers inland (i.e., left) of the grounding line. Beyond approximately five kilometers inland of the grounding line, the two models behave identically. For the model with a frozen bed (figure 2.3), flexural and axial stresses decay exponentially with distance inland of the grounding line with similar decay rates. The influence of the ice shelf on the deformation near the grounding line is explored more fully in appendices 2A and 2B.

Not surprisingly, the displacement field in our two-dimensional models mirrors the stress field, as figure 2.4 demonstrates for the ice shelf models. Panel A shows the displacement results for the model with a sliding bed, while panel B shows the results for a model with a frozen bed. In each panel, the mesh is warped by the displacement values exaggerated by a factor of 1000 for the sliding base model and 50,000 for the frozen base model. This figure is useful to determine the general character of the displacement field, which also exhibits an exponential decay with distance inland of the grounding line. Linear elasticity predicates that the decay of displacements matching that of the stress. Thus, the same L_{tr} in tables 2.3 and 2.4 calculated for the stress also represents the behavior of the displacements.

2.3.2 Three-Dimensional Results

Figure 2.5 shows the values of τ_{eq} from a representative three-dimensional model that is one kilometer thick and ten kilometers wide. Each line represents horizontal profiles taken at a ten meter depth interval and a transverse spacing of one kilometer. The stress decays exponentially at approximately the same rate regardless of the Y or Z coordinates chosen. Recall that the ice stream in our three-dimensional model slides frictionless along the bed; thus, the exponential decay of stress within the three-dimensional ice stream is clearly different from the constant stress behavior of our free-sliding two-dimensional model. The presence of the lateral margins of the ice stream alone induces an exponential decay of the stresses in the ice stream as a function of distance inland of the grounding line.

Figure 2.6 shows the full basal stress field (i.e., the six independent stress components) of the representative three-dimensional model. Only the longitudinal normal stresses (σ_{xx}), transverse normal stresses (σ_{yy}), and the shear due to the sidewalls (σ_{xy}) are nonzero beyond a distance of a few kilometers from the forced edge. The other stress components are direct consequences of stress concentration at the transition from no slip to sliding ice at the base, and decay rapidly with distance from both the margins and the grounding line. Note that the lack of basal friction accounts for the lack of basal shear stresses (σ_{yz} and σ_{xz}).

Figure 2.7 shows a view of the three-dimensional mesh with a stream width of five kilometers, warped by the displacement vector magnitude multiplied by a factor of 500,000. The fixed basal condition beneath the lateral margins of the ice stream clearly has a strong influence on the displacement field, which follows a polynomial profile in

plan-view. Such a displacement field is akin to the solution to for an elastic (Bernoulli-Euler) beam under a constant pressure that is simply supported at both edges (e.g., Turcotte and Schubert, 2002). Additionally, recall that the displacements in our three-dimensional models decay exponentially with inland distance at the same rate that the stress signal decays due to the elastic rheology of the ice.

2.4 Transmission of Tidal Stresses

As seen in all models with either basal or lateral stress resistance, the tidal stresses decay exponentially with distance inland of the grounding line. We use L_{tr} , the stress-transmission length-scale, as a direct measure of the inland extent of tidal influence on the motion of an ice stream. Throughout the remaining discussion in this chapter, we estimate L_{tr} using τ_{eq} , as the value of L_{tr} calculated from the equivalent stress matches the longest L_{tr} derived from the individual stress components (see table 2.2). Table 2.3 and 2.4 show the value of L_{tr} for many different combinations of geometry and elastic moduli for the two- and three-dimensional models, respectively. For the two-dimensional models, we vary h and E while for the three-dimensional models we vary h , w , and E .

Using the information found in tables 2.3 and 2.4, figures 2.8 and 2.9 show the full variability of our solutions with the geometric and rheological parameters in our models. Increasing the size of the model domain (i.e., h and w) and the amplitude of the applied load increases the value of the stress, while displacements vary proportionally to the applied load and inversely to Young's modulus. However, only the geometric parameters determine the value of the stress decay (as evidenced by the constant value of L_{tr} for models of the same geometry). For our two-dimensional model (with a frozen

bed), L_{tr} varies linearly with thickness. For our three-dimensional model, L_{tr} increases nonlinearly with increasing thickness and width.

We adopt an empirical functional form describing the relationship between stresses, displacements, and model parameters using the aforementioned model results. For the two-dimensional model, we find:

$$\begin{aligned}\sigma(x, z) &= \tilde{\sigma}_{GL}(h, z) \cdot \overline{\Delta h} \cdot 10^{-x \frac{\bar{h}}{\tilde{L}_{tr}}} \\ u(x, z) &= \tilde{u}_{GL}(h, z) \cdot \frac{\overline{\Delta h}}{\bar{E}} \cdot 10^{-x \frac{\bar{h}}{\tilde{L}_{tr}}}\end{aligned}\tag{2.2}$$

$\tilde{\sigma}_{GL}$ and \tilde{u}_{GL} are, respectively, the centerline basal stress and surface displacement at the grounding line for reference model one kilometer thick with a one meter tidal load using the value of 9.33 GPa for E . \tilde{L}_{tr} is the transmission length-scale for the reference model, \bar{E} is the normalized Young's modulus with respect to the canonical value, \bar{h} is the normalized model thickness with respect to one kilometer, and $\overline{\Delta h}$ is the normalized tidal height with respect to a one meter tide. Recall that as ρ and g are held constant, $\overline{\Delta h}$ really reflects a change in tidal load, and thus is a characteristic change in loading rather than a characteristic length-scale. For the three-dimensional models, the empirical forms of stress and displacement are:

$$\begin{aligned}\sigma(x, y, z) &= \tilde{\sigma}_{GL}(y, z, h, w) \cdot \overline{\Delta h} \cdot 10^{\frac{-x}{\tilde{L}_{tr}(h, w)}} \\ u(x, y, z) &= \tilde{u}_{GL}(y, z, h, w) \cdot \frac{\overline{\Delta h}}{\bar{E}} \cdot 10^{\frac{-x}{\tilde{L}_{tr}(h, w)}}\end{aligned}\tag{2.3}$$

These results indicate that the distribution of stresses depends only on model loading style and geometry, and are completely independent of the elastic properties of the model, assuming the Young's modulus for the ice is homogenous.

From comparing the model results in table 2.4, a rough rule of thumb is that L_{tr} is between 1.2 and 1.5 times the width of the ice stream and only increases slightly with increasing ice stream thickness in our three-dimensional models. Thus, tidal stresses at a distance inland of the grounding line equal to 2.5 times the ice stream width, there should be no tidal influence on the ice stream motion. For our models of Bindschadler and Rutford Ice Streams, this rough rule of thumb suggests that the tidal influence should die out at 100 kilometers and 75 kilometers, respectively, (flagged models in Table 4; mesh sizes shown in figure 2.10). However, figure 2.11 demonstrates that even this decay is too severe to match the maximum observed displacement at stations inland of the grounding line (GPS data reported in Anandakrishnan et al., 2003; Gudmundsson, 2007 and provided by S. Anandakrishnan and H. Gudmundsson).

Note that for Bindschadler Ice Stream, the grounding line curls along the edge of the ice stream for almost 75 kilometers. The modeled trend in figure 2.11 ignores this feature, which is a clear simplification of the model geometry. From our simple models, we find that the effective ice stream width would have to be over 250 kilometers for the model decay rates to match the observations. While a more representative geometry would result in a better approximation of the value of L_{tr} (a value that is likely different for the convergence zone of Bindschadler and MacAyeal Ice Streams and Bindschadler Ice Stream proper), our modeling suggests that an elastic model of Bindschadler Ice Stream cannot reproduce the decay length-scale observed by Anandakrishnan et al. (2003).

Of course, real ice streams are neither frozen to nor sliding frictionlessly over their beds. Frictional sliding plays a major role in determining the ice stream's total flow

(e.g., Weertman, 1957; 1964; Engelhardt and Kamb, 1998; Hughes, 1998; Cuffey and Paterson, 2010). The values of L_{tr} from our frozen bed two-dimensional models should be considered as a minimum value for frozen bed flow-line models, while our three-dimensional models should be taken as maximum values as we assume frictionless sliding in our models. As our three-dimensional models predict a tidal influence that decays too rapidly to match observations when the base is frictionless, we conclude that a homogenous elastic ice stream is not capable of transmitting tidal stresses the many tens of kilometers inland that have been observed.

2.5 Discussion

As our results, along with those of Sergienko et al. (2009) and Anandakrishnan and Alley (1997), predict an exponential decay of stress while many other researchers found no such exponential decay of a tidal load (e.g., Bindschadler et al., 2003; Gudmundsson, 2011; Walker et al., 2012; Winberry et al., 2009), our discussion begins with this inconsistency in modeling results. After establishing that exponential decay of a tidal load is the expected result, we then discuss how our modeling compares to, and in many cases, refutes the results of other published models. Our discussion concludes by considering the shortcomings of our modeling as a motivation of chapter 3 of this thesis.

2.5.1 Comparison to Previous Models

St. Venant's Principle states that the influence of an applied load on an elastic body is negligible at great distances away from the applied load (e.g., Goodier, 1942; Timoshenko and Goodier, 1982). A clear extension of this principle is that an external load should decay rapidly when near a fixed edge. For instance, Goodier (1942) demonstrates that an axially forced block, when restrained from below, has a stress field

that is only important local to the edge of the applied load. Additionally, Goodier establishes the same conclusion when the block is fixed from both above and below. These two cases are identical to our two-dimensional model with a fixed base and the two-dimensional version (in map view) of our three-dimensional ice stream model, respectively. Timoshenko and Goodier (1982) provide an explicit form of the stress solution for similar, albeit not identical, models. In their article 24, Timoshenko and Goodier describe the expectation of exponential decay of stress with distance away from a point load applied to the opposite edges of a beam.

Comparing our present results to those of Anandakrishnan and Alley (1997), our two-dimensional model results represent extremes of Anandakrishnan and Alley's model. Our frozen bed model corresponds to Anandakrishnan's and Alley's model with either a zero-thickness viscous layer or an infinitely viscous ($\eta \approx \infty$) layer. Our sliding bed model corresponds to Anandakrishnan and Alley's model with an infinitely weak ($\eta \approx 0$) viscous layer. Our models bracket those of Anandakrishnan and Alley where two-layer models have the additional free parameter of till viscosity. Anandakrishnan and Alley's models can either constrain the viscosity of the viscous till layer using the transmission length of stress, or constrain the transmission length of stress using the till viscosity, but not both simultaneously. Additionally, the lack of lateral restraint in the model allows the physically unrealistic case of infinite stress-transmission. The same issue is present in all the flow-line models, and as such, the two-dimensional assumption of negligible lateral resistance is not physically realistic for ice streams.

Of all the published models, Sergienko et al. (2009) is the only study to explicitly account for lateral resistances. Removing the basal drag condition from Sergienko et

al.'s model results in a one-dimensional approximation of our three-dimensional modeling. However, the lack of a length-scale relationship for the elastic springs in Sergienko et al.'s model is a major deficiency in using the Sergienko et al.'s model to help constrain a stress-transmission length-scale. As our finite element modeling shows, the presence of non-sliding lateral margins and a zero-sliding basal condition both result in exponential decay of a tidal load with distance inland of the grounding line. Thus over the stick-slip cycle in Sergienko et al.'s paper, we expect that the stress-transmission would cycle between a thickness-controlled value when stuck and a width-controlled value when slipping.

2.5.2 Model Shortcomings

Our models are, by design, geometrically and rheologically simple. Even in our simple box models, the stress supported by the lateral margins directly controls the transmission of a tidal load on ice streams. Extending these results, models with a realistic geometry will vary substantially from the equivalent box model approximation only if the real ice stream's width changes dramatically along the flow direction. For channelized ice streams like Bindschalter and Rutford Ice Streams, the width of either ice stream does not change significantly through the region with CGPS observations (e.g., figure 2.10). For the Whillans Ice Plain, the extreme width of the unconfined ice plain (~ 100 kilometers wide) suggests that our channelized three-dimensional model may not be a good representation of this one ice stream.

To address the Whillans Ice Plain, we ran a constant-thickness model approximating the geometry of the ice plain, as shown in figure 2.13. For this model, we selected the location of the non-streaming ice by using RadarSAT imagery (from

nsidc.org) to determine the location of shear margins, where the basal boundary condition was fixed in all directions. The grounding line was matched to that found by Brunt et al. (2010), and an axial-only tidal load was applied normal to the entire length of the grounding line. The model also included a portion of ice shelf solely to increase the rate of convergence of our model. Having an explicit ice shelf in the model prevents the possibility of an unphysical buckling mode along the grounding line. The rate of convergence is increased by several orders of magnitude while having no effect on the stress state within the grounded ice.

As seen in figure 2.13, the stress decays exponentially with distance inland of the grounding line as expected from our other three-dimensional modeling. Due to the variable position and angle of the grounding line, the reference-frame independent stress components are more characteristic of the stress state for this model, demonstrating that the general stress pattern follows that of the channelized ice stream models. Shear stresses peak near the transition from stuck to sliding ice, as locally there are large shear stresses in the vertical direction. Across the main body of the ice plain, the octahedral shear stress is dominated by shear along the horizontal plane. The overall stress state is dominated by the normal component of the tidal load. L_{tr} in this model ranges from 50 to 125 kilometers, meaning that over the ice plain itself, tidal loading is fairly well transmitted over the ice plain. Note that the magnitude of stress drops rapidly in Mercer and Whillans Ice Streams, with the decay rate controlled by the ice stream width, as expected. In these cases, the values of L_{tr} are about 45 kilometers and 30 kilometers, respectively. Thus, only in the case of a very wide, unconstrained ice stream, elastic stress may be transmitted far upstream; however, for ice streams with a more common

channel morphology, incorporating a more realistic model geometry is unlikely to have a major impact on the transmission of stress.

The models presented thus far adopt a homogeneous linear elastic rheology, which is not the most realistic material model for ice. In the next chapter, we discuss two modifications to the rheological model for ice streams: strain-weakening within the lateral shear margins of the ice stream and nonlinear viscoelastic rheology to account for the interplay of viscous and elastic deformation at short timescales.

A final major simplification of our modeling is the lack of a frictional basal boundary. Instead we explored either zero displacement or zero friction basal condition. Our free slip three-dimensional models and our two-dimensional frozen bed models bookend the expected behavior of a frictional bed and thus adding basal friction will cause the transmission length-scale of a tidal load to range from that controlled primarily by the ice stream width for low friction to that controlled primarily by the ice stream thickness for high friction. As ice streams are wider than they are thick, we expect that friction hinders, rather than enhances, the transmission of a tidal stress.

The exception to the frictional reduction of the transmission length-scale would be if the slow-moving ice that buttresses the ice stream on the sides slides frictionally instead of being fixed at the bed. Should this be the case, the stress-transmission length-scale for a given model will be larger than we predict here. The overall effect would be equivalent to having a larger effective width of the ice stream. In the case of Antarctica, the role of basal sliding in the ice stream itself, or for the slow-moving marginal ice, is negligible due to the small driving stress, as discussed in section 1.5. We note that in the case of the ice-rock margins of the fjord-bounded Greenland outlet glaciers discussed in

chapter 1, the ice stream does slide along the lateral margins; however, the fairly rapid decay of tidal stresses with distance inland of the grounding line suggests the such an effect is limited at best.

2.6 Summary and Conclusions

The models presented here draw into question the hypothesis that the observed influence of ocean tides on ice stream motion occurs as elastic transmission through the bulk of the ice stream itself. This result implies one of two possible conclusions: one, that there is a mechanism, not explored here, that almost completely decouples the ice stream from its shear margins, essentially reducing the lateral support of the ice stream to nearly zero; or two, that a mechanism external to the ice stream bulk is necessary to explain the tidal component of ice stream motion. The uniform flow-line models which are the current state-of-the-art, implicitly assume the first. Our models demonstrate that the ice streams considered here are not wide “enough” to neglect the resistance of the lateral margins. Furthermore, even the name “shear margins” implies that there is an amount of lateral support sufficient to induce shear in the ice stream’s margins, making large-scale decoupling improbable.

We conclude that a mechanism external to the ice stream bulk underlies the transmission of ocean tidal loading far inland of the grounding line. While not explored here, our preferred hypothesis is that the ocean tides perturb the stress balance at the ice-bed interface through the subglacial hydrologic network. Any further discussion of such a process relies on quantifying the spatial extent that ocean tides are ‘felt’ through the subglacial hydrologic network, which is beyond the scope of this paper.

| | Variable Names | Units |
|--|--|--------------------|
| | E Young's modulus | Pa |
| | g Gravitational acceleration | m s^{-2} |
| | H Ice stream thickness | m |
| | Δh Tide amplitude | m |
| | L_{tr} Stress-transmission length-scale | km |
| | \tilde{L}_{tr} Reference stress-transmission length-scale | km |
| | T_{max} Maxwell relaxation time | S |
| | \tilde{u}_{GL} Centerline displacement magnitude at the grounding line | cm |
| | w Ice stream width | km |
| | η Viscosity | Pa s |
| | ν Poisson's ratio | -- |
| | ρ Ice density | kg m^{-3} |
| | σ_{ij} Stress component | Pa |
| | $\tilde{\sigma}_{GL}$ Centerline stress magnitude at the grounding line | Pa |
| | σ_{tide} Tidal stress | Pa |
| | τ_{eq} Equivalent (Von Mises) stress | Pa |
| | " $\bar{\quad}$ " Normalized quantity | |

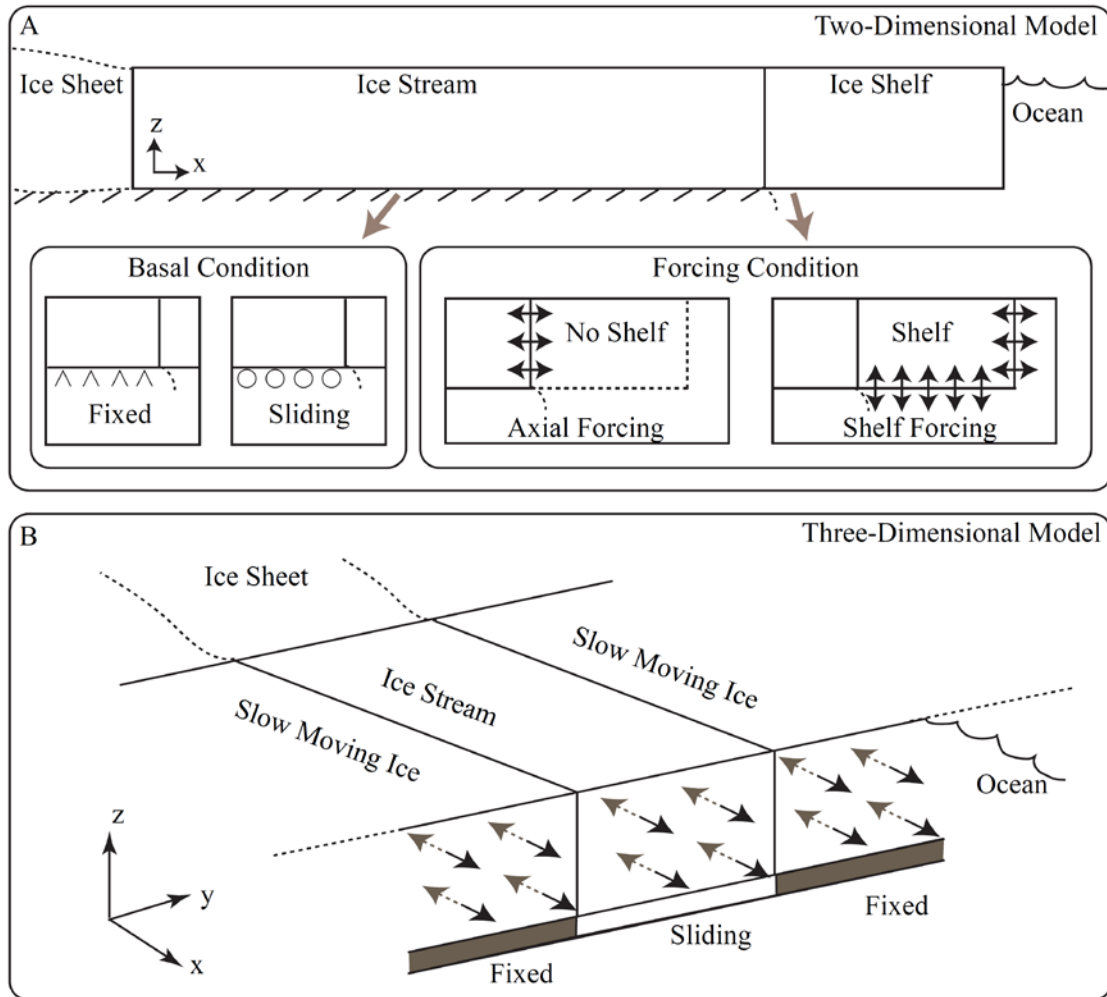


Figure 2.1: Schematics of the models used in this chapter. Inset boxes show options used in each model. For the two-dimensional models, these options are either a fixed ($u_x = u_y = u_z = 0$) or sliding ($u_z = 0$) basal condition, and either a pure axial loading condition or a shelf model. The three-dimensional model assumes a uniform, isotropic value for the Young's modulus throughout the entire domain.

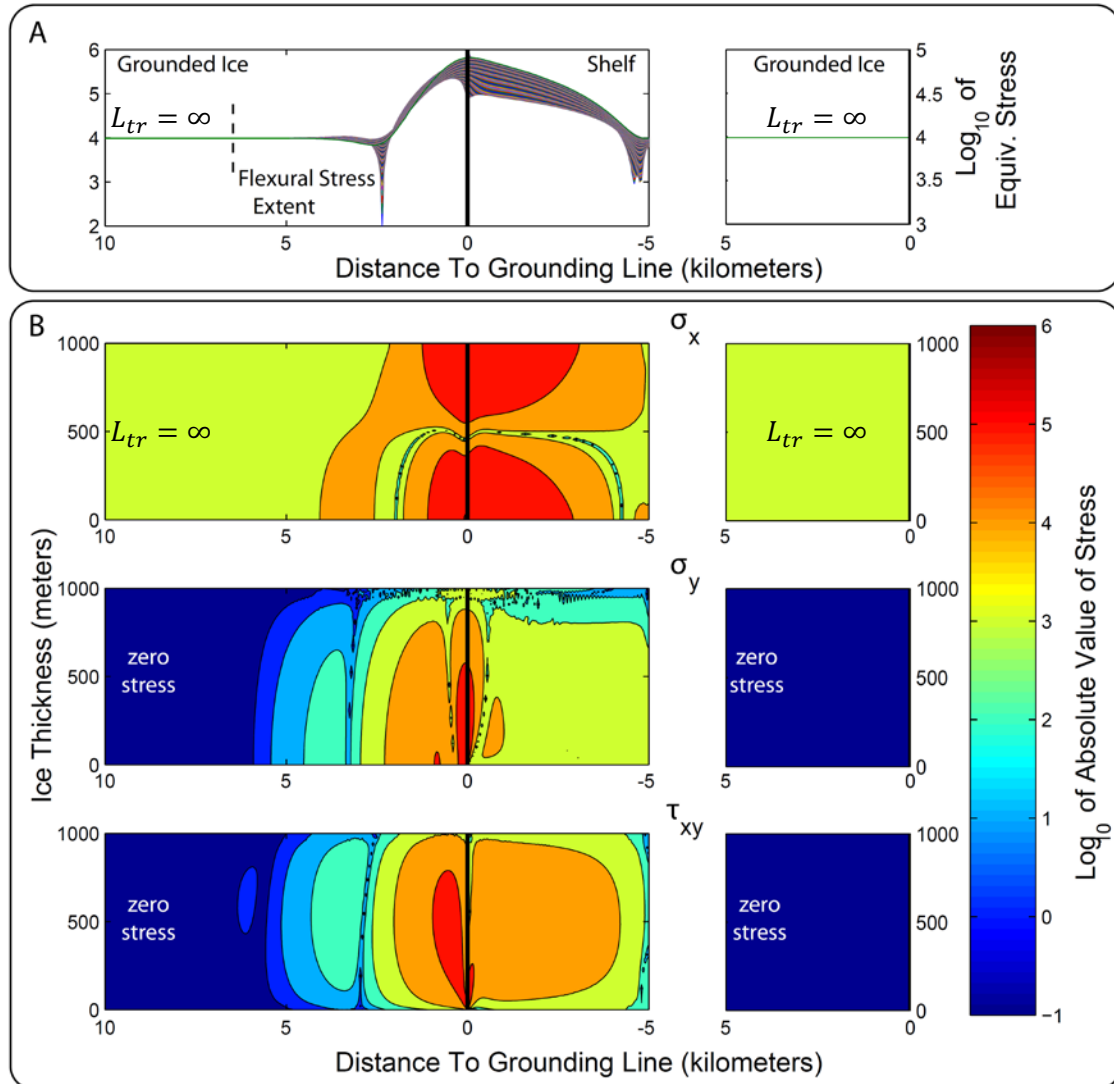


Figure 2.2: Distributions of stress for a two-dimensional model with frictionless basal sliding. Panel A shows profiles of longitudinal τ_{eq} profiles at a depth interval of 10 meters, while panel B shows the σ_x , σ_y , and τ_{xy} components of stress. The left column for both panels shows a model with an ice shelf; the right column for both panels shows a model with no ice shelf and only an axial loading. In these frictionless models, axial stress does not decay with distance and flexural stress rapidly decays near the grounding line. L_{tr} is the stress decay length, and is defined in the main text.

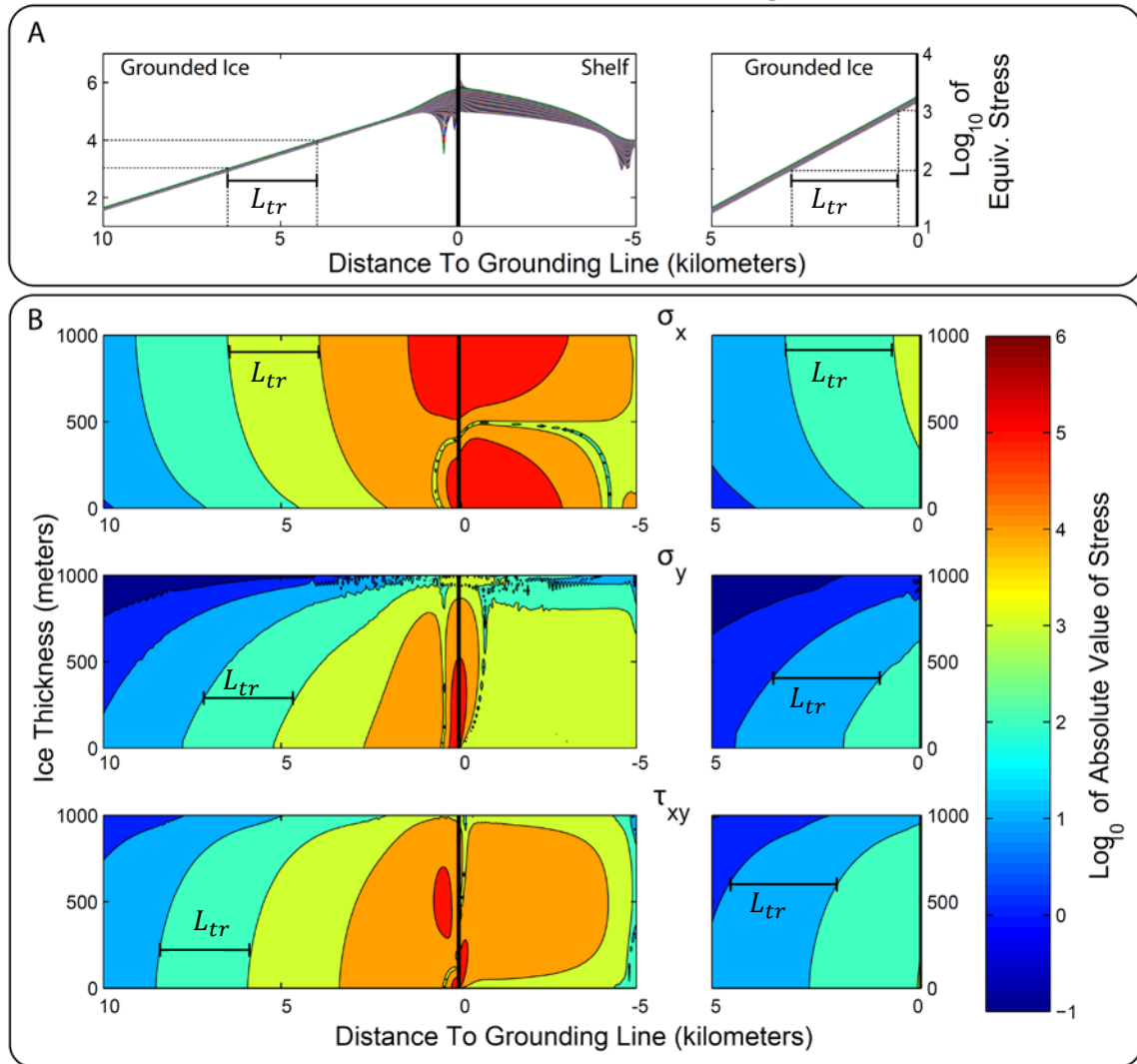


Figure 2.3: Stress distributions for a two-dimensional model with no basal sliding. The panels are the same as in figure 2.2. Stress at the grounding line is higher in the model with an ice shelf than without a shelf, but L_{tr} is the same between the two model setups.

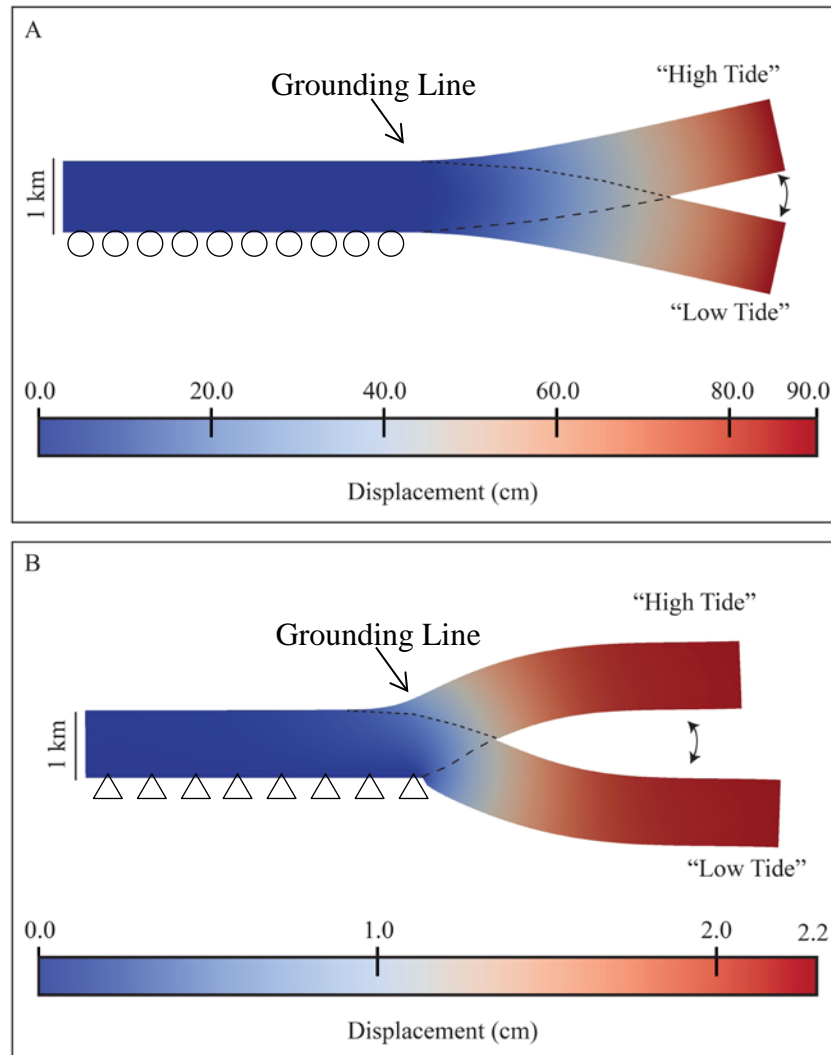


Figure 2.4: Displacement fields for the two-dimensional models with attached shelves.

The color shows the overall displacement magnitude, and the mesh is warped by the displacement multiplied, by a factor of 1000 for panel A and by a factor of 50,000 for panel B. Panel A shows the results for the model with a sliding basal condition and panel B shows the results for the model with a fixed basal condition. The high tide position corresponds to a shelf forcing of magnitude $\sigma_{tide} = \rho g \Delta h$ (inward traction) while the low tide position corresponds to a shelf forcing of magnitude of $\sigma_{tide} = -\rho g \Delta h$ (outward traction).

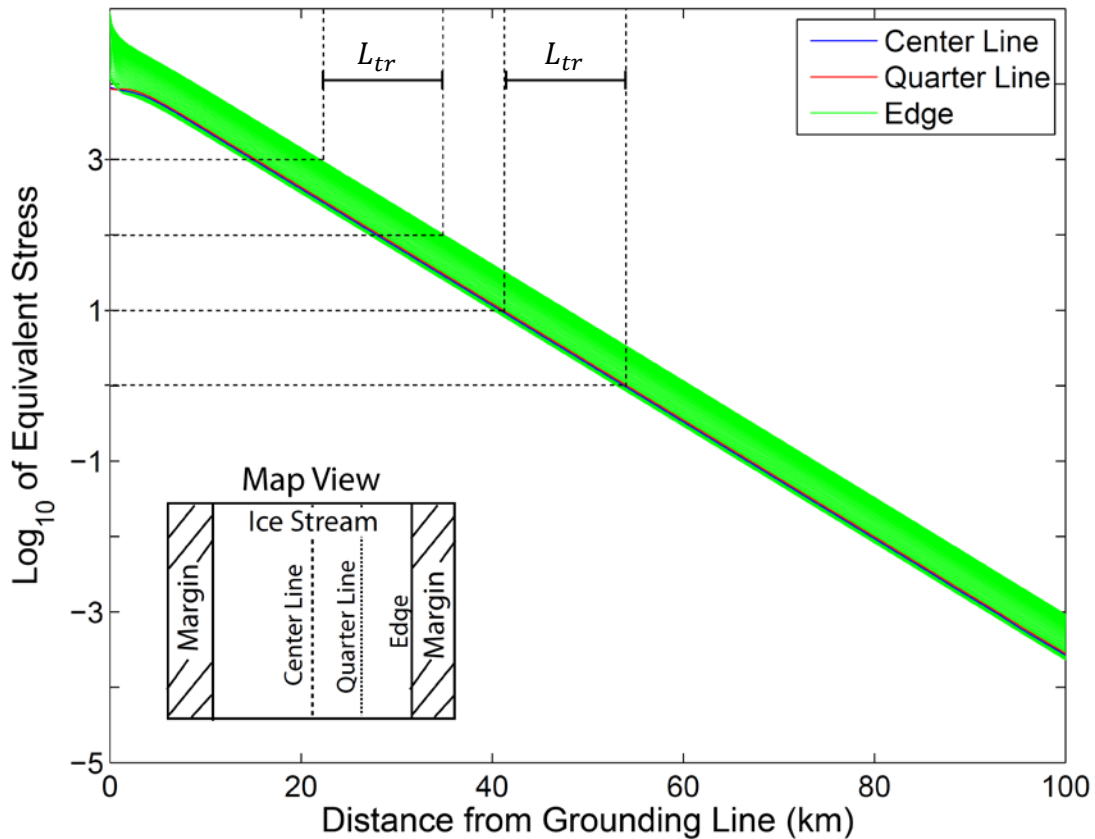


Figure 2.5: Stacked equivalent stress (τ_{eq}) profiles for three different locations in a three-dimensional model with uniform elasticity, a width of 10 kilometers, and a thickness of 1 kilometer. The inset shows the locations of the three profiles in map view. For each location, 101 lines are stacked, taken at 10 meter depth intervals. For the center and quarter lines, there is very little difference in stress value with depth, while for the edge of the ice stream, the stress value changes with depth by about an order of magnitude. However, between all these profiles, L_{tr} is constant.

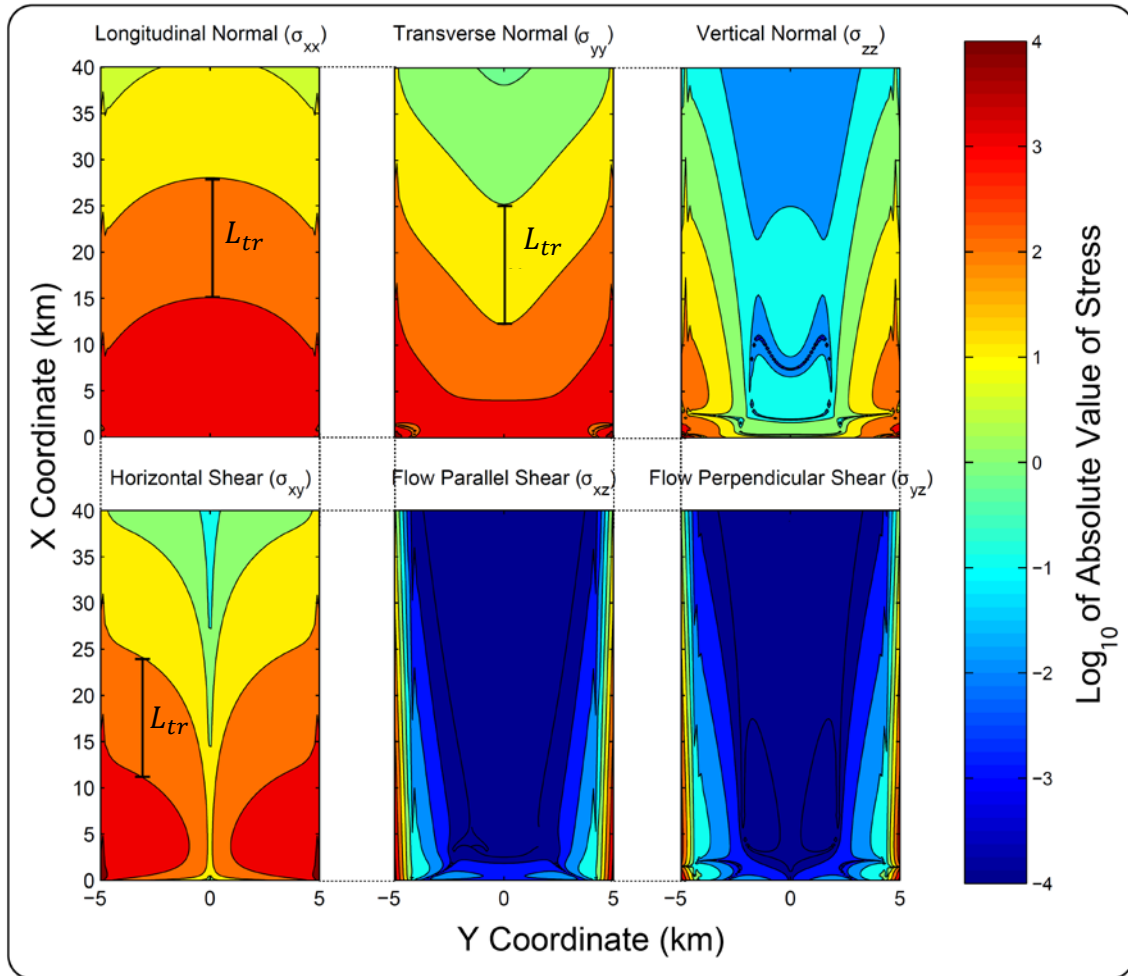


Figure 2.6: Representative stress distribution along the base of a three-dimensional model with homogenous elasticity, showing the six unique stress components. The streaming portion of the model has a width of ten kilometers and a thickness of one kilometer. L_{tr} is drawn in the σ_{xx} , σ_{yy} , and τ_{xy} components where it is easiest to observe.

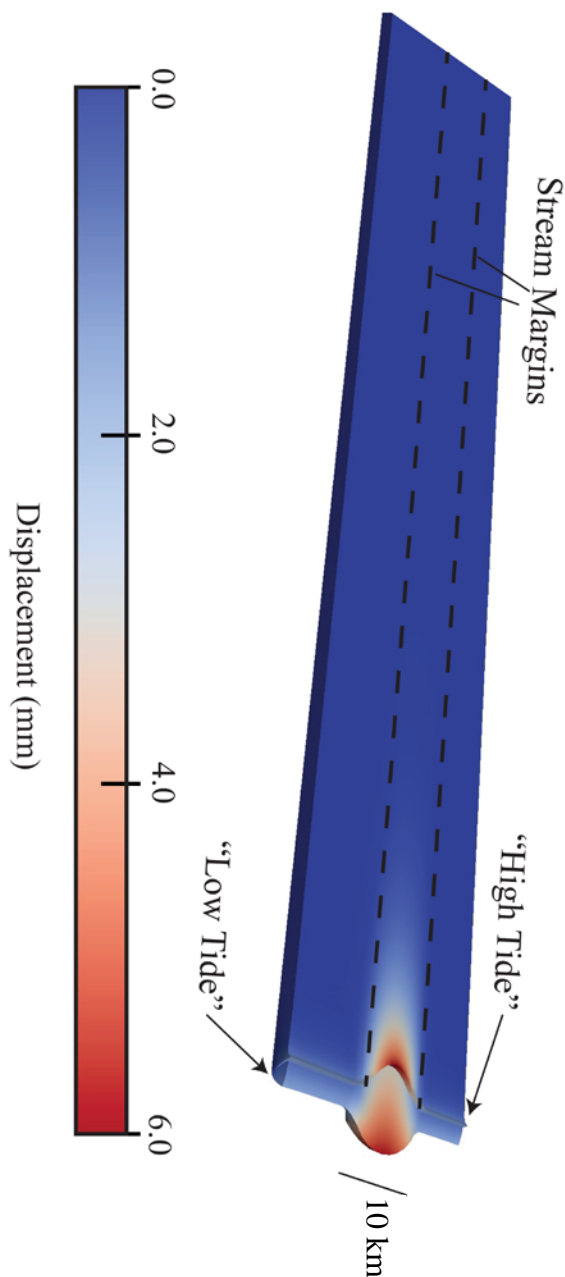


Figure 2.7: Three-dimensional displacement field for a high and a low tidal amplitude.

The high tide corresponds to an applied traction of magnitude $\sigma_{tide} = \rho g \Delta h$ and the low tide corresponds to a traction of magnitude of $\sigma_{tide} = -\rho g \Delta h$. The ice stream is 10 kilometers wide, with the surface projection of the lateral margins draw in dashed black lines.

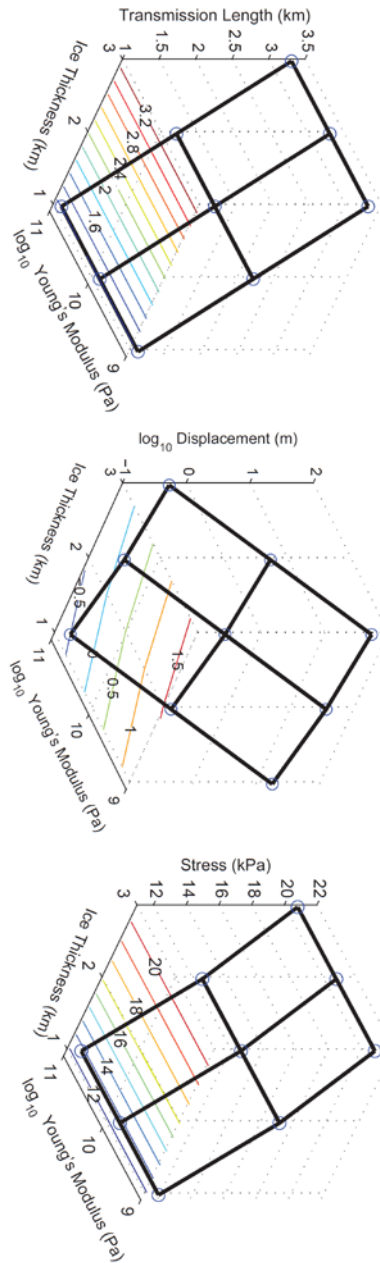


Figure 2.8: Trend in the two-dimensional models as function of Young's modulus (E) and ice thickness (h). The three figures plot the transmission length-scale (L_{tr}), centerline surface displacement above the grounding line, and the centerline equivalent stress at the surface above the grounding line. The circles are the model results, while the colored contours at the bottom of each plot show the values of the quantity on the vertical axis.

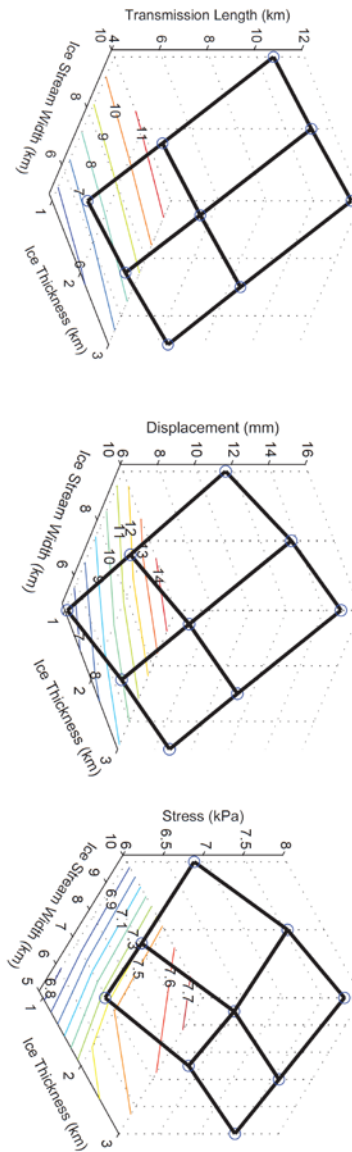


Figure 2.9: Trend in the three-dimensional models as function of ice stream width (w) and ice thickness (h). The three figures plot the transmission length-scale (L_{tr}), centerline surface displacement above the grounding line, and the centerline equivalent stress at the surface above the grounding line. The circles are the model results, while the colored contours at the bottom of each plot show the values of the quantity on the vertical axis.

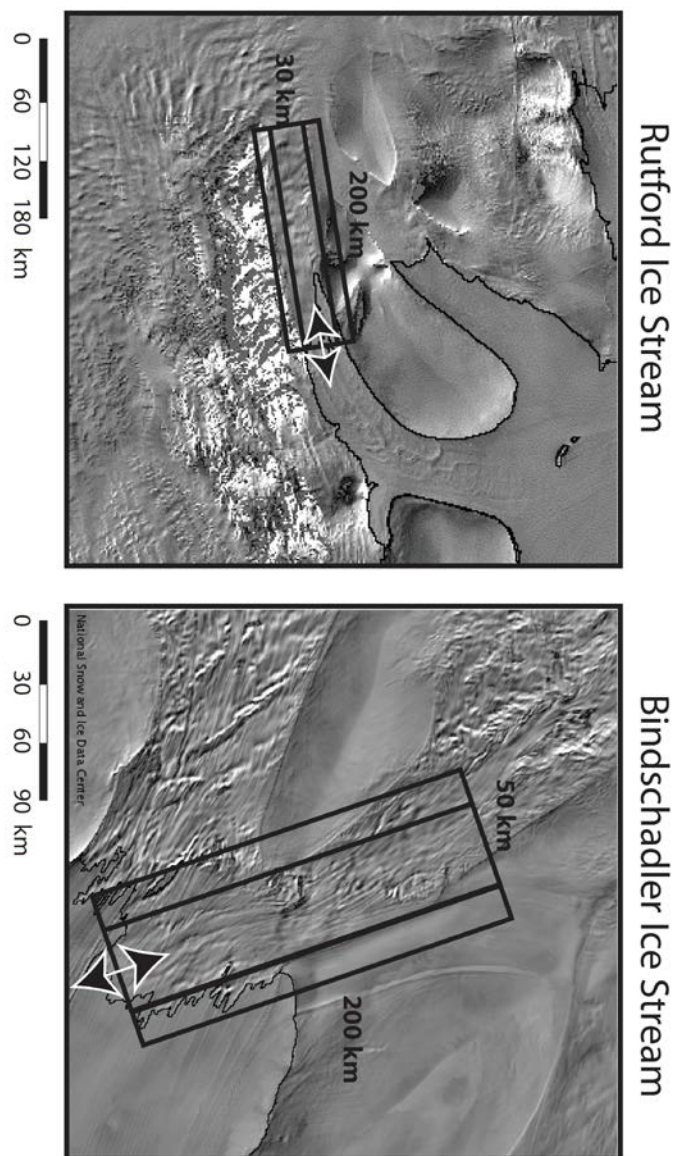


Figure 2.10: Comparison of our side-wall shear models with the real geometry of Rutford Ice Stream, and Bindschadler Ice Stream. The arrow denotes the forced edge, the central region is the sliding portion of the model and the flanking regions are the fixed portions of the model. Numerical values denote the length and width of the modeled ice stream. Background images from the NSIDC RAMP imagery database (<http://nsidc.org/data/ramp/>).

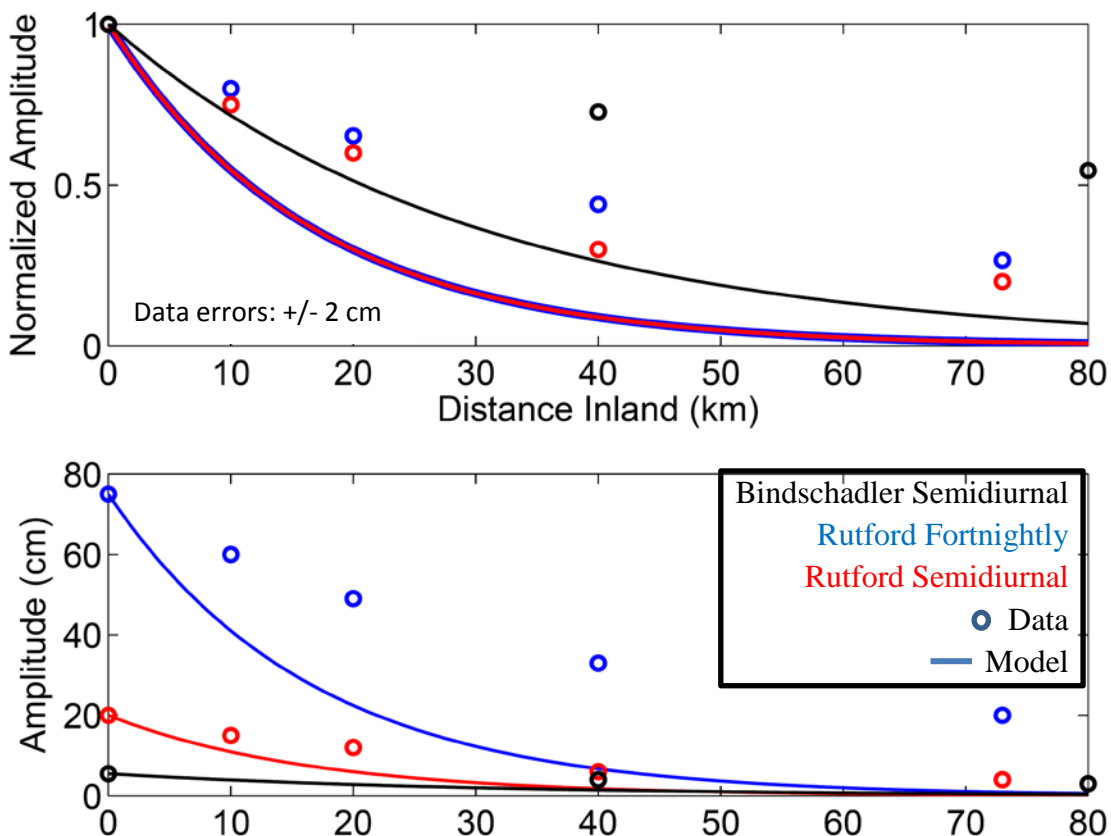


Figure 2.11: Diagram comparing GPS tidal displacement amplitudes to modeled displacement amplitudes. Circles show the data taken from observation on Rutford and Bindschadler Ice Stream (Bindschadler data from figure 2 of Anandakrishnan et al., 2003; Rutford data courtesy of H. Gudmundsson). The error on the approximated tidal displacement amplitudes is two centimeters. The slopes of the modeled surface displacements are taken from models approximating the Rutford Ice Stream and Bindschadler Ice Streams, as shown in table 2.4. As in figure 1.6, the upper panel shows the normalized tidal amplitudes, while the lower panel shows the true amplitude values.

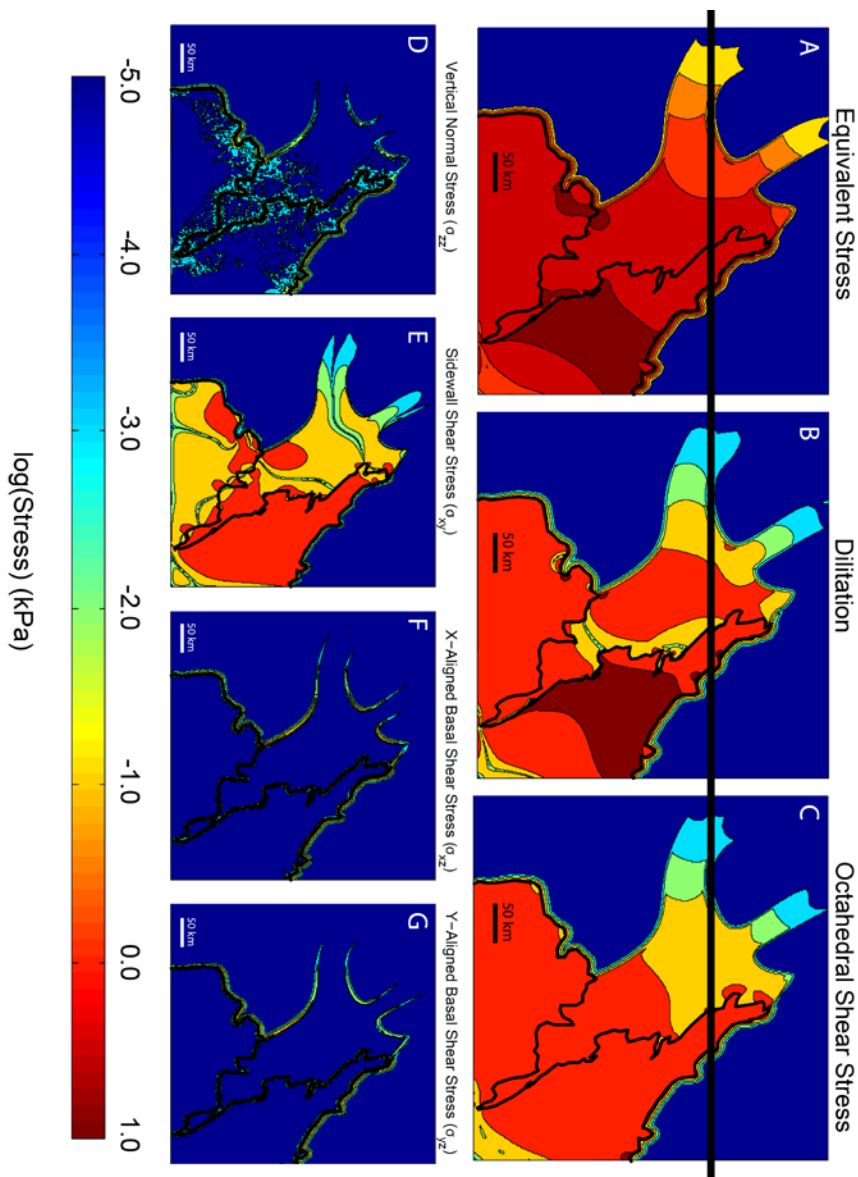


Figure 2.12: Basal stress results from our Whillans Ice Plain model. Panels A-C show equivalent stress, dilatation, and octahedral shear stress, respectively. Panels D-G show vertical normal stress, side-wall shear stress, x-aligned basal shear stress, and y-aligned basal shear stress, respectively. All panels are scaled to the same logarithmic scale, shown at the bottom of the figure. The models are forced only along the grounding line, shown in the panels as the bolded black line.

| <i>Parameter</i> | <i>Symbol</i> | <i>Value</i> |
|------------------------|---------------|---|
| Young's Modulus | E | 9.33 GPa |
| +Poisson's Ratio | ν | 0.325 |
| *Shear Modulus | G | 3.52 GPa |
| *Bulk Modulus | K | 8.90 GPa |
| +Density (at 0 °C) | ρ | 917 kg/m ³ |
| +Viscosity coefficient | A | 5.86x10 ⁻⁶ MPa ³ /s |
| +Stress exponent | n | 3 |

Table 2.1: Elastic and viscous parameters used to define the ice properties in our finite element modeling. Values of elastic parameters, except for density, are taken from Petrenko and Whitford (2002) using data from Gammon et al. (1983A; 1983B). Viscous parameters are taken from Paterson (1997). Parameters marked with an asterisk (*) denote quantities that are calculated from the other moduli and material properties. Parameters marked with a plus (+) are fixed through all models.

| <i>Fixed Base</i> | | | | <i>Sliding Base</i> | | | |
|-------------------|------------------|----------------------------|-----------------|---------------------|--------------|----------------------------|-----------------|
| <i>Condition</i> | <i>Component</i> | <i>L_{tr} (km)</i> | <i>St. Dev.</i> | <i>Condition</i> | <i>Comp.</i> | <i>L_{tr} (km)</i> | <i>St. Dev.</i> |
| Shelf | X | 2.586 | 0.004 | Shelf | X | 1.304 | 9.049* |
| | Y | 2.619 | 0.095 | | Y | 1.101 | 0.013 |
| | XY | 2.590 | 0.015 | | XY | 1.078 | 1.4e-5 |
| Axial Only | X | 2.517 | 0.023 | Axial Only | X | ∞ | N/A |
| | Y | 2.618 | 0.068 | | Y | N/A | N/A |
| | XY | 2.616 | 0.018 | | XY | N/A | N/A |

Table 2.2: Transmission length-scales (L_{tr}) for the two-dimensional models shown in figures 3 and 4. See text for description of how the parameters are found. All cases save the marked (*) case have very low standard deviations. In the marked case, the standard deviation is large as the value of σ_x falls to zero near the middle of the ice stream vertically, making L_{tr} vary dramatically near these locations. Near the upper and lower portions of the ice stream, the stress decay for σ_x is more consistent with the values for the other stress components.

| <i>Model #</i> | <i>Figure #</i> | <i>h</i> (<i>km</i>) | <i>E</i> (<i>GPa</i>) | <i>Disp. @ GL</i> (<i>mm</i>) | <i>Stress @ GL</i> (<i>kPa</i>) | <i>L_{tr}</i> (<i>km</i>) |
|----------------|-----------------|---------------------------|----------------------------|------------------------------------|--------------------------------------|--|
| 1 | 2.3 | 1 | 9.33 | 1.68 | 11.80 | 2.5 |
| 2 | 2C.1 | 2 | 9.33 | 3.46 | 17.06 | 5.1 |
| 3 | 2C.2 | 3 | 9.33 | 5.22 | 20.75 | 7.6 |
| 4 | 2C.3 | 1 | 0.933 | 16.83 | 11.80 | 2.5 |
| 5 | 2C.4 | 2 | 0.933 | 34.59 | 17.06 | 5.1 |
| 6 | 2C.5 | 3 | 0.933 | 52.24 | 20.75 | 7.6 |
| 7 | 2C.6 | 1 | 93.3 | 0.17 | 11.80 | 2.5 |
| 8 | 2C.7 | 2 | 93.3 | 0.35 | 17.06 | 5.1 |
| 9 | 2C.8 | 3 | 93.3 | 0.52 | 20.75 | 7.6 |

Table 2.3: Model parameters and results from our two-dimensional models. The

displacement measurement is the magnitude of the modeled surface displacement vector above the grounding line (i.e., at $x=0$). The stress value is the equivalent stress at the surface above the grounding line. The transmission length-scale L_{tr} is the value found for the decay of the equivalent stress, which matches the value found using the surface displacement magnitude.

| <i>Model #</i> | <i>Figure #</i> | <i>h</i> (<i>km</i>) | <i>w</i> (<i>km</i>) | <i>E</i> (<i>GPa</i>) | <i>Disp. @</i> <i>GL (mm)</i> | <i>Stress @</i> <i>GL (kPa)</i> | <i>L_{tr}</i> (<i>km</i>) |
|----------------|-----------------|---------------------------|---------------------------|----------------------------|----------------------------------|------------------------------------|--|
| 1 | 2.6 | 1 | 10 | 9.33 | 6.13 | 6.779 | 12.2 |
| 2 | 2D.1 | 2 | 10 | 9.33 | 7.64 | 7.349 | 12.7 |
| 3 | 2D.2 | 3 | 10 | 9.33 | 8.81 | 7.453 | 12.7 |
| 4 | 2D.3 | 1 | 14 | 9.33 | 8.29 | 6.817 | 13.6 |
| 5 | 2D.4 | 2 | 14 | 9.33 | 10.04 | 7.500 | 15.0 |
| 6 | 2D.5 | 3 | 14 | 9.33 | 11.22 | 7.585 | 17.5 |
| 7 | 2D.6 | 1 | 20 | 9.33 | 11.55 | 6.845 | 18.4 |
| 8 | 2D.7 | 2 | 20 | 9.33 | 13.68 | 7.439 | 19.6 |
| 9 | 2D.8 | 3 | 20 | 9.33 | 14.94 | 7.775 | 24.6 |
| 10 | 2D.9 | 1 | 10 | 0.933 | 61.30 | 6.790 | 25.6 |
| 11 | 2D.10 | 1 | 10 | 93.3 | 0.61 | 4.778 | 26.7 |
| 12* | 2D.11 | 2 | 50 | 9.33 | 31.99 | 7.584 | 69.1 |
| 13 | 2D.12 | 2 | 40 | 9.33 | 25.85 | 7.581 | 52.2 |
| 14** | 2D.13 | 2 | 30 | 9.33 | 19.75 | 7.577 | 38.2 |

Table 2.4: Model parameters and results from our two-dimensional models. The stress, displacement, and transmission length-scales are found in the same manner as discussed in the description of table 2.3.

Appendix 2A: Importance of the Ice Shelf

As all of the ice streams that display far-field tidal effects have a connected ice shelf, we now consider the role that the ice shelf plays as the intermediary between the ocean tides and the grounded ice stream. Recall the two-dimensional model results shown in figures 2.2 and 2.3 for models both with and without an ice shelf. For a given basal condition, any variation between the two model results must be due to the presence of the shelf alone.

For the model with a frozen base, the presence of an ice shelf has two effects. First, there is a perturbation to the stress field near the grounding line (about two kilometers inland at most), due to flexural stresses introduced by the ice shelf. Second, the overall magnitude of stresses in the ice stream is elevated compared to models with only axial loading as there is an overall increase in the magnitude of the loading applied in the model. This effect does not change L_{tr} . Thus for ice with no basal sliding, including an ice shelf affects the magnitude, but not the nature of the stress field, far inland of the grounding line.

For the two-dimensional model with basal sliding, stresses due to ice flexure decay to inconsequential levels 5-7 kilometers inland of the grounding line. Beyond this point, the stress state of the ice stream is identical to the stress state for a model with axial loading only. Thus, for an ice stream with no basal resistance, the ice shelf does not influence the modeled results farther inland than the first five to ten kilometers of grounded ice.

The general finding that flexural stresses only perturb the stress field near the grounding line is consistent with the observations of ice flexure transmission of ten

kilometers or less, as summarized in table 1.1. Additionally, our constant loading shelf condition overestimates flexural stress by almost a factor of four compared to a more realistic floating condition (see appendix 2B). This indicates that flexural stresses may decay to small values over a shorter distance than predicted here. Our models reproduce the observation that the flexural stresses, as induced by the presence of an ice shelf, are not important far inland of the grounding line.

The basal condition beneath the ice stream determines the influence of the ice shelf on the overall magnitude of the stress in the far-field ice stream. As ice streams have little basal resistance, the finding that the overall stress magnitude is independent of the ice shelf outside of the flexure zone is applicable here. Our interest is in the value of stresses many tens of kilometers inland of the grounding line, thus we can safely neglect the ice shelf in our models without changing the transmission of tidal, non-flexural stresses.

Appendix 2B: Flotation Condition for a One-Dimensional Ice Shelf

As shown in figure 2.1, we apply two tractions to a model ice shelf to simulate the stress change on an ice shelf due to a change in tide height. First, we consider the axial load of the tide on the ice shelf's edge. A simple comparison is to look at the stress within an axial bar that is compressed axially with a constant stress. Assume the bar to be fixed at the unforced end. By the compatibility condition:

$$\delta\sigma/\delta x = 0 \quad (2.B1)$$

the stress and strain in such a model must be constant throughout the bar. This corresponds to infinite stress-transmission.

Second, we model the ice shelf as a Bernoulli-Euler beam subjected to a distributed load, with this load coupled to the beam deflection by a flotation condition. This approach is similar to the methodology of Reeh et al. (2000). The governing equation of such a model is:

$$EI \frac{\delta^4 w}{\delta x^4} = \rho_w g (\Delta h - w) \quad (2.B2)$$

where ρ_w is the density of water, g is gravitational acceleration, w is the (vertical) deflection of the beam, E is the Young's modulus of ice, $I = \left(\frac{w}{12}\right) \cdot (h)^3$ is the second moment of area for the ice shelf.

The solutions of this equation for multiple ice shelf lengths are found and shown in figure 2.B1. The primary result is that, for a one meter tide, a shelf of longer than five kilometers no longer influences the stresses at the grounding line, meaning that for our

purposes, we only need to consider a shelf of five kilometers length in our finite element modeling.

Additionally, we model a linearly thinning ice shelf (through the modification of I , using $I = \left(\frac{w}{12}\right) \cdot \left[h_0 - (h_0 - h_1)\frac{x}{L}\right]^3$ where the thickness linearly changes from h_0 to h_1) and find that this has only a small influence on the stress and deflection throughout the shelf. Thus these effects will not be considered further.

Lastly, we model the results for a simpler, uncoupled stressing condition. In figure 2.B1, the red dashed line corresponds to a constant loading function equal to $\rho_w g \Delta h$. This simpler condition overestimates the stress and deflection over the model domain compared to the more correct flotation condition. However, as the boundary condition does not depend on, and thus is decoupled from, the deflection w , we use this constant loading as our ice shelf boundary “pseudo-flotation” condition in our finite modeling.

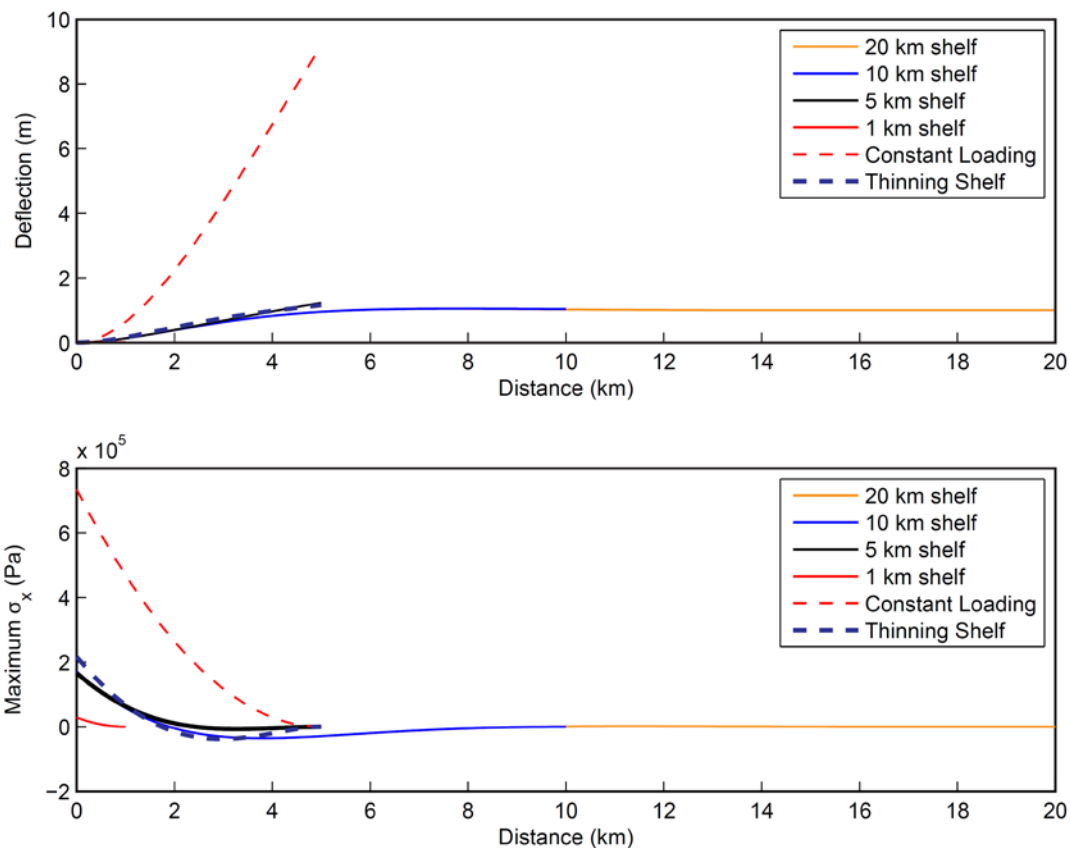


Figure 2B1: Results of the one-dimensional flexural beam approximation of a floating ice shelf. The upper figure shows the beam deflection while the lower section shows the stress at the upper edge of the beam. See text for a description of the governing equations and boundary conditions for the models shown.

Appendix 2C: Two-Dimensional Model Results

Here, we present the complete summary of our model results for our “frozen bed” model, as demonstrated in figure 2.3. We ran a total of nine models, investigating the dependence of the stress and displacement distributions on the ice thickness, h , and the ice’s elastic modulus, E . Table 2.3 provides details to each model, including the values of h and E , as well as the values of basal stress and surface displacement at the grounding line (i.e., the maximum values), and the e-folding length of the stress and displacement decay. Figures 2C.1 to 2C.8 demonstrate the stress and displacement distributions in each model not shown in the main paper, following the example set by figure 2.3.

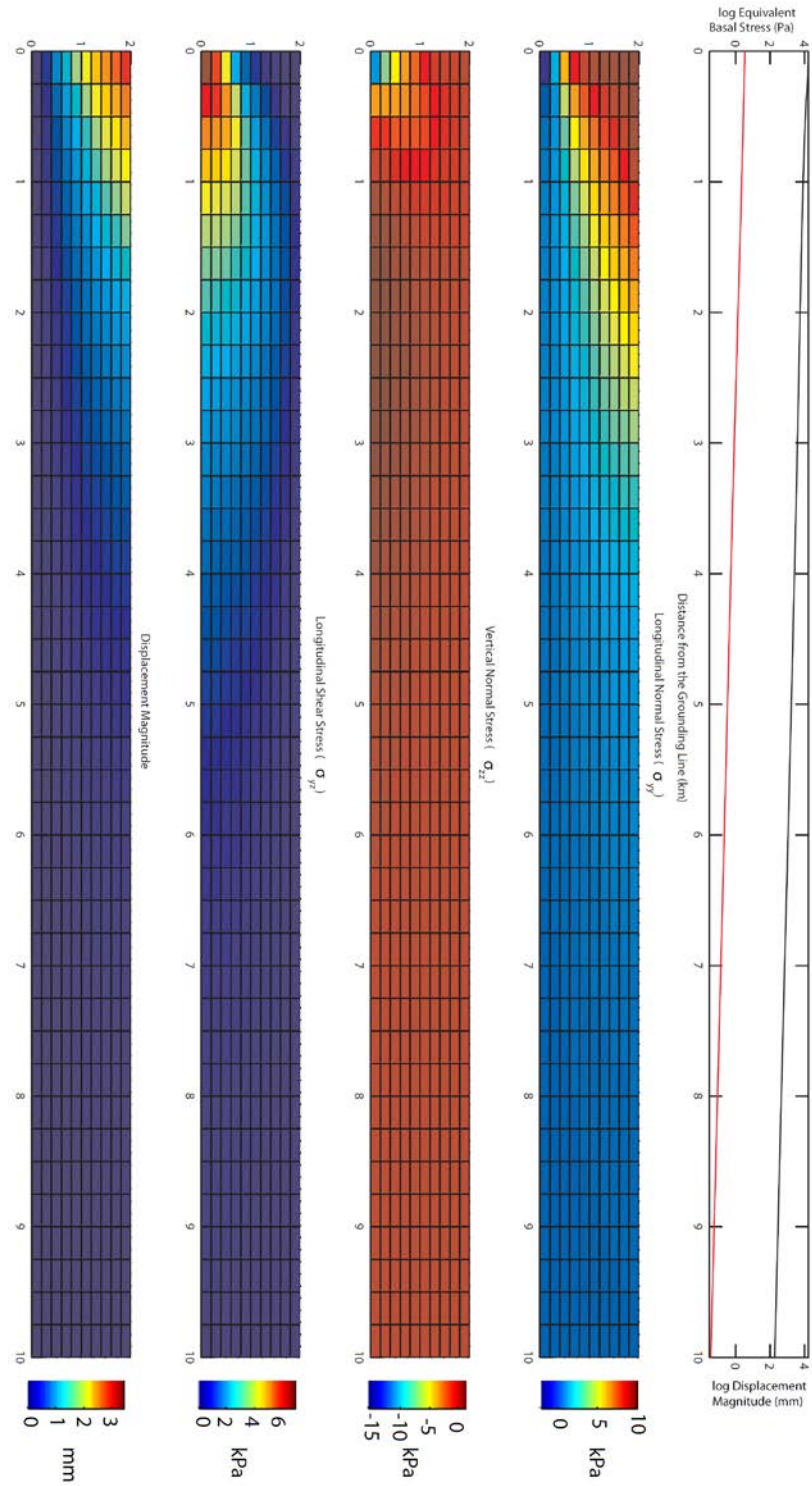


Figure 2C.1: Stress and displacement fields for the two-dimensional frozen bed model with $h=2\text{ km}$ and $E=9.33\text{ GPa}$.

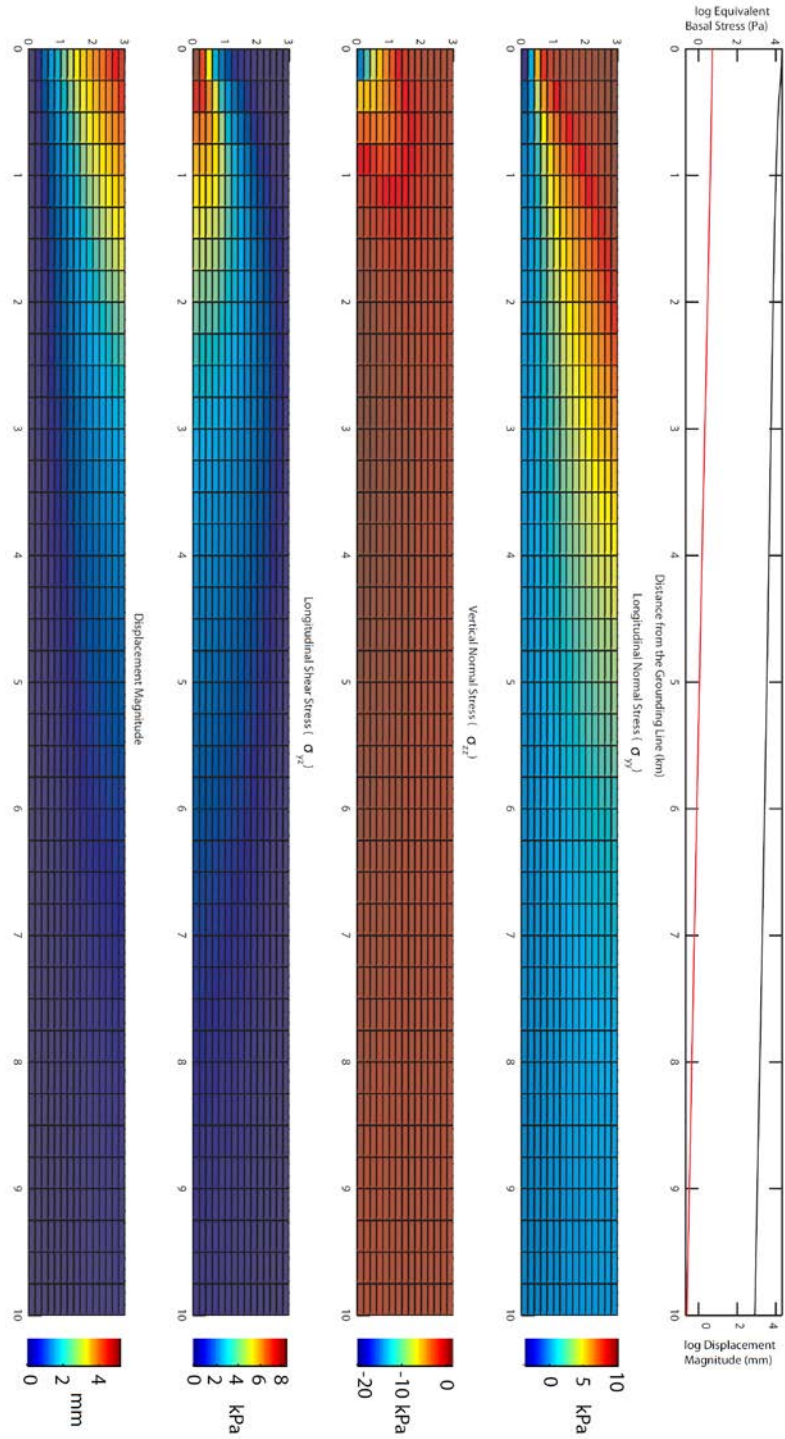


Figure 2C.2: Stress and displacement fields for the two-dimensional frozen bed model with $h=3km$ and $E=9.33 GPa$.

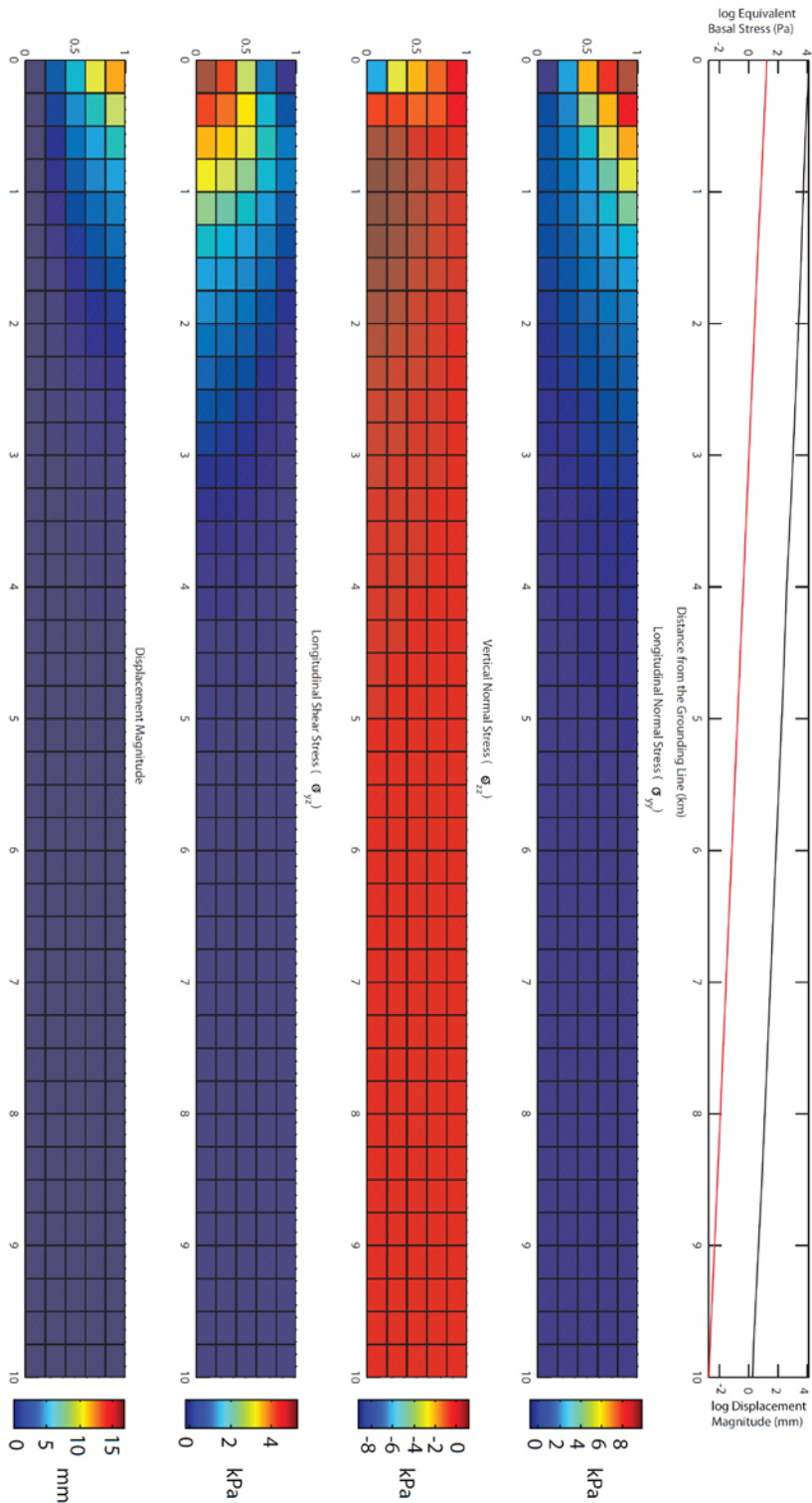


Figure 2C.3: Stress and displacement fields for the two-dimensional frozen bed model with $h=1km$ and $E=0.933 GPa$.

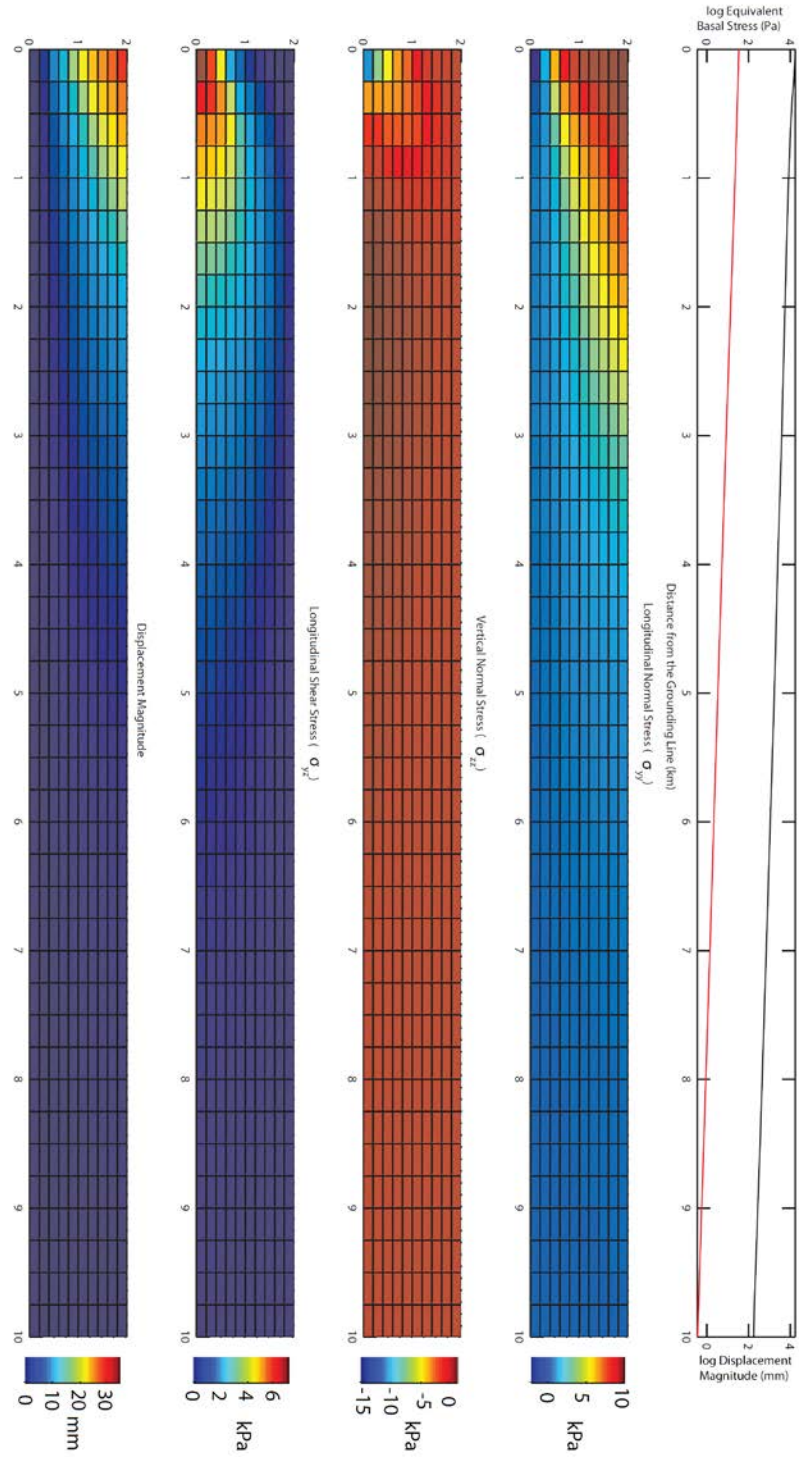


Figure 2C.4: Stress and displacement fields for the two-dimensional frozen bed model with $h=2\text{km}$ and $E=0.933\text{ GPa}$.

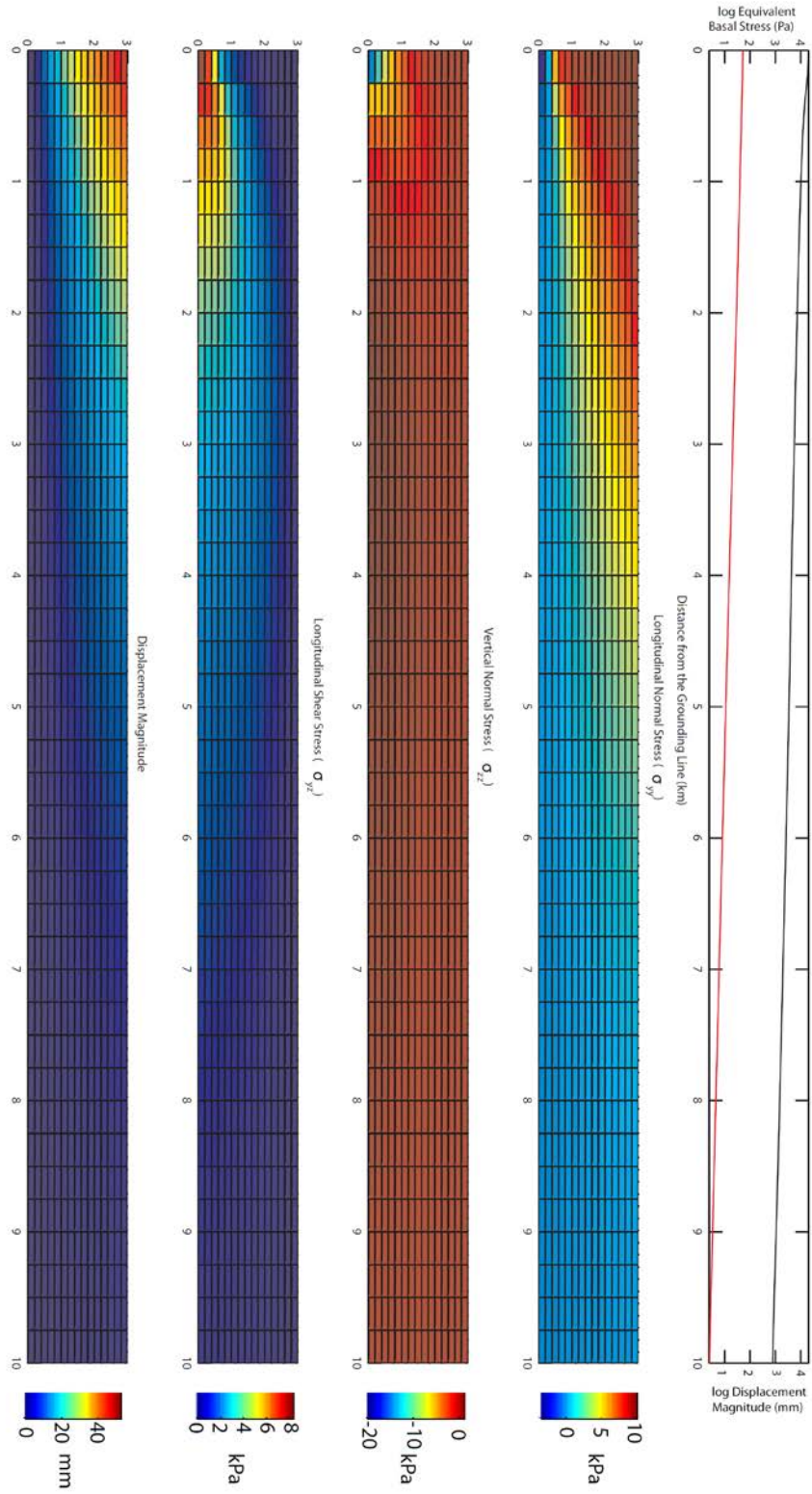


Figure 2C.5: Stress and displacement fields for the two-dimensional frozen bed model with $h=3km$ and $E=0.933 GPa$.

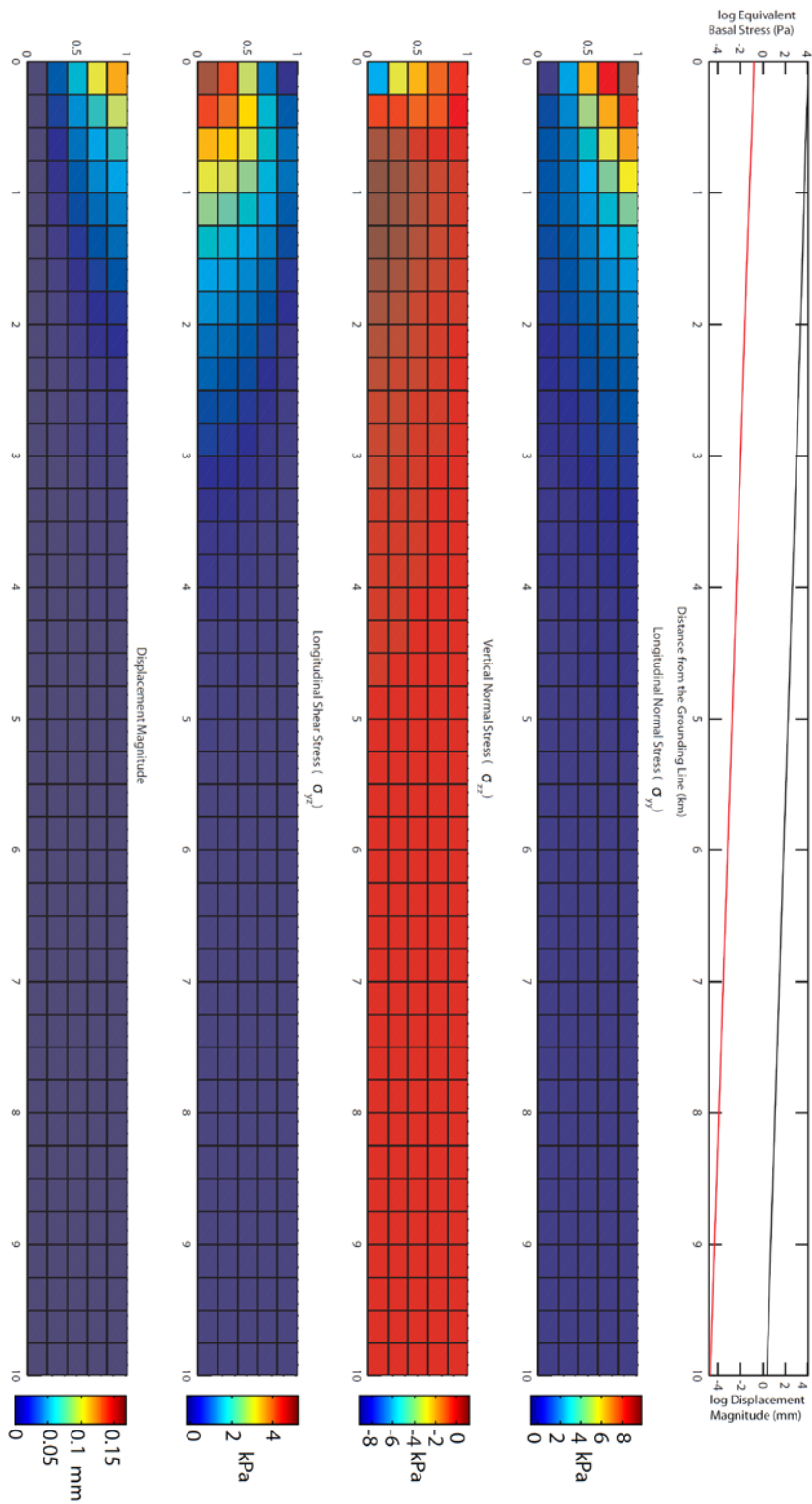


Figure 2C.6: Stress and displacement fields for the two-dimensional frozen bed model with $h=1\text{ km}$ and $E=93.3\text{ GPa}$.

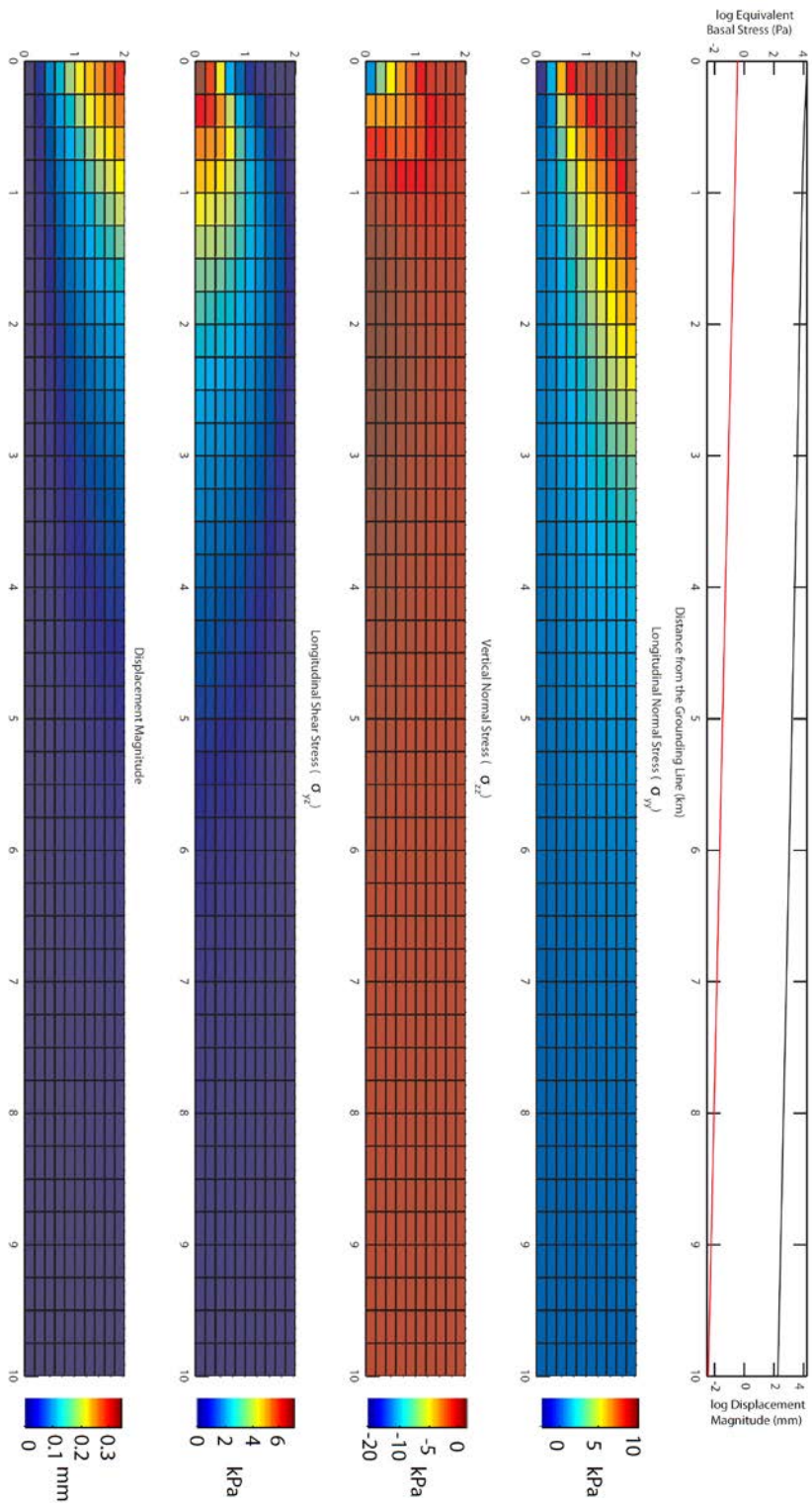


Figure 2C.7: Stress and displacement fields for the two-dimensional frozen bed model with $h=2\text{km}$ and $E=93.3\text{ GPa}$.

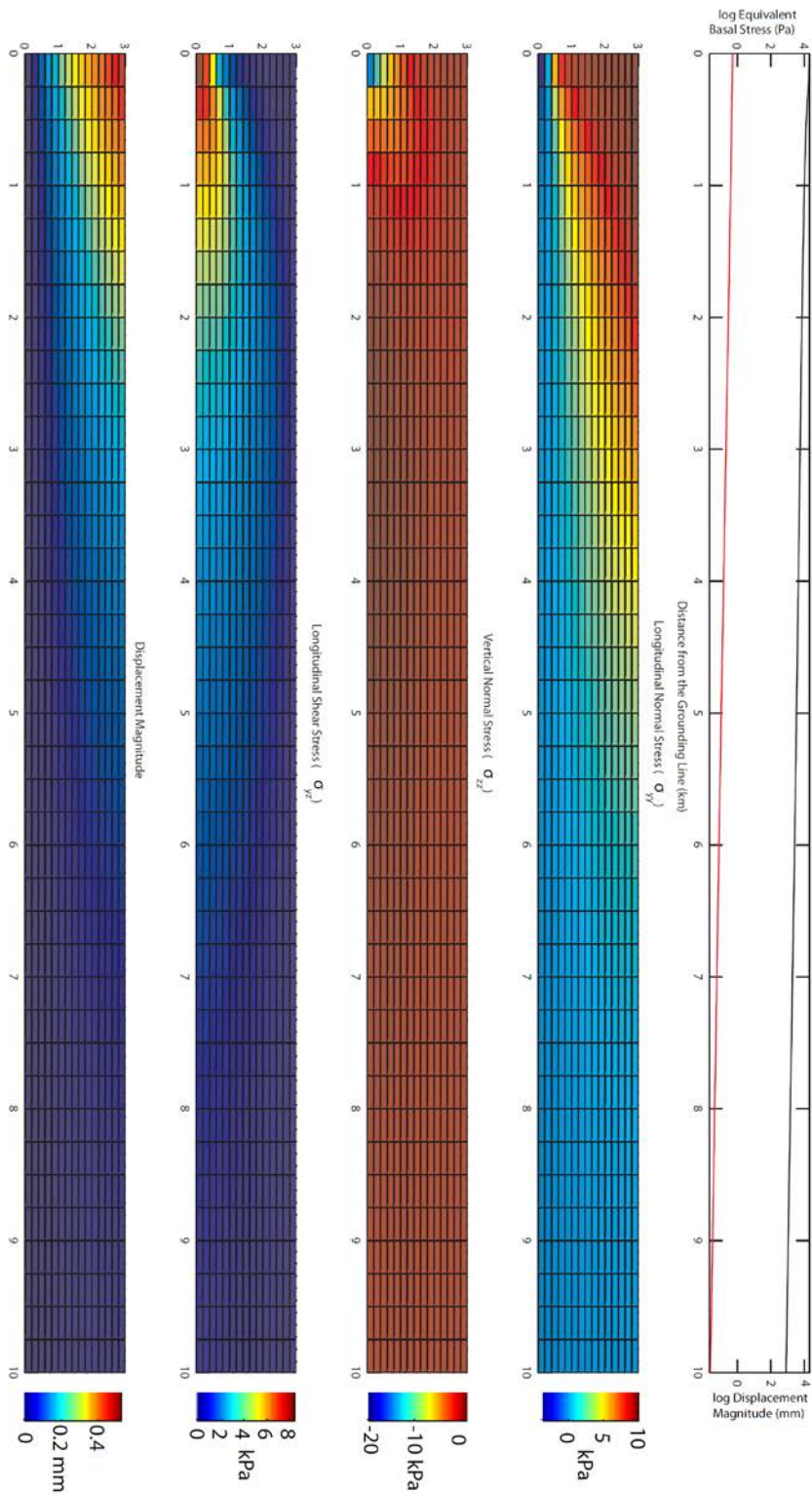


Figure 2C.8: Stress and displacement fields for the two-dimensional frozen bed model with $h=3\text{km}$ and $E=93.3\text{ GPa}$.

Appendix 2D: Three-Dimensional Model Results

In this section, we present the results from our entire three-dimensional model suite. In these models, we varied the ice thickness, h , the ice stream width, w , and the elastic modulus E . We present a total of 14 model results. The first nine models (figures 2.6 and figures 2D.1 to 2D.8) explore the dependence of the results on the geometric parameters h and w . Models 10 and 11 (figures 2D.9 and 2D.10) demonstrate the linear dependence of the model results on the elastic modulus. Models 12 to 14 (figures 2D.11 to 2D.13) represent the geometries of Bindschadler Ice Stream, Pine Island Glacier, and Rutford Ice Stream, respectively. Due to the lack of GPS data from Pine Island Glacier, these model results are not compared to observations. Table 2.4 summarizes the model parameters, as well as the output results of surface displacement and basal stress at the grounding line in the middle of the ice stream (the global maximum value), as well as the e-folding length in each model. Figures 2D.1 to 2D.13 show the modeled stress distributions, following the example of figure 2.6 from the main body of this paper.

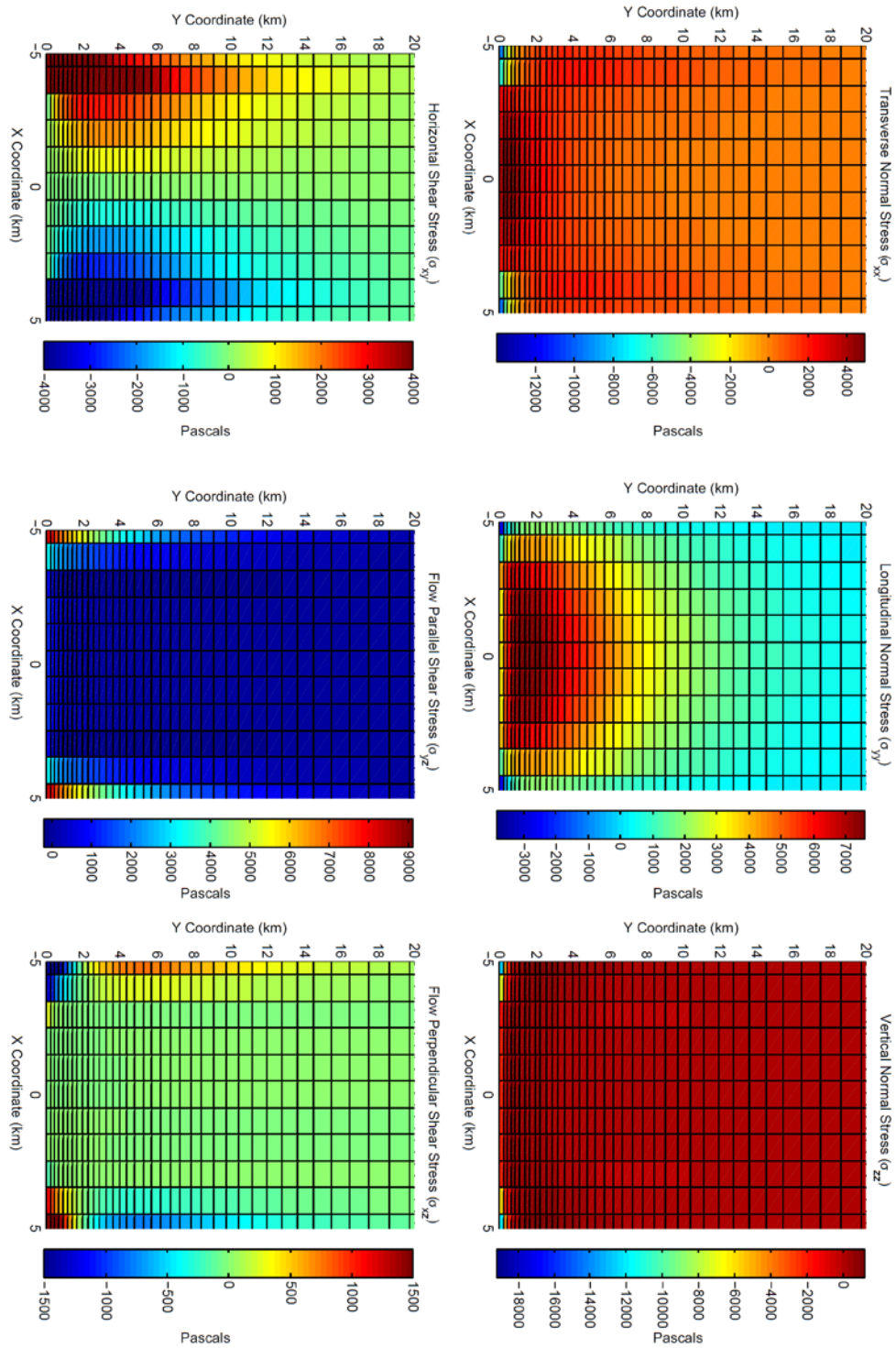


Figure 2D.1: Stress field for the three-dimensional model with $h=2$ km, $w=10$ km, and $E=9.33$ GPa.

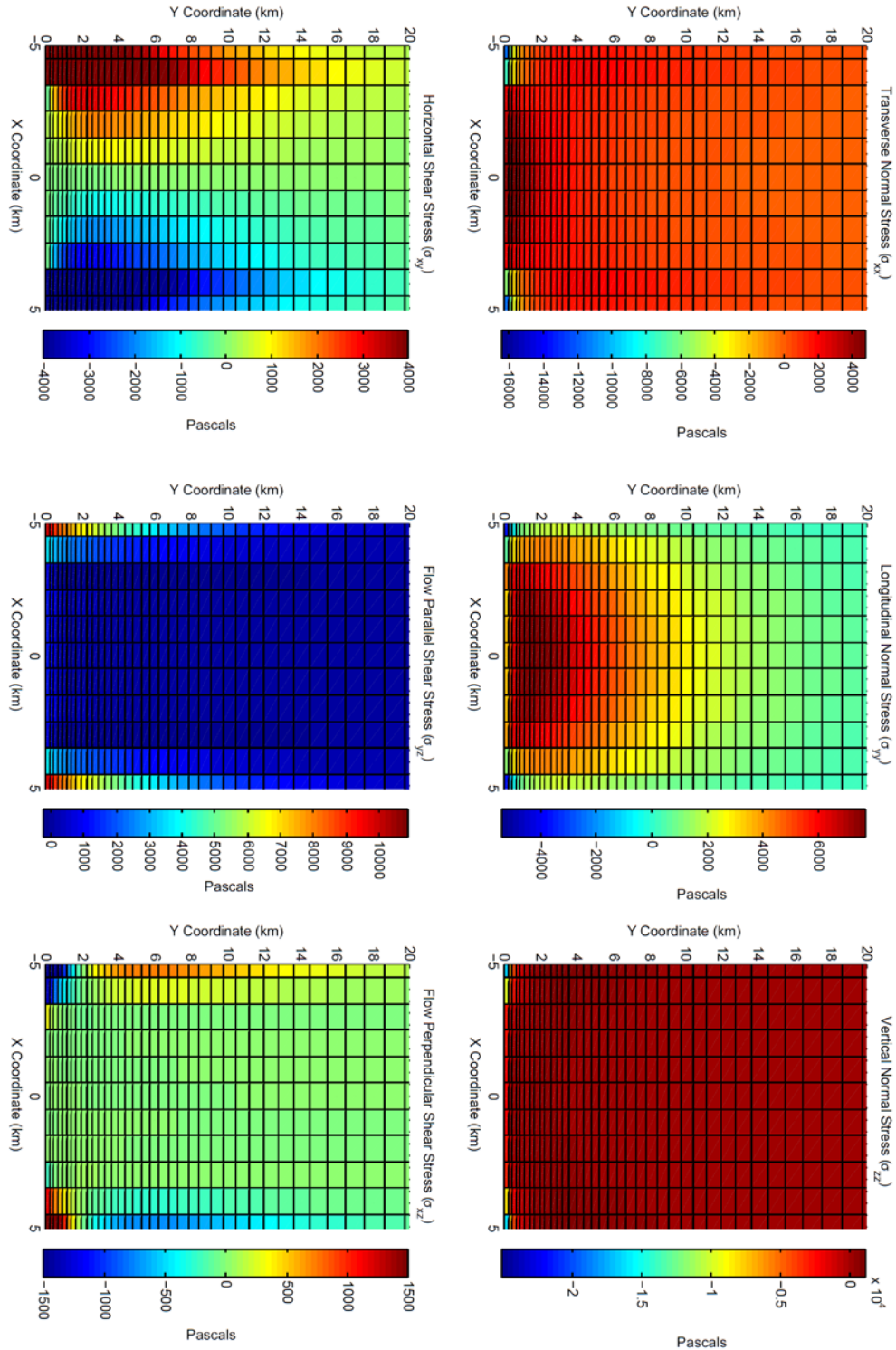


Figure 2D.2: Stress field for the three-dimensional model with $h=3$ km, $w=10$ km, and $E=9.33$ GPa.

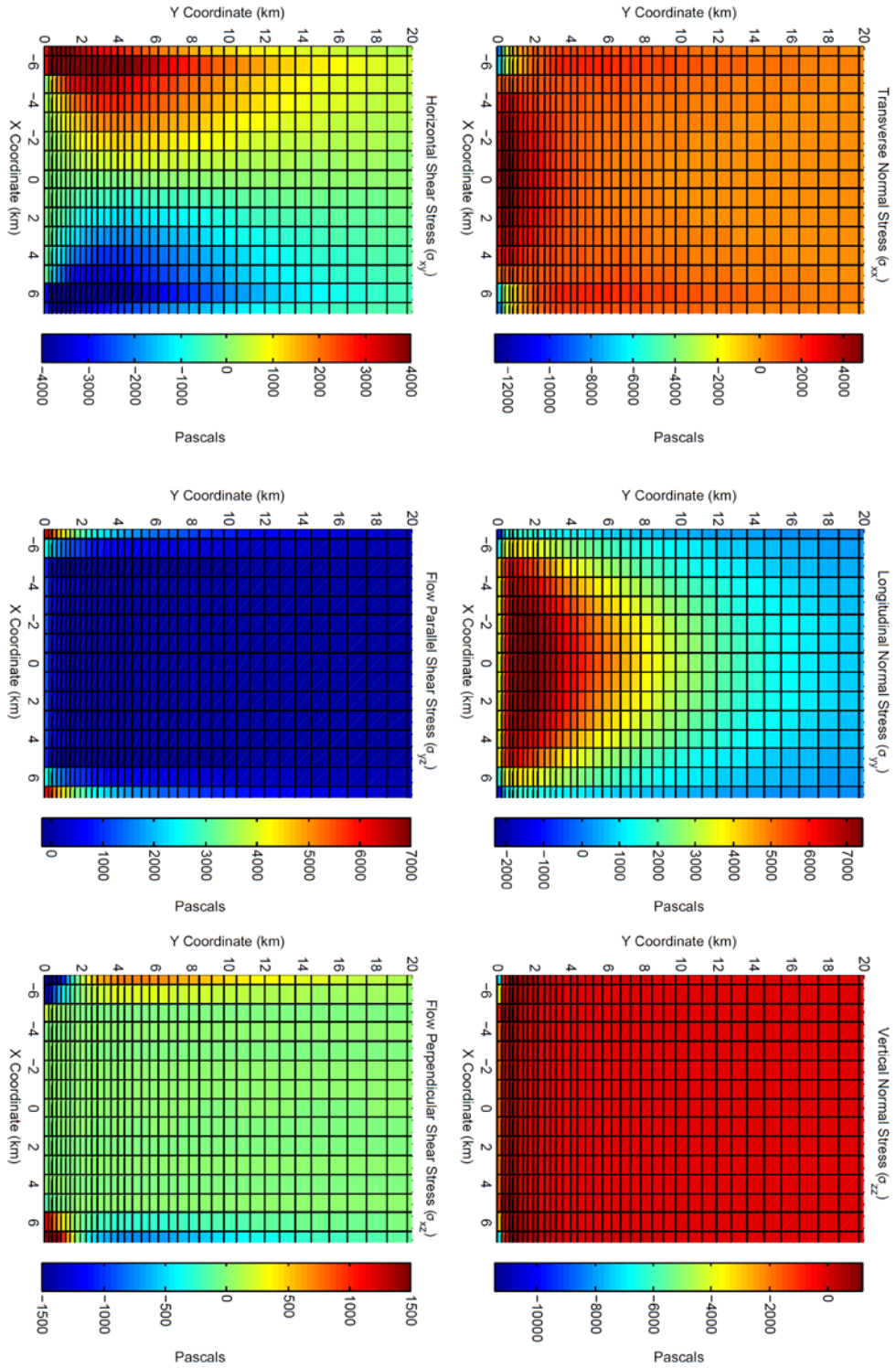


Figure 2D.3: Stress field for the three-dimensional model with $h=1$ km, $w=14$ km, and $E=9.33$ GPa.

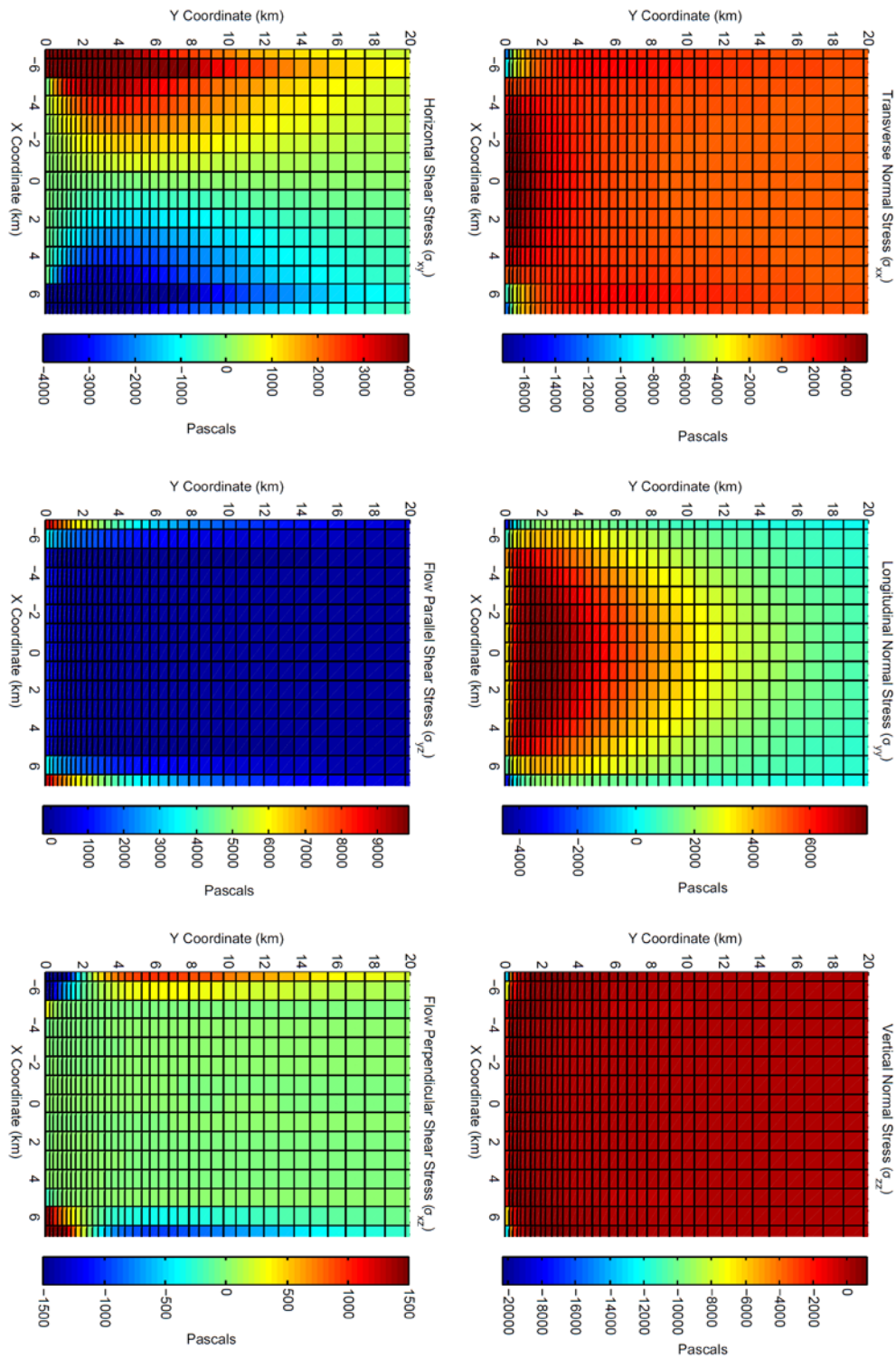


Figure 2D.4: Stress field for the three-dimensional model with $h=2$ km, $w=14$ km, and $E=9.33$ GPa.

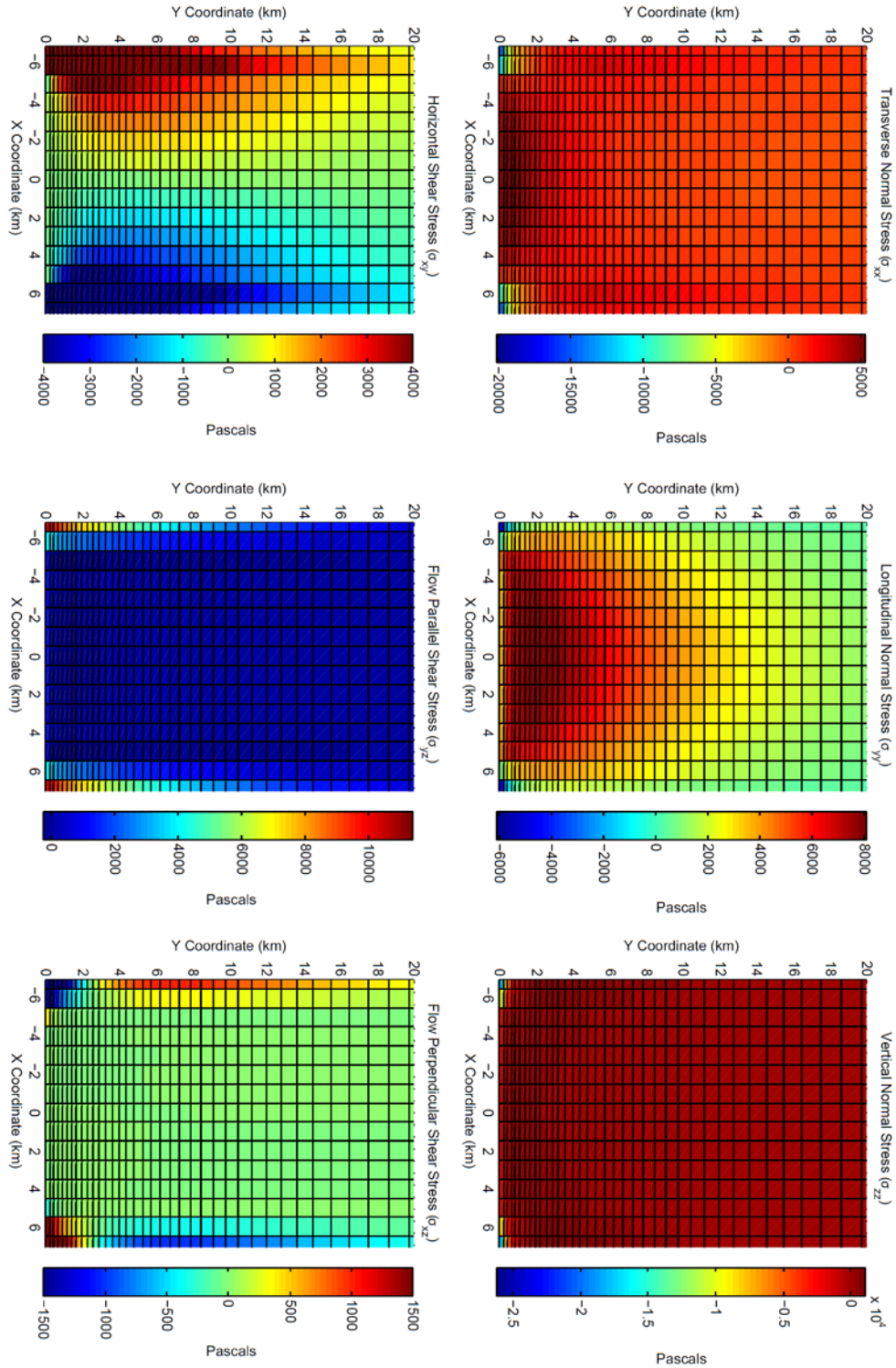


Figure 2D.5: Stress field for the three-dimensional model with $h=3$ km, $w=14$ km, and $E=9.33$ GPa.

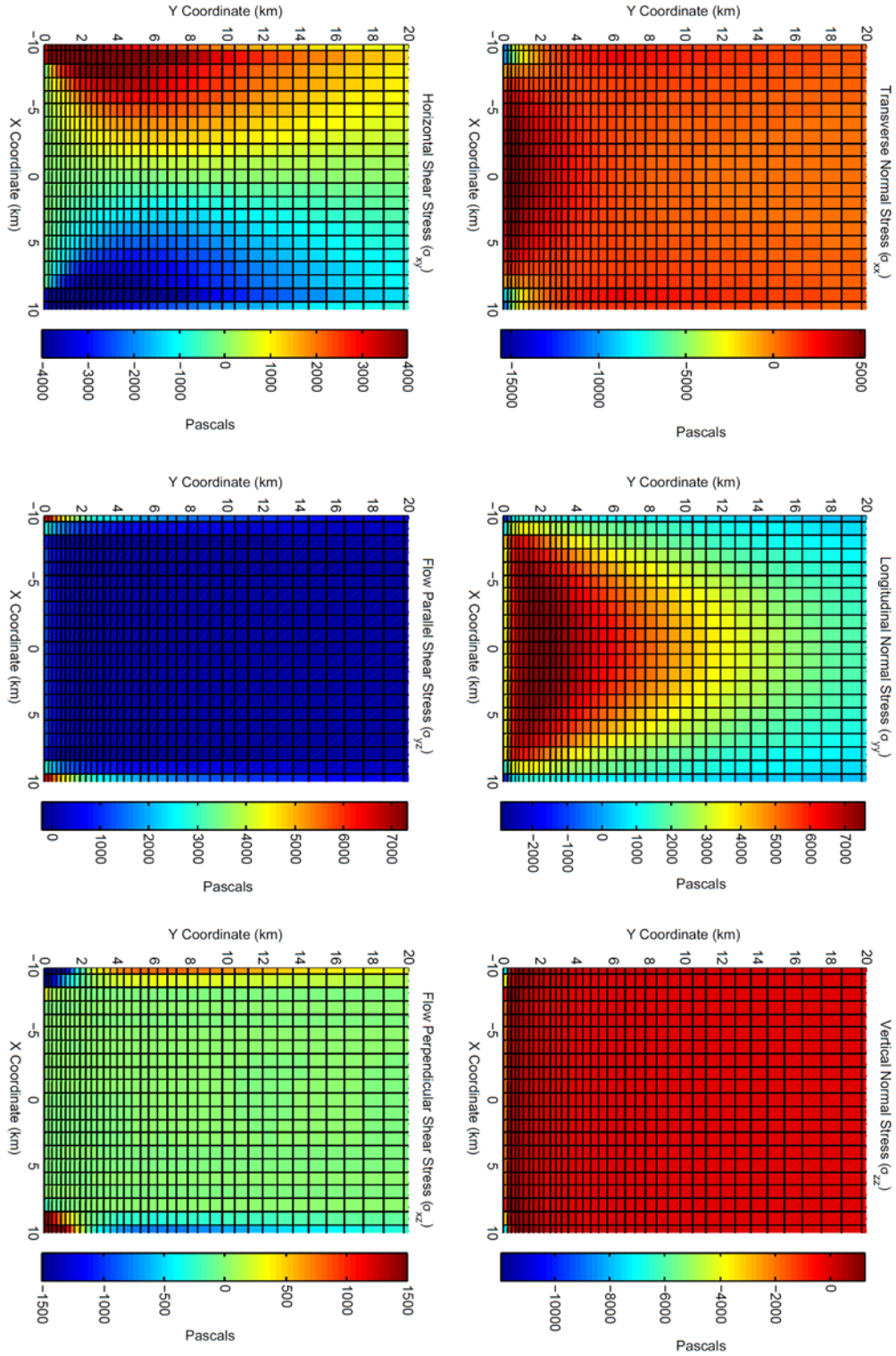


Figure 2D.6: Stress field for the three-dimensional model with $h=1$ km, $w=20$ km, and $E=9.33$ GPa.

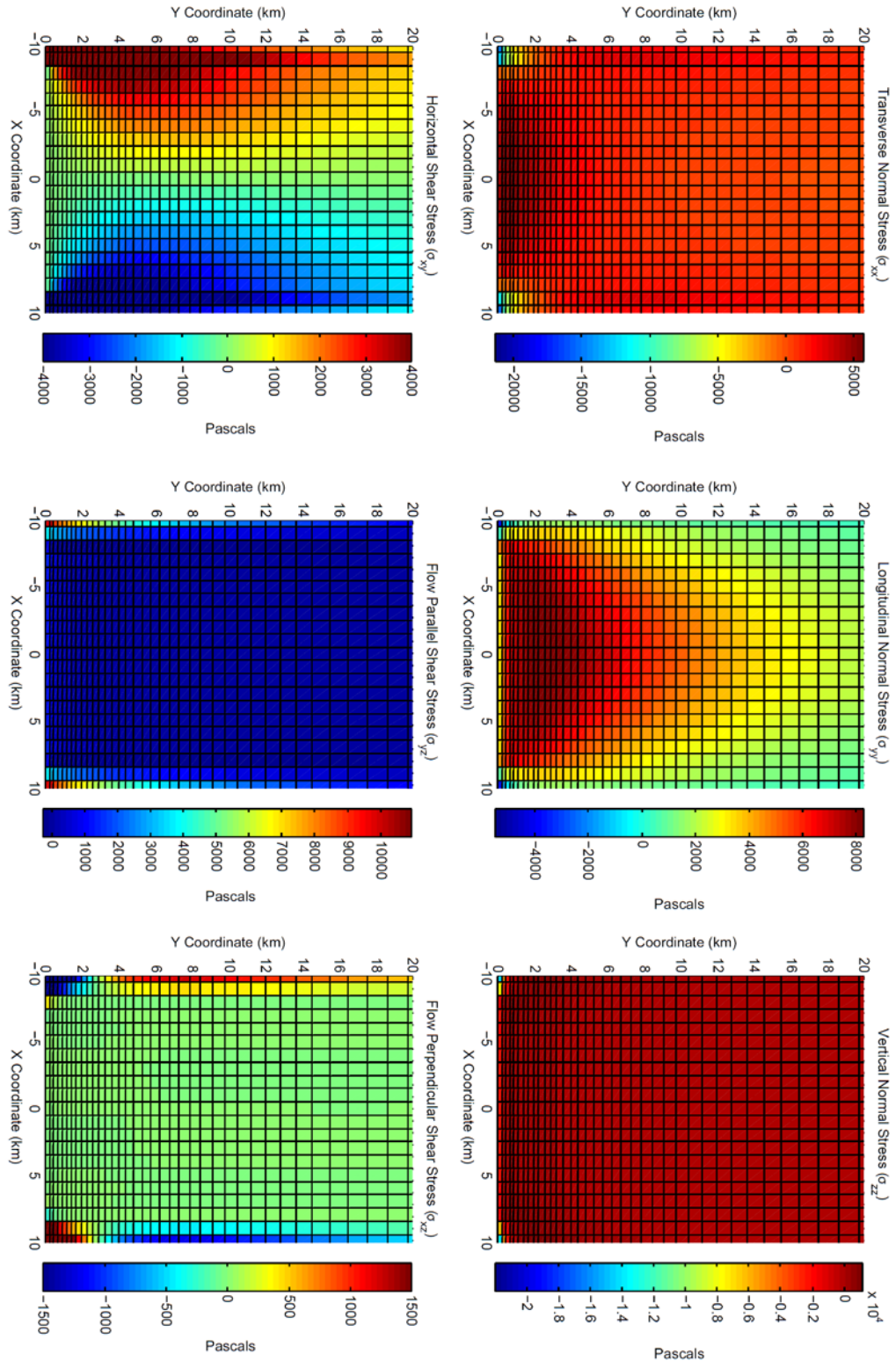


Figure 2D.7: Stress field for the three-dimensional model with $h=2$ km, $w=20$ km, and $E=9.33$ GPa.

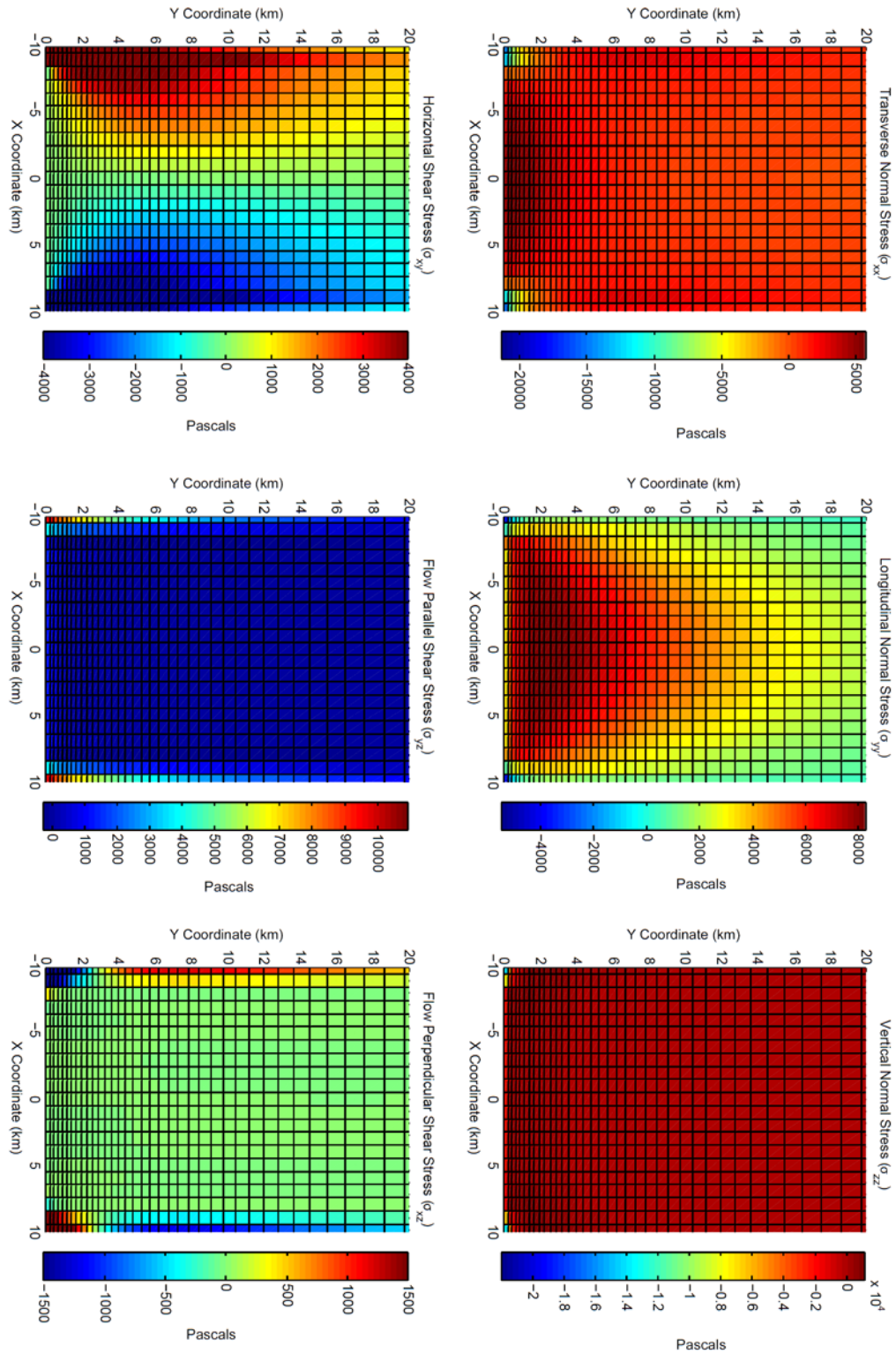


Figure 2D.8: Stress field for the three-dimensional model with $h=3$ km, $w=20$ km, and $E=9.33$ GPa.

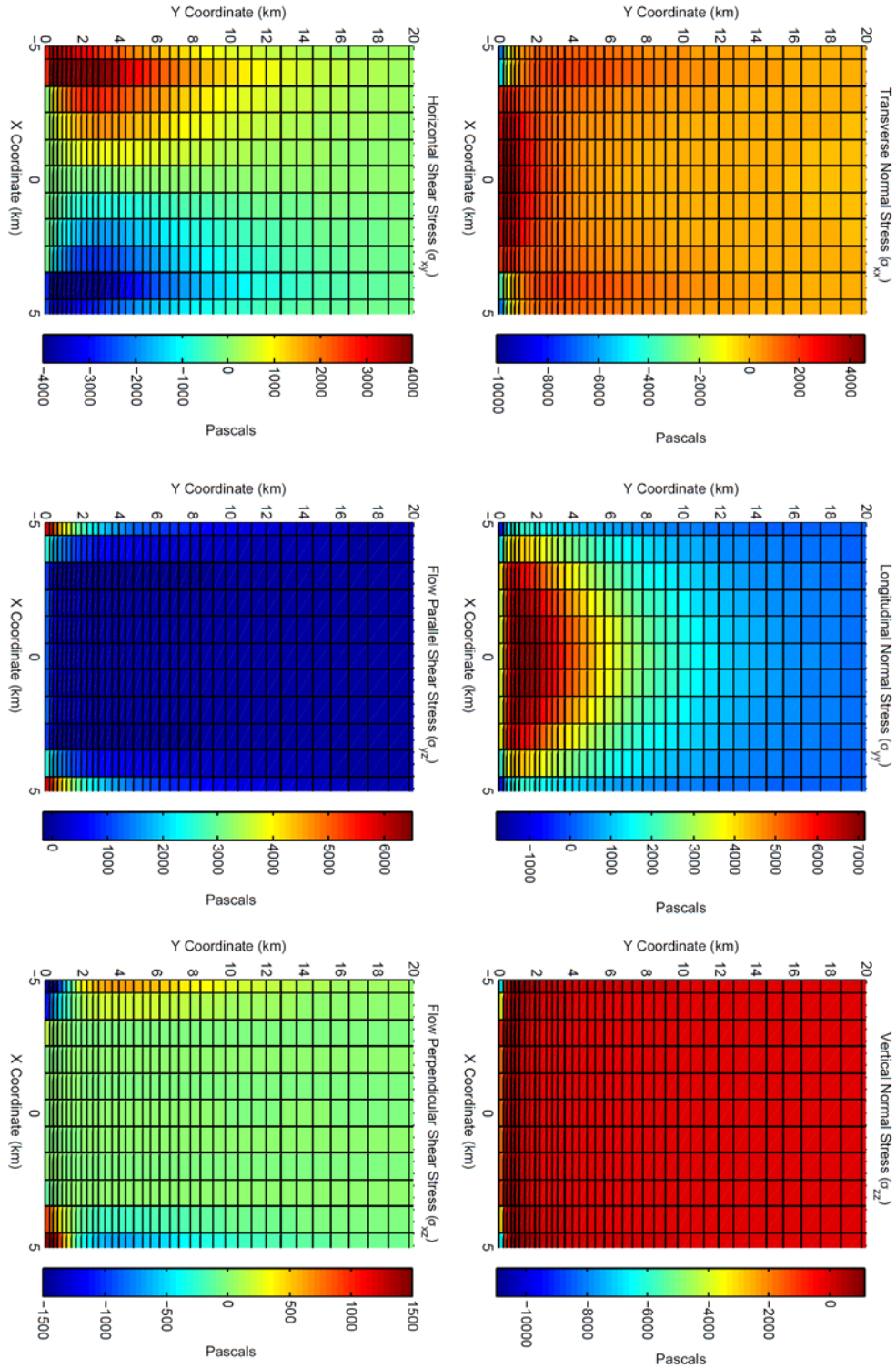


Figure 2D.9: Stress field for the three-dimensional model with $h=1$ km, $w=10$ km, and $E=0.933$ GPa.

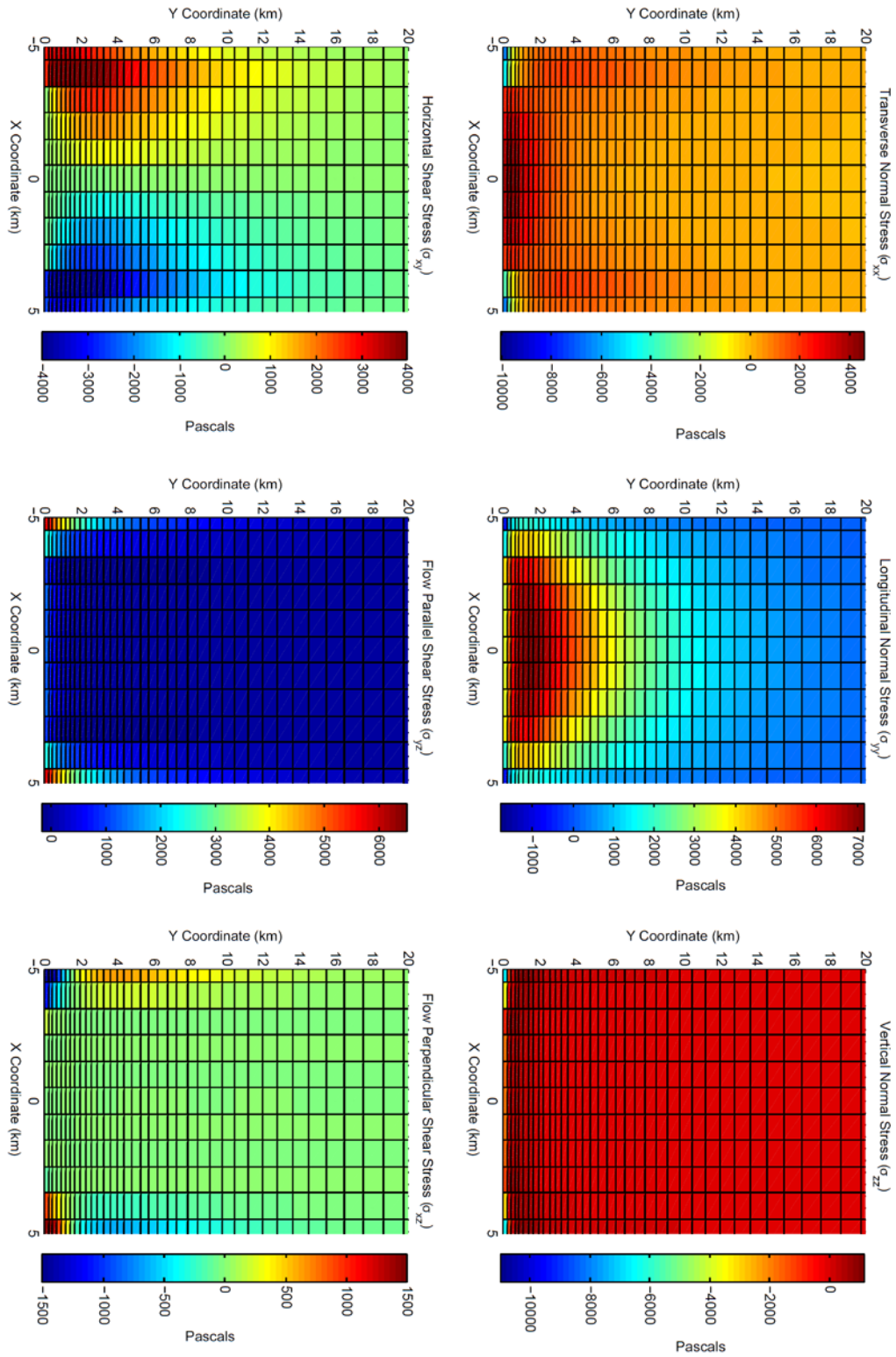


Figure 2D.10: Stress field for the three-dimensional model with $h=1$ km, $w=10$ km, and $E=93.3$ GPa.

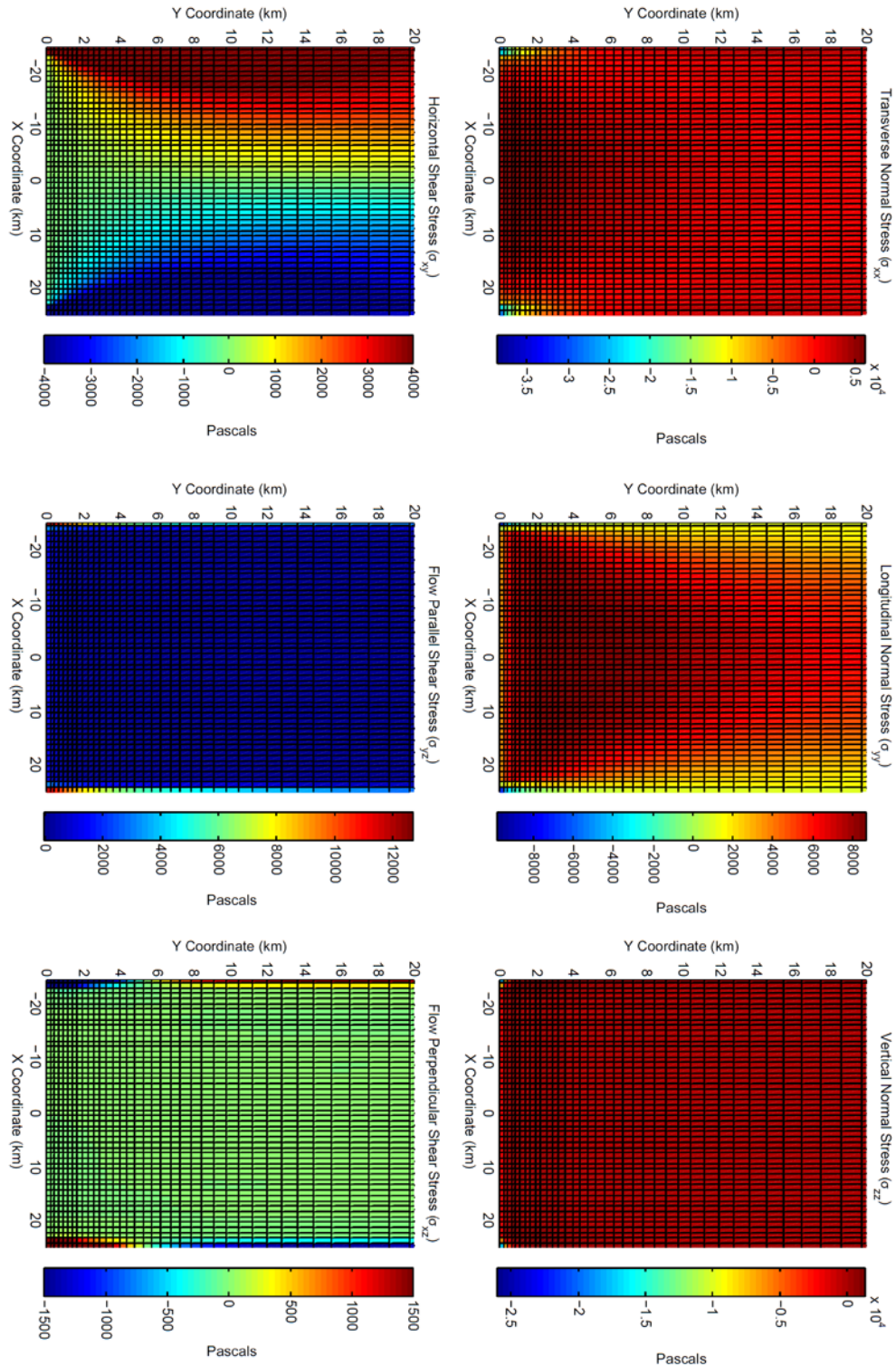


Figure 2D.11: Stress field for the three-dimensional model approximating Bindschadler Ice Stream, with $h=2$ km, $w=50$ km, and $E=9.33$ GPa.

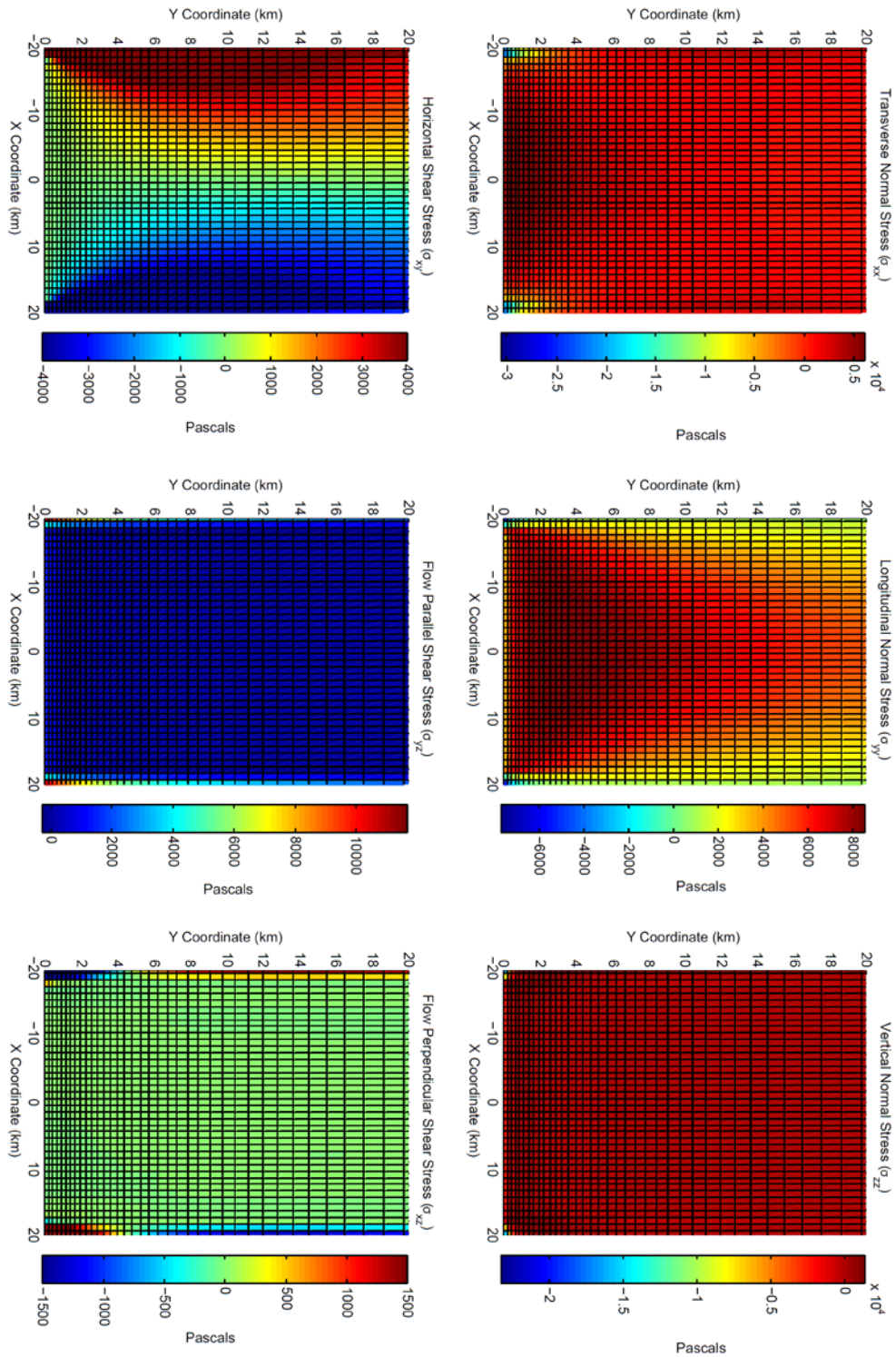


Figure 2D.12: Stress field for the three-dimensional model approximating Pine Island Glacier, with $h=2$ km, $w=40$ km, and $E=9.33$ GPa.

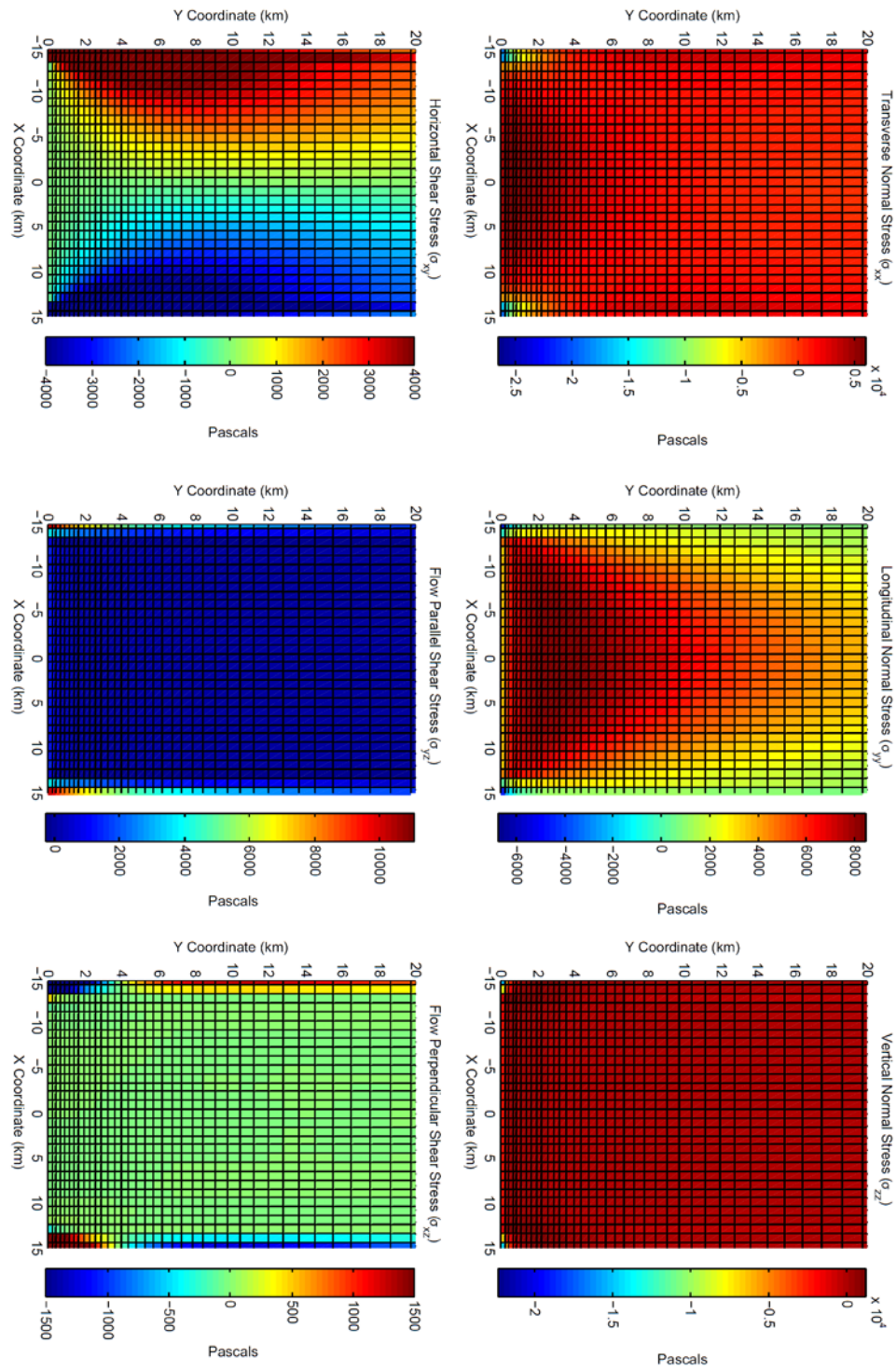


Figure 2D.13: Stress field for the three-dimensional model approximating Rutford Ice Stream, with $h=2$ km, $w=30$ km, and $E=9.33$ GPa.

Chapter 3

Inhomogeneous Elasticity and Viscoelasticity: Effects on Stress-transmission in Ice Streams

As demonstrated in the previous chapter, the geometry of a homogeneous elastic ice stream imposes a stringent restriction on the distance that ocean tidal loads can be transmitted inland of the grounding line. However, ice streams are not uniform elastic bodies. There are bulk material inhomogeneities due to enhanced shear in the marginal ice and vertical temperature gradients in the ice. Additionally, ice deforms viscously over long timescales and preferential flow directions due to ice's polycrystalline nature can align, resulting in anisotropic deformation. In this chapter, we first consider the effect of elastic inhomogeneity on the length-scale of the transmission of tidal stresses inland of the grounding line—specifically investigating an increase in the compliance of the ice stream's lateral margins. Increasing the marginal compliance reduces the stress supported by the ice stream's sidewalls, resulting in an increase in the length-scale of stress-transmission. We then explore the role of viscoelasticity in the deformation of the ice stream, in order to quantify the effect that viscoelasticity has on the inferred transmission length-scale of a tidal stress. While we find that viscoelasticity plays an important role in determining the time delay between the peak tidal signal and peak surface motion of the grounded ice stream, the effect on the stress-transmission length-scale is too minor to explain the long-distance observations from Bindschadler and Rutford Ice Streams. Ultimately, we conclude that lacking a mechanism which essentially decouples an ice stream from its lateral margins, a process outside of the bulk

of the ice stream must be responsible for the large zone of tidal influence observed on some Antarctic ice streams.

3.1 Introduction

As alluded to at the end of chapter 2, representing ice as a homogeneous elastic body is not the most realistic rheological model for ice. The choice of material model will directly affect the stress-transmission behavior in our ice stream models. As the calculated stress-transmission length-scales in our three-dimensional ice stream models are too short to match the observations from Rutford and Bindschadler Ice Streams (Gudmundsson, 2007; 2008; 2011; Anandkrishnan et al., 2003), for a realistic rheological change to be significant, the new rheology must weaken the resistance of the ice stream's lateral margins. In this introductory section, we first describe several common inhomogeneities in ice's elastic behavior before introducing the range of viscoelastic constitutive laws used in glaciology to model ice deformation. We consider inhomogeneity in elasticity created by the large-scale crevassing of an ice stream's shear margins and what effect such marginal weakening has on the ice stream's ability to transmit tidal loads. We also consider the impact of incorporating a viscous component of ice deformation over the tidal timescales has on the extent of tidally induced deformation of an ice stream. Given the independence of these two rheological considerations we discuss each separately. This chapter closes with a discussion of both elastic and viscoelastic homogeneity as related to field observations from Antarctica.

3.1.1 Elastic Rheological Effects

The impacts of temperature, crystal fabric, and ice purity on the viscous deformation of ice are better constrained than their potential to modify the effective elastic moduli of ice.

While there is no reason to believe *a priori* that the same processes that alter viscous flow of ice will also alter the elastic response of ice, investigating these processes that influence ice viscosity does provide a touchstone for understanding the physical mechanisms behind potential elastic inhomogeneity. For viscous flow, we focus on how three different processes impact the viscosity parameters: temperature-dependent viscosity, fabric-induced preferential viscous flow directions, and enhanced shear in ice stream margins. For each process, we first summarize that process's ability to perturb viscosity of ice then discuss that process's potential to change the (elastic) compliance of ice.

3.1.1.1 Temperature-Dependent Rheology

The West Antarctic ice sheet and ice streams are polythermal glaciers, with temperatures ranging from the pressure melting point to as low as $-50\text{ }^{\circ}\text{C}$ (e.g., Gow et al., 1968; Engelhardt, 2004a, 2004b; Salamatin et al., 2008). A bevy of field observations (e.g., Nye, 1953; Jezek et al., 1985, MacAyeal et al., 1996, 1998) and laboratory experiments (e.g., Budd and Jacka, 1989) show a clear temperature dependence in the viscosity coefficient of ice. Following Cuffey and Paterson (2011), the temperature dependence of ice viscosity can be summarized by two different Arrhenius relationships: one for temperatures between 0 and $-10\text{ }^{\circ}\text{C}$, and the other for temperatures colder than $-10\text{ }^{\circ}\text{C}$. For reference, the viscosity coefficient, the nonlinear analog to viscosity, changes by about a factor of 10 between 0 and $-10\text{ }^{\circ}\text{C}$. The large change in the magnitude of ice's viscous deformation with temperature implies that the viscosity coefficient in ice streams can be substantially varied as a function of ice stream depth.

Jellinek and Brill (1956) find that the Young's modulus of ice varies by about 40% over a temperature range of -5 to -15 °C, though there is a large amount of variability in measured moduli. The temperature dependence of elasticity is quite a bit smaller than that of viscosity for a given temperature profile. As a demonstration of how negligible the temperature dependence of ice elasticity is, Jellinek and Brill construct a well-fit rheological model for ice using data from their creep relaxation experiments where only the viscous deformation of the ice is temperature dependent. Of course, if the ice is heated to the point of melting, then the elastic strength of the ice will necessarily plummet; however, for our purposes we will assume that melting is negligible.

3.1.1.2 Fabric Dependence

Glacial ice, being polycrystalline, is known to be strongly anisotropic once creep establishes a preferred crystal orientation. The direction of ice motion relative to the preferred crystalline glide direction dictates the deviation in observed strain rate from that of isotropic ice. The anisotropy of a mature crystal fabric in ice can enhance the strain rate of ice in a "weak" orientation by up to 100 times that of ice in a "strong" orientation (Shoji and Langway; 1988).

Such polycrystalline anisotropy also influences the elastic behavior of ice, as demonstrated through the measurement of seismic anisotropy in glacial ice by Blankenship and Bentley (1987). They found that the variation in seismic P-wave speed in glacial ice is about 10%. This change in wave speed corresponds to a variation in elastic moduli on the order of 20%. Focusing on the slower-moving ice stream, Blankenship and Bentley suggested that a preferentially oriented ice fabric is the cause of the observed change in wave speed. The faster-moving ice stream could conceivably

develop a stronger fabric that could result in an increased influence on the elasticity of ice.

Laboratory results for anisotropy in the Young's moduli of sea ice found a peak to peak variation between 10% and 41%, depending on the nature of the columnar crystallization (Nanthikesan and Sunder; 1995 and references therein). While such laboratory results are not strictly usable to determine the behavior of glacial ice due to the presence of salt in the sea ice's crystalline structure, all the studies presented here suggest that the variation in elastic moduli for polycrystalline ice, with a preferred crystal orientation relative to isotropic ice, is less than a factor of two.

3.1.1.3 Enhanced Deformation in the Shear Margins

In some cases, a single Glen-style viscous flow law is unable to explain observed viscous flow velocities in glaciers over long timescales. Examples include the depth-variable age of ice in ice caps (Paterson, 1991), basal impurities in mountain glaciers (Dahl-Jensen and Gundestrup, 1987; Echelmeyer and Wang, 1987), and most importantly the highly strained ice in the shear margins of West Antarctic ice streams (Echelmeyer et al., 1994). These studies adopted an *ad hoc* spatially variable viscous enhancement factor to the strain rate, effectively reducing the viscosity in regions where the researchers observed rapid velocities.

For the case of ice stream shear margins, this viscous enhancement can be as large as a factor of twelve. In Echelmeyer et al.'s (1994) study of Whillans Ice Stream, the regions of viscous enhancement correspond to a "chaotic zone" of intense, irregular crevassing. While these researchers did not physically model the interaction between the crevasses and the viscous flow of the ice stream, they point to the crevassing as an

indication of high shear strain, suggesting that a strain-weakening process (such as shear heating, their preferred hypothesis) could be the cause of the necessary enhancement to ice velocity. Such an approach is equivalent to increasing the effective ice stream width.

As discussed earlier, the temperature dependence of ice elasticity is substantially smaller than that of ice viscosity, suggesting that shear heating is not a major player in potentially changing the elasticity of an ice stream's margins. However, the presence of crevasses (or more generally, cracks) within elastic bodies is known to influence the effective elastic moduli of the damaged body. As demonstrated by Walsh (1965) for a penny-shaped crack, a reduction in the magnitude of the Young's modulus of an elastic body can approximate the increased deformation of the body due to the presence of void space or frictional cracks.

The number of crevasses is difficult to accurately quantify as only surface crevasses are directly observable, making any attempt to create a "crevasse distribution" for a given glacier intractable from a remote sensing perspective. Furthermore, small scale cracking in ice can be pervasive, rendering it impossible to calculate an effective rheology from an applied mechanics formulation such as Walsh (1965). The limitations on the measurement of cracks in glacial ice suggests that using an empirical fit of damage parameters estimated from observations is the simplest method of finding the approximate magnitude of the enhancement in ice's elastic response due to damage in the bulk of the ice.

Unfortunately, current measurement of the magnitude of the elastic response of ice streams is limited to GPS stations placed near to short-term perturbations to the background stressing of an ice stream. Of most immediate relevance are the GPS surveys

of the ocean tidal loading of ice streams in Antarctica presented in Chapter 1. However, with the exception of the surveys of Whillans Ice Plain by Winberry et al. (2009; 2011), these GPS surveys lack the spatial coverage to resolve the potential difference in displacement response of the shear margins versus the interior of the ice stream. And, in the case of the Whillans Ice Plain, the stick-slip nature of the GPS data obscures any simple variation in the elastic response between the central and marginal ice. The stick-slip behavior, controlled by poorly understood basal friction properties of the ice plain, would necessarily be convolved with any increased effective compliance in the shear margins due to damage in the margins. As such, we cannot rule out strain-weakening in the shear margins as a potentially important elastic inhomogeneity based on the current suite of field observations alone.

3.1.2 Appropriateness of Viscoelasticity

The analysis of ice motion is traditionally treated as a problem of viscous, rather than elastic, deformation (e.g., Cuffey and Paterson, 2011). While the timescale in the standard ice problem is months and years rather than hours and days, the prevailing large-scale deformation of ice is clearly viscous in nature. As such, we now explore the possibility that the viscous component of deformation in ice streams is important at hourly to weekly timescales in the context of the transmission of tidal loads inland of an ice stream's grounding line.

Recent research suggests that viscoelasticity is necessary to correctly model the tidal behavior of ice streams. Gudmundsson (2007) and King et al. (2011) explicitly state that viscoelastic effects within the ice stream may play a role in the phase delay of the ice stream's response to tidal loading. Gudmundsson (2011) and Walker et al. (2012) carry

out two-dimensional flow-line models with viscoelastic rheologies and find that these models fit observations more satisfactorily than an equivalent elastic ice model. Even though we have demonstrated that flow-line models fail to correctly predict the length-scale of the transmission of tidal stresses, the flow-line models of Gudmundsson and Walker et al. suggest that viscoelasticity can play a role in the transmission of tidal stresses inland of the grounding line of an ice stream.

Additionally, rheological modeling of ice deformation in the laboratory suggests that ice behaves viscoelastically (e.g., Jellinek and Brill, 1956; Goldsby and Kohlstedt, 1997; 2001; Morland, 2009; Riesen et al., 2010). These studies focus on using viscoelastic fluid models to improve the mathematical representation of the three creep regimes of ice (primary, secondary, and tertiary creep). As will be discussed in subsection 3.1.2.1, our choice of a Maxwell viscoelastic material model is a simpler rheology than those suggested by the aforementioned laboratory studies. A Maxwell model captures the behavior most relevant to the tidal perturbation of ice stream flow. Following this discussion, section 3.1.2.2 outlines our expectations for the relative importance of the viscous and elastic deformations in our models at different timescales, using the Maxwell relaxation time as an intuitive metric.

3.1.2.1 Simple Rheological Models for Viscoelasticity

Multiple models for viscoelasticity exist, so we must contemplate the most appropriate model for ice. We consider the three simple viscoelastic material models shown in figure 3.1: the Maxwell, Kelvin-Voigt, and Burgers models. We will choose to implement viscoelasticity in ice as an isotropic Maxwell model, which has the benefit of capturing

the most relevant characteristics of ice deformation while being simple enough to be well constrained using laboratory data.

A Maxwell viscoelastic model is comprised of a spring (elastic) element in series with a dashpot (viscous element). The canonical one-dimensional form of a linear Maxwell element is given as:

$$\dot{\varepsilon} = \frac{\sigma}{\eta} + \frac{\dot{\sigma}}{E} \quad (3.1)$$

A Maxwell material represents a fluid, as a constant stress will converge to a constant strain-rate, and thus linear time-dependent deformation. An advantage of the Maxwell model is that the elastic and viscous responses of the material are easily separable for problems with a characteristic stress as these responses are additive.

In contrast, the Kelvin-Voigt material is comprised of a spring element in parallel with a dashpot element. Equation 3.2 shows the canonical form of a linear Kelvin-Voigt element:

$$\sigma = E\varepsilon + \eta\dot{\varepsilon} \quad (3.2)$$

At its core, the Kelvin-Voigt model is that of a deformable solid, as a constant stress will result in the time-dependent relaxation to a strain value of that of an equivalent elastic model. And opposed to the Maxwell model, the Kelvin-Voigt model is easily separable into elastic and viscous portions for problems with a characteristic strain.

A third common viscoelastic rheology, the four element Burgers model, combines a Maxwell element in series with a Kelvin-Voigt element. The one-dimensional constitutive law is given by:

$$\sigma + \left(\frac{\eta_1}{E_1} + \frac{\eta_1}{E_2} + \frac{\eta_2}{E_2} \right) \dot{\sigma} + \frac{\eta_1\eta_2}{E_1E_2} \ddot{\sigma} = \eta_1\dot{\varepsilon} + \frac{\eta_1\eta_2}{E_2} \ddot{\varepsilon} \quad (3.3)$$

where the subscript 1 corresponds to the Maxwell element and the subscript 2 corresponds to the Kelvin-Voigt element. The defining characteristics of a Burgers model are that there is both an instantaneous and a long-term viscous response controlled by the Maxwell element, but that the transition between these two is smoothed due to the viscous deformation of the Kelvin-Voigt element (see figure 3.2).

Recalling that ice is best represented by a stress dependent viscous term, the gravitational stress driving the flow of the ice stream cannot be separated from the tidal perturbation of the stress field. As this limitation requires that our ice model can flow under its own weight, a fluid model is required, thus ruling out the (solid) Kelvin-Voigt model as an appropriate ice model.

From the published literature, ice is commonly modeled as a four element Burgers body with a nonlinear Maxwell body and a linear Kelvin-Voigt element (e.g., Jellinek and Brill, 1956; Reeh et al., 2003; Gudmundsson, 2007; Tsai et al., 2008). However, we opt to use a Maxwell material for ice in our modeling for two reasons. First, Reeh et al. (2003) demonstrates that the use of the simpler Maxwell rheology to fit tidal flexure data is only slightly worse than the fit using the Burgers rheology. Second, the experimental data of Jellinek and Brill (1956) suggests that the retardation time in the Kelvin-Voigt element is on the order of 10^2 seconds. As our tidal forcing acts on the timescale between 10^4 and 10^6 seconds, the influence of the Kelvin-Voigt element will be negligible compared to the behavior of the Maxwell element (shown in figure 3.2). Figure 3.2 demonstrates that the Maxwell element captures the initial elastic response and the tertiary creep of ice, with only the transitional region being poorly fit. Thus, we use the following nonlinear Maxwell material model for the viscoelasticity of ice:

$$\dot{\epsilon} = A\sigma^n + \frac{\dot{\sigma}}{E} \quad (3.4)$$

3.1.2.2 The Maxwell Relaxation Time

In a Maxwell viscoelastic model the relative importance of elastic and viscous deformation in the material is quantified by a Maxwell relaxation time, T_{Max} :

$$T_{Max} = \frac{\eta}{E} \quad (3.5)$$

If T_{Max} is large, the material will response elastically to an applied load. If T_{Max} is small, then the material's response to an applied load will be viscous in nature. However, tidal loading is not a constant force but rather acts as a time-variable stress. The dimensionless Deborah number, De , quantifies the relative importance of the viscous or elastic response to the timescale of the loading function and is given by:

$$De = \frac{T_{Max}}{t_f} \quad (3.6)$$

where t_f is the period of the forcing function. If De is small, then the material's response will be primarily viscous; if De is large, then the response will be primarily elastic.

Given the stress dependence of the effective viscosity of ice, De is inexorably tied to the amplitude of the deviatoric stress in the material, and will vary with the magnitude of the stress field in the material. As such, we define a transitional stress, σ_{trans} , to be where the material's response changes from being primarily viscous to primarily elastic, though in the region of this transitional stress, both components of deformation are important. σ_{trans} is defined as:

$$\sigma_{trans} = (AEt_f)^{-\frac{1}{n}} \quad (3.7)$$

Stresses higher than σ_{trans} denote a viscously dominated response, while an elastic response dominates when the stresses fall below σ_{trans} . As the frequencies of the tidal components vary, there are separate transitional stress levels for the semi-diurnal, diurnal, and fortnightly tides. Table 3.1 summarizes the expected transitional stresses using a value of A for $T=0^{\circ}\text{C}$ through $T=-25^{\circ}\text{C}$ and a value of $n=3$ (Cuffey and Paterson, 2011). σ_{trans} varies between a few and a few hundred kPa, which is the same order of magnitude as background driving stresses and the tidal stresses in our ice stream models. Thus, we expect there to be an even partitioning of stress and deformation between ice's elasticity and viscosity. The ice's response is unlikely to be well approximated by either a purely elastic or a purely viscous model. Reducing Young's modulus (while holding the viscosity coefficient fixed) increases the transitional stress to a viscously dominated response. Thus, invoking damage as a mechanism to increase the compliance in the ice margins may reduce the effective stress support of the margins in an elastic model. However, such a damage model implies that the viscoelastic response of the ice margins will be less pronounced than that of the central ice unless the effective viscosity of the lateral margins is reduced along with the Young's modulus.

3.2 Strain-Weakening in the Shear Margins

From the previous discussion, only damage in the shear margins provides the potential for large-scale elastic decoupling of an ice stream from its lateral margins. We begin with a continuum damage mechanics formulation to provide some physical basis for introducing an inhomogeneous Young's modulus into our three-dimensional elastic models from chapter 2. We investigate two different profiles for spatial variations in elasticity. We then discuss the implications of increasing compliance in the shear

margins, comparing our results to observations of both tidal stress-transmission and damage estimates from Antarctica.

3.2.1 Continuum Damage Mechanics Formulation

As the theoretical and observational constraints suggest that the variability of ice stream elasticity with the temperature and fabric is limited to a factor of two at best, we focus solely on the effect of strain-weakening on the elastic moduli of ice. To model the impact of individual crevasses is intractable due to the lack of a complete understanding of crevasse formation and distribution (e.g., Cuffey and Paterson, 2011), and the computational burden such a model would require when considering an ensemble of crevasses. However, the finite element formulation allows for spatially variable material parameters. Implementing a continuum damage mechanics approximation of the damage due to crevassing potentially allows our models to connect crevassing with the effective material moduli of the ice, without needing to explicitly model individual fractures.

To parameterize damage, we consider a parameter D such that

$$\dot{\epsilon} = A \left(\frac{\sigma}{1 - D} \right)^n \quad (3.8)$$

is the modification of the viscous (Glen) flow law due to the presence of damage in the given viscous element of the model. This formulation is equivalent to following *Kachnov-Rabotonov theory* (Kachanov, 1958, 1986; Rabotnov, 1968) with no evolution of D , a fair assumption over the short timescales in our problem. The damage parameter D can take a value between 0 (no damage) to 1 (complete plastic failure of element), and can be interpreted of a fraction of volume in the problem that can no longer support a load due to the opening of void space in the damaged body (see figure 3.3). This linear

damage mechanics formulation breaks down at large damages ($D > \sim 0.90$), where a real body would lose coherence. However, for small to moderate damages, a linear damage mechanics formulation provides a physical connection between fracture and a reduction in effective material parameters.

For the modification of elastic moduli, this form of continuum damage maps directly into the linear elastic constitutive equation (Chaboche 1977; Lemaitre and Chaboche, 1978) as:

$$\varepsilon = \left(\frac{\sigma}{E(1-D)} \right) \quad (3.9)$$

If the two rheological models are connected as a Maxwell viscoelastic material, it follows directly from conservation of effective stress that the rheological model with damage looks similar to equations 3.8 and 3.9, except that the viscous response D_1 may be different from the elastic response D_2

$$\dot{\varepsilon} = A \left(\frac{\sigma}{1-D_1} \right)^n + \left(\frac{\dot{\sigma}}{E(1-D_2)} \right) \quad (3.10)$$

The above equation only holds if the values of D are held constant through time. Figure 3.3 shows a schematic for such a viscoelastic damage formulation. For the analysis in this chapter, we will only consider equation 3.9 (linear elasticity with damage).

A critical piece of information is the value of D that approximates the expected damage within an ice stream's shear margin. We begin by making the assumption that $D_1 = D_2 = D$ as there are neither laboratory nor observational constraints on the effects of damage on ice elasticity. The results from Echelmeyer et al.'s (1994) study on the viscous enhancement of ice stream flow are used to approximate the viscous D .

Following the derivation of Borstad et al. (2012), the relationship between D and the enhancement factor En of Echelmeyer et al. is:

$$En = (1 - D)^{-n} \quad (3.11)$$

Using the peak enhancement factor of 12 from Echelmeyer et al. and the canonical $n=3$ gives $D=0.56$, which corresponds to a reduction in Young's modulus by about a factor of two. Given our uncertainty in the relationship between the D values of viscous and elastic ice, we extend our search to include values of D that change the Young's modulus by up to three orders of magnitude. Albeit unphysical, this broad selection of values allows us to empirically derive a robust relationship between D and L_{tr} . Based on estimates of damage necessary for crevassing, discussed in more detail later, we expect that the physical range of values for D are between 0.0 and about 0.6 (e.g., Borstad et al., 2011).

We must still decide how to distribute damage throughout an ice stream. We begin with models that have a linearly varying value of $D=0$ at the margins to a predetermined D at the edge of the ice stream ("continuous margins"). We use these models to explore a large range of effective Young's modulus values in order to characterize the relationship between the length-scale for transmission of stress L_{tr} and the relative magnitude of the reduction of Young's modulus in the margins (as discussed in section 3.2.2). We then move to models where there is a step-function transition from $D=0$ to $D \neq 0$ at a predetermined shear margin boundary ("discrete margins"). Such models explore the importance of the size of a shear margin on the value of L_{tr} using a pattern of D meant to approximate that seen viscously in ice streams (see section 3.2.3). Figure 3.4 shows sample profiles for both types of models.

3.2.2 Continuous Margin Results

Figure 3.3 shows a representative stress state from a model with a linear variation in Young's modulus of one order of magnitude between the compliant margins and the more rigid central ice. While the stress state is similar to that of the homogeneous elasticity model in figure 2.6, there are important differences when the elasticity is inhomogeneous. First, L_{tr} is longer throughout the model with the compliant margin than in the homogeneous model. In this specific model, the length-scale for the transmission of stress is about 1.6 times longer than that of a homogeneous model. Note that the value of L_{tr} is constant across the profile of the model ice stream (save immediately near the grounding line), even though the Young's modulus is not. Second, the continuous margin model concentrates stress at the center of the ice stream, as is apparent most readily in the longitudinal normal stress component. In this stress component, the stress is almost an order of magnitude higher in the central regions of the ice stream with the inhomogeneous elasticity than with the homogeneous Young's modulus. The potential for concentration of stress in the central portion of the ice is another example of a three-dimensional effect that simple flow-line models miss.

We considered twelve models with varying values of E at the lateral margins and central ice, ranging from ice 1000 times more compliant in the center to ice 1000 times more rigid in the center. For each of these models, figure 3.6 shows the trend of the change in L_{tr} compared to the homogeneous model as a function of the ratio of E between the central and marginal ice. Thus, as marginal ice is made progressively more compliant, an applied load will decay over longer distances. The converse is also true for situations where the marginal ice is more rigid than the central ice. Finally, the power

law form of the relationship between L_{tr} and E implied an effect for increasing the compliance of the margins. Over the range of models investigated here, the maximum increase in L_{tr} is a factor of about 4.2 when the margins are 1000 times more compliant than the central ice. The change to L_{tr} depends not on the absolute values for E in the model, but rather only on the ratio of E_H and E_L .

3.2.3 Discrete Margin Results

Figure 3.7 shows a representative distribution of the six stress components for a model with discrete ice margins chosen to be one quarter of the ice stream width. When compared to the homogeneous elastic model in figure 2.6, the stress state in the inhomogeneous model looks similar in general pattern to the homogeneous model, but there is a noticeable perturbation in stress state near the transition between compliant margins and rigid central ice. In the inhomogeneous model, stress is concentrated in either the central ice (longitudinal normal stress, σ_{xx}) or the margins (the other five components). Unlike the continuous margins models, L_{tr} is not constant across a transverse profile of the ice stream. Additionally, values for L_{tr} in these discrete margin models are larger than that of the homogeneous elastic models, just as was seen earlier in the continuous margins models.

To quantify the increase in L_{tr} due to the presence of compliant margins, we consider the vertically-averaged value of L_{tr} derived from the equivalent stress, rather than component by component. Figure 3.8 illustrates the behavior of different margin widths and L_{tr} for two models with discrete margins one order of magnitude more compliant ($E_H/E_L=10$) than that the central ice. The first panel (A) shows the results for an ice stream 10 kilometers wide and 1 kilometer thick, while the second panel (B) shows

the results for an ice stream 20 kilometers wide but otherwise identical. Consider first the left-hand plots, which show the transmission length-scales for eleven models that have discrete margins making up from 0% to 100% of the ice stream width at intervals of 10%. Circles represent the locations of the transition between the marginal and central ice. We note three features:

- 1) The values of L_{tr} are identical for models with 0% and 100% compliant margin widths. This result is expected as these models equivalent to uniform elasticity.
- 2) The variation of L_{tr} across the ice stream's profile (i.e., in the x-direction) is strongly dependent on the model parameters, such as the relative size of the margins and the absolute width of the ice stream. Take, for example, the 50% margin width and the 80% margin width profiles in panel A. In the former, L_{tr} peaks in the marginal ice near the transition between the two rheologies and is slightly decreased in the central ice. In the latter, L_{tr} in the central ice is elevated compared to that of the margins. Further, note that the profiles of L_{tr} between the two models are different.
- 3) The largest value of L_{tr} occurs in the models that have margins that make up 50% of the ice stream half-width or 25% of the ice stream full-width. As an aside, we note that this margin width is similar to the best-fit marginal width found by Echelmeyer and others (1994) for viscous flow models of Kamb Ice Stream. More work is necessary to determine if the similarity in peak margin width between elastic and viscous

models is coincidental or if this result suggests that our assumption that $D_1=D_2=D$ is permissible.

- 4) The discontinuities in the profiles of L_{tr} are due to the use of the equivalent stress to define the transmission length-scale. This jump in L_{tr} is caused by: one, the equivalent stress depends on the longitudinal stress (σ_{xx}); two, the longitudinal stress can be discontinuous across the jump in Young's modulus. The displacements are continuous across the discontinuities in Young's modulus.

The right-hand plots in figure 3.8 demonstrate the relationship between margin size and L_{tr} for a tidal forcing. These plots show the average value of the L_{tr} (with error bars indicating 1 standard error of the mean) as a function of relative margin width. As mentioned earlier, we find that the maximum increase in L_{tr} relative to the homogeneous elastic model occurs when the shear margins are one quarter of the ice stream width. However, due to the polynomial form of L_{tr} as a function of margin width, even a fairly small shear margin can increase L_{tr} by a factor of 2 to 3. Additionally, the average value of L_{tr} shows only a minor dependence on the geometry of the ice stream, as demonstrated by the small difference in maximum value of L_{tr} between 10 and 20 kilometer wide models.

3.2.4 Strain-Weakening Discussion

The results of our models incorporating inhomogeneous elasticity in the shear margins demonstrate that the nature and variability of ice's elastic moduli within the ice stream can have a profound effect on the transmission of a tidal load inland of the grounding line. This connection between elastic moduli and stress-transmission exists even though

the transmission of stress in homogeneous elastic models is independent of the elastic moduli. Thus, if the elastic moduli of ice vary across an ice stream, it is not sufficient to calculate effective elastic moduli for the entire ice stream as this cannot correctly model the stress-transmission.

While the relative increase in L_{tr} in our models is only between 1 and 3 times the value of L_{tr} in our homogeneous models for values of strain-weakening D that match those seen viscously, this variability represents a difference in many tens of kilometers of stress-transmission—the very length-scale of tidal stress-transmission seen geodetically. To our knowledge, there currently are no observations of *in situ* ice elasticity that suggest there is a reduction in Young's modulus within the shear margins of ice streams. However, simple models of ice fracture and crevassing suggest that an ice stream's shear margins should be more compliant than the (relatively) undamaged central portions of the ice stream.

As independent constraints on the variability of elasticity do not exist, our results from these inhomogeneous finite element models define the range of potential parameter space necessary to explain the observed tidal signal from the GPS stations on Rutford and Bindschadler Ice Streams, rather than test specific values. Referring back the values of L_{tr} found in section 2.4 for the homogeneous elastic models, figure 3.9 shows that an increase in the range of 2.67 (fortnightly tide) to 3.32 (semidiurnal tide) for Rutford Ice Stream and about 4.40 (semidiurnal tide) for Bindschadler Ice Stream from the homogeneous elastic stress decay length would be close enough to explain the amplitudes of displacement seen in the GPS records.

We can create an empirical margin-width dependence from our 20-kilometer-wide model, fitting the model results shown in figure 3.8B. We fit the model results using a polynomial fit of degree four as this is the lowest degree polynomial that falls within one standard error of the mean for the average stress decay length increase values. We also impose the added constraints that the end points must have a value of relative \hat{L}_{tr} equal to 1 as our shear margin results must necessarily converge to the homogeneous elastic solution when there is no variation in elastic moduli.

We now use the marginal-compliance relationship from figure 3.6 to define the dependence of changes in L_{tr} on the relative value of E in the compliant margins. We use these two fits to create a map in margin-width vs. compliance space that allows for the model to match the observations (figure 3.9). Figure 3.9 shows the range of margin-widths and reductions in Young's modulus necessary to increase the overall value of L_{tr} by certain amounts. Not surprisingly, the maximum increase to L_{tr} occurs when the shear margins are about 50% of the ice stream half-width (25% of the ice stream full-width), and when the lateral margins are substantially more compliant than the central ice stream. This plot also shows the three lines in margin size-compliance ratio space that would be sufficient to match the values of L_{tr} found for compliant margins models approximating Bindschadler and Rutford Ice Streams to the observations of the decay of tidally induced displacements. In these cases, the minimum values of D are found to be: 0.988 for the fortnightly Rutford tide, 0.996 for the semidiurnal Rutford tide, and 0.999 for the semidiurnal Bindschadler tide.

To add some physical meaning to these estimates of D , we compare these modeled values to the critical damage threshold values of D , commonly named D_C , found

in the literature. From laboratory experiments, D_C has been approximated from between 0.45-0.56 for ice (Pralong and Funk, 2005; Duddu and Waisman, 2012). From analysis and numerical inverse modeling of a continuum damage mechanical viscous model of the Larsen B Ice Shelf collapse, Borstad et al. (2012) found the value of D_C for calving to be 0.6 ± 0.1 . To compare D_C with our model results, we must remember that the above values for D_C are for nonlinear viscous flow, such that the “enhancement” value is governed by equation 3.11. Thus, the corresponding enhancements are between about 6 (for 0.45) and 37 (for 0.7) using the canonical power law exponent for Glen flow of $n=3$. Unfortunately, even our smallest necessary enhancement has a value of 467.7 ($10^{2.67}$, for the fortnightly tide on Rutford Ice Stream), strongly suggesting that the necessary damage to have marginal compliance be the sole explanation of our models and observations is too high to be physically reasonable. The situation is exacerbated for other tidal periods, with the necessary enhancement being factors of $\sim 2,000$ and $\sim 25,000$. Thus, marginal compliance alone is insufficient to bring our modeled stress decay length-scales into line with those found observationally from GPS stations on the Rutford and Bindschadler Ice Streams.

3.3 Viscoelasticity

As strain-weakening of the shear margins does not explain the difference between our modeling results and the long-distance stress-transmission observed on some Antarctic ice streams, we now investigate the potential for viscoelasticity to decouple the ice stream from its lateral margins and thus increase the transmission length-scale of a tidal load. Section 3.3 begins with a discussion of the modeling considerations necessary in a nonlinear viscoelastic model that are otherwise not present in a linear elastic finite

element model. We then present results from two types of viscoelastic models: one set with a homogeneous viscosity coefficient (section 3.3.2) and another with a temperature-dependent viscosity coefficient (section 3.3.3). The final portion of this section relates our viscoelastic modeling to the observed stress-transmission length-scales from Antarctica.

3.3.1 Viscoelastic Model Considerations

Incorporating both viscoelasticity and nonlinearity into our constitutive law for ice introduces many additional modeling concerns in order to correctly study the link between ocean tides and ice stream motion. The first change is that our model has stress-dependent viscosity, and thus stresses within the ice stream other than the tidal loading can no longer be neglected, as was done for the linear elastic models. Also, as viscous deformation is a time-dependent process, our viscoelastic models must explicitly account for the time-variability of our tidal loading condition. We address both of these issues in turn.

3.3.1.1 Nonlinearity and the Loss of Superposition

In our linear elastic models, the principle of linear superposition allowed us to isolate tidally induced deformation from the background driving stresses in our models. With the change to a nonlinear viscoelastic rheology, we must now consider the stress state of our model ice stream more carefully as we cannot simply neglect the non-tidal stresses when designing our models. As the ice's viscosity depends on the total deviatoric stress throughout the ice stream, the effective viscosity of the ice stream will be both spatially and temporally variable. The total deviatoric stress necessarily includes the tidal and non-tidal deviatoric stresses. To correctly account for the "true" value of viscosity, our

models must now incorporate the deviatoric component of the gravitationally-derived driving stress and the extensional stress balance at the interface between the ice stream end and the ocean.

(1) Driving Stress in the Ice Stream

All glaciers, by definition, flow under their own weights, as discussed earlier in section 1.4. As a reminder, the shear (deviatoric) stress induced in the direction of flow is commonly taken as (e.g., Cuffey and Paterson, 2011):

$$\tau_b = \rho g H \sin \alpha \quad (3.12)$$

where α is the surface slope of the glacier. The basal slope of the glacier is, to first order, not important in determining the basal shear stress.

Very shallow surface slopes, and thus low basal shear stress values, are characteristic of the Antarctic ice streams with long-distance stress-transmission. Using estimates of ice stream basal stress from ice streams on the Siple Coast (~ 100 kPa, Cuffey and Paterson, 2011), we estimate a reasonable surface slope of about 0.57 degrees. While a stress of 100 kPa is small when compared to the hydrostatic pressure at the base of these ice sheets (which can be upwards of 10 MPa), this driving stress is still larger than the stress change due to a one meter oceanic tide. Furthermore, this deviatoric stress value suggests that ice is about ten orders of magnitude more viscous at the ice stream's base than at the surface due to the stress dependence of the effective viscosity!

For our models, we apply only the downhill (i.e., deviatoric) portion of the gravitational driving stress. Figure 3.10 shows our approach schematically. The modeled ice stream is assumed to have a constant surface slope of α and thickness H , such that our deviatoric gravitational vector is at an angle α to the model's horizontal

coordinate axis. This modeling approach is a permissible simplification of an ice stream's geometry as the basal slope does not strongly affect the induced shear stress at the base and the shallow surface slope means that the ice stream's thickness would not change dramatically over the length-scale of the tidal stress-transmission. In the finite element formulation, we apply the horizontal component of gravity, with a magnitude of $g_{horiz} = g \sin \alpha$, to our model as a time-constant acceleration acting on the entire ice body.

Neglecting the non-deviatoric component of gravity is convenient as the model viscosity is independent of the hydrostatic stress and additionally removes the need to apply a pre-stress to cancel out the compression due to "turning on" gravity at the initial timestep. However, at the ends of the ice stream, the hydrostatic pressure for real ice streams is not balanced completely by the ocean tide. The excess hydrostatic pressure acts as a force that "pulls" the ice stream in the direction of flow, which causes a deviatoric extensional stress on the edge of the ice stream (Cuffey and Paterson, 2011). We discuss this extensional stress next.

(2) Ocean-Ice Interface

At the downstream edge of an ice stream, the hydrostatic pressure due to a glacier's weight is resisted primarily by the hydrostatic force of the ocean acting on the ice shelf. Due to the dependence of the effective viscosity on the deviatoric stress, any mismatch in hydrostatic pressures between the ice stream and the ocean will result in a deviatoric stress that reduces the ice stream's viscosity near the grounding line. This deviatoric stress is independent of any flexural stresses caused by a rising and falling ice shelf.

In Appendix 3A, we consider the effects of these stresses on the viscoelasticity deformation of an ice stream. There we show that any extensional or flexural stresses do not perturb the effective viscosity near the grounding line enough to cause significant variation in our model results from those following the much simpler tidal condition used in the elastic models. Therefore, we model the ocean tidal perturbation in ice stream velocity as an oscillatory normal stress acting at the ice stream's grounding line—the same configuration as in our linear elastic models.

3.3.1.2 Time-Dependent Behavior

Deformation of a viscoelastic (or more generally, viscous) material will inherently be time-dependent. Thus, our models must accurately resolve the time-dependent behavior of our ice stream system. Time-dependence enters our problem in two ways: the time-varying nature of the forcing function, and the time-dependence of ice stream's tidal response.

(1) Time-Dependent Loading

Oscillations of the ocean tides represent a time-dependent force on an ice stream. While there are numerous tidal frequencies, we focus on the three largest tidal constituents acting on ice streams: the semidiurnal, diurnal, and fortnightly tides. The GPS surveys of Anandakrishnan et al. (2003), Gudmundsson (2007; 2008; 2011), and Winberry et al. (2009; 2011) all use the GPS vertical deformation of a station placed on the (floating) ice shelf as a measurement of the ocean tides. The observed ocean tidal amplitude displays a strong beat frequency (see figure 3.11). To approximate the amplitude of the tidal component, we select the two largest semidiurnal and diurnal components, along with the fortnightly tide, from the FES2004 tidal model (Lyard et al., 2006) to create a synthetic

tidal signal. The tidal data is then fit using a nonlinear least squares algorithm to find the amplitude and phase of these five tidal components in the data from the Ross and Weddell Seas (data courtesy of S. Anandakrishnan and H. Gudmundsson). For reference, the Ross Sea abuts the ice streams of the Siple Coast, while Rutford Ice Stream flows into the Weddell Sea. Table 3.2 summarizes the tidal amplitudes and phases from FES2004 and the observational fits, while figure 3.11 shows the real and synthetic tides for the Ross and Weddell Seas.

The agreement between the tidal model and the observations is not strong, with only the semidiurnal and diurnal components in the Weddell Sea coming close to matching. As the point of this section is not to analyze the difference between tidal data and tidal models but rather to approximate the tidal amplitudes for our model ice stream, we choose to use the floating ice GPS stations for constraining the tidal forcing function. These data demonstrate that:

- 1) The semidiurnal tide is stronger (i.e., larger amplitude) than the diurnal tide which in turn is stronger than the fortnightly tide in the Weddell Sea results, but not in the Ross Sea results.
- 2) The fortnightly tide, while not always of the smallest amplitude, is subordinate to the either the semidiurnal or diurnal tide, depending on which is the dominant tidal amplitude.
- 3) The maximum tidal amplitude has a one to two meter amplitude in the two major Antarctic seas. While amplitudes may be larger locally (e.g., Gudmundsson, 2007), we will use a one meter tide as our characteristic amplitude.

We use three tidal constituents (i.e., the semidiurnal tide, the diurnal tide, the fortnightly tide) as forcing functions in our nonlinear viscoelastic finite element models. For simplicity, we approximate the tidal periods of these tidal constituents as 12 hours, 24 hours, and 14 days, respectively. As a reminder, the three tidal constituents cannot strictly be separated due to the nonlinearity in this viscous deformation. However, modeling the response of our ice stream model to a single tidal component is more straightforward and provides an estimate of the expected change in stress-transmission as a function of the tidal forcing period.

(2) Time-Dependent Stress and Displacement Fields

A viscoelastic medium will experience a phase delay between an applied oscillatory load and the deformation response. In the context of ice streams under tidal forcing, this phase delay is expressed as a time-lag in the peak stress and displacement perturbation of the ice stream. In the GPS observations of Rutford Ice Stream (Gudmundsson 2007, 2008, 2011), a phase shift is both observed and seen to vary with distance inland of the grounding line.

In our models, we need to differentiate between the effects of the oscillatory loading of the ocean tides and those of the static loading due to the gravitational driving stress in the ice stream. To this end, we run models both with and without the oscillatory component of the tide. We then subtract the non-oscillatory results from the tidally-forced models. Due to the nonlinear viscoelasticity, the resulting stress field is not strictly the ice stream's response to the oscillatory loading, but rather the change in ice stream response due to the addition of the time-variable component of the tide. As the oscillatory load is several orders smaller than the static loads for most ice streams, we

expect that the response to the variation in total deviatoric stress due to the tides will be approximately linear, and thus the above approach provides results that are close to the ice stream's response to the ocean tides alone.

3.3.1.3 Temperature-Dependent Viscosity

As mentioned in section 3.1.1, the viscosity of ice is strongly temperature dependent (e.g., Cuffey and Paterson, 2011; and references therein), with ice having reduced viscosity at higher temperatures. Numerous laboratory experiments and field observations show that this temperature dependence takes the form of an Arrhenius relationship in the viscosity coefficient A , with two distinct regimes depending on the proximity of the ice temperature to the pressure melting point of ice (Weertman, 1983; Hooke and Hanson, 1986; Paterson, 1994). The temperature dependence of the viscosity coefficient, from Cuffey and Paterson (2011), is:

$$\begin{aligned}
 A &= 3.5 * 10^{-25} \exp\left(\frac{-6 * 10^4}{8.314} * \left[\frac{1}{T} - \frac{1}{263}\right]\right) Pa^{-3} s^{-1} \\
 &\quad \text{for } T < 263 \text{ K} \\
 A &= 3.5 * 10^{-25} \exp\left(\frac{-1.39 * 10^5}{8.314} * \left[\frac{1}{T} - \frac{1}{263}\right]\right) Pa^{-3} s^{-1} \\
 &\quad \text{for } T > 263 \text{ K}
 \end{aligned} \tag{3.13}$$

where T is measured in Kelvins.

Antarctic ice streams have been observed to have a strong temperature gradient from base to surface (e.g., Engelhardt et al., 1990; Engelhardt and Kamb, 1993; 1998; Engelhardt 2004a/b), with some ice stream beds being up to twenty degrees Kelvin warmer than the ice stream's surface. This temperature range corresponds to a variation in the viscosity coefficient by almost a factor of 60. Therefore, we impose a temperature

gradient in our models and use a temperature-dependent viscosity. We adopt an empirical fit of temperature data from Whillans Ice Stream as the temperature profile in all our models. The temperature gradient of such a temperature profile is defined by Engelhardt and Kamb (1993) as:

$$\frac{dT}{dz} = q_b e^{-y^2} + \frac{\lambda a u l}{\kappa} e^{-y^2} \int_0^y e^{-t^2} dt \quad (3.14)$$

where $y = z/l$, $l = 2\kappa H/a$, q_b is the basal temperature gradient, a is the accumulation rate, u is the ice stream horizontal velocity, κ is the thermal diffusivity, H is the ice stream thickness, and λ is the temperature gradient in air. All values of these parameters, save for model geometries, are taken from Engelhardt and Kamb (1993). In solving for the temperature profile, we set the basal temperature equal to the pressure melting point of ice, -0.7 °C. The results based on a homogeneous temperature field are discussed in section 3.3.2., while the temperature-dependent results are discussed in section 3.3.3

3.3.1.4 Enhanced Flow in the Margins

Observations suggest that enhanced viscous flow exists in the shear margins of ice streams, with the enhanced viscous deformation in the marginal ice being up to twelve times that expected for models using homogeneous laboratory values of ice viscosity (e.g., Dahl-Jensen and Gundestrup, 1987; Echelmeyer and Wang, 1987; Paterson, 1991; Echelmeyer et al., 1994). From equations 3.9 through 3.11, we expect that marginal ice would need a reduction to the value of the nonlinear viscosity coefficient by a value of about 0.56 to produce such an enhanced flow. As increasing the elastic compliance of the margins of a model ice stream resulted in an increase in the distance a tidal load can be transmitted inland of the grounding line, we expect that a reduction in viscosity would produce a similar increase in the stress-transmission length-scale.

However, we do not specifically model possible enhancement in both the elastic and viscous deformation of the shear margins in this thesis. The relative influence of damage on the elastic and viscous deformation is not known, making any assumption about the interaction of D and En difficult to justify. For example, if D is assumed to be constant between the viscous and elastic enhancement, then the viscosity would decrease by $(1 - D)^{n-1}$ compared to the drop in elasticity of $(1 - D)$. The result is a decrease in the Maxwell time of the margins, meaning that the viscous response would be relatively more important. However, if En is assumed to be constant between the viscous and elastic enhancement, then the Maxwell time is unaffected in the marginal ice, suggesting that viscoelastic deformation is no more important in the margins than in the central ice. Finally, if the presence of crevassing has a larger effect on the elasticity relative to the viscosity, then the Maxwell time of the margins would be increased relative to the undamaged ice, suggesting that viscoelastic deformation would be most important in the undamaged portions of the ice stream. A more complete understanding of the role of damage in influencing the viscoelastic deformation of ice is necessary to have a physically based model for viscoelastic damage in the shear margins. While it is possible to approach the problem of viscoelastic damage in the same manner as we did for elastic damage, the increased computational time of the nonlinear viscoelastic models puts such an effort well beyond the scope of this chapter.

3.3.2 Homogeneous Viscoelastic Modeling Results

We describe results from three viscoelastic models using homogeneous viscosity (assuming 0 °C ice) and tidal frequencies corresponding to the semidiurnal, diurnal, and fortnightly ocean tides. Recall that for each model, two versions are run: one with only

the background gravitational body force (“background model”) and a second with both the background force and the axial tidal load (“tidal model”). Figure 3.12 shows a sample stress field for the basal profile of the semidiurnal tidal model at the peak tidal amplitude with the background model subtracted. Qualitatively, the stress distribution for the viscoelasticity model is similar to that of the elastic model (figure 2.6), though there are clearly some differences in the shear margins of the ice stream. The value of L_{tr} can be seen in multiple stress components and does not vary substantially between the different stress components. As with the elastic model, tidal stress decays exponentially with distance inland, and while the peak normal stress occurs in the center of the ice stream, the decay length-scale L_{tr} is roughly constant across the ice stream’s profile.

Figures 3.13 to 3.15 show the value of L_{tr} as a function of depth at the centerline of the ice stream for the models forced at the three tidal frequencies. As seen in panels A, the stress-transmission length-scale does not vary greatly with depth for any of the models. However, the value of L_{tr} varies with the period of the forcing frequency. For the semidiurnal, diurnal, and fortnightly tides, the length-scales are 15.6 kilometers, 15.0 kilometers, and 40.9 kilometers, respectively. L_{tr} for the corresponding elastic model is 12.2 km, meaning such viscoelastic values of L_{tr} correspond to 123%, 118%, and 335% of the elastic value. Thus, using viscoelasticity does increase the extent of tidal stress-transmission relative to the elastic model.

Another major change in the move from elasticity to viscoelasticity is that we must consider the time-history of the stress solution, not just the stress state at a single moment. As a demonstration, figure 3.15 compares the value of σ_{yy} at the base of the center of the model ice stream forced with the semidiurnal tide as a function of time at

several locations inland of the grounding line. In addition to the decay of the stress amplitude with distance inland of the grounding line, there is a phase delay in the ice stream's stress response to the tidal load that also varies with distance inland of the grounding line. In order to find the correct amplitude and phase, we fit stress profiles along the modeled ice stream's length with:

$$\sigma_{yy} = A \sin(\omega t + \varphi) \quad (3.15)$$

where A is the stress amplitude, ω is the tidal frequency of the applied tide, and φ is the phase delay. Panels B and C of figure 3.12 to 3.14 show the fitted amplitudes and phase delays for the centerline profiles over of the ice stream model over the first 100 kilometers of the ice stream. The dashed lines correspond to the 95% confidence intervals of the fits. The slopes of the amplitude and phase are the values of the length-scale for the decay of the tidal stress, L_{tr} , and the phase velocity, c , respectively. Table 6.3 summarizes the values of L_{tr} and c for the homogeneous models.

The ice stream's response to all three forcing frequencies displays a phase delay that increases with distance away from the grounding line, as seen in panel C. However, the phase does not seem to correlate with L_{tr} in these models. The phase velocities of the three tides are, in order of increasing tidal period, 4.6 m/s, 11.1 m/s, and 0.60 m/s. The phase velocities are not monotonically increasing with tidal period as the fortnightly tide has a significantly longer tidal period than the shorter period tides, but not a significantly increased phase delay.

3.3.3 Temperature-Dependent Viscosity Results

For our temperature-dependent viscosity models, we present results for the isolated semidiurnal, diurnal, and fortnightly tidal components, as well as a single model that

forces the models with a combined tidal forcing function based on the amplitudes of the Weddel Sea's tides (see Table 3.2). Figures 3.17 to 3.20 show the values of L_{tr} , stress, and phase delay for the semidiurnal, diurnal, fortnightly, and combined tidal signal.

As with the homogeneous viscosity model, all three viscoelastic models have larger values of L_{tr} than the homogeneous elastic model. The fortnightly tide has a longer L_{tr} than the other two tides while the diurnal tide in turn has a larger value of L_{tr} than the semidiurnal tide. Additionally, the absolute amplitude of the change is less pronounced than in the homogeneous case, with the semidiurnal L_{tr} being 101% of the elastic case, the diurnal tide's L_{tr} being about 102%, and the fortnightly tide's L_{tr} being 145%.

In all three cases, the phase delay at the grounding line is zero degrees, suggesting a purely elastic response. The phase delay increases with inland distance, with the maximum phase delay reaching about 15 degrees for the semidiurnal tide, 90 degrees for the diurnal tide, and 270 degrees for the fortnightly tide. Unlike the homogeneous model, the increase in the phase delay correlates with an increase in L_{tr} . Such a result is due to the increased average viscosity, and thus the value of T_{max} , of the temperature-dependent ice stream relative to the homogeneous ice stream. We discuss the phase response to the ocean tides further in chapter 4. Finally, the phase velocities of the three tides are 1.8 m/s, 1.7 m/s, and 0.94 m/s for the semidiurnal, diurnal, and fortnightly tides, respectively.

3.3.4 Viscoelasticity Discussion

Our primary interest in modeling viscoelasticity was to determine if stress-dependence of viscosity would result in a substantial decoupling of the ice stream from its lateral margins due to the higher stress concentration along the lateral margins. Recalling our earlier comparisons to the estimated tidal stress decay over Bindshadler and Rutford Ice

Streams (figure 2.11), viscoelasticity would need to increase the value of L_{tr} by between a factor of two to five to match the field observations of Anandakrishanan et al. (2003) and Gudmundsson (2007; 2008; 2011). While models with a homogeneous viscosity at long tidal periods have values of L_{tr} that fall into the range necessary to fit the Antarctic observations, incorporating a temperature-dependency to the viscosity severely diminishes the increase in L_{tr} relative to the elastic model. For these temperature-dependent models, the increase in L_{tr} is less than 50%—insufficient to match the observations.

The lack of a substantial increase in L_{tr} due to the ice viscosity calls into question our assumption that incorporating nonlinear viscoelasticity will substantially reduce the viscosity in the shear margins. However, as figure 3.20 shows, the shear margins have a substantially reduced viscosity when compared to the central ice. This viscosity contrast is found to be essentially independent of the tidal forcing, suggesting that the background flow, even for very low driving stresses, is large enough that the tidal forcing does not strongly perturb the effective ice viscosity. As such, response of an ice stream to a tidal load can be approximated as a linear viscoelastic as long as the ice stream is modeled with a spatially variable effective linear viscosity. Such a simplification allows the use of the principle of linear superposition and thus decouples the effects of the tides from any background stresses. Clearly linear models are also less computationally expensive, allowing us to explore a wider range of model parameters.

However, the large drop in viscosity in the shear margins fails to cause a substantial increase in L_{tr} . The simplest explanation is that while the ice is less viscous in the shear margins, the overall value of the viscosity is too still large to promote

substantial viscous deformation. When compared with approximations of linear ice viscosities, the smallest viscosities in our models are about two orders of magnitude larger than those found for the solid response of laboratory ice (e.g., $1e12 Pa\cdot s$, from Jellinek and Brill, 1956). As the smallest Maxwell time for our modeled ice stream is about 10^4 seconds (~ 3 hours), the model ice stream responds primarily as an elastic material. Only when the model is forced with long period oscillations (e.g., the fortnightly tide, with a period of $\sim 10^6$ seconds) does the viscoelasticity of the ice stream substantially influence the stress-transmission length-scale. Such an explanation matches the modeling result that a temperature-dependent viscosity has a smaller impact on the transmission length-scale than the equivalent homogeneous model. As our homogeneous model is calibrated to match ice at the melting point, the homogeneous model has an average effective viscosity that is about 30 times smaller than the average effective viscosity in the temperature-dependent model. For the temperature-dependent models, the larger viscosity in the body causes the ice response to be more elastic in nature, explaining the diminished change in L_{tr} from the viscoelastic model.

Our results demonstrate that a viscoelastic ice stream will have a phase delay in the ice's response to a tidal loading that is distance dependent, whereas a linear elastic ice stream will never have an induced tidal phase delay. While our results are too limited to draw any sweeping conclusions about the interplay between the phase delay, tidal forcing frequency, and the effective viscosity of the ice, the results do suggest that a measureable phase delay in the tidal response can provide information about the viscoelastic behavior of the ice. We explore this idea further in the next chapter.

3.4 Summary and Conclusions

We explored changes in the overall state of stress in an ice stream due to two different rheological modifications to a homogeneous linear elastic rheology. The goal was to determine if either an increased elastic compliance in the shear margins or nonlinear viscoelastic effects would decouple the ice stream from its lateral margins to such an extent as to explain the discrepancy between the short stress-transmission length-scales of our models with the large spatial extent of tidally perturbed surface displacement observations from some Antarctic ice streams. We find that neither of these two rheological effects have sufficient input on estimates of L_{tr} to explain differences between our models and observations.

The first portion of this chapter considered models using a linear continuum damage mechanics formulation of crevassing in the highly-deformed shear margins of ice streams to reduce the margins' effective elasticity. Our models demonstrated that the resulting inhomogeneity in ice elasticity causes a net increase in L_{tr} for a tidal load if the marginal ice is more compliant than the central ice. While a perfect constraint on the damage in the ice stream margins is not well established, we assume that the upper bound on damage for ice calving is an approximate bound on the marginal damage. Using this constraint, the magnitude of the damage necessary to rectify the observations and our model results must be unrealistically large.

The second rheological consideration is the impact of incorporating a nonlinear viscoelastic constitutive law for ice instead of the linear elastic law used in chapter 2. The hypothesis was that the stress-dependent viscous component of the viscoelastic rheology would decouple the ice stream from surrounding ice by reducing the viscosity

of the shear margins due to the large shear stresses in these margins. Our viscoelastic models demonstrated that generally, viscoelasticity increases L_{tr} and that the viscous response is stronger for longer period tidal forcings. However, for a model incorporating the temperature dependence of the viscosity coefficient of the ice stream approximating the temperature profile of Antarctic ice streams, viscosity remains too large to increase the stress-transmission length-scale of tidal load by more than about 50% compared to the elastic model. Ultimately, due to the low driving stresses that control the magnitude of the effective viscosity within the model ice stream, for the Antarctic ice streams of interest, viscoelasticity cannot increase L_{tr} enough to rectify the observations and the model results.

Figure 3.21, an updated version of figure 2.11, demonstrates graphically that the decay of displacements is still too severe to match the maximum observed displacement if the influence of physically reasonable damage or viscoelasticity is added to our models. Recall that for linear elasticity, an exponential decay of stress corresponds to an exponential decay of displacement with the same decay length-scale. Thus, using a value of L_{tr} calculated from the tidal stress-transmission can be used to represent the decay of tidally induced displacements with distance inland of the grounding line. For nonlinear viscoelastic models, as the total stress state is dominated by the elastically supported stresses it is still reasonable to approximate the displacement decay using the stress-transmission length-scale. The estimated L_{tr} for elastic model geometries approximating Bindschadler and Rutford Ice Streams are approximately 70 and 40 kilometers, respectively (GPS data reported in Anandakrishnan and others, 2003; Gudmundsson, 2007 and was provided by S. Anandakrishnan and H. Gudmundsson). The increase in

the stress-transmission length-scale is 60% for the maximum reasonable damage model. In our viscoelastic models, the increase in L_{tr} for the semidiurnal tidal forcing is about 1% while for the fortnightly forcing the increase in L_{tr} is about 45%. Such values are insufficient to match the observed stress-transmission length-scales of 265 and 110 kilometers, respectively for Bindschadler and Rutford Ice Streams.

The models presented here draw into question the hypothesis that the observed influence of ocean tides on ice stream motion occurs as elastic transmission through the bulk of the ice stream itself. This result implies one of two possible conclusions: one, that there is a mechanism not explored here that almost completely decouples the ice stream from its shear margins, essentially reducing the lateral support of the ice stream to zero; or two, that a mechanism external to the ice stream bulk is necessary to explain the tidal component of ice stream motion. The uniform flow-line models, which are the current state-of-the-art, implicitly assume the first, though we have demonstrated here that the ice streams considered here are not wide “enough” to neglect the resistance of the lateral margins. Furthermore, even the very name of the shear margins implies that there must be an amount of lateral support sufficient to induce shear in the ice stream’s margins, making large-scale decoupling very unlikely.

Thus, we conclude that a process external to the ice stream is the most likely mechanism for allowing the impact of ocean tidal loads to extend far inland of the grounding line. While not explored in detail here, our preferred hypothesis is that the ocean tides perturb the nature of streaming through the subglacial hydrologic network. As the basal traction beneath these fast-moving ice streams must be small as to encourage sliding and as these Antarctic ice streams are underlain by water-logged tills (e.g., Alley

et al, 1986; Smith, 1997; Engelhardt and Kamb, 1998; Tulaczyk et al., 2000a; Adalgeirsdottir et al., 2008; Raymond Pralong and Gudmundsson, 2011), the fluid pressure within the subglacial till is likely sufficient to cause the till to deform plastically. Our hypothesis is that the change in ocean tidal height can move the onset of streaming, the transition from slow- to fast-moving ice at the upstream edge of the ice stream, inland and seaward over the course of a tidal cycle. As demonstrated by figure 3.22, when the onset of streaming is pushed inland, the ice stream at a given point should increase velocity as a longer portion of the glacier is streaming. The opposite is true when the onset of streaming moves towards the ocean. Furthermore, as the magnitude of the fluid pressure perturbation due to the ocean tide should decay with distance inland of the grounding line, the effect is expected to be most pronounced near the grounding line. Perhaps this distance dependence on the subglacial tidal pressure could explain the phase delay between ocean amplitude and the ice stream's response to changes in ocean tide.

The distance the tidal pressure change travels could easily be farther inland than the 5 kilometers zone through which the grounding line moves due to the ocean tides (e.g., Stephenson, 1984; Rignot, 1998; Heinert and Riedel, 2007; Brunt et al., 2010). As the water pressure within the basal till is not constrained by the ice stream's width (the ice stream dimensions controlling L_{tr}) but rather by the hydraulic properties of the subglacial drainage network, such a pressure modulation could potentially reach farther inland than a tidal load acting through the bulk of the ice stream does. However, any further discussion of such a process relies on quantifying the spatial extent that ocean tides are 'felt' through the subglacial hydrologic network, which is beyond the scope of this chapter.

| | Variable Names | Units |
|--|--|--------------------------------|
| | A Viscosity coefficient | $\text{Pa}^{-n} \text{s}^{-1}$ |
| | a Accumulation rate | kg/yr |
| | C Phase velocity | m/s |
| | D Damage parameter | -- |
| | D_c Critical damage parameter | -- |
| | D_1 Viscous damage parameter | -- |
| | D_2 Elastic damage parameter | -- |
| | De Deborah number | -- |
| | E Young's modulus | Pa |
| | E_{eff} Effective Young's modulus | Pa |
| | E_H Higher Young's modulus | Pa |
| | E_L Lower Young's modulus | Pa |
| | En Enhancement factor | == |
| | g Gravitational acceleration | m s^{-2} |
| | g_{horiz} Horizontal component of gravitation acceleration | m s^{-2} |
| | H Ice stream thickness | m |
| | H_I Cliff height | m |
| | L_{tr} Stress-transmission length-scale | km |
| | l Diffusion length-scale | km |
| | N Stress exponent | -- |
| | q_b Basal temperature gradient | $^{\circ}\text{C/m}$ |
| | T Temperature | $^{\circ}\text{C}$ |
| | T_{max} Maxwell relaxation time | s |
| | T Time | s |
| | t_f Forcing timescale | s |
| | u Ice stream velocity | m/s |
| | x Ice stream transverse coordinate | km |
| | y Dimensionless depth | -- |
| | Z Depth | m |
| | α Surface slope | $^{\circ}$ |
| | ε Strain | -- |
| | η Viscosity | Pa s |
| | κ Thermal diffusivity | $\text{m}^2 \text{s}$ |
| | λ Temperature gradient in air | $^{\circ}\text{C/m}$ |
| | ν Poisson's ratio | -- |
| | ρ Ice density | kg m^{-3} |
| | σ Stress | Pa |
| | σ_{ij} Stress component | Pa |
| | σ_{trans} Transitional stress | Pa |
| | τ_b Basal stress | Pa |
| | φ Phase delay | $^{\circ}$ |
| | ω Forcing frequency | s^{-1} |
| | " $\bar{\quad}$ " Normalized quantity | |
| | " $\hat{\quad}$ " Non-dimensionalized quantity | |

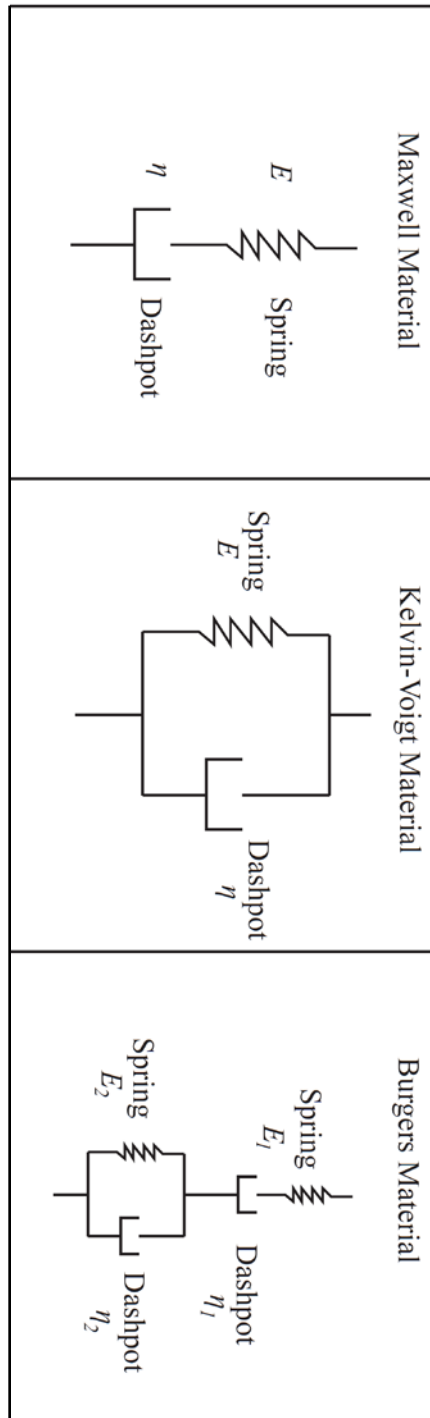


Figure 3.1: Schematic views of the one-dimensional Maxwell, Kelvin-Voigt, and Burgers viscoelastic models. The models are made up of spring and dashpot elements, with the associated moduli shown next to each element.

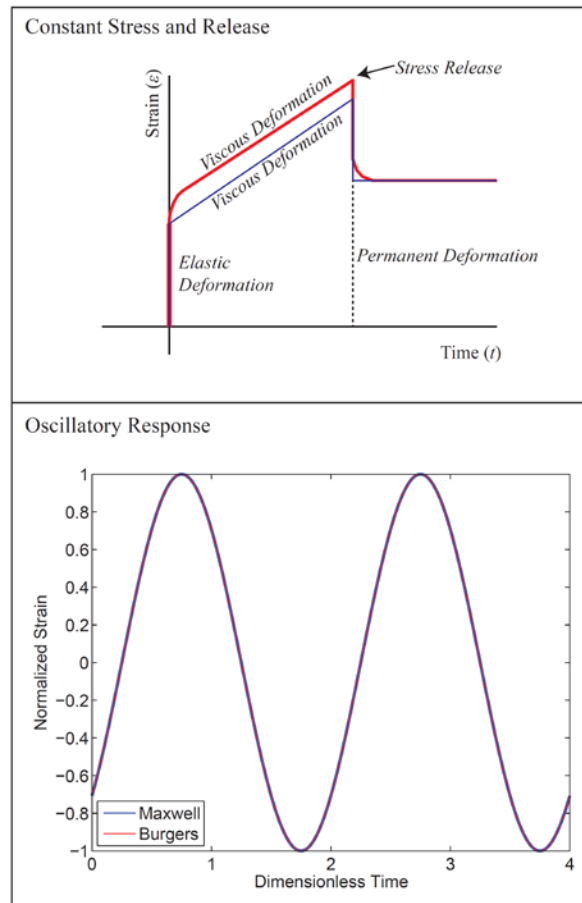


Figure 3.2: Comparison of the response of a one-dimensional Maxwell (blue) and Burgers model (red). In the upper panel, a constant stress is applied to the two materials, and the released at an arbitrary time. The Burgers model has a tapered response due to the solid element, but converges on the Maxwell model's response. In the lower panel, the oscillatory response of a Maxwell material and the response of a Burgers material are plotted as a function of dimensionless time. The Burgers model has a Kelvin-Voigt element that has a retardation time that is 100 times smaller than the relaxation time of the Maxwell material. Such a model is approximately what is expected for ice (e.g., Jellinek and Brill, 1956). The oscillatory responses of the two rheologies are negligibly different.

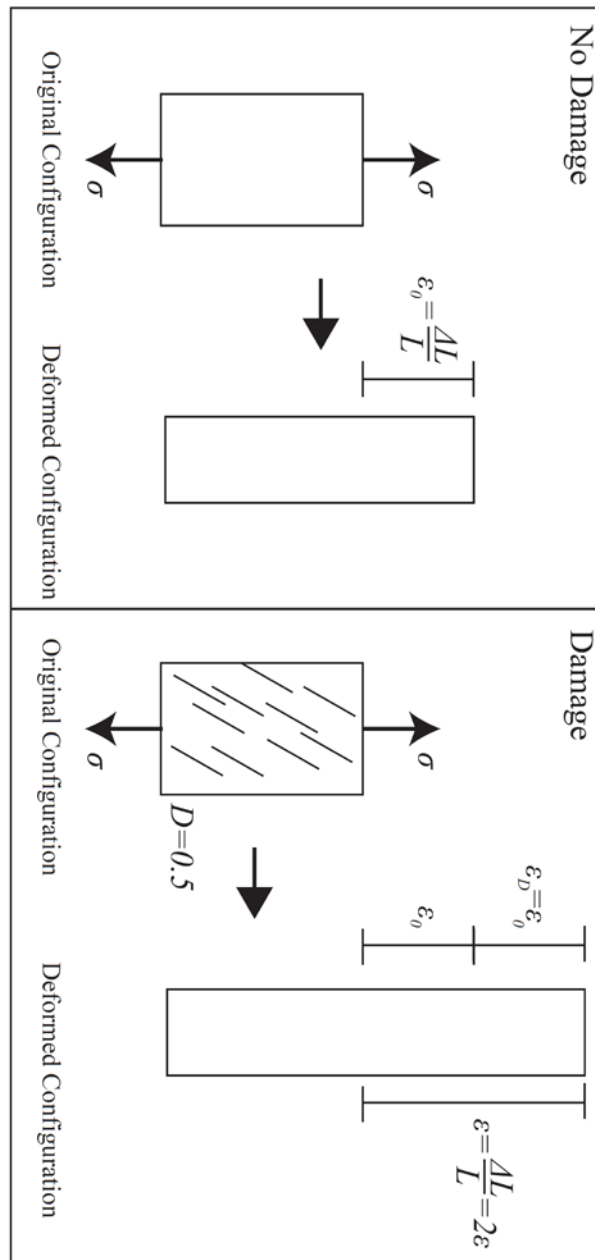


Figure 3.3: Schematic of the continuum damage mechanics formulation. The left panel shows the undamaged uniaxial strain of an elastic material. The right panel shows the strain of a damaged version of the same uniaxial strain. As the damage parameter in this example is chosen to be $D=0.5$, the total strain is twice the undamaged version, as the effective Young's modulus of the damaged material is $E_{eff} = (1 - D)E = 0.5E$.

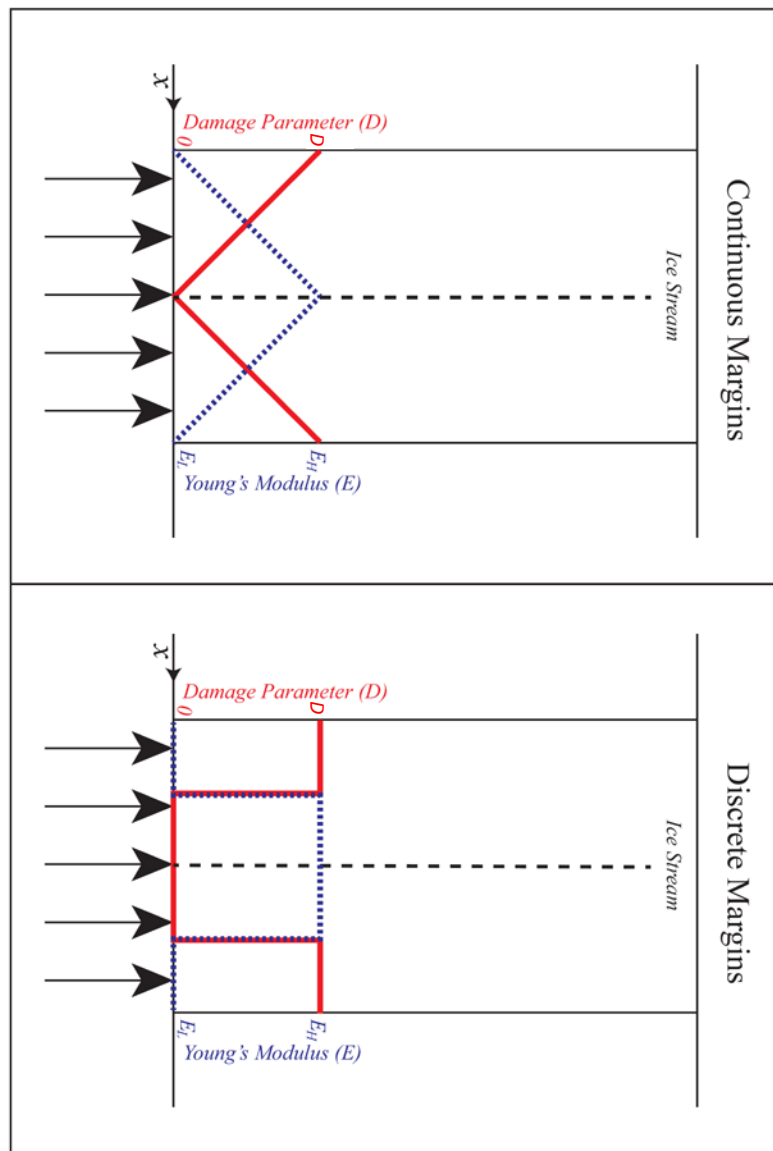


Figure 3.4: Diagram of the elasticity and damage profiles used in our marginal analysis models. The panel on the left shows the continuous margin model, while the right panel shows the discrete margin model. In each panel, the damage parameter D is plotted in red while the effective Young's modulus E is plotted in blue. The profiles are constant with inland distance of the grounding line. The grounding line is marked with arrows, as the grounding line is the location of the applied tidal forcing.

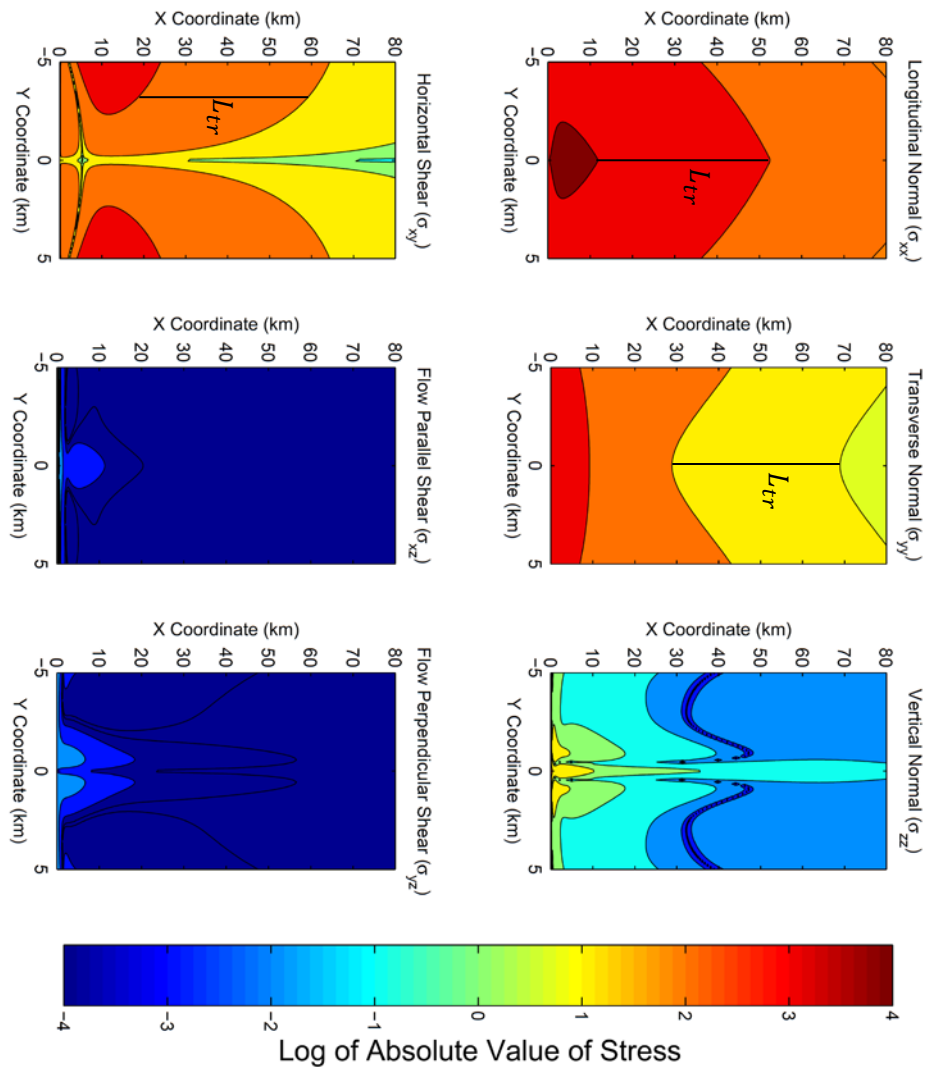


Figure 3.5: Representative stress state for a continuous margin model that has a one order of magnitude variation in Young's modulus between the central (strong) ice and the marginal (weak) ice. The transmission length-scale L_{tr} is shown on some of the stress components. Note that near the grounding line, the stress is elevated, but that away from the grounding line, the value of L_{tr} is constant along the transverse profile of the ice stream.

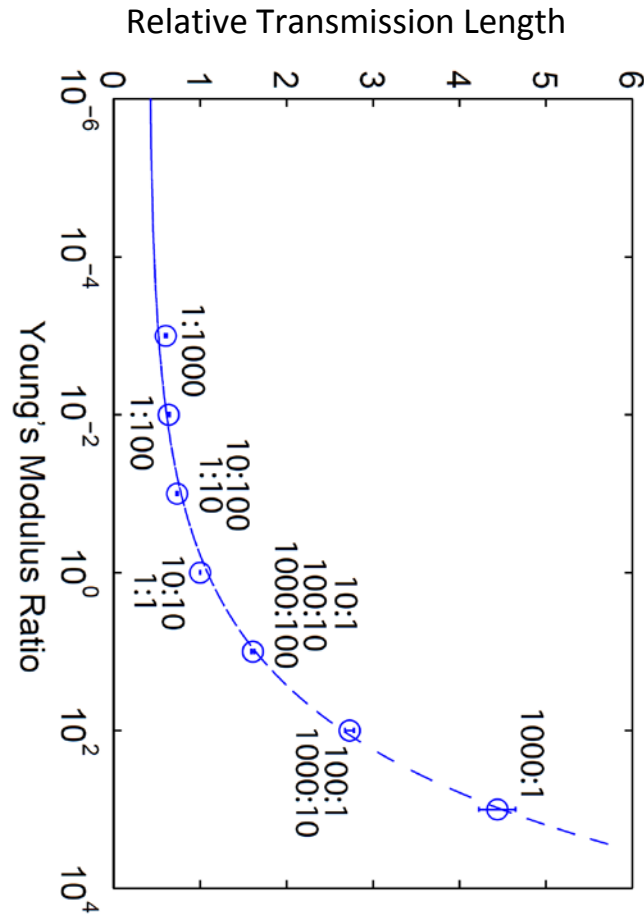


Figure 3.6: Change in average L_{tr} increase for models with continuous margins as a function of relative Young's moduli between the margins and central ice. The relative values of central Young's modulus, E_H , and marginal Young's modulus, E_L , listed in the corresponding data point. Error bars represent one standard error of the mean. The dashed line is a best-fit power law function. The equation for the fit is: $\hat{L}_{tr} = 0.699 * 1.790^{\log(\hat{E})} + 0.392$, where \hat{E} is the ratio of the Young's modulus in the central ice divided by the Young's modulus of the lateral margins.

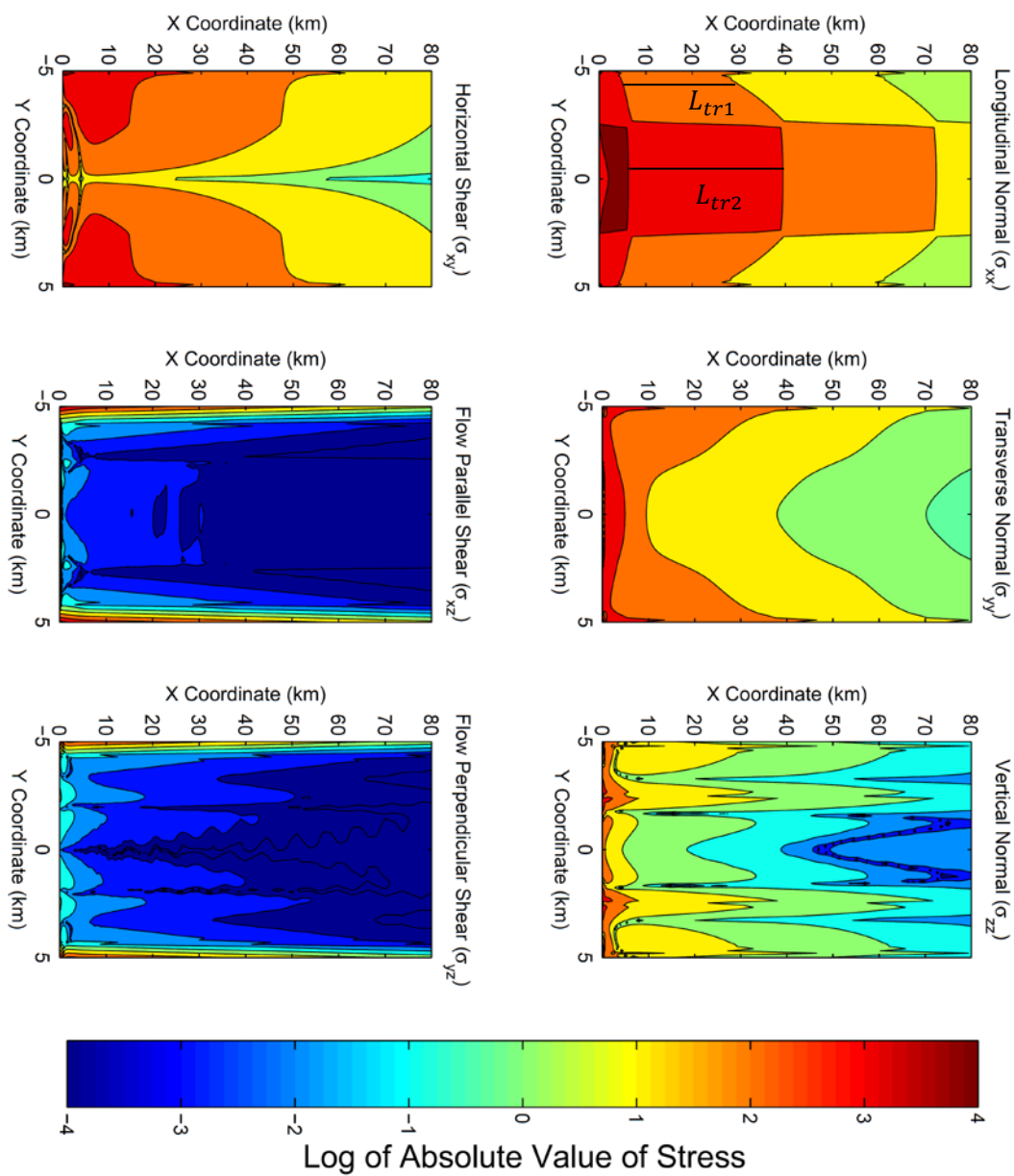


Figure 3.7: Representative stress distribution for a model with the same geometry as figures 2.6 and 3.5, but with ice margins that are one quarter of the ice stream's total width. These margins are a factor of 10 more compliant than the central ice. A variable L_{tr} as a function of transverse location is highlighted in the σ_{xx} component of stress.

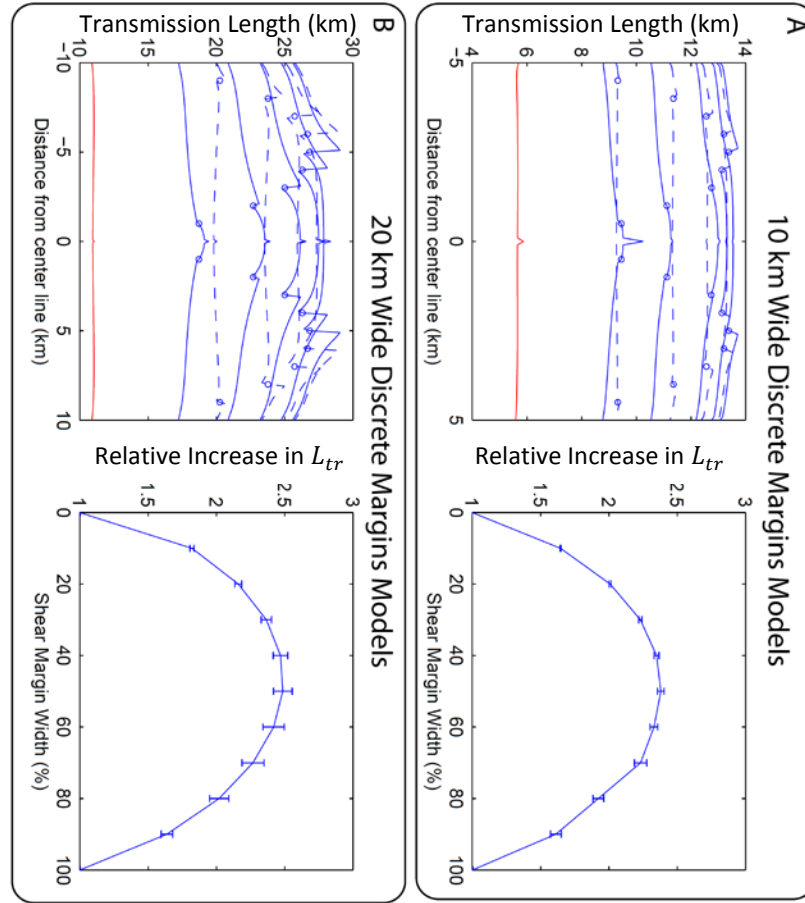


Figure 3.8: The relationship between the marginal width and L_{tr} compared to a uniform model for discrete margins. Top figures are for a model 10 kilometers wide, while bottom figures are for a model 20 kilometers wide. Figures on the left show the transverse profile of L_{tr} , with select profiles dashed to aid with visibility. Circles represent the location of the edge of the ice margins. The models that have homogeneous elasticity (0% and 100% width shear margins) are plotted in red. Figures on the right show the increase of the relative values of L_{tr} as a function of shear margin width. The error bars indicate one standard error of the mean. The fit for figure 3.8B, as described in the main text, is: $\hat{L}_{tr} = \frac{L_{tr}}{L_{tr,homog}} = -11.94\hat{x}^4 + 25.45\hat{x}^3 - 23.14\hat{x}^2 + 9.64\hat{x} + 1$, where \hat{x} is the non-dimensional width of the marginal shear zone, ranging from 0 to 1.

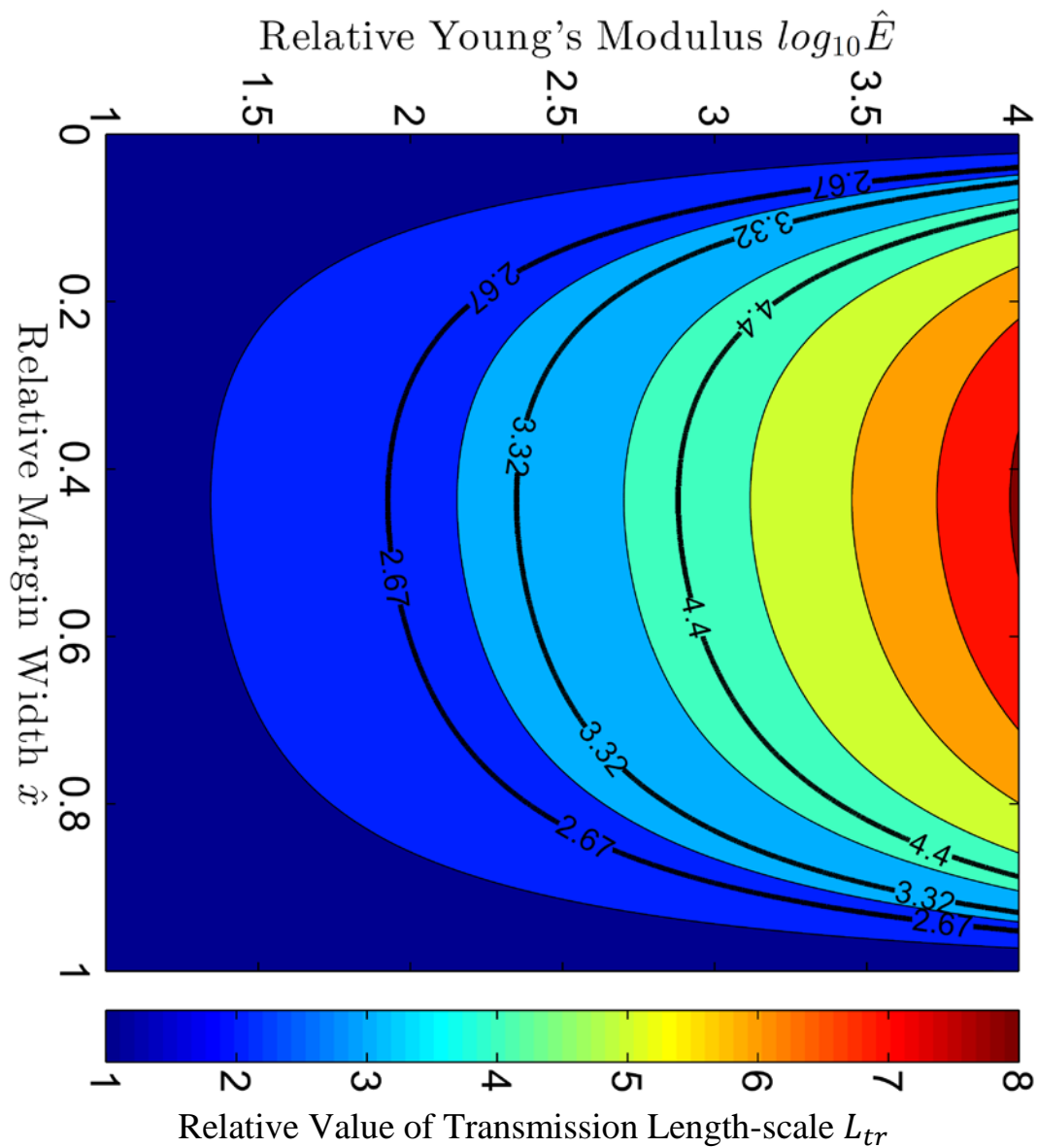


Figure 3.9: Young's modulus and margin width space for the increase in L_{tr} for a discrete margin model relative to the homogeneous elastic model described in chapter 2. The three bolded contours correspond to the conditions necessary to single-handedly explain the observations of the Rutford fortnightly tidal signal 4(2.67), the Rutford semidiurnal tidal signal (3.32), and the Bindschadler semidiurnal tide (4.40).

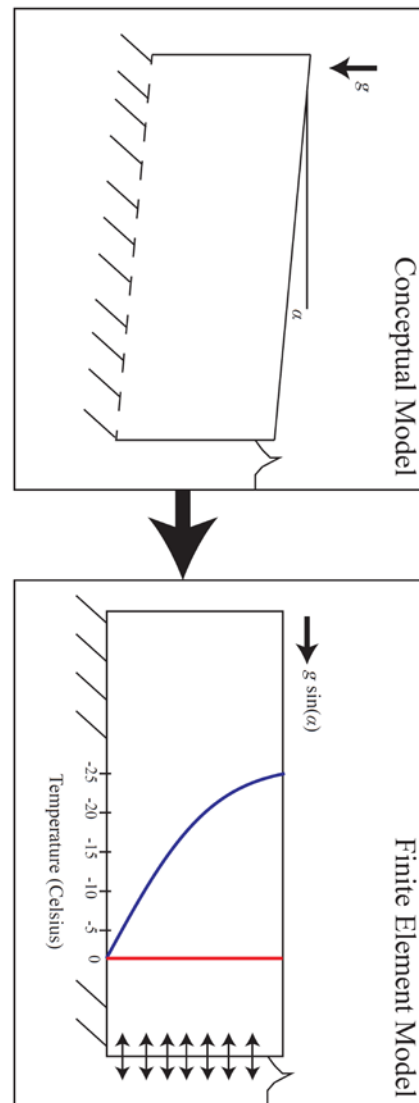


Figure 3.10: Conceptual and finite element model implementation of the gravitational driving stress. While in the conceptual model, there is a surface slope α , this is approximated by applying the deviatoric (horizontal) component of the gravitational acceleration, with a magnitude of $g \sin \alpha$. The finite element model also shows the two temperature profiles used in our viscoelastic models. The red line is the homogeneous temperature profile at 0°C , while the blue curve is the temperature profile defined in equation 3.14.

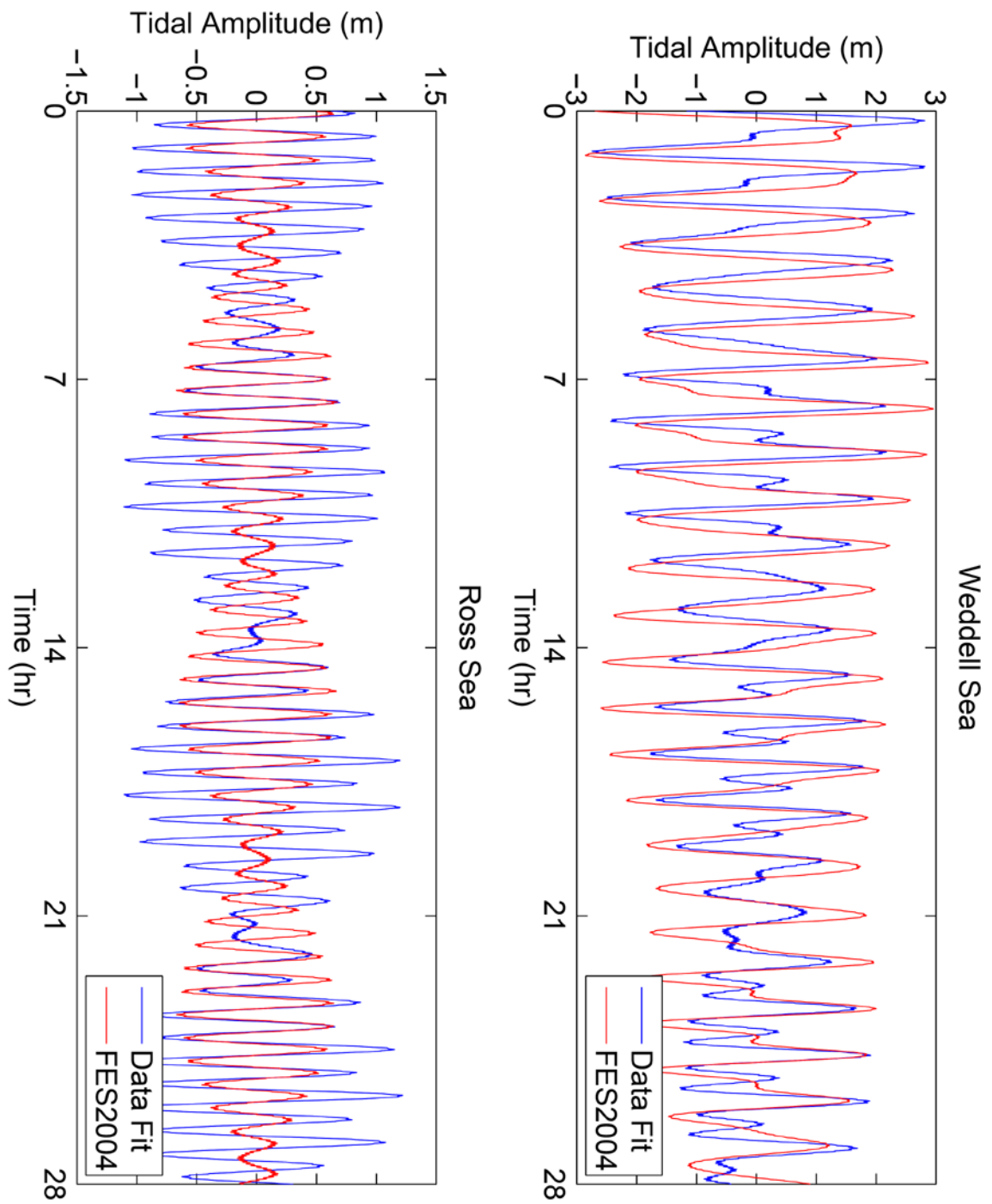


Figure 3.11: Comparison of the global tidal model FES2004 (red) to a five-component fit of tide-height data (blue) from the Weddell and Ross Seas. Tidal amplitudes and phases are listed in table 3.2.

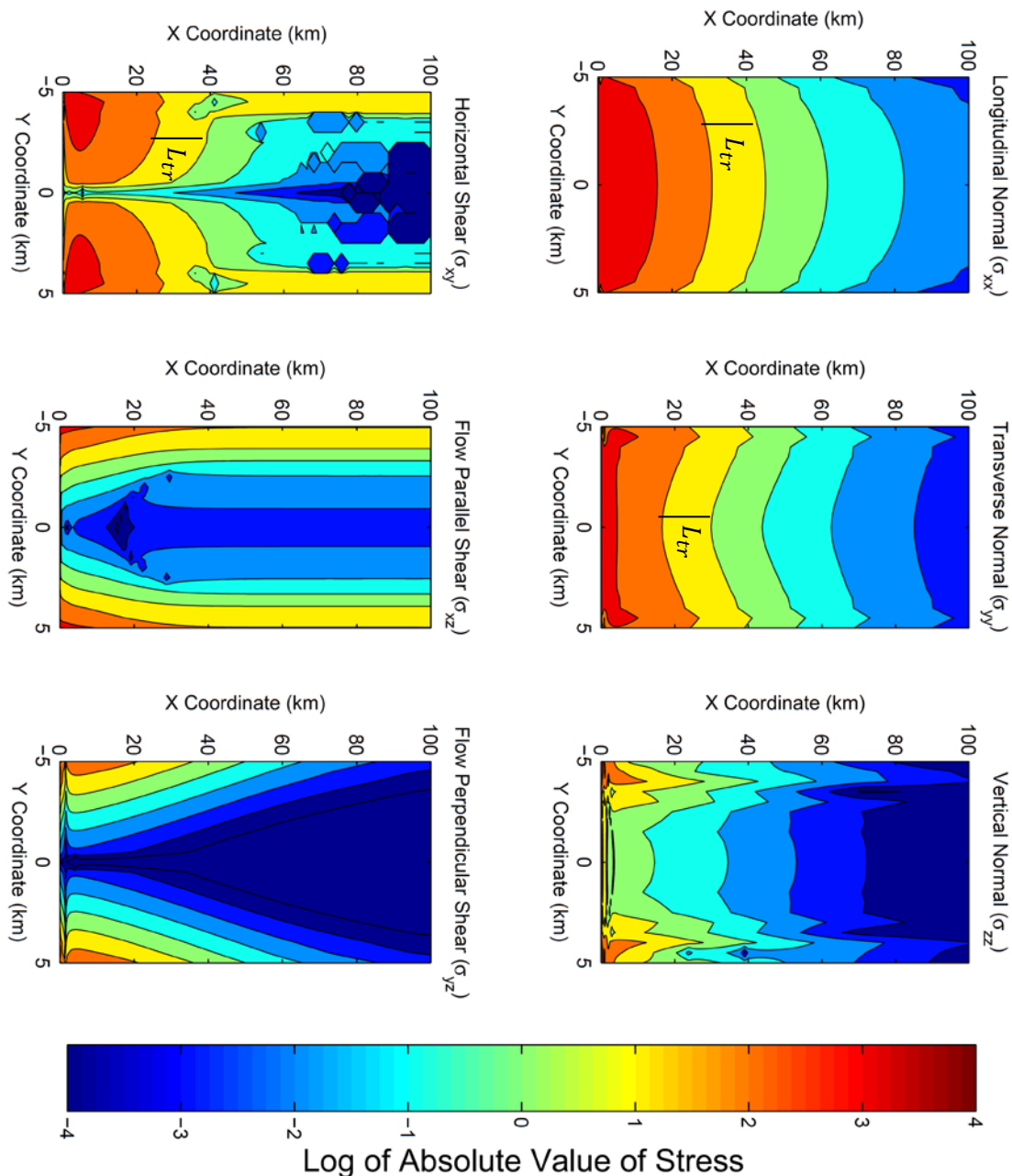


Figure 3.12: Stress state at the base of a modeled ice stream ten kilometers wide, one kilometer thick, and forced by a semidiurnal one meter tide. The stress values plotted are the “tidal” model with a “background” model subtracted, as discussed in section 3.3.4. The physical length of L_{tr} is drawn on the stress components where such a distance is easily seen.

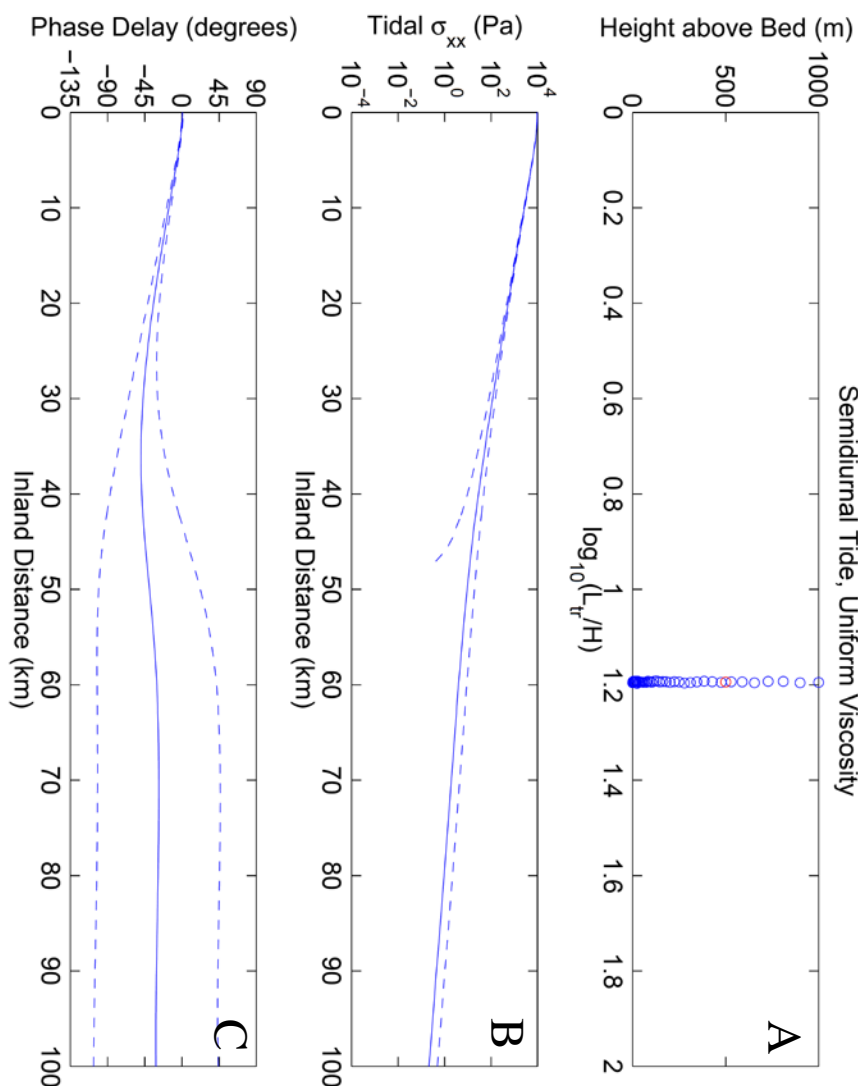


Figure 3.13: Model results for a viscoelastic model with a uniform temperature profile that is forced by a semidiurnal tide. Panel A shows the calculated values of L_{tr} for depth profiles of the stress. The average value of L_{tr} is 15.63 ± 0.04 km. Panel B shows the value of the longitudinal normal stress (σ_{yy}) as a function of horizontal coordinate. Panel C shows the fitted phase shift φ as a function of horizontal coordinate. In panels B and C, the dashed lines correspond to the 95% confidence interval values of the fit described in equation 3.15.

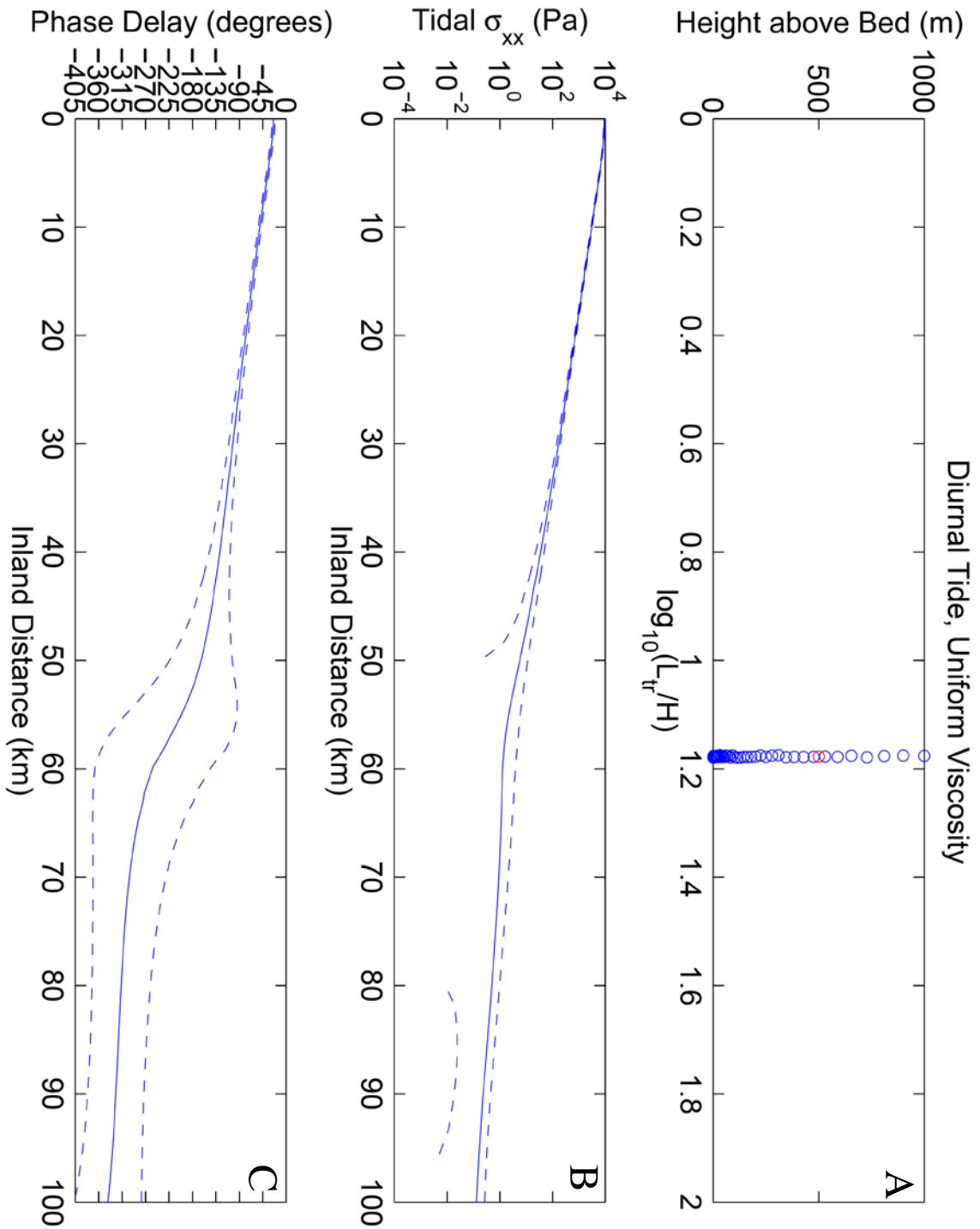


Figure 3.14: Model results for a homogeneous viscoelastic model forced by a diurnal tide. The values in the three panels match the description in figure 3.13. The average value of L_{tr} is 15.04 ± 0.04 km.

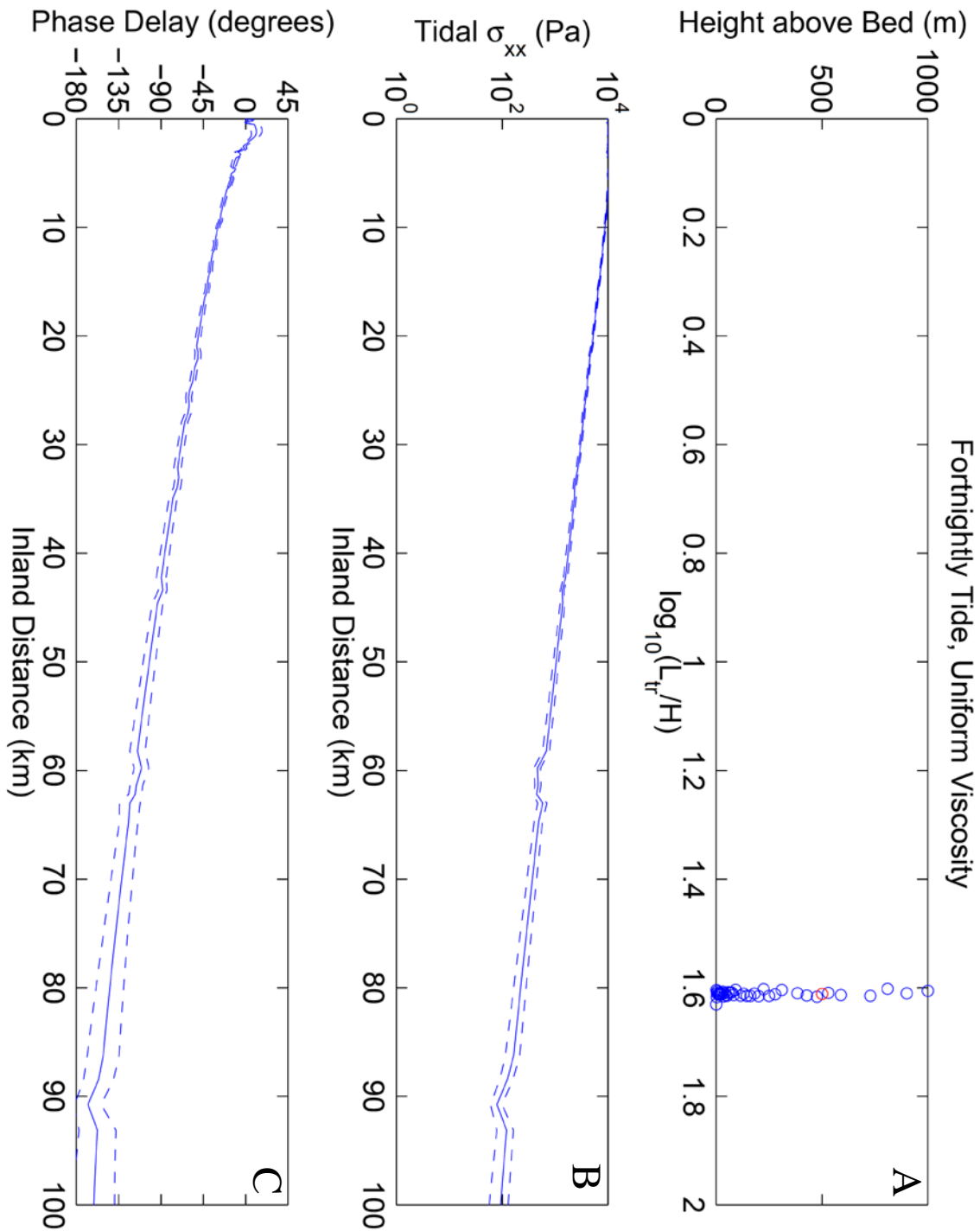


Figure 3.15: Model results for a homogeneous viscoelastic model forced by a fortnightly tide. The values in the three panels match the description in figure 3.13. The average value of L_{tr} is 40.87 ± 0.47 km.

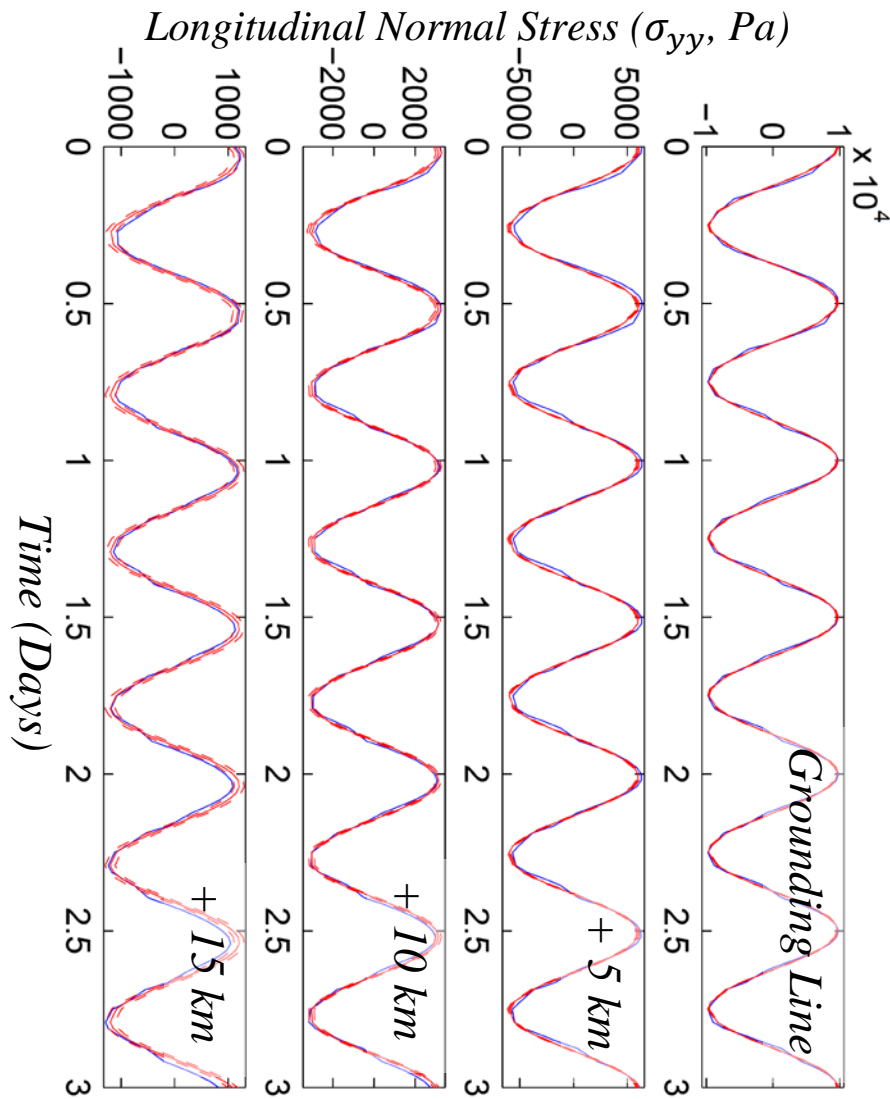


Figure 3.16: Model results and fits for locations on the model surface at the grounding line, and 5, 10, and 15 kilometers inland of the grounding line. The model has a homogeneous viscoelastic rheology and is forced with a semidiurnal tide. The blue lines are the model output, the solid red lines are the model fits using equation 3.15, and the dashed red lines are the 95% confidence intervals. The tidal stress diminished with distance inland of the grounding line, and the phase of the stress becomes increasingly delayed relative to the forcing frequency, which has a phase of zero degrees.

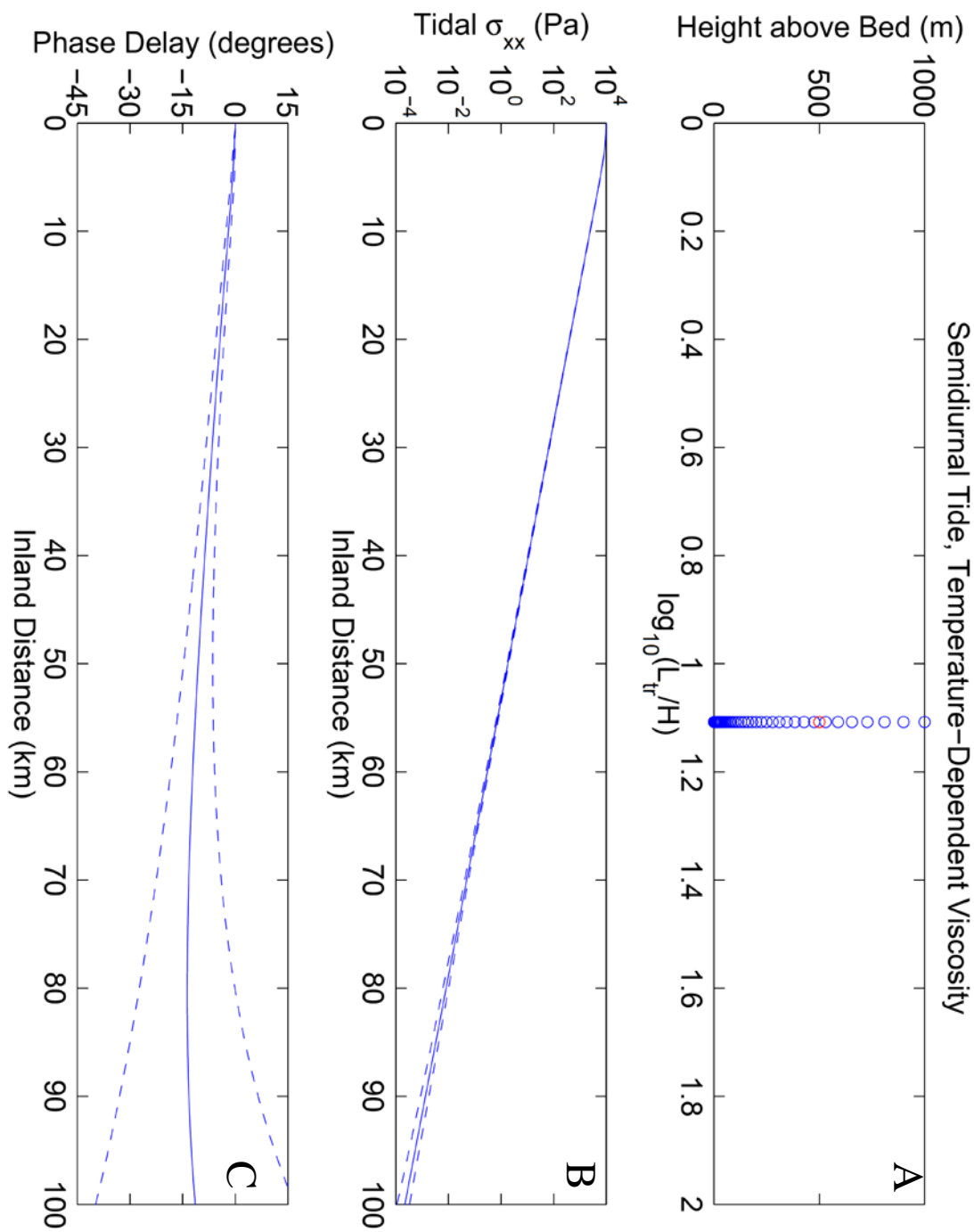


Figure 3.17: Model results for a temperature-dependent viscoelastic model forced by a semidiurnal tide. The values in the three panels match the description in figure 3.13. The average value of L_{tr} is 12.81 ± 0.001 km.

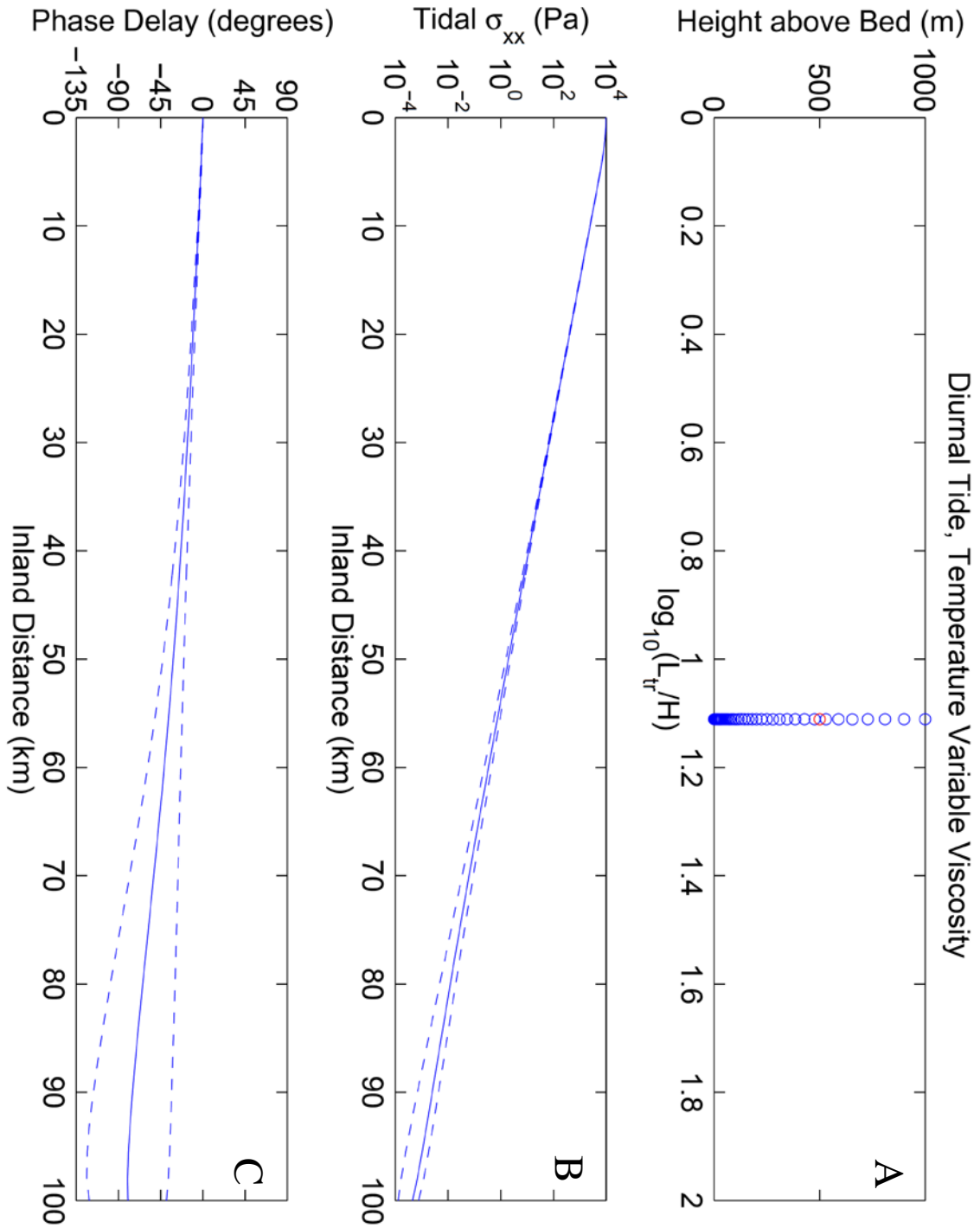


Figure 3.18: Model results for a temperature-dependent viscoelastic model forced by a diurnal tide. The values in the three panels match the description in figure 3.13. The average value of L_{tr} is 12.91 ± 0.002 km.

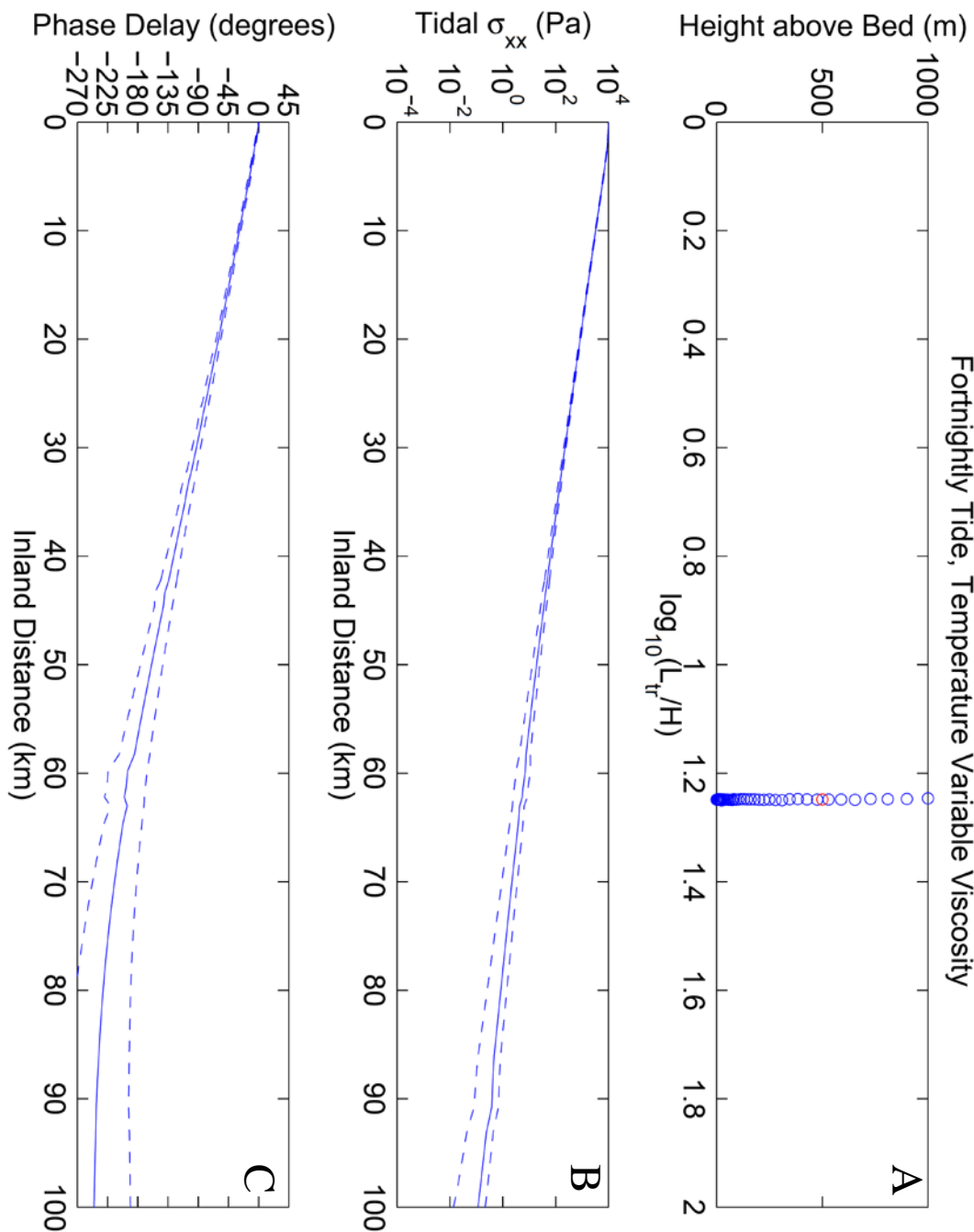


Figure 3.19: Model results for a temperature-dependent viscoelastic model forced by a fortnightly tide. The values in the three panels match the description in figure 3.13. The average value of L_{tr} is 17.72 ± 0.03 km.

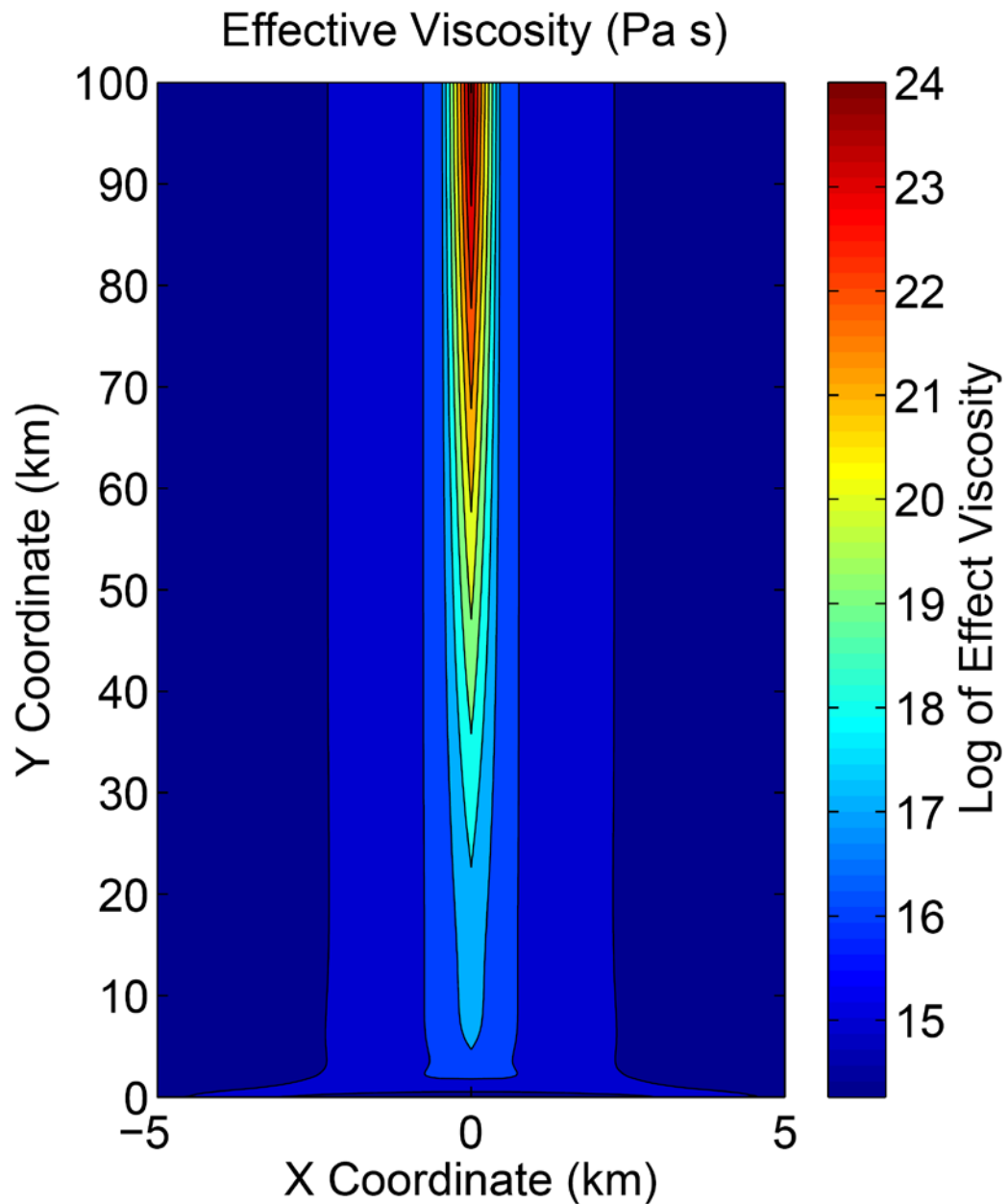


Figure 3.20: Figure showing the basal effective viscosity of our semidiurnal models for the homogeneous viscosity model. This figure demonstrates that the shear margins have substantially reduced viscosity relative to the central ice.

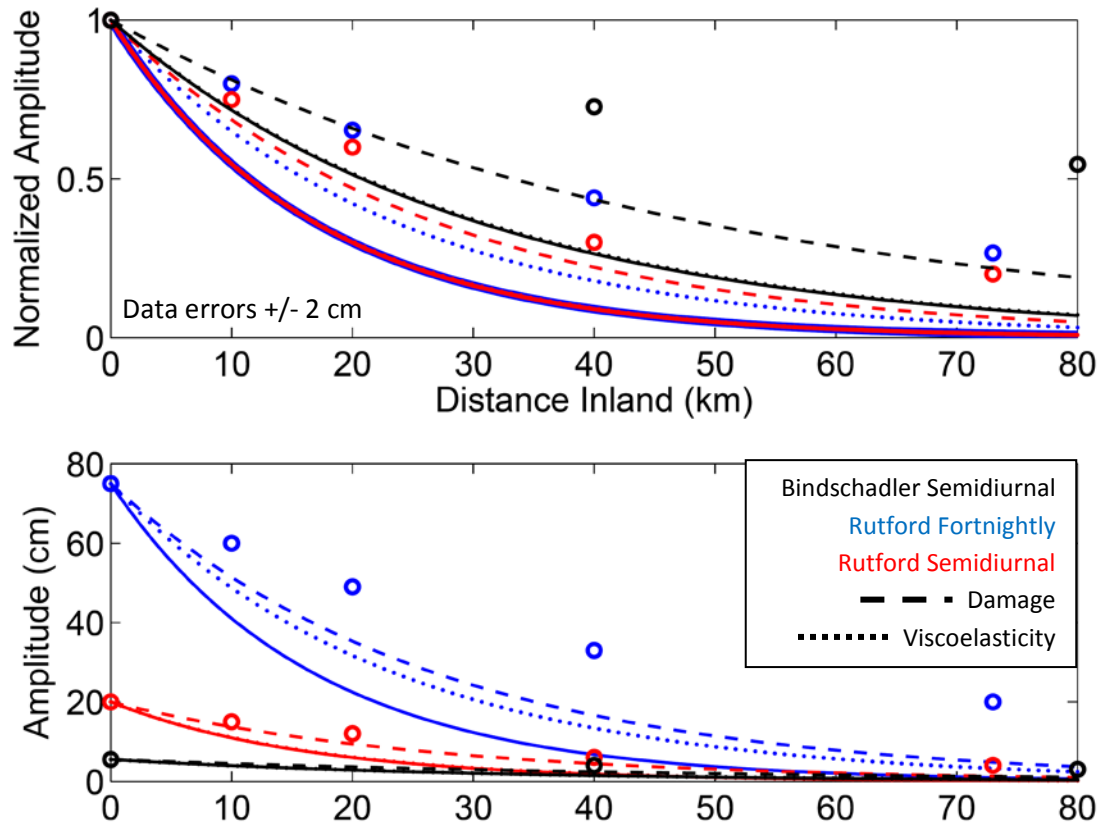


Figure 3.21: An updated version of figure 2.11 to reflect the added maximum effects of elastic damage in the shear margins (dashed) and temperature-dependent viscoelasticity (dotted). The solid line shows the linear elastic solution. The colors of the circles (data points) and lines refer to: blue, Rutford fortnightly tide; red, Rutford semidiurnal tide; black, Bindschadler semidiurnal tide. The upper panel shows the normalized amplitude of each tidal signal, while the lower panel shows the true amplitude.

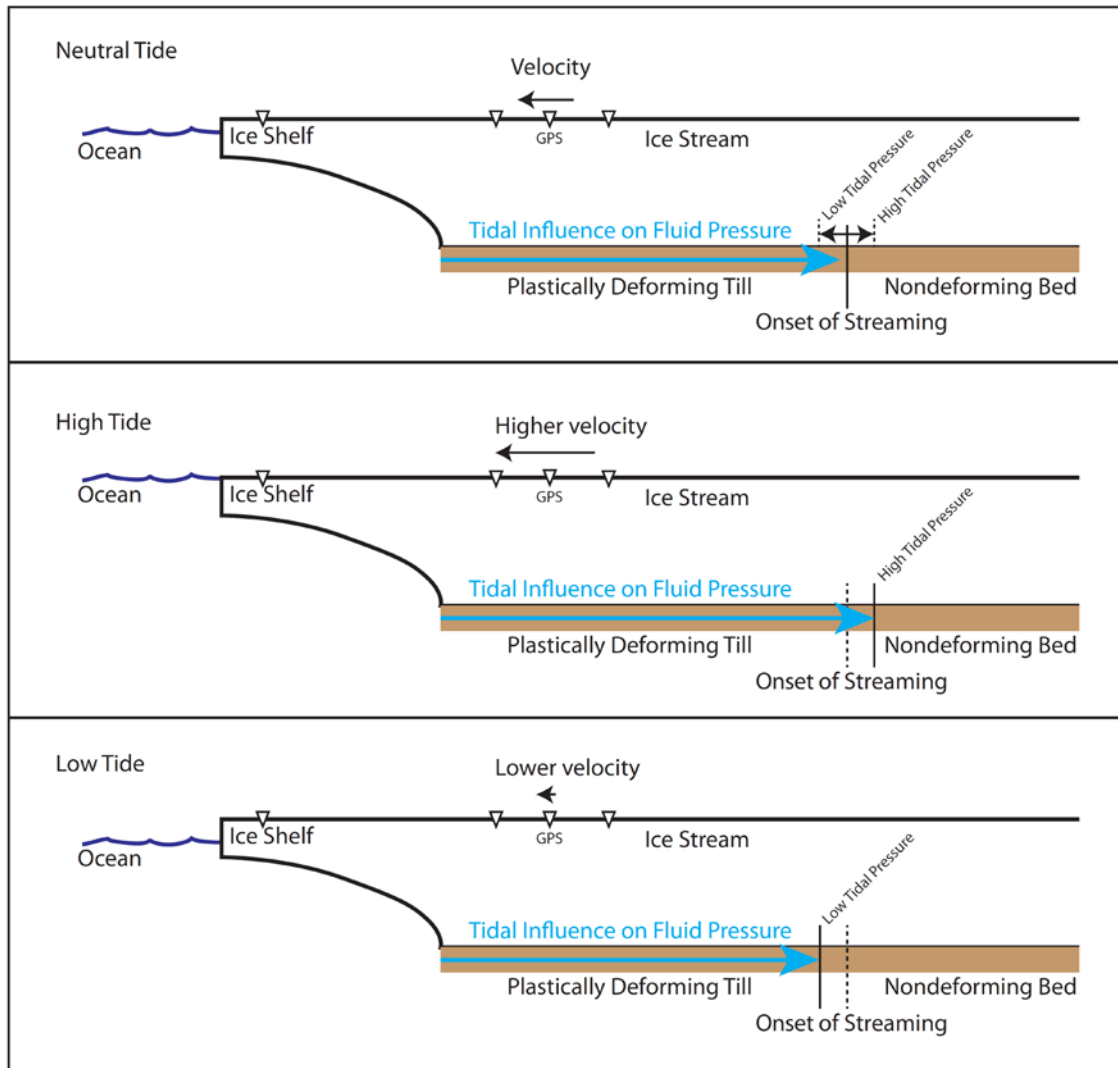


Figure 3.22: Schematic view of our hydrology hypothesis at a neutral, high, and low tidal amplitude, respectively. The triangles represent GPS stations on the surface of the ice stream and ice shelf. The brown layer represents the subglacial till. The onset of streaming is shown as a vertical line, and should vary in position with changes in the ocean tidal amplitude. Then the onset of streaming is farther inland, the GPS stations move faster relative to a neutral position as more of the ice is streaming. Furthermore, when the onset of streaming is closer to the grounding line, the relative velocity of the GPS stations is smaller than at a neutral tide.

| Tidal Period | E (GPa) | 0°C | -5°C | -10°C | -15°C | -20°C | -25°C |
|--------------|-----------|-------|--------|--------|--------|--------|--------|
| S | 10 | 31.06 | 49.89 | 81.33 | 104.99 | 138.89 | 184.50 |
| S | 1 | 98.21 | 157.77 | 257.17 | 332.01 | 439.21 | 583.45 |
| D | 10 | 21.96 | 35.28 | 57.51 | 74.24 | 98.21 | 130.46 |
| D | 1 | 69.44 | 111.56 | 181.85 | 234.77 | 310.56 | 412.56 |
| F | 10 | 5.87 | 9.43 | 15.37 | 19.84 | 26.25 | 34.87 |
| F | 1 | 18.56 | 29.82 | 48.60 | 62.74 | 83.00 | 110.26 |

Table 3.1: Transitional stresses σ_{trans} for a range of ice temperatures, tidal frequencies,

and Young's moduli. The transitional stress is defined in equation 3.7 and related

discussion is in section 3.1.2.2. All values in table 3.1 are in *kPa*. The tidal period

category uses the following abbreviations: S for semidiurnal, D for diurnal, and F for

fortnightly.

| | <i>Semidiurnal</i> | | | | <i>Diurnal</i> | | | | <i>Fortnightly</i> | |
|--------------------|--------------------|-------|-------------|-------|----------------|-------|-------|-------|--------------------|-------|
| | M_2 | | S_2/N_2^* | | K_1 | | O_1 | | M_f | |
| | Amp | Phase | Amp | Phase | Amp | Phase | Amp | Phase | Amp | Phase |
| Weddell Data | 1.52 | 35 | 0.843 | 339 | 0.620 | 11 | 0.497 | 57 | 0.0652 | 66 |
| Weddell FES2004 | 1.30 | 59 | 0.886 | 92 | 0.419 | 62 | 0.405 | 56 | 0.0301 | 198 |
| Ross Data | 0.105 | 325 | 0.119 | 108 | 0.587 | 274 | 0.432 | 348 | 0.0286 | 5 |
| Ross FES2004 | 0.012 | 30 | 0.028 | 352 | 0.367 | 316 | 0.261 | 295 | 0.0313 | 205 |

Table 3.2: Observational and tidal model amplitudes (in meters) and phases (in degrees)

for the Weddell and Ross Seas. The flagged component of the semidiurnal tide is the only component that had a varying second-largest tidal component, with the S_2 being subdominant in the Weddell Sea while the N_2 being so in the Ross Sea. Note that the agreement between the tidal model and the floating ice data is not great (see text for discussion).

| Tidal Period | Applied Force | Viscosity | L_{tr} (km) | c (m/s) |
|--------------|---------------|-----------|---------------|-----------|
| S | Full | Temp. | 14.4 | -- |
| S | Simple | Temp. | 12.8 | 1.8 |
| S | Simple | Homog. | 15.6 | 4.6 |
| D | Full | Temp. | 13.1 | -- |
| D | Simple | Temp. | 12.9 | 1.7 |
| D | Simple | Homog. | 15.0 | 11.1 |
| F | Simple | Temp. | 17.7 | 0.94 |
| F | Simple | Homog. | 40.9 | 0.60 |

Table 3.3: Calculated values for the length-scale of stress-transmission in our viscoelastic models. The tide column describes the forcing frequency of the applied ocean load. The applied load defines the load as either the full tidal condition or the simple tidal condition (see Appendix 3A). The viscosity column defines if the given model for nonlinear viscosity used a temperature-dependent viscosity or a homogeneous viscosity coefficient. The values of L_{tr} are quoted in kilometers. The phase velocity, c , is the slope of the phase vs. distance plot, and is shown in units of m/s. Note that no phase velocity is calculated for the “full” tidal forcing functions. The tidal period category uses the following abbreviations: S for semidiurnal, D for diurnal, and F for fortnightly.

Appendix 3A: Full Tidal Loading vs. Partial Tidal Loading

Following the rationale of Cuffey and Paterson, 2011 (and references therein), the stress balance for an ice stream/shelf system would involve balancing the hydrostatic pressure at the edge of the ice shelf and that of the ocean. As the ice shelf is floating, there is a net “pull” on the ice stream due to the excess pressure in the ice shelf compared to that of the ocean. As our viscosity is stress dependent, to be strictly accurate, we need to account for this end stress in our models to accurately model the viscous deformation in the ice stream. However, as the problem is more numerically tractable with a simple oscillatory tidal condition based on our elastic loading condition, we compare the model output for these two tidal loads (called “full” and “simple,” respectively). We find that having the more complex full tidal condition changes the length-scale for stress-transmission decay, L_R , by only about 20%, far below the factor of 3-4 change necessary to match observations. Thus, we use this as justification to use the more numerically favorable simple tidal condition.

3A.1 Full Tidal Loading Condition

In addition to the oscillatory load of the ocean tide, there are three major tidally-important stresses that a full tidal loading condition needs to consider. These stresses are incorporated into the balance of: the hydrostatic pressure of the flowing ice, the hydrostatic pressure of the static ocean water, and the flexural stress imposed on the grounding line due to the vertical motion of the ice shelf. Figure 3A.1 shows a schematic picture of the interaction of these stresses on an ice stream at neutral, high, and low tides.

First consider that the hydrostatic pressure of the ice and the water. For the ice, the value of the stress at a given depth is simply $\rho_I g(H_I - z)$. For the water, we first use

the flotation condition at the grounding line to find that the water rises to a height of $H_T = H_I(1 - \rho_I/\rho_W)$, which in turn leads to the definition of the hydrostatic pressure at levels where water exists as: $\rho_W g(H_T - z)$. However, this stress balance occurs at the edge of the ice shelf, not at the grounding line. We make use of the assumption that the ice shelf behaves elastically, which, following the results from our two-dimensional shelf models in chapter 4, allows us to move this stress balance to the grounding line without any decay of these stress values.

To account for the bending stress from ice flexure, we use the same simple beam theory presented in Appendix 2A of chapter 2. From this simple model for flexure, we expect that the flexural stress at the grounding line will be on the order of a few 100 *kPa* at a maximum (the exact value depends on the ice thickness and the geometry of the ice shelf).

The full load applied at the grounding line is the sum of these three stresses: the differential gravitational stress at the end of the ice stream, the flexural stress induced by the floating ice shelf, and the change in water weight due to the tide. Figure 3A.1 shows a graphical representation of these tidal loads, while equation 3A.1 shows the total form of this loading:

$$\sigma_{applied} = \begin{cases} -\rho_i g(H_i - z) & \text{if } z > H_t \\ -\rho_i g(H_i - z) + \rho_w g(H_t - z) & \text{if } z \leq H_t \end{cases} + \quad (3A.1)$$

$$F_{Tide}(t) * \left[\sigma_{flex} \Delta h \left(z - \frac{1}{2} H_i \right) + \rho_w g \Delta h \right]$$

where H_i is the ice thickness, H_t is the water level relative to the base of the ice stream, $F_{Tide}(t)$ is a unit tidal forcing as a function of time, and σ_{flex} is the maximum amplitude of flexure for a unit tide. For a reasonable tidal loading, the maximum force comes from

the static “pull,” which is on the order of 1 *MPa* at the base of a one-kilometer-thick ice stream, while the flexural stress is a few 100 *kPas* and the tidal weight is a few 10 *kPas*.

3A.2 Simple Tidal Loading Condition

For our simple loading condition, we apply the variable portion of the ocean tidal load as a normal traction to the grounding line. Mathematically, this condition is:

$$\sigma_{applied} = F_{Tide}(t) * \rho_w g \Delta h \quad (3A.2)$$

This is identical to the approach taken in our linear elastic model, save that the applied stress is time-variable.

3A.3 Stress-transmission Comparison

Figure 3A.2 shows a comparison between the tidally induced σ_{yy} component of stress (as described in section 3.3.1) for a map view of the base of a model with our full (left) and simple (right) loading conditions taken at a peak in stress response. We first note that overall, the stress field is remarkably similar between the full and simple loading conditions. The only major difference occurs in the portion of the ice stream near the grounding line, where the full loading condition has elevated stress values than those of the simple loading model. Such an increase in the value of the stress near the grounding line in the full model is not surprising as the value of the applied load is larger in this model than with the simple loading condition.

However, beyond this point inland, the model stress states are nearly indistinguishable, suggesting strongly that neither the hydrostatic “pull” on the ice stream edge nor the flexural stress due to the ice shelf bending viscosity of the ice stream near the grounding line significantly enough to dramatically change the nature of the transmission of stress viscoelastically in the ice stream. Such results are keeping with the

earlier observation and model results suggesting that tidal flexure is a stress that is only seen locally to the grounding line. The similarity in the model results is reflected in the values of L_R calculated between these two models, which fall within 20% of one another (see table 3.3).

As the difference between model results in this case is only on the order of 20%, we feel safe in neglecting the full tidal loading condition for our purposes. In the current form of our problem, we are sensitive to changes in the value of L_R that amount to a factor of 3-4, and thus 20% is far below the threshold of usefulness to justify the increase complexity (and thus computation time) of our models with the full loading condition.

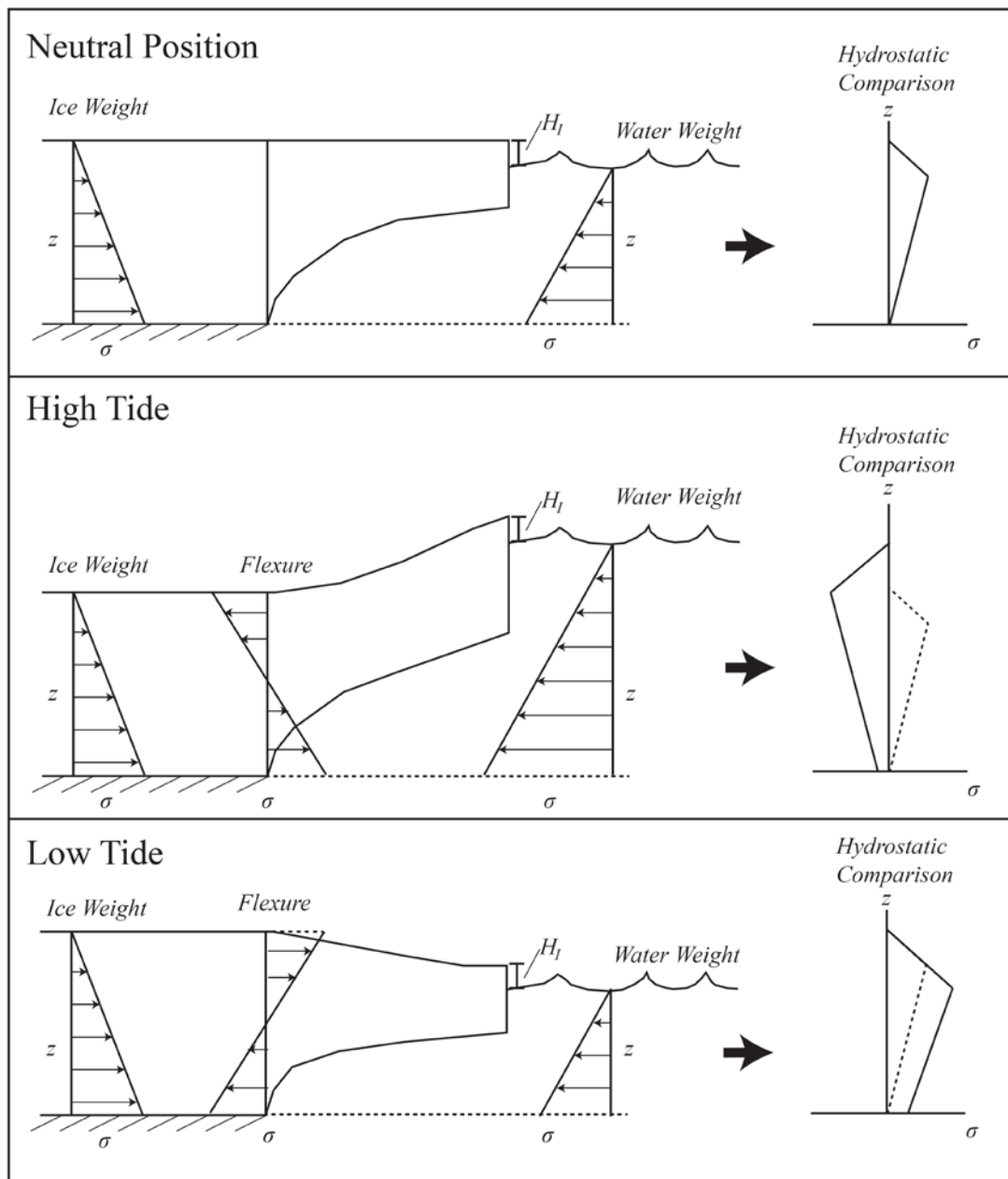


Figure 3A.1: Schematic diagrams of the full tidal forcing condition at a neutral, high, and low tide. The tidal stress will be the extensional/compressional stress due to the different in hydrostatic pressure at the edge of the ice shelf (shown in the graph on the right of the figure) and the flexural stresses due to the presence of the ice shelf. H_I is the distance between the surface of the ice shelf and the surface of the ocean.

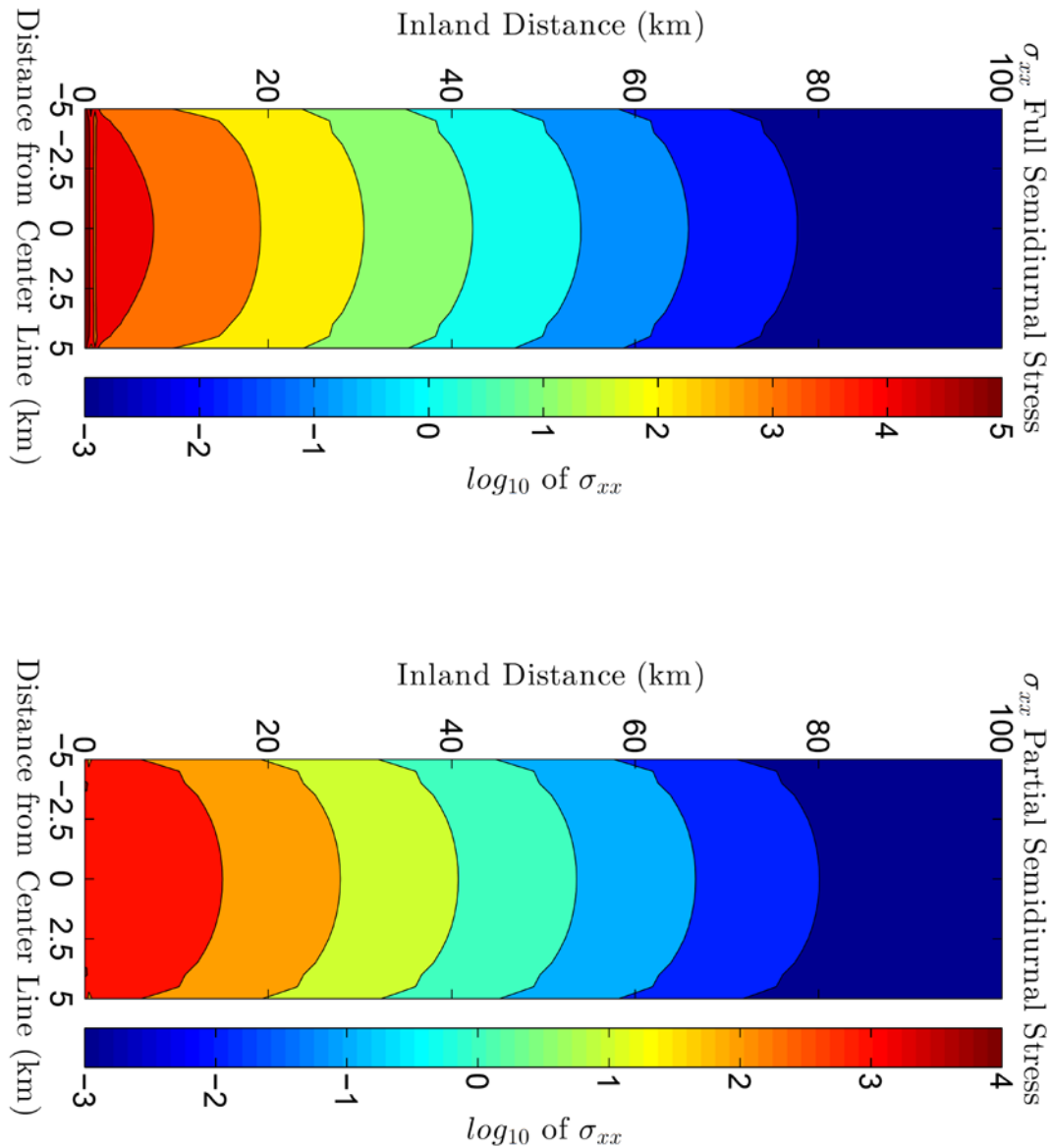


Figure 3A.2: Comparison of the value of the longitudinal normal stress (σ_{xx}) for the full tidal forcing condition (left) and the partial tidal forcing condition (right) at peak tidal amplitude. The full condition has a higher normal stress at the grounding line and a slightly more rapid decay of the stress due to the inclusion of the flexural stress. Once inland of the grounding line by five to ten kilometers, the stress-transmission length-scales are comparable between the two forcing conditions.

Chapter 4

Using Tidal Modulation of Ice Stream Motion to Constrain Viscoelastic Parameters *in Situ*

A phase delay in the response of a body to an oscillatory load is potentially related to that body behaving as a viscoelastic material. Geodetic studies of Rutford Ice Stream, Antarctica and Helheim Glacier, Greenland definitively show there is a significant phase lag between the tidally modulated surface motion of grounded ice and the peak ocean tides. In this chapter, we present a preliminary modeling framework outlining the relationship between the rheological parameters of a viscoelastic ice stream and the expected phase delay in its response to an oscillatory forcing. We then use these one- and two-dimensional results to suggest the configuration and requirements of a geodetic survey with the specific goal of constraining the viscoelastic parameters of *in situ* glacial ice.

4.1 Introduction

The previous two chapters demonstrated that ice streams are unlikely to transmit tidal stress through the bulk of the ice stream itself to the extreme distances seen observationally. However, near to the grounding line, a tidal load can still be transmitted through the ice stream bulk. And throughout the ice stream, the issue of the observed phase delay in the ice stream's response to ocean tides remains. As ice behaves as a viscoelastic material over tidal timescales (e.g., chapter 3 of this thesis), our expectation is that the near-grounding line behavior of an ice stream could provide a measurement of the viscoelastic parameters for *in situ* ice. While such a measurement would necessarily

be convolved with other processes that are tied to the ocean tides, this chapter provides a “proof-of-concept” for using observed tidal phase lags to constrain viscoelastic properties for glacial ice.

Our goal is to establish a methodology that uses the multiple timescales of the oscillatory tidal load in conjunction with the observed phase shift in tidal response to infer constraints on the ice stream’s viscoelastic parameters. As most of the introductory material has already been covered in chapters 2 and 3, we address only the most salient points in this chapter’s introduction, and suggest that this chapter is best understood after reading the introductory material in these two earlier chapters.

High-rate continuous global positioning satellite (CGPS) observations of Rutford Ice Stream and Helheim Glacier indicate an appreciable phase shift between the ocean tides and the tidal perturbation in ice position (Gudmundsson, 2006; 2007; 2013; de Juan 2009; 2010a/b; and de Juan-Verger 2011). A zero degree phase shift corresponds to the case of the peak de-trended inland motion of the ice being synchronous with the high tide, with a positive phase lag indicating that the ground motion’s peak response is delayed relative to the tidal peak. While our previous work suggests that the far-field observations of Rutford are probing a system other than the glacial rheology, the observations close to the grounding line of both Rutford Ice Stream and Helheim Glacier suggest that the phase lag is many tens of degrees. Equally important is that the phase delay may increase as a function of distance inland of the grounding line, suggesting that there is a calculable phase velocity to the propagation of the ice’s response to the changing tides.

A phase lag to an oscillatory response is a classic characteristic of a viscoelastic material when the stress relaxation timescale is within several orders of magnitude of the forcing frequency (e.g., Findley et al., 1976). Given the forcing frequencies ranging from 12 hours to 14 days for the major tidal constituents, we expect that a material relaxation time between $\sim 10^2$ and $\sim 10^8$ seconds (~ 2 minutes to ~ 76 years) will result in a measurable phase shift, with the strongest phase response occurring when the relaxation time is approximately the same order of magnitude as the forcing frequency. This range matches the estimate of the linearized relaxation timescale for ice of approximately 10^2 to 10^4 seconds (~ 2 minutes to ~ 3 hours), based on the experimental work of Jellinek and Brill (1956) and the model fitting of Reeh et al. (2003).

We explore the feasibility and data quality necessary to provide constraints on the rheology based solely on the measured phase shift to a tidal forcing. This chapter starts with an analysis of the complex moduli of three canonical one-dimensional linear viscoelastic models in shear, focusing on the expected phase shifts as a function of the material parameters. We then investigate the phase response of nonlinear viscoelastic materials over a range of reasonable ice models for the nonlinear viscous deformation expected during steady-state tertiary creep. We then present results from two-dimensional finite element modeling exploring the spatial variability of a tidal phase shift and the role that model boundary conditions play in determining the spatial variation in any phase shift. We use these model results to provide a test case for determining the viscoelastic properties of ice using data from Helheim Glacier (i.e., from de Juan, 2009; 2010a/b; de Juan-Verger, 2011). We close this chapter with a discussion of the expected

precision of the constraints on *in situ* viscoelastic parameters that tidal phase shift can provide and discuss factors necessary to select the ideal survey configuration and target.

4.2 Phase Shift in Analytic Models

Before exploring phase delay on a modeled outlet glacier, we first consider the behavior of three one-dimensional viscoelastic models—linear Maxwell, Kelvin, and Burgers—to an oscillatory forcing. These three models are shown schematically in the previous section (in figure 3.1). The Maxwell model is made up of a linear spring element and linear dashpot element in series, the Kelvin model is a linear spring and dashpot in parallel, and the Burgers model is a Maxwell element in series with a Kelvin element.

The governing equations for these three models in shear are:

$$-\frac{\sigma}{\mu} + \frac{\dot{\sigma}}{\eta} = \dot{\varepsilon} \quad (4.1a)$$

$$\sigma = \mu\varepsilon + \eta\dot{\varepsilon} \quad (4.1b)$$

$$\sigma + \left(\frac{\eta_1}{\mu_1} + \frac{\eta_1}{\mu_2} + \frac{\eta_2}{\mu_2}\right)\dot{\sigma} + \frac{\eta_1\eta_2}{\mu_1\mu_2}\ddot{\sigma} = \eta_1\dot{\varepsilon} + \frac{\eta_1\eta_2}{\mu_2}\ddot{\varepsilon} \quad (4.1c)$$

where μ is the shear modulus, η is the viscosity, and, for the Burgers model, the subscripted 1 refers the Maxwell element and the subscripted 2 refers to the Kelvin element. We now apply an oscillatory shear load of frequency ω constant amplitude τ_0 :

$$\sigma = \tau_0 e^{i\omega t} \quad (4.2)$$

We expect that the strain response will be oscillatory at the same frequency as the applied stress but shifted by a phase delay δ , such that:

$$\varepsilon = \varepsilon_0 e^{i(\omega t + \delta)} = \varepsilon^* e^{i\omega t} \quad (4.3)$$

Taking the ratio of strain to stress gives us the *complex creep modulus*, J^* :

$$J^* = \frac{\varepsilon}{\sigma} = \frac{\varepsilon^*}{\tau_0} = \frac{\varepsilon_0}{\tau_0} e^{i\delta} = J_1 + iJ_2 \quad (4.4)$$

Table 4.1 shows relevant values of J_1 and J_2 , taken from Findley et al. (1976). We can also relate the phase shift to the components of J^* using:

$$\tan \delta = \frac{J_2}{J_1} \quad (4.5)$$

Lastly, we can define a natural timescale associated with each material model. For a Maxwell material, the stress due to a constant strain will decay exponentially with time, as controlled by the relaxation time T_{Max} . For a Kelvin material, a constant stress will induce a creep strain that exponentially approaches the equivalent elastic strain. The timescale of this creep is controlled by the retardation time, T_{Kelv} . In the Burgers model, there is both a relaxation time T_{Burg1} and a retardation time T_{Burg2} . The values of these natural timescales are shown for each model in table 4.1.

4.2.1 One-Dimensional Phase Shift

We are now equipped to determine the expected phase shift for a given material model of ice for a forcing function of known frequency. However, as there are two separate free parameters (the appropriate relaxation/retardation timescale and the forcing frequency), we again introduce the Deborah number, De :

$$De = \frac{T_R}{T_F} \quad (4.5)$$

where the Deborah number is the ratio of a material's relaxation time to the period of an applied forcing. When De is large, the material behaves elastically, when De is small, the material behaves viscously, and when De is around one, the material behaves viscoelastically. The Deborah number encapsulates the choice of the material parameters

(shear modulus and viscosity) and the forcing frequency, allowing us to calculate the phase shift with respect to a single nondimensional quantity.

Figure 4.1 shows the phase shift in the strain response to an oscillatory stress for the linear Maxwell, Kelvin, and Burgers models (assuming $\eta_1 = \eta_2 = \eta$ and $\mu_1 = \mu_2 = \mu$). From this figure, we see that all the linear models predict a phase shift between 0 and 90 degrees, with the Maxwell and Burgers models predicting the phase shift to increase at small De while the Kelvin model demonstrating a larger phase shift at large De . All three models meet at a phase shift of 45 degrees, when $De \approx 10^{-0.8} = 0.158$.

As seen in the linear phase curves, the Maxwell and Burgers models act most similarly to the expected phase response, where a material that behaves more viscously than elastically will have a stronger out-of-phase displacement response than a comparatively more elastic model. Thus, the Kelvin model, a representation of a solid material, is a poor model choice for phase shift in ice and will not be considered further. Second, while the trend in phase is distinct between the Maxwell and Burgers models, a large number of high quality data would be necessary to adequately distinguish between these two models. As the constraining data in $\delta - De$ space should only vary with tidal frequency, any rheological fitting would be based on, at best, a handful of observations with different De . Thus, given the relative sparsity of our expected data and the fewer numbers of parameters, we choose to continue our investigation of ice rheology by assuming a Maxwell material for the ice response to a tidal load.

4.2.1 Phase Shift for a Nonlinear Maxwell Material

The nonlinear viscosity of ice complicates the understanding of the phase shift in the oscillatory response of a one-dimensional nonlinear material model. We explore the

phase shift in a nonlinear Maxwell model with the nonlinearity limited to the viscous component of deformation, such that the constitutive law is given by:

$$A\sigma^n + \frac{\dot{\sigma}}{\mu} = \dot{\epsilon} \quad (4.6)$$

where n is the power law exponent and A is the nonlinear viscosity coefficient. Note that for these simple models, the temperature dependence of A is neglected. The approach used in the previous section to calculate the phase shift δ becomes untenable for an oscillatory nonlinear model as the effective linear viscosity would necessarily oscillate with the forcing function amplitude, resulting in a time-dependence on the phase shift. Instead, we adopt a different method to finding the one-dimensional phase shift for our nonlinear Maxwell model.

First, we choose the periodicity of the stress forcing function to match that of the three major tidal constituents, rounded to the nearest integer hour: 12 hours for the semidiurnal tide, 24 hours for the diurnal tide, and 14 days for the fortnightly tide. We then solve for the strain rate of each of these tides, as well as the linear combination of the three tides (a “combined tide” forcing), using equation 4.6. The values of A and n used in this analysis match the values from the Glen and Goldsby rheological models for ice at 0°C in tertiary creep (Glen, 1955; 1958; Goldsby and Kohlstedt, 1997; 2001), and μ from the canonical values of E and ν (Petrenko and Whitford, 2002). As we are forcing our tides at a known period and the longer tides are integer multiples of the shorter tides, we can use a Fourier analysis to find the exact phase for the applied forcing functions. Lastly, shifting the phase of the strain rate by 90° gives us the phase delay in the modeled strain as the strain rate is the time derivative of strain.

The phase shift values for the semidiurnal, diurnal, fortnightly, and combined tides are shown in figure 4.2 as functions of De and for a linear, Glen, and the two Goldsby rheologies. For all the models, the expected phase shift trends are fairly similar, and the value of δ ranges from 0° to 90° . At a given tidal frequency, the predicted phase shifts are independent of the material parameters. A single forcing frequency will not perturb the amplitude of the forcing function, and thus will not change the effective viscosity of the material. However, as highlighted in table 4.2, the combined tide does show a nonlinear effect on the phase of any given tidal constituent, such that some of the phase shifts are slightly elevated or depressed for a given De compared to the value for the individual tidal frequency. The value of De for a given phase shift can vary by as much as a factor of two for the rheologies considered here. With the stress-dependent rheology, the discrepancy between the phase shift when the model is forced with the individual tides compared to the combined tides is more severe the higher the power law exponent is.

4.3 Two-Dimensional Finite Element Models

Having established some intuition for the phase shift from our one-dimensional models, we now present results from a range of two-dimensional, nonlinear Maxwell finite element models exploring the phase shift of a higher dimension viscoelastic body to an oscillatory force. First the variation in observable surface phase shift is categorized as a function of the modeled ice streams' boundary conditions, the choice of rheology, and the spatial variability of the phase shift across the model's profile. Then, this model approach is validated using data from Helheim Glacier to estimate viscoelastic

parameters for ice. Such parameters are found to be within a range compatible with laboratory values for ice viscoelasticity.

4.3.1 Methodology

As with our earlier models, we use the *PyLith* software package (as described in section 1.4) for our finite element modeling. The model geometry is a simplified version of the lower portion of Helheim Glacier (750 meters thick and six kilometers wide). We explore two different model boundary conditions in our analysis, as are shown in figure 4.3. First is the case of an outlet glacier that is stuck to its bed, such that the controlling dimension is the ice thickness. This model is equivalent to the “frozen bed” model from chapter 2. Second is a two-dimensional outlet glacier that is stuck to its lateral margins. For each of models, we apply the tide as an oscillatory traction boundary condition along one edge of the model domain. As discussed above, we choose to model a single tidal frequency at a time, rather than combining tides of multiple frequencies.

4.3.2 Numerical Results

Figures 4.4 and 4.5 show the behavior of the phase for our basal and side-wall models, respectively, as a function of De . In figure 4.3, our models show the phase at the grounding line and at locations one, two, and three kilometers inland, while figure 4.5 includes the grounding line and locations five, ten, fifteen, and twenty kilometers inland. The difference in length-scale is needed because the side-wall models have a larger decay length-scale, L_{tr} , than the basal models. In each figure, we include model results for a linear viscoelastic model (shown in blue) and nonlinear viscoelastic models (other colors) forced at multiple tidal frequencies. For the basal model, the only nonlinear model considered has a power law exponent of $n=3$, while for the side-wall models, we also

consider $n=1.8$ and $n=4$. These three power laws correspond to the rheologies associated with a Glen flow law (Glen, 1955; 1958), superplastic flow (Goldsby and Kohlstedt, 1997; 2001), and climb-limited dislocation creep (Goldsby and Kohlstedt, 1997; 2001). Due to the exceedingly small stable timestep in the low-viscosity nonlinear models, the range of De explored is more limited than for the linear case.

For both model boundary conditions, the linear models demonstrate the arctangent form of the phase-Deborah number relationship produced analytically for a one-dimensional Maxwell material, with the phase ranging from zero degrees (elastic behavior) to ninety degrees (viscous behavior). The change in the material behavior occurs over a range of about two and a half orders of magnitude—such that $10^{-2.5} < De < 10^0$. However, unlike the one-dimensional case, in the region where the phase is neither zero nor ninety, the phase shows a dependence on distance from the grounding line, as demonstrated by the spread in phase values over the locations shown in figure 4.4 and 4.5.

To better demonstrate this distance dependence, figures 4.6 and 4.7 show the phase shift of the centerline ice as a function of inland distance (note that the horizontal length-scale varies due to the difference in L_{tr} between the two models). These two figures are remarkably similar, suggesting that the expected phase shift trend with inland distance, at least in a two-dimensional model, is not dependent on the absolute distance away from the grounding line but rather on the relative strength of the tidal signal. Appendix 4A shows the phase shift seen across the model domain for the side-wall models.

For each model, the nonlinear solutions are shifted to the left (i.e., towards lower De) compared to the corresponding linear viscoelastic model. This behavior matches that of the one-dimensional solution. As seen in both figures 4.3 and 4.4, the solutions for a given rheology at different tidal frequencies agree fairly well, confirming that the Deborah number is a controlling parameter of the phase shift. Another implication of the dependence on De is that phase data collected for multiple tidal frequencies will provide multiple data points along the same curve, rather than each tidal frequency belonging to unique functions.

Unfortunately, the models presented here are insufficient to provide a well-constrained fit to the arctangent form of the phase response of each model to the applied oscillatory loads. In the case of the linear model, such a deficiency could be addressed through filling out the model space through additional modeling. For the nonlinear scenarios, the finite element models for the lowest values of De are already on the verge of taking too long to run to be computationally viable. These models currently take about one week per model, and are not easily parallelizable due to the sequential nature of timestepping. Thus, every order of magnitude decrease in De would increase the run time by approximately an order of magnitude, as the stable timestep of the Maxwell rheology is small enough (compared to the forcing function) to require extensive calculations for even a single tidal cycle. Thus, we suggest that extrapolating the linear trend onto the nonlinear data would provide an estimate for the nonlinear viscoelastic response at these lower values of De . For the purposes of demonstration here, we assume that the phase varies linearly between the data points. This approach is clearly inadequate, but as we lack the model results necessary for an accurate functional fit to the

phase points, such an approach is a practical alternative to a poorly constrained arctangent function.

4.3.3 Application to Helheim Glacier Data

We now present a simple test example of using ice stream phase data to provide constraints on the viscoelastic properties of ice. For our purposes, we use calculated phase delays from Helheim Glacier (de Juan, 2009; 2010a/b; de Juan-Verger, 2011) as our dataset, even though the errors for the phases can quite substantial. For each of the three surveys from de Juan-Verger, the data point closest to the grounding line is used to approximate the phase response at the grounding line, so that the distance dependence of the phase response can be negated. While de Juan-Verger (2011) presents linear extrapolations of the phase measurements to the calving front of Helheim Glacier, we choose to use the closest data point rather than the extrapolated value due to the large data uncertainties influencing the linear fit. For the three surveys, the phase differences are $27^\circ \pm 3^\circ$, $53^\circ \pm 15^\circ$, and $55^\circ \pm 15^\circ$.

Figure 4.8 shows the location of these phases on the basal model (panel A) and the side-wall model (panel B), with the values of the fitted effective viscosities listed in table 4.3. The fits are relative to the linear model (blue) and the extrapolated nonlinear model for $n=3$ (red). The extrapolated line is found by shifting the linear model by a constant offset until the new line matches the finite element values for the nonlinear phase shift. The differences between the predicted values of the effective viscosities are minimal between the two models. In all cases, T_{Max} is on the order of 10^2 to 10^3 seconds (~2 to ~20 minutes), though the variation between the lowest and highest estimates differs by a factor of about 60. Assuming a Young's modulus of 9.33 GPa (Petrenko and

Whitford, 2002), the estimates of the ice viscosity from these Helheim Glacier phases data fall between $1.01e12 \text{ Pa} \cdot \text{s}$ and $5.83e13 \text{ Pa} \cdot \text{s}$. Considering the uncertainty in our model trend and the wide range in errors of the Helheim phase data, these values are remarkably close to the estimated linear viscosity value for ice of Jellinek and Brill (1956) of $1e12 \text{ Pa} \cdot \text{s}$ to $1e14 \text{ Pa} \cdot \text{s}$ for similar stresses.

In this brief demonstration, the distance dependence of the solution is not considered, as the phase data from Helheim Glacier is not constrained enough to adequately show a convincing distance dependence. However, as our work demonstrates, the distance dependence of the phase is diagnostic of the ice's material properties, such that if the phase data is accurate, the variation in phase with distance inland of the grounding line could potentially differentiate between rheologies (i.e., n could be fit, rather than assumed).

4.4 Discussion

While our model for constraining the viscoelasticity of *in situ* ice is fairly rudimentary, our ability to get close to the expected value of effective viscosity using a few, somewhat unconstrained data points and a suboptimal suite of models is encouraging. In this section, we first focus on the expected accuracy of the material parameter estimates found by the approach outlined here. We then provide a blueprint for an ideal survey to collect data necessary to constrain rheological parameters of ice streams, including a discussion of the characteristic of an outlet glacier that would make that glacier a prime survey target.

4.4.1 Data Constraints and Accuracy

As only two data sets exist in the published literature quantifying the observed tidal phase shift from ice streams, quantifying the relative error within the current dataset is relatively straightforward. Gudmundsson (2006; 2007; 2011) used the MATLAB script *T_TIDE* (Pawlowicz et al., 2002) to solve for the phase delays in the Rutford Ice Stream GPS records over a range of tidal frequencies to an accuracy of about $\pm 8^\circ$.

Gudmundsson's GPS survey lasted for seven-weeks, providing several fortnightly periods and many dozens of diurnal and semidiurnal tidal periods. De Juan-Verger (2011) estimated the phase delay in the Helheim Glacier GPS network for the semidiurnal tide. The accuracy of the phase delay in those data ranged from $\pm 3^\circ$ to as much as $\pm 90^\circ$. The survey near the grounding line for Helheim Glacier only lasted for between 2 and 5 days, depending on the site location.

The error in the estimated ice Maxwell time is directly related to the error in the phase estimate. Due to the arctangent form of the phase as function of Deborah number, when the phase is close to either zero or ninety degrees, even a small error in the phase can result in several orders of magnitude in uncertainty in the estimated value of De . Conversely, when the measured phase is around 45° , the range in De for a given error in phase is small. For example, there is less than one order of magnitude change in De for phase shifts ranging from 15° to 75° .

Recall that our two-dimensional models all have a phase shift bounded between 0° and 90° relative to the forcing function. In both the observations of Rutford Ice Stream (Gudmundsson, 2006; 2007; 2011) and the viscoelastic three-dimensional models presented earlier in chapter 3, the phase of ice response was greater than 90° . Phases

greater than 90° cannot result from the two-dimensional models in this chapter but are seen in the three-dimensional viscoelastic models shown earlier in chapter 3. Thus, our two-dimensional models are necessarily over-simplifications to the phase behavior of ice streams. However, for a rough estimate of the viscoelastic properties, these two-dimensional models provide a general constraint on the rheology. A more accurate estimate of the viscoelastic material parameters would require the use of a three-dimensional viscoelastic model specific to the target glacier.

4.4.2 Survey Requirements

As the number of studies demonstrating a tidal phase delay is limited to only a handful, the collection of more data would aid in the understanding of *in situ* ice rheology. As such a study necessarily would focus on the surface response of a tidally-forced ice stream, the survey would be geodetic in nature. From our modeling, the most important phase constraint is the phase delay near the grounding line, where the stresses (and thus displacements) caused by the tides are at a maximum. In the case of an ice stream primarily constrained by its lateral margins, our work in chapters 2 and 3 suggests that a geodetic survey should remain within three ice stream widths of the grounding line. Farther inland, the tidal forcing is expected to be at least two orders of magnitude smaller than at the grounding line, which is likely too small to be detectable above the background ice velocity. Our modeling also suggests some lateral variation in the observable phase shift (see appendix 4A), especially for a nonlinear viscoelastic rheology. Therefore, we suggest that a grid pattern of geodetic stations would be an ideal deployment, as both the lateral and inland variations in phase shift would be recorded.

As the fitting of the tidal amplitudes and phases has been shown to be fairly rough (at best within a few degrees), the positional accuracy of the GPS survey is not expected to be an important concern relative to the error in fitting the tidal phase. Due to the rugged nature of the lowest reaches of many ice streams, deploying relatively inexpensive (perhaps even expendable) GPS stations is preferred as there is a nontrivial chance that any given station would be lost due to iceberg calving, crevassing, or some other potentially destructive ice process. Due to the inherent instability of the ice, using geodetic satellite observations would seem like a good alternative to on-ice geodetic stations. However, the repeat time between satellite orbits is probably too long to sufficiently resolve semidiurnal and, perhaps, the diurnal tides.

Another consideration would be the duration of the survey. Ideally, the survey would be as long as possible, as the longer the survey duration, the better the estimates of the periodicity and phase delay of the ice response would be. While the difference in the size of the errors between Gudmundsson (2006; 2007; 2011) and de Juan-Verger (2011) is not due to the difference in survey duration alone, the shorter survey of de Juan-Verger certainly does not help estimate the phase. Independent of the estimation errors, longer surveys provide the opportunity to use the longer period ocean tides as additional data points for fitting the phase in $\delta - De$ space. We recommend that a survey long enough to capture two full fortnightly periods would be a minimum survey duration for a rheologically motivated study.

Given the high rate of ice motion in ice streams and outlet glaciers, a one-month timeframe puts a limit on how close stations could be placed to the grounding line without the ice carrying the station past the grounding during the course of the

observation period. Assuming a maximum ice velocity of 11 km/yr (for Helheim Glacier, Thomas et al., 2000; Howat et al., 2005), the nearest to the calving front that a recording station for a month-long survey could safely be placed is about 850 meters inland. For ice streams with an attached ice shelf, while the GPS station would not be lost if carried past the grounding line, the nature of the station's phase response would necessarily change if the ice beneath it begins to float. Such a dramatic change in ice behavior could greatly increase the difficulty in interpreting the ice properties from the phase data.

Lastly, the methodology for determining viscoelastic properties discussed here only provides information about the relaxation time of the glacier, rather than an intrinsic value of either the effective viscosity or the Young's modulus. Recall that the viscosity for our test problem in section 4.3.3 could only be found by assuming the Young's modulus matched the laboratory value (from Petrenko and Whitford, 2002). However, as the density of ice is a well-constrained material property (e.g. Cuffey and Paterson, 2011), the acoustic wave speed within an ice stream can provide a constraint on the value of Young's modulus for ice independent of the phase delay. Glacial seismicity happens regularly enough to be used as a reliable source of acoustic waves in outlet glaciers. As a range of possible glacial earthquake sources have been suggested (e.g., Neave and Savage, 1970; VanWormer and Berg, 1973; Weaver and Malone, 1979; Wolf and Davis, 1986; Qamar, 1988, Anandakrishnan and Bentley, 1993; Anandakrishnan and Alley, 1997; Deichmann et al., 2000; Ekström et al., 2003; Stuart et al., 2005; Smith, 2006; O'Neel et al., 2007; Tsai and Ekström, 2007; Tsai et al., 2008), the best approach would be to have an array of seismic monitoring stations that could measure the relative arrival

time between stations of a wave, and thus estimate the wave speed independent of the source location. From the wave speed, the average ice density could then be used to determine the ice's elastic moduli. Such a seismic array would not need to be placed close to the grounding line, and a wide coverage might even be ideal due to the increased travel times of various waves increasing the accuracy of estimating ice's elastic parameters.

4.4.3 Ideal Survey Targets

Equally important as the survey configuration is the choice of glacier to target for a rheologically-motivated tidal phase study. From our analysis of simple models, as well as the results presented earlier in chapters 2 and 3, we propose a series of criterion for selecting a glacier most likely to provide data of a high enough quality to constrain *in situ* viscoelastic parameters. Such criteria include the type of glacier to study, the nature of the ocean-ice interaction, the geometric complexity of the target glacier, and the thermal characteristics of the glacier. Each of these selection characteristics will be discussed separately.

4.4.3.1 Glacier Type

Glaciers exhibit a wide range of geometries, sliding velocities, boundary conditions, and ice properties. Ice streams make a natural target for a tidal phase survey as these glacier have the benefits of being fast moving, of having large ice fluxes, and of all having continuous contact with the ocean. The rapid ice velocity makes distinguishing between the secular flow rate and a tidally-perturbed signal more straightforward than for an equivalent slow moving glacier. In cases where the rapid ice motion is due to low resistive stresses, we expect a larger region where the tidal perturbation is measurable

than for slower moving glaciers. The large ice flux also ensures that the glacier is always in contact with the ocean, such that the tidal interaction does not “turn off” as a function of time. Lastly, and perhaps most importantly, the surveys of Rutford Ice Stream and Helheim Glacier demonstrate that a phase lag on ice streams is measurable. Such may not be the case for other types of tidewater glaciers, where the existence of a tidal perturbation to ice motion, let alone the existence of a phase lag in that perturbation is not yet established.

4.4.3.2 Ocean-Ice Interaction

From the observations summarized in the introduction of chapter 2, glaciers can be grouped into three categories based on the glacier’s response to a tidal perturbation: little to no tidal response, measurable perturbation in the ice stream’s displacement, and stick-slip response to ocean tidal loading. Clearly, given the need for a signal and the desire to avoid unnecessary complications, the ideal target glacier would, the ideal target glacier resides in the second category. Such glaciers are expected to show a perturbation in surface displacement that varies smoothly in response to a change in tidal amplitude.

Additionally, the presence of an ice shelf is a key consideration in determining the interaction between an ice stream and the ocean tide. For a tidewater (i.e. shelf-free) glacier, the change in ocean tide acts only as a change in the water pressure acting on the glacier’s ocean-ward cliff. For a glacier with an attached shelf or tongue, the rise and fall of the ice shelf introduces flexural stresses on the glacier in the first five to ten kilometers (i.e., ice thicknesses) of the grounding line (as demonstrated in chapter 2, appendix 2A and observations in table 2.1). While our determination of the stress transmission length-scale of ice streams shows that the tidal stress can influence ice

stream motion farther inland than ice flexure will for a wide enough glacier, the added flexural stresses of an ice shelf will influence the value of the stress-dependent effective viscosity, complicating the determination of the ice viscosity. The 2007-2008 data from de Juan-Verger's (2011) study of Helheim Glacier demonstrates that an ice shelf is not a critical factor in determining the phase shift between an ice stream and the ocean tide, we suggest that a target glacier should not have an ice shelf.

4.4.3.3 Geometric Complexity

Glaciers span a wide range of morphologies, from being a single linear feature to being a meandering convergence zone of multiple glacial streams. A prime target glacier would be nearly linear and sourced from a single region of ice. From a geometric perspective, a complex flow field is expected to differ from our simple, linear models due to the geometry alone. Additionally, if a glacier is made up of multiple ice sources coalescing into a single flow near to the grounding line, the possibility of rheological variations across its profile becomes greater. Such lateral variations could influence the phase shift seen on the ice stream, such that the estimated viscoelastic parameters are representative of neither ice constituent but rather some bulk average. While such a result is not wrong *per se*, the apparent viscoelastic parameters would be useful only to that one system and could not be used as a general measurement of *in situ* glacial ice rheology.

Glaciers also can be underlain by deformable till (soft bedded) or by undeformable rock (hard bedded). The two-dimensional models in this chapter and the three-dimensional models in chapter 3 demonstrate that the choice of boundary condition acting on the glacier is important to determining the precise phase-shift due to the rheology. While both soft and hard bedded glaciers are likely to have boundary-specific

modifications to the phase shift that need to be distinguished from rheological effects, the added material of the subglacial till in soft bedded glaciers presents an additional constitutive law necessary to understand any observed phase shift. Thus, soft bedded glaciers are more complex than their hard bedded counter parts, leading us to suggest that an ideal test glacier would be hard bedded.

4.4.3.4 Thermal Complexity

Glaciers fall into two categories based on the nature of the temperature of the ice: isothermal warm glaciers and polythermal cold glaciers. As discussed in chapter 3, the ice streams of Antarctica (and Greenland) are definitively polythermal, with basal temperatures as much as twenty degrees warmer than the surface temperatures. Most other glaciers on Earth, by their nature of being much smaller, are isothermal, with the ice at the melting temperature throughout the glacier. As ice viscosity is strongly temperature dependent (e.g., Nye, 1953; Jezek et al., 1985; Budd and Jacka, 1989; MacAyeal et al., 1996; 1998) and ice elasticity weakly temperature dependent (Jellinek and Brill, 1956), an ideal target glacier would be isothermal, where the confounding effects of temperature could be avoided.

4.4.3.5 Ideal Target Selection

Using the above criteria, we compile a list of ice streams in table 4.4 that would be potential targets for a rheologically-motivated GPS survey. This table focuses on major ice streams and outlet glaciers in a range of environments, including: Bindschadler Ice Stream, Ekstrom Ice Shelf, Kamb Ice Stream, Pine Island Glacier, Thwaites Glacier, Whillans Ice Plain (Antarctica); Helheim, Kangerdlussuaq, Jakobshavn Isbrae glaciers (Greenland); Columbia and LeConte glaciers (Alaska). Among these major ice streams,

there is not a single “perfect” target glacier. The best targets are Columbia Glacier, Alaska and Helheim Glacier, Greenland due to confirmed tidal interactions, rapid ice motions, a lack of an ice shelf, and the confining nature of these fjord-bounded glaciers.

Of special importance is that these ice streams have no ice shelves, as shelf-less glaciers have a much simpler tidal forcing configuration and thus a less involved calculation of the tidal phase. An ice shelf adds the complications of ice flexure and grounding line migration to the tidal perturbation of ice velocities. Detailed modeling work of the interplay between the grounding line and ice shelves demonstrates that the stress and deformations of glaciers near the grounding line are inexorably tied to these shelf behaviors (e.g., Schoof, 2007a/b; Goldberg et al., 2009; chapter 2 of this thesis). Ultimately, we suggest that the single strongest selection criterion should be the presence (or lack) of an ice shelf.

4.5 Summary and Conclusions

In this chapter, we outlined a methodology for inferring the viscoelastic properties of an ice stream from the phase shift in the ice stream’s response to the forcing of the ocean tides. From our modeling, a phase delay is expected when the value of De falls between 10^{-3} and 10^1 . While the models used here to calibrate the relationship between phase and rheology are simple two-dimensional models, our ability to use these models in conjunction with observations from Helheim Glacier to estimate a reasonable value of viscosity suggests that using the phase lag to invert for the *in situ* material properties of ice could produce meaningful results. While more detailed analysis is beyond the scope of this work, we outline a potential observational campaign to constrain ice rheology. Lastly, while the previous two chapters discussed ways in which the tidal loading of ice

have been modeled inappropriately, this chapter highlights the potential use of the short-timescale geodetic observation of ice stream's response to ocean tides to constrain the viscoelastic properties of natural glacial ice.

| | Variable Names | Units |
|--------------------------|---|--------------------------------|
| <i>A</i> | Viscoelasticity coefficient | $\text{Pa}^{-n} \text{s}^{-1}$ |
| <i>De</i> | Deborah number | -- |
| <i>J*</i> | Complex creep modulus | Pa^{-1} |
| <i>J₁</i> | Real part of <i>J*</i> | Pa^{-1} |
| <i>J₂</i> | Imaginary part of <i>J*</i> | Pa^{-1} |
| <i>L_{tr}</i> | Transmission length-scale | km |
| <i>n</i> | Power law exponent | -- |
| <i>T_F</i> | Forcing function period | s |
| <i>T_{Burg1}</i> | Burgers relaxation time (Maxwell element) | s |
| <i>T_{Burg2}</i> | Burgers retardation time (Kelvin element) | s |
| <i>T_{Kelv}</i> | Kelvin retardation time | s |
| <i>T_{Max}</i> | Maxwell relaxation time | s |
| <i>T_R</i> | Relaxation time (general) | s |
| <i>t</i> | Time | s |
| <i>δ</i> | Phase delay | ° |
| <i>ε</i> | Strain | -- |
| <i>ε*</i> | Complex Strain | -- |
| <i>ε₀</i> | Strain amplitude | -- |
| <i>η</i> | Linear viscosity | Pa s |
| <i>η₁</i> | Maxwell element viscosity (Burgers body) | Pa s |
| <i>η₂</i> | Kelvin element viscosity (Burgers body) | Pa s |
| <i>μ</i> | Shear modulus | Pa |
| <i>μ₁</i> | Maxwell element shear modulus (Burgers body) | Pa |
| <i>μ₂</i> | Kelvin element shear modulus (Burgers body) | Pa |
| <i>ν</i> | Poisson's ratio | -- |
| <i>σ</i> | Stress | Pa |
| <i>τ₀</i> | Stress amplitude | Pa |
| <i>ω</i> | Frequency | s^{-1} |
| " · " | Indicates time derivate | |

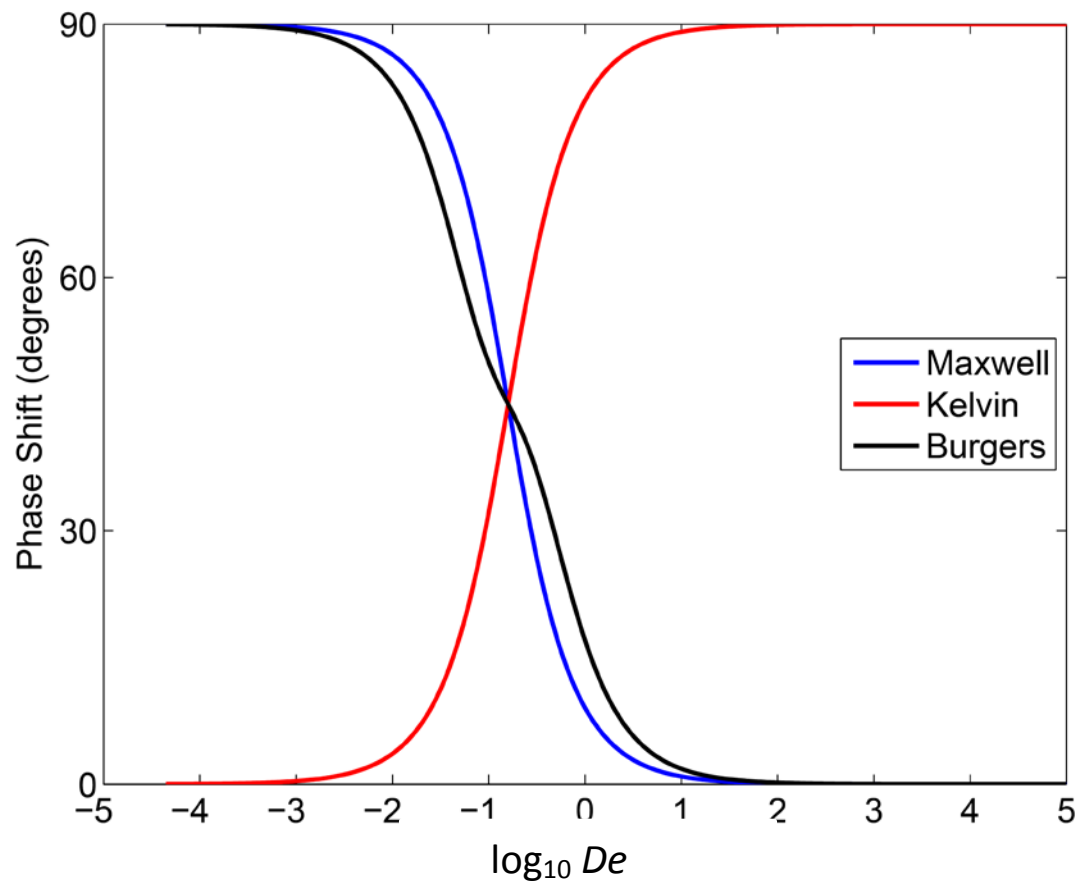


Figure 4.1: Diagram showing the phase delay in the response of a one dimensional Maxwell (blue), Kelvin (red), and Burgers (black) viscoelastic element, as a function of the Deborah time of that model.

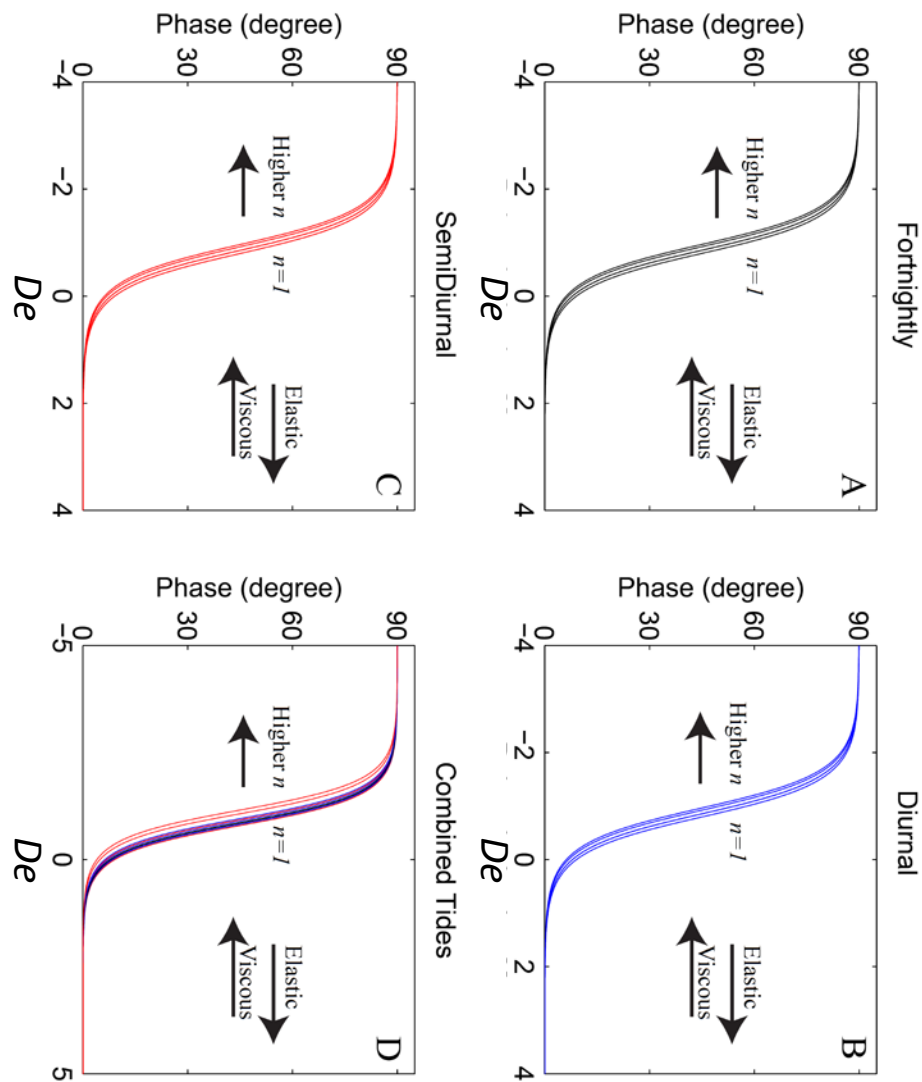


Figure 4.2: Phase shift for linear and nonlinear Maxwell models over a range of forcing frequencies and rheologies. Panel A shows results for the fortnightly tide (black), panel B the diurnal tide (blue), panel C (red), and panel D the combined tide (all three colors). In all cases, the lines represent increasing values of n from right to left. Values in table 4.2 are collected from figure 4.2D, and will aid in distinguishing the different behaviors of each tidal signal as part of the combined tide.

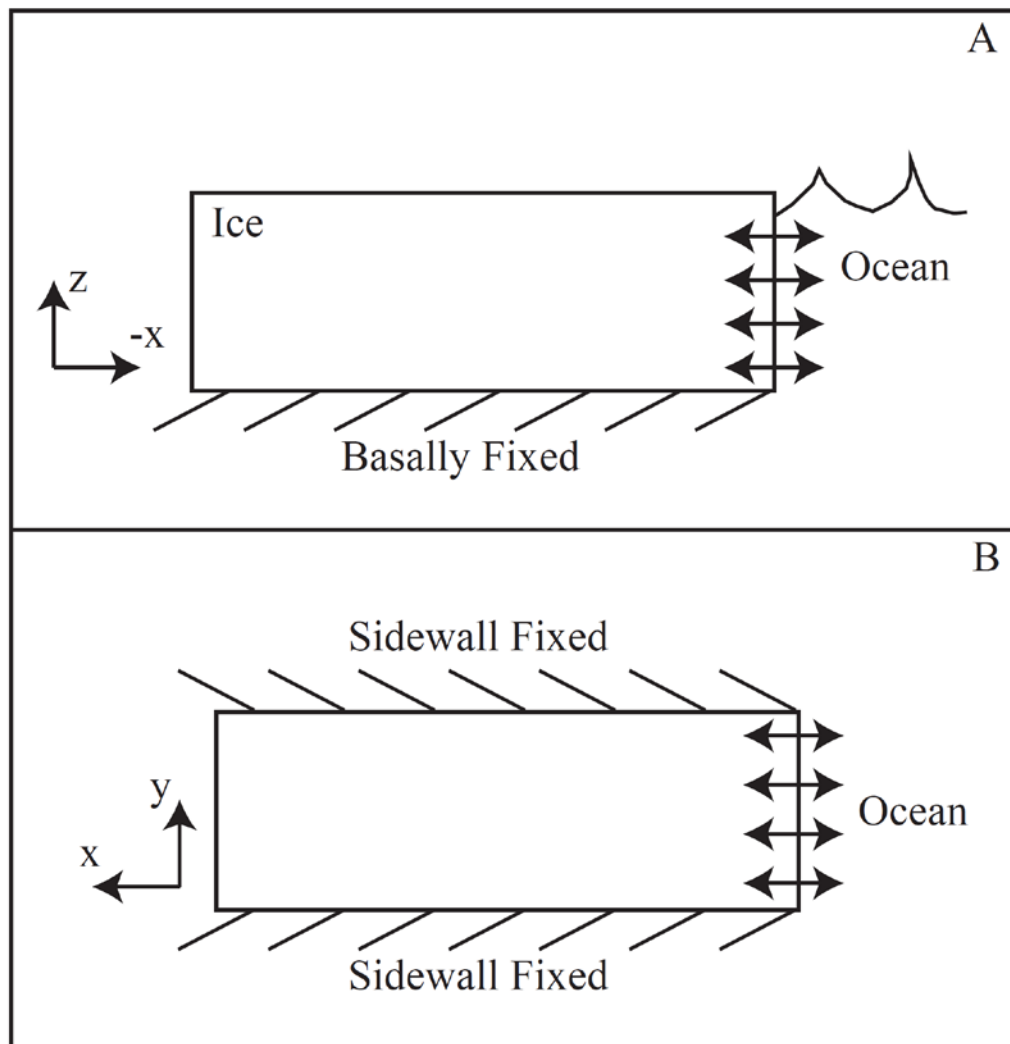


Figure 4.3: Schematic diagrams of the two model configurations for our finite element models. Panel A shows a vertical cross-sectional view of a model ice stream that is fixed at its bed. Panel B shows a map view of an ice stream that is fixed on each lateral margin. The arrows show the location of the applied tidal forcing function.

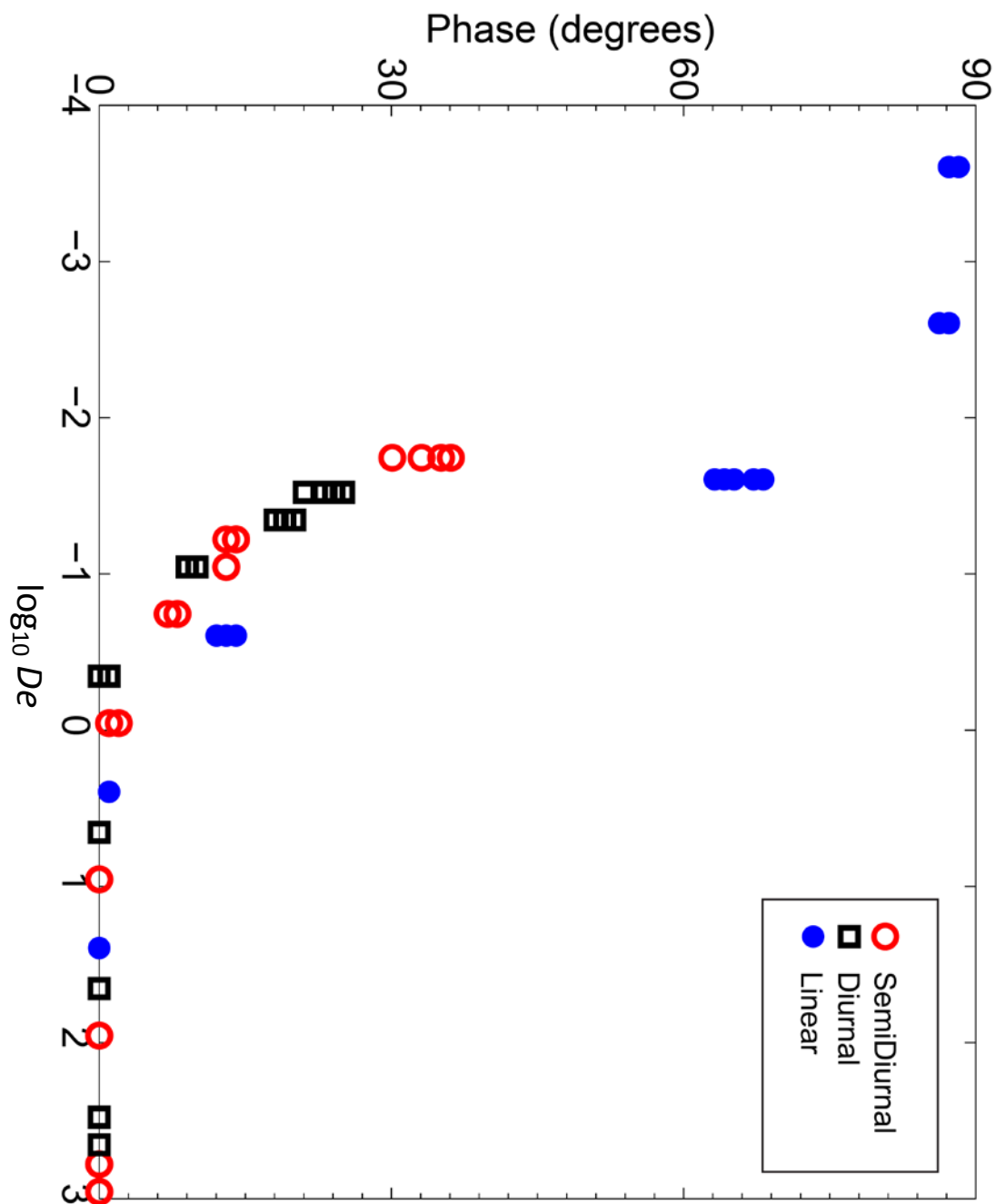


Figure 4.4: Modeled phase shift results for our models fixed at the bed (see figure 4.3A).

The filled blue circles show the results for a linear Maxwell model, while the red circles and black squares show results for a nonlinear Maxwell model with $n=3$ forced by a semidiurnal and diurnal tide, respectively.

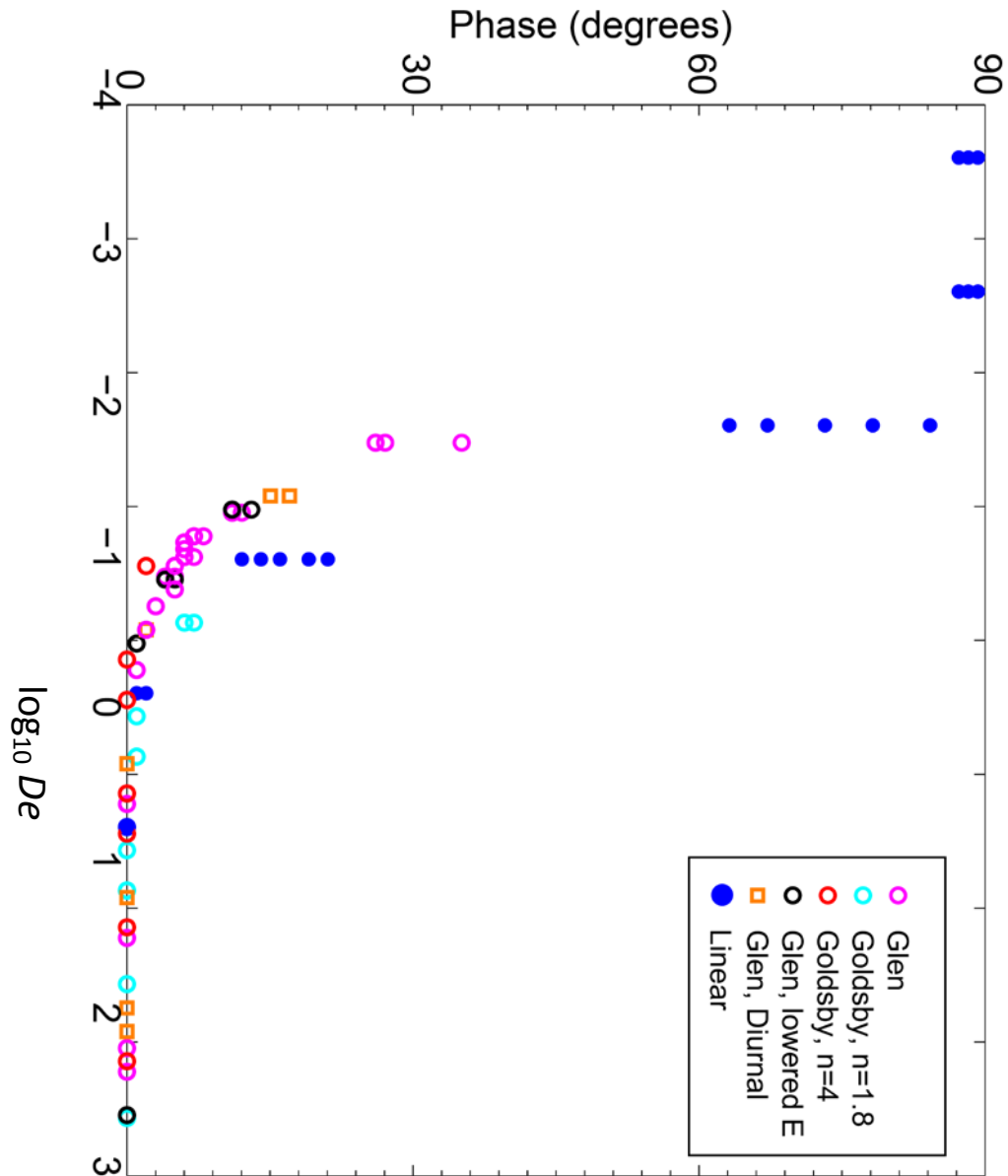


Figure 4.5: Modeled phase shift results for our models fixed on the side walls (see figure 4.3B). The filled blue circles show the results for a linear Maxwell model, while all the open circles represent nonlinear models forced with a semidiurnal tide and all squares represent nonlinear models forced with a diurnal tide. The colors correspond to a Glen rheology (pink, black, and orange), a Goldsby rheology with $n=1.8$ (light blue), and a Goldsby rheology with $n=4$ (red).

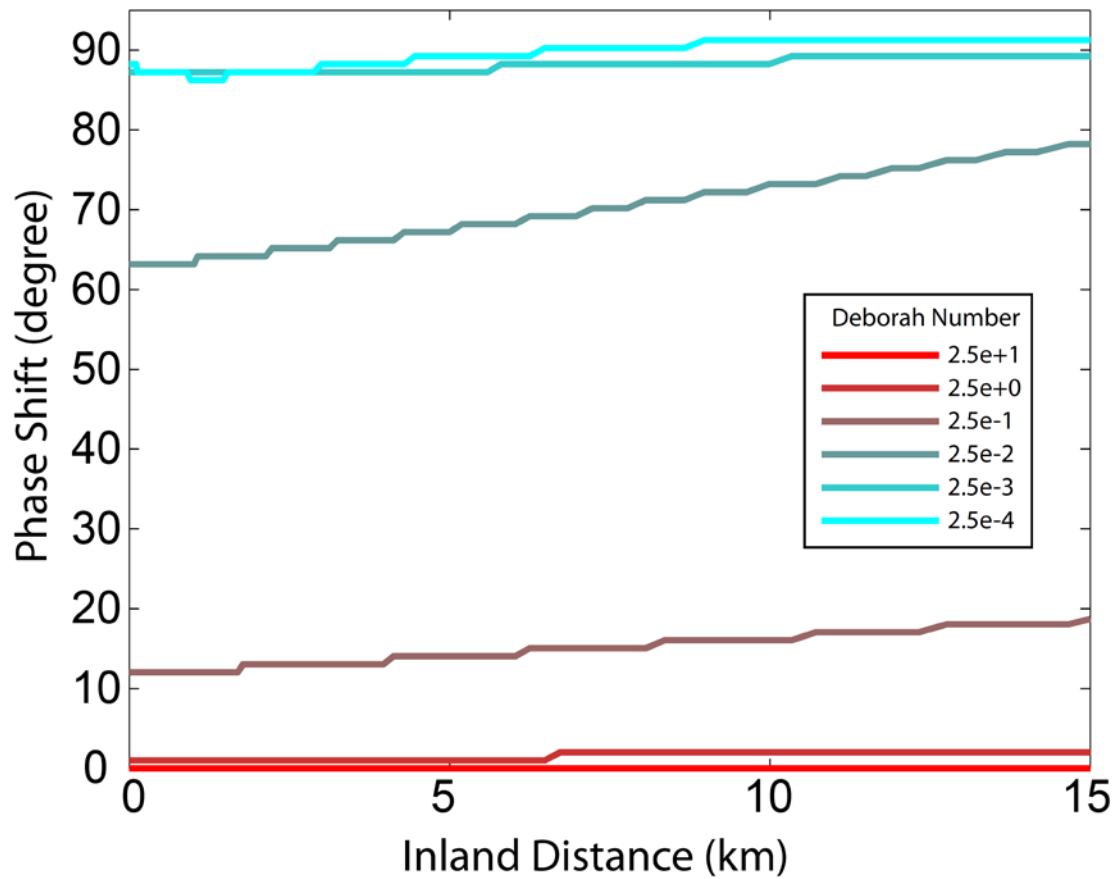


Figure 4.6: Distance dependence of the phase shift for basally-locked models at a range of Deborah numbers. The redder colors represent more elastic models (higher De) while the bluer colors represent more viscous models (lower De).

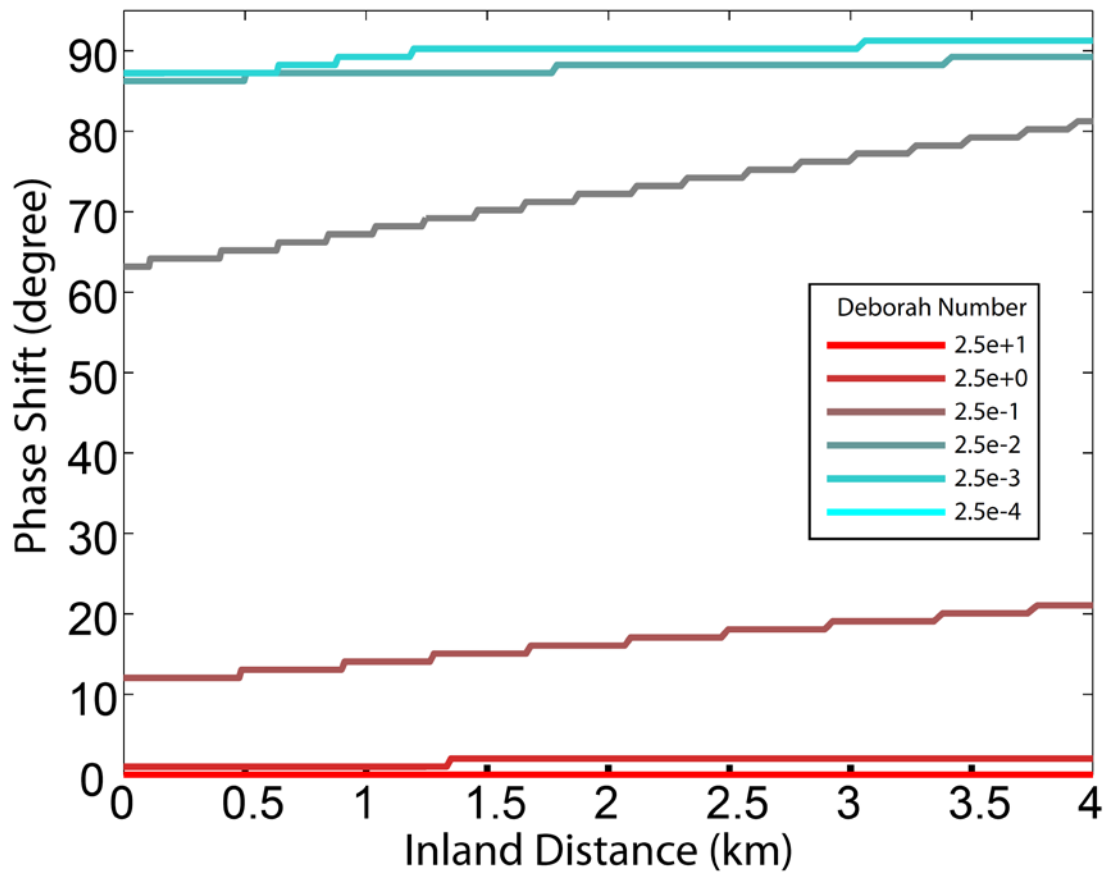


Figure 4.7: Distance dependence of the phase shift for laterally-locked models at a range of Deborah numbers. The redder colors represent more elastic models (higher De) while the bluer colors represent more viscous models (lower De).

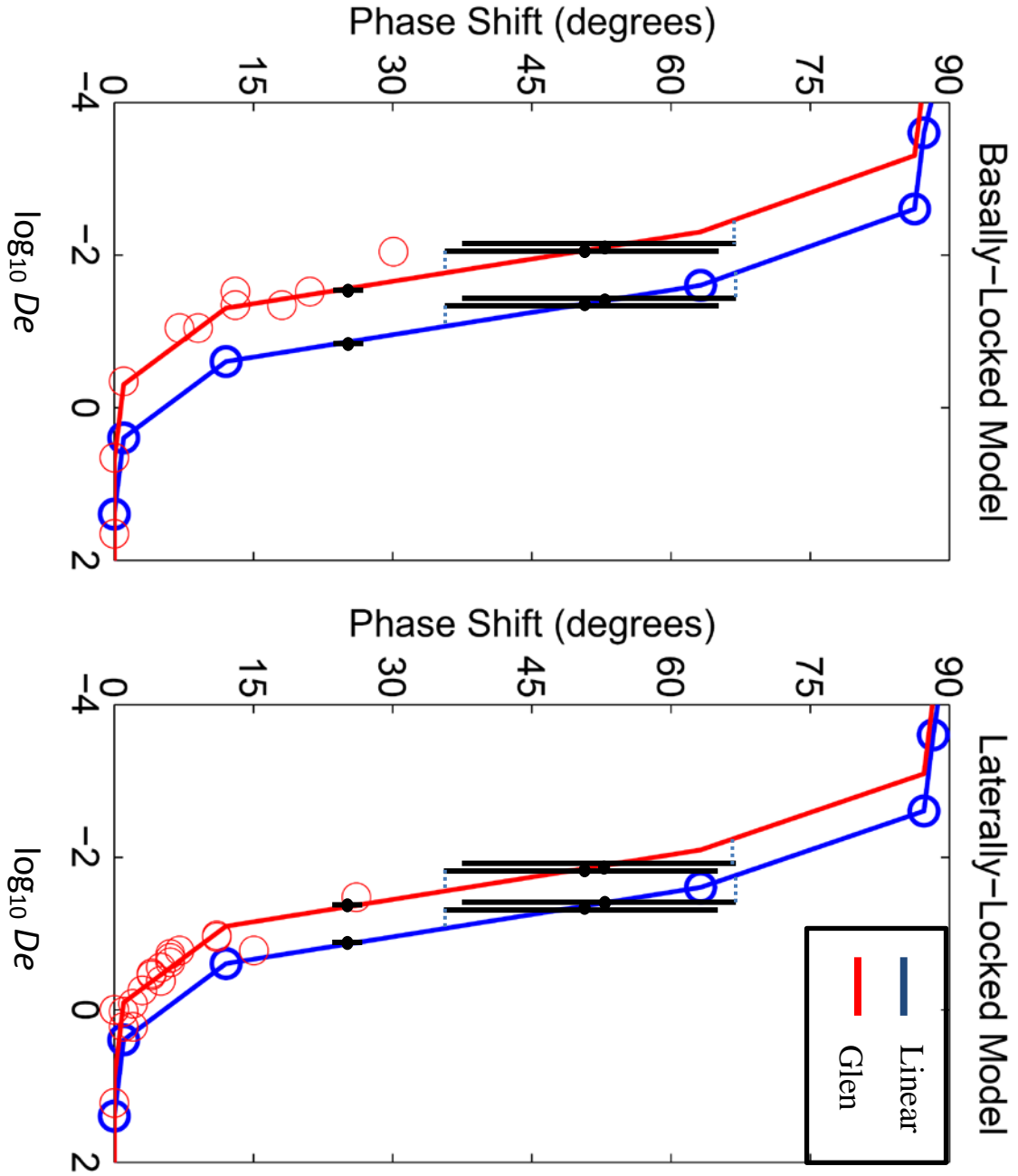


Figure 4.8: Fitting results for the data from Helheim Glacier (see section 4.3.3). The blue line is a linear fit, while the red line is an extrapolated version of the Glen flow fit. Finite element model results are shown as open circles. The data from Helheim Glacier are the solid black points, with error bars shown as the black lines. The values of the fit are tabulated in table 4.3.

| | J_1 | J_2 | Relaxation Time | Retardation Time |
|---------|--|--|--|------------------------|
| Maxwell | $\frac{1}{\mu}$ | $\frac{1}{\eta\omega}$ | $\frac{\eta}{\mu}$ | N/A |
| Kelvin | $\frac{\mu}{\mu^2 + (\eta\omega)^2}$ | $\frac{\eta\omega}{\mu^2 + (\eta\omega)^2}$ | N/A | $\frac{\eta}{\mu}$ |
| Burgers | $\frac{1}{\mu_1} + \frac{\mu_2}{\mu_2^2 + (\eta_2\omega)^2}$ | $\frac{1}{\eta_1\omega} + \frac{\eta_2\omega}{\mu_2^2 + (\eta_2\omega)^2}$ | $\frac{p_1 \pm \sqrt{p_1 - 4p_2}}{2p_2}$ | $\frac{\eta_2}{\mu_2}$ |

Table 4.1: Complex creep modulus real (J_1) and imaginary components (J_2), material relaxation and retardation time (where applicable) for a Maxwell, Kelvin, and Burgers model in one dimension. The placeholder variables used in the Burgers relaxation time correspond to: $p_1 = \left(\frac{\eta_1}{\mu_1} + \frac{\eta_2}{\mu_2}\right)$ and $p_2 = \left(\frac{\eta_1 \eta_2}{\mu_1 \mu_2}\right)$.

| | | 15° | 30° | 45° | 60° | 75° |
|-----------|-------------|-------|-------|-------|-------|-------|
| $n = 1$ | Semidiurnal | -0.23 | -0.56 | -0.80 | -1.04 | -1.37 |
| | Diurnal | -0.23 | -0.56 | -0.80 | -1.04 | -1.37 |
| | Fortnightly | -0.23 | -0.56 | -0.80 | -1.04 | -1.37 |
| $n = 1.8$ | Semidiurnal | -0.36 | -0.69 | -0.93 | -1.17 | -1.50 |
| | Diurnal | -0.26 | -0.59 | -0.83 | -1.07 | -1.40 |
| | Fortnightly | -0.26 | -0.59 | -0.83 | -1.07 | -1.40 |
| $n = 3$ | Semidiurnal | -0.50 | -0.82 | -1.07 | -1.31 | -1.64 |
| | Diurnal | -0.32 | -0.66 | -0.90 | -1.13 | -1.47 |
| | Fortnightly | -0.29 | -0.63 | -0.85 | -1.09 | -1.43 |
| $n = 4$ | Semidiurnal | -0.59 | -0.92 | -1.16 | -1.40 | -1.73 |
| | Diurnal | -0.39 | -0.72 | -0.96 | -1.20 | -1.53 |
| | Fortnightly | -0.29 | -0.63 | -0.87 | -1.10 | -1.44 |

Table 4.2: Logarithmic values of the Deborah number at a selection of phase shift values

for the combined tidal solutions shown in figure 4.2D. Note that the phase shift behaves the same for the tidal forcing frequencies with a value of $n = 1$, and the value varies between the other solutions for nonlinear viscosity models.

| | Linear Base | Glen Base | Linear Wall | Glen Wall |
|-----------|-------------|-----------|-------------|-----------|
| 24 | 5.83 | 1.16 | 5.83 | 2.12 |
| 27 | 5.07 | 1.01 | 5.07 | 1.84 |
| 30 | 4.42 | 0.882 | 4.42 | 1.60 |
| 38 | 3.13 | 0.625 | 3.13 | 1.14 |
| 53 | 1.57 | 0.313 | 1.57 | 0.569 |
| 68 | 0.624 | 0.125 | 0.624 | 0.227 |
| 40 | 2.85 | 0.569 | 2.85 | 1.04 |
| 55 | 1.73 | 0.285 | 1.73 | 0.519 |
| 70 | 0.507 | 0.101 | 0.519 | 0.184 |

Table 4.3: Summary of the effective viscosities calculated for the Helheim Glacier using data from de Juan-Verger (2011). The columns correspond to the linear and Glen models for the basely-locked model (figure 3.8A) and the laterally-locked model (figure 3.8B). The data correspond to the data points from de Juan-Verger (2011) described in section 4.3.3 in bold, with the upper and lower error bars calculated as well. Each value is in terms of 10^{13} Pa · s.

| | Ice Velocity | Tidal Interaction | Ice Shelf | Geometry | Basal Character | Thermal Profile |
|----------------------------|---------------------|-------------------------|-----------|--|--------------------|--------------------|
| Bindschadler Ice Stream | 300- 800 m/yr | Continuous Motion | Yes | Wide and flat | Till | Poly. |
| Ekstrom Ice Shelf | 250+ m/yr | None at 3 km inland | Yes | Narrow and flat | ? | Poly. |
| Kamb Ice Stream | 20-50 m/yr | Seismic evidence | Yes | Wide and flat | Till | Poly. |
| Pine Island Glacier | 2 km/yr | None at 55 km inland | Yes | Narrow and flat | Till | Poly. |
| Thwaites Glacier | 2 km/yr | ? | Yes | Narrow and flat | Till | Poly. |
| Rutford Ice Stream | 400- 700 m/yr | Continuous Motion | Yes | Narrow and flat | Till | Poly. |
| Whillans Ice Plain | 300- 800 m/yr | Stick-slip | Yes | Wide and flat | Till | Poly. |
| Kangerdlussuaq | 5 km/yr | ? | Variable | Narrow and steep | Rock | Poly. |
| Helheim | 8-11 km/yr | Continuous Motion | Variable | Narrow and steep | Rock | Poly. |
| Jakobshavn Isbrae | 4-8 km/yr | ? | Yes | Narrow and steep, tributary glaciers bend | Rock | Poly. |
| Columbia Glacier | 2+ km/yr | Continuous Motion | No | Narrow and flat | Till | ? |
| LeConte Glacier | 4+ km/yr | Continuous Motion | No | Narrow and flat, with bend | Rock | ? |

Table 4.4: Summary of target glacier characteristics for a range of Antarctic, Greenland, and Alaskan glaciers. The columns show the ice velocity, the tidal behavior, the presence of an ice shelf, a brief summary of the geometry, the nature of the ice stream's bed, and

the temperature profile of the ice stream. For temperature, poly. refers to polythermal glaciers. References for most glaciers are summarized in chapter 1. References for Thwaites, Columbia, and LeConte glaciers are: Krimmel and Vaughn, 1987; Walters and Dunlap, 1987; Walters, 1989; Humphrey et al., 1993; Meier et al., 1994; O'neel et al., 2001; 2003; Rignot et al., 2002; Shepherd et al., 2002.

Appendix 4A: Spatial Distribution of Phase Shift

This appendix lists nine figures demonstrating the spatial distribution of the value of phase shift in the laterally-locked models. The first five figures (4A.1 to 4A.5) shows the phase shift for linear viscoelastic models at progressively smaller De . The other four figures show model results for the nonlinear viscoelastic models with the smallest De (and thus the largest spatial variability). Figures 4A.6 and 4A.7 show Glen model results, figure 4A.8 shows results for a Goldsby rheology with $n=1.8$, and figure 4A.9 shows phase shifts for a Goldsby rheology with $n=4$.

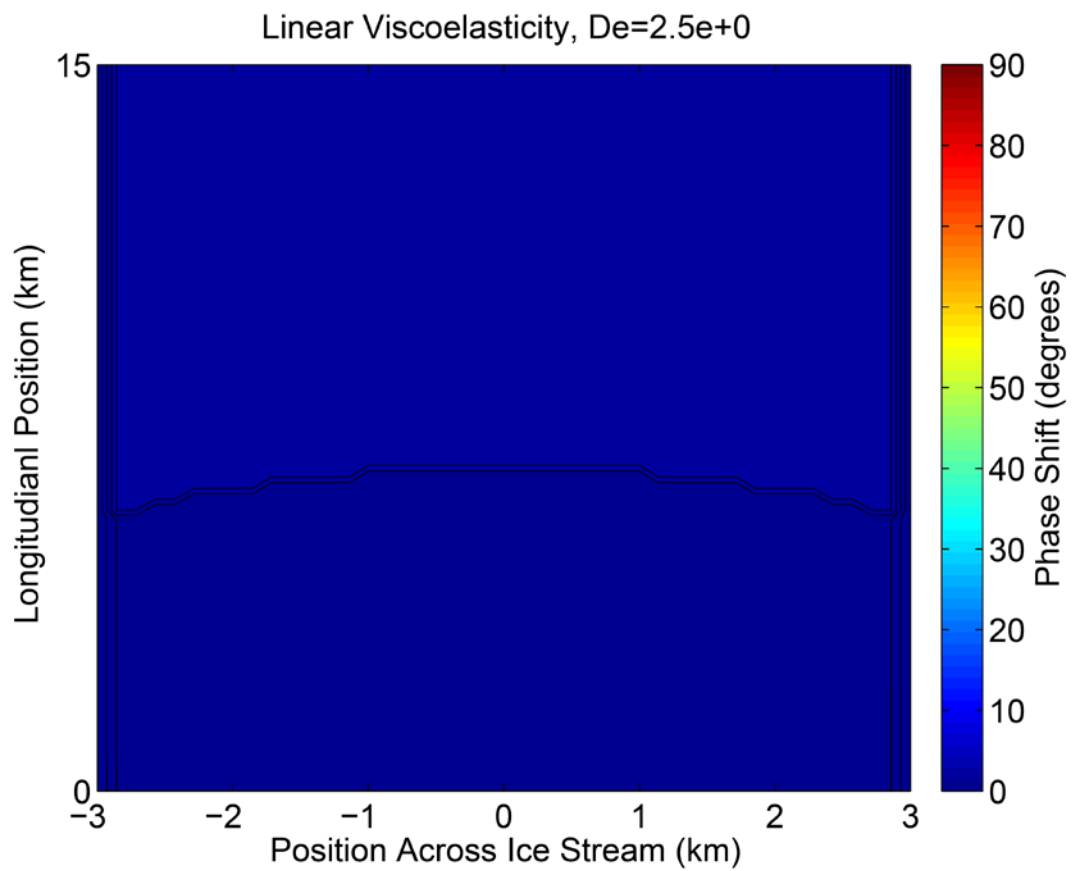


Figure 4A.1: Phase shift distribution for a linear viscoelastic model with $De = 2.5e0$

$\text{Pa} \cdot \text{s}$.

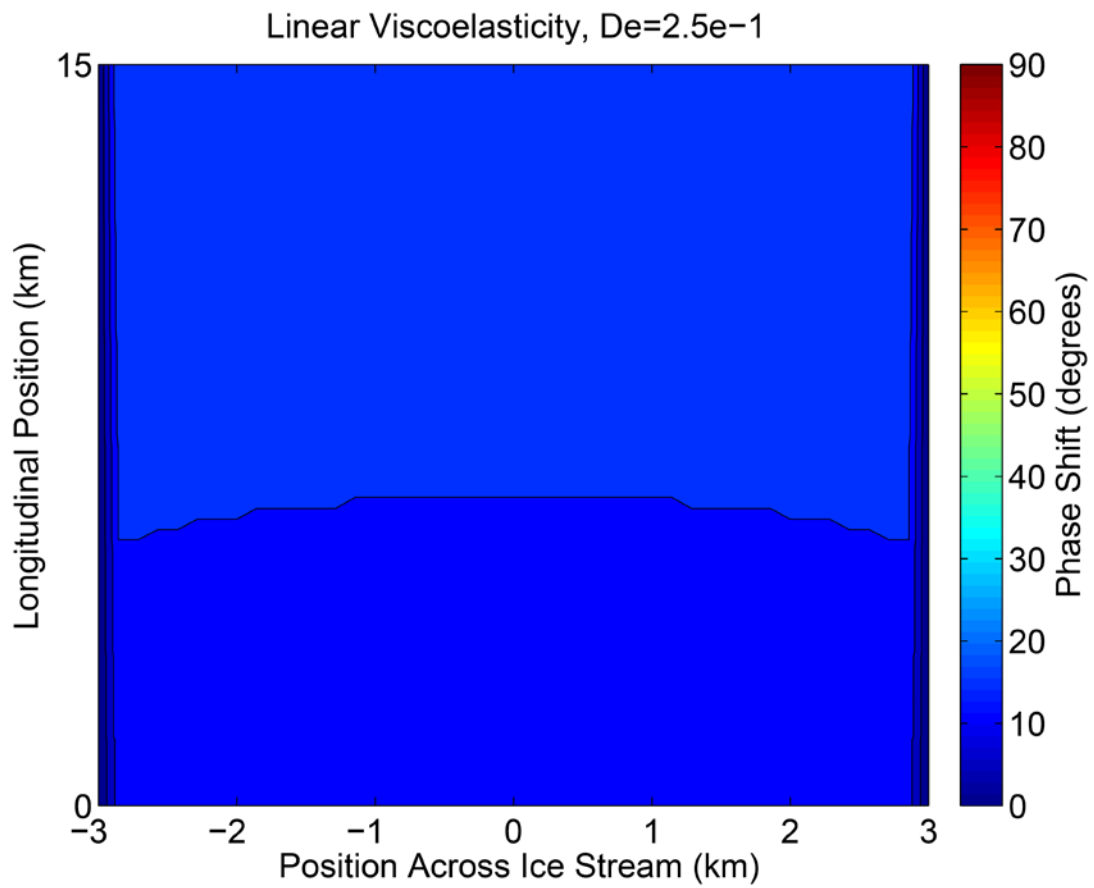


Figure 4A.2: Phase shift distribution for a linear viscoelastic model with $De = 2.5e-1$
 $\text{Pa} \cdot \text{s}$.

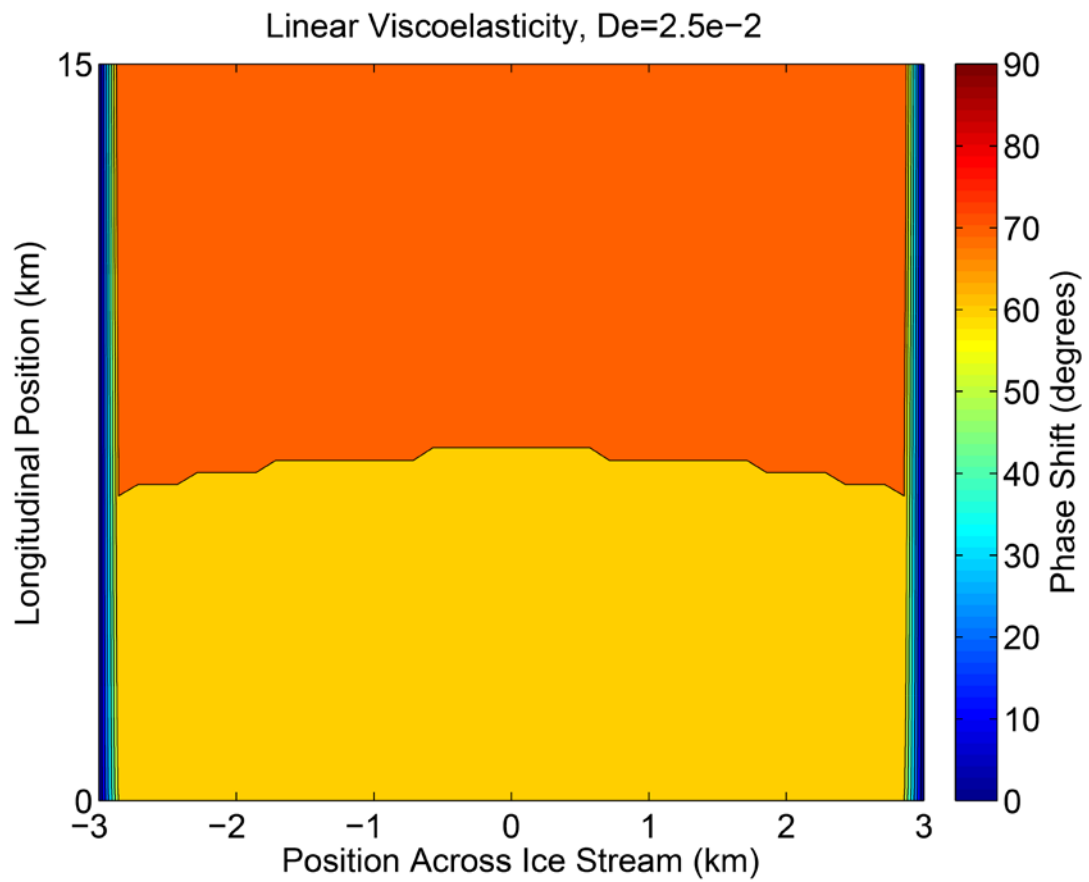


Figure 4A.3: Phase shift distribution for a linear viscoelastic model with $De = 2.5e-2$

Pa · s.

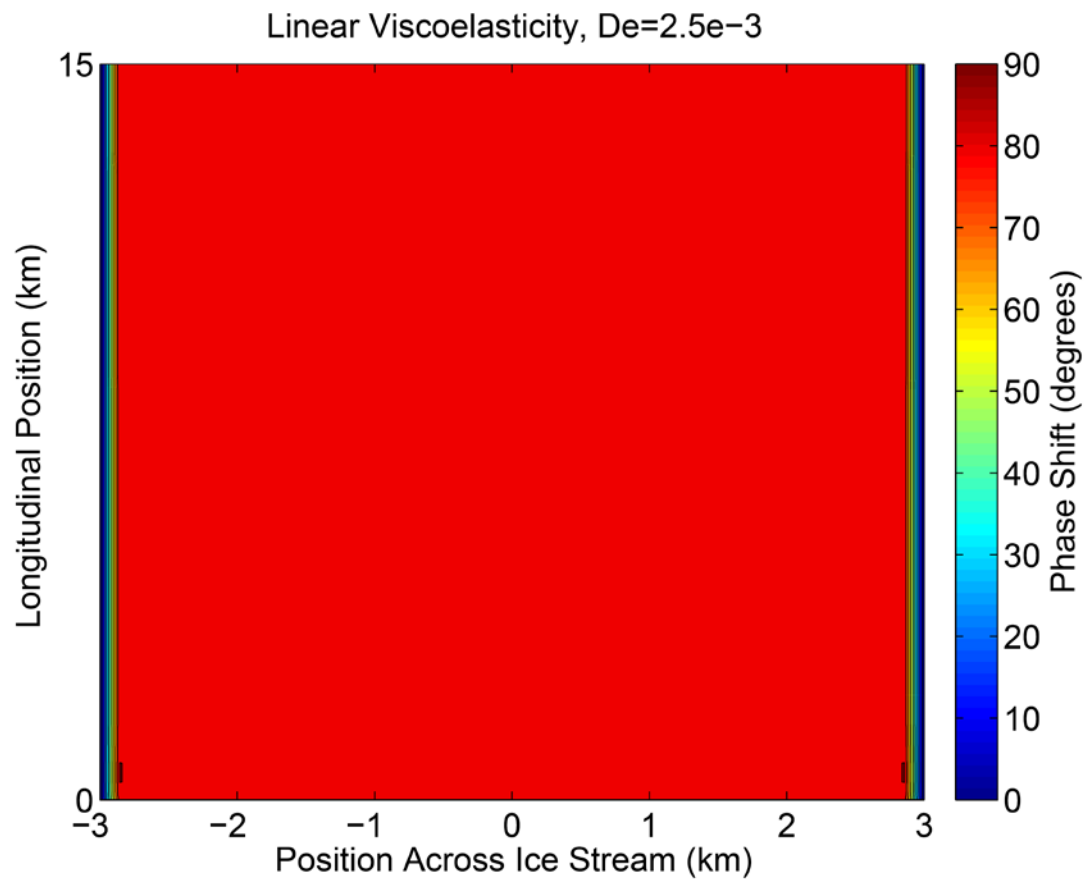


Figure 4A.4: Phase shift distribution for a linear viscoelastic model with $De = 2.5e-3$

Pa · s.

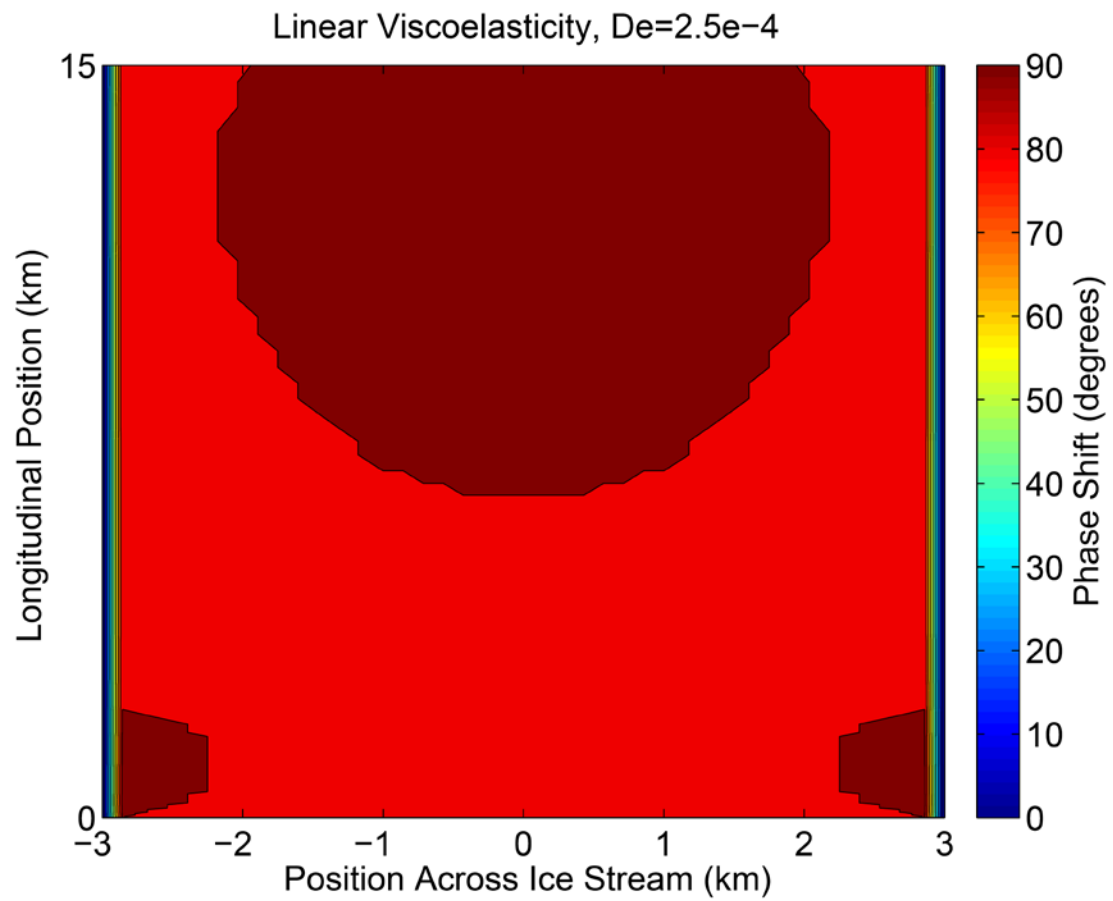


Figure 4A.5: Phase shift distribution for a linear viscoelastic model with $De = 2.5e-4$

$\text{Pa} \cdot \text{s}$.

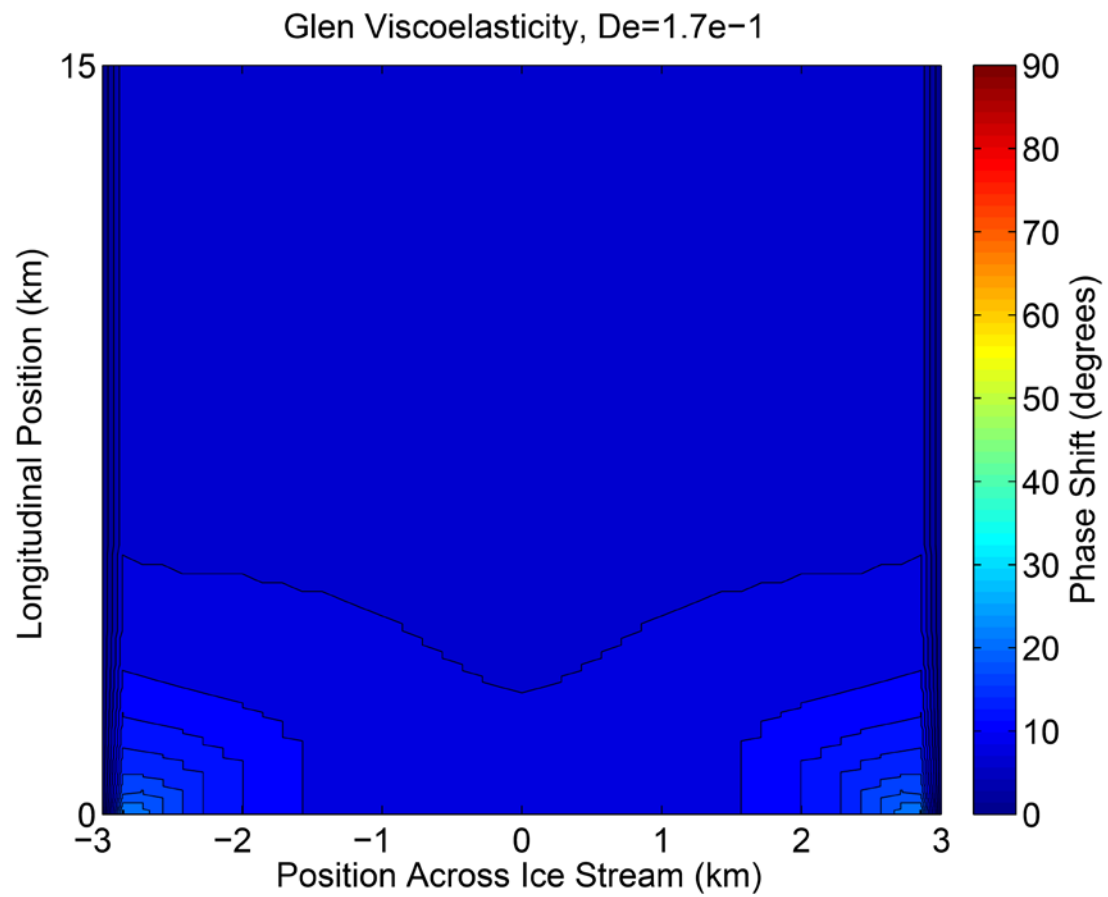


Figure 4A.6: Phase shift distribution for a Glen viscoelastic model ($n=3$) with $De = 1.7e-1 \text{ Pa} \cdot \text{s}$.

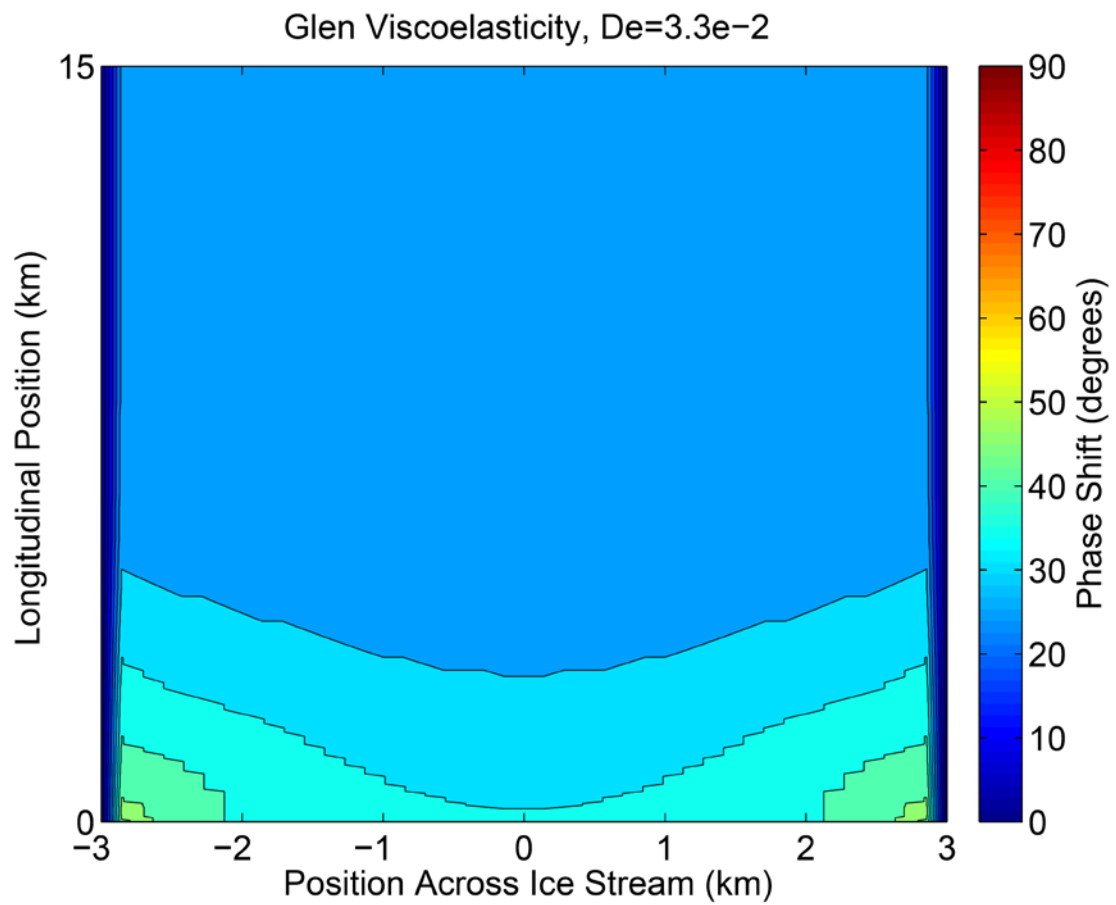


Figure 4A.7: Phase shift distribution for a Glen viscoelastic model ($n=3$) with $De = 3.3e-2$ Pa \cdot s.

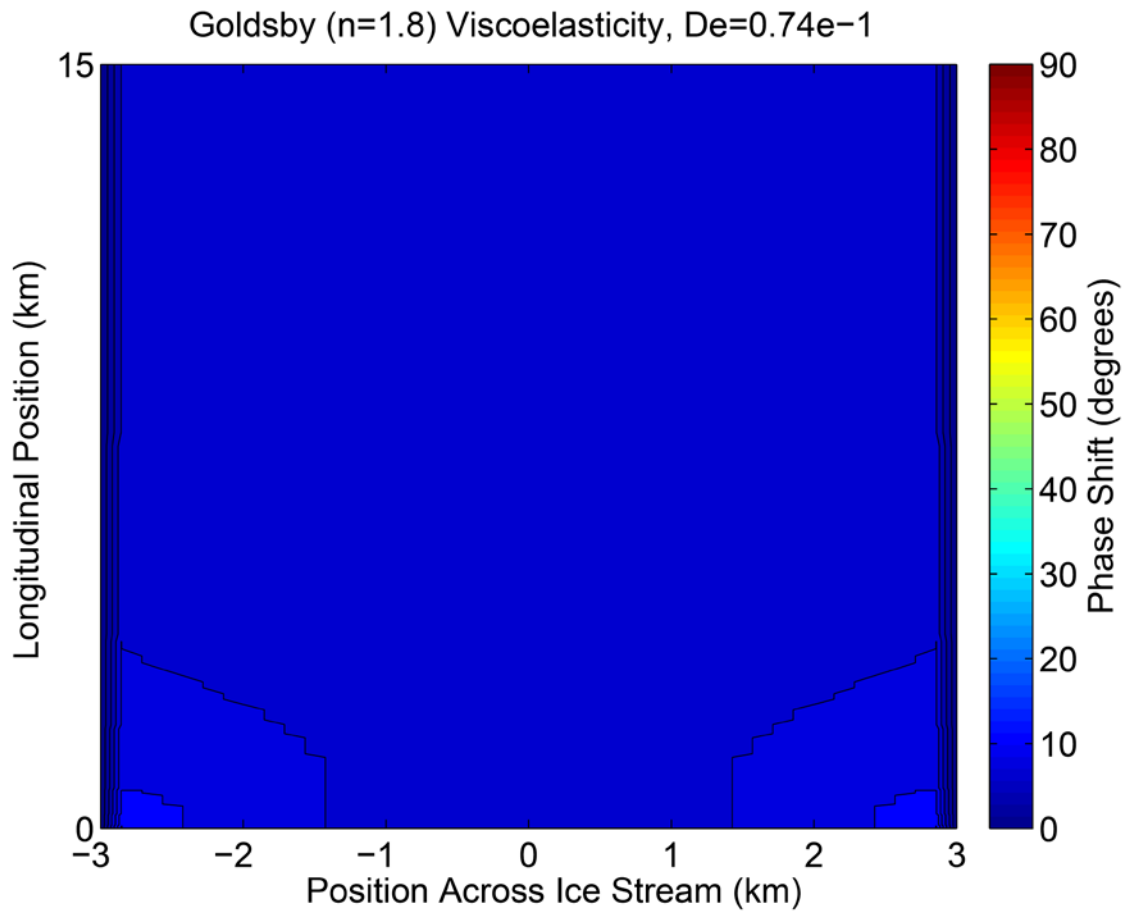


Figure 4A.8: Phase shift distribution for a Goldsby viscoelastic model ($n=1.8$) with $De = 0.74e-1 \text{ Pa} \cdot \text{s}$.

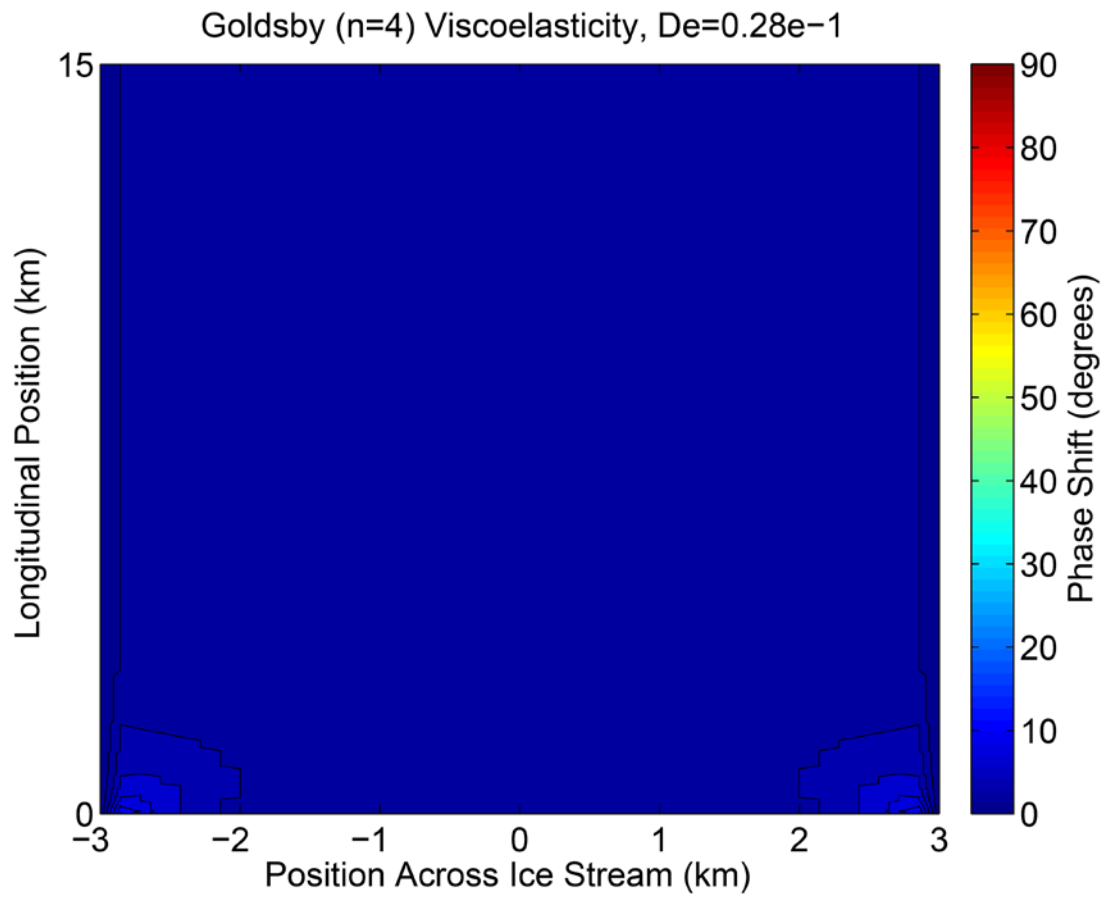


Figure 4A.9: Phase shift distribution for a Goldsby viscoelastic model ($n=4$) with $De = 0.28e-1$ Pa \cdot s.

Chapter 5

Viscoelastic Effects during the Drainage of a Supraglacial Meltwater Lake

Meltwater lakes are seasonal features on the surface of some glaciers, appearing when there is bountiful surface melting. These lakes can reach several kilometers in diameter and can hold over one million cubic meters of water. As observed by Das et al. (2008), once these lakes begin to drain to the glacier's bed, they can drain completely over the course of a few hours. During these drainage events, the drainage rates can rival that of major waterfalls. In this work, we expand the turbulent hydraulic fracture model of Tsai and Rice (2010, 2012) to include ice viscoelasticity. We first present a direct adaptation of Tsai and Rice's semi-analytic model using an effective stress formulation for linear viscoelasticity (after Kojic and Bathe, 1987; Aagaard et al., 2011). We then use finite element models to investigate the effects of applying a more appropriate nonlinear viscoelastic ice rheology for a stationary basal crack. The solutions of the nonlinear models become increasingly similar to the linear solutions at long crack lengths, where the ice above the basal crack begins to behave in a beam-like manner. By fitting our nonlinear solutions with equivalent linear solutions at multiple crack lengths, we define an evolution law for an effective linear viscosity approximating the nonlinear viscosity. The solution for such a "pseudo-nonlinear" viscoelastic model diverges strongly from the linear models at crack lengths longer than a few ice thicknesses. However, while our

models over-predict the lake drainage rates compared to observations, the impact of viscoelasticity, linear or otherwise, is at best a few percent different from comparable elastic models for rapid drainage events of supraglacial lakes with a radius of a few kilometers.

5.1 Introduction

Summer meltwater lakes are ephemeral features on the surfaces of large glaciers and ice sheets. While such lakes can grow to considerable size—up to three kilometers across and several meters deep (e.g., Das et al., 2008; Krawczynski et al., 2009)—once connected to the subglacial hydrologic network, these lakes can drain completely over the span of only a few hours. As these lakes can hold millions of cubic meters of water, the draining lake water perturbs the movement of the overriding ice during and immediately following the pulse of water reaching the glacier's base. While the impact of a single lake drainage event is short-lived, research suggests that the combined effect of a full season of lake drainages can increase the overall flow rate of glacier and may be an important process on the Greenland Ice Sheet (Zwally et al., 2002; Parizek and Alley, 2004; Bartholomew et al., 2011; Hoffman et al., 2011; Palmer et al., 2011). The supraglacial lake drainage phenomenon provides a powerful natural laboratory for investigating the link between ice deformation and basal hydrology.

A dichotomy exists in the duration of supraglacial lake drainage events. Based on field observations, the drainage can either occur slowly over many days (e.g., Raymond and Nolan, 2000) or can last only a few hours (e.g., Box and Ski, 2007; Das et al., 2008; Selmes et al., 2011). These two types drainage event occur through distinct drainage

processes, such that there is not a continuum between fast and slow drainage events. Slow draining lakes use preexisting supraglacial hydrologic features (spillways, moulins, etc.) as pathways for water to reach the glacier's bed and thus also use the subglacial hydrologic system. Rapid drainage events, in contrast, commence when the weight of the supraglacial lakewater fractures the ice down to the glacier's bed, creating a conduit that drains the entire lake's volume to the bed in a few hours. Such a process will overwhelm the preexisting subglacial hydrological network.

This chapter focuses on modeling the transient behavior of the drained water upon reaching the bed of a glacier but before the fluid diffuses beneath the glacier to such an extent that the natural subglacial hydrologic network can accommodate the water. For perspective, while we focus only on the rapid lake drainage events here, the occurrence of rapid lake drainage events are somewhat rare, ranging from less than 1% to 25% of all lake drainage events across Greenland, depending on the region studied (Selmes et al., 2011).

The observation motivating this work is a meltwater lake drainage event observed by Dal et al. (2008) on the Greenland Ice Sheet near Jakobshavn Isbrae in July of 2006. This event represented the best observed event to date. Over the month of July, a meltwater lake with a volume of about $4.4 \times 10^7 \text{ m}^3$ of water formed on the glacier's surface. This lake proceeded to drain completely into the ice sheet in less than 1.5 hours, causing about a meter of uplift and lateral translation at a GPS monitoring station located 1.7 kilometers away from the main drainage conduit. Shortly after the lake finished draining, the displacement signal began to decay from its peak value and fell to a constant offset from the original position after about 2.5 hours. Prior to drainage, a crack about 3

kilometers long and 0.5 meters wide appeared near the lake, suggesting that this crack may have triggered the drainage event by connecting the lake to the subglacial hydrologic network.

To date, the mathematical modeling of these drainage events is somewhat limited. Most models focus on the conditions necessary to drive a pulse of surface water to the bed of the ice sheet (e.g., Alley et al., 2005; Krawczynski et al., 2009) or the conditions within the supraglacial lake (e.g., Tedesco et al., 2012), rather than investigating the diffusion of the fluid beneath the ice sheet once the water reaches the bed. Tsai and Rice (2010, 2012) model the drainage of the lake as a fluid-filled crack propagating horizontally along the base of an elastic ice sheet. The models of Tsai and Rice predict that a sizeable basal crack (5-10 kilometers in length) is necessary to accommodate the draining water, but are unable to accurately match the magnitude of the observed surface displacement from Das et al. (2008).

While viscoelasticity has not been investigated for the lake drainage problem, the research discussed in the previous chapters suggests that viscoelasticity may be important during processes on hourly to weekly timescales. For example, viscoelasticity has been cited as a necessity in the modeling of the tidal loading of Antarctic ice streams (e.g., Anandakrishnan and Alley, 1997; Gudmundsson 2006; 2007; 2011; Walker et al., 2012) and our own work has demonstrated that viscoelasticity is important for determining the timing of an ice stream's response to a tidal load. Despite the timescale for lake drainage being only about two hours, we find a Maxwell relaxation time of similar magnitude for our loading stresses of approximately 10^6 Pa ($\tau_{max} = \frac{\eta_{eff}}{E} \approx 10^2 - 10^3$ s). As the

Maxwell relaxation time is within a few orders of magnitude of the duration of lake drainage events, we expect measureable viscoelastic effects during such drainage events.

We present results from both linear and nonlinear viscoelastic modeling of the drainage of a supraglacial lake, using the hydraulic crack propagation model of Tsai and Rice (2012) as the basis for our work. We modify the model of Tsai and Rice (2012) using an effective stress formulation for linear viscoelasticity after Kojic and Bathe (1987) and Aagaard et al. (2011). We then compare these linear results to equivalent finite element models using nonlinear viscoelasticity, finding that these nonlinear solutions can be approximated using a variable (effective) linear viscosity. We end with a comparison of our model results to the field observations of the July 2006 lake drainage event observed by Das et al. (2008).

5.2 Model Methodology

This section discusses the model methodology used throughout this chapter. The opening subsection begins with a discussion of the approach of Tsai and Rice (2010; 2012) for modeling the opening of a crack at the base of a glacier that is filled with a turbulent fluid. Additionally, we highlight the modifications necessary to apply a linear viscoelastic rheology to the material surrounding the crack. In the next subsection, we discuss the hybrid Chebyshev/series minimization method used to find our model solutions. The methods section closes with a discussion of the finite element models used to explore the importance of using a nonlinear viscoelastic rheology for ice.

5.2.1 General Model for Turbulent Hydraulic Fracture

We model the supraglacial lake drainage system as a two-dimensional water-filled crack of length $2L$ at the base of an impermeable viscoelastic (ice) body of thickness H above a similarly viscoelastic half-space, as shown in figure 5.1A. The crack grows as a function of time, as long as the fluid pressure at the drainage conduit is greater than the hydrostatic overburden pressure in the basal conduit. Our model unknowns are the crack opening (w), the excess fluid pressure compared to overburden pressure (p), and the fluid velocity (U) that satisfy the appropriate fluid flow, conservation, fracture, and rheological equations. As previously mentioned, our methodology only varies from Tsai and Rice (2012) in our choice of rheology.

The Reynold's number of the fluid flow in our model is $Re \approx 10^6 m^{-1} \cdot L$, suggesting turbulent flow in cracks longer than ~ 10 cm. As we expect a much longer basal crack, we adopt the turbulent flow model of Manning and Strickler (Manning, 1891; Strickler, 1923; Strickler, 1981) using the Darcy-Weisbach friction factor of $f = f_0(k/w)^{1/3}$ where f_0 is a reference value of f and k is the Nikuradse roughness height (Rubin and Atkinson, 2001; Gioia and Chakraborty, 2006; Tsai and Rice, 2010; 2012). The resulting fluid flow relationship is:

$$-\frac{\partial P}{dx} = \begin{cases} -\frac{f_0 \rho U^2}{4} \frac{k^{1/3}}{w^{4/3}} & \text{for } x > 0 \\ \frac{f_0 \rho U^2}{4} \frac{k^{1/3}}{w^{4/3}} & \text{for } x < 0 \end{cases} \quad (5.1)$$

where ρ is the fluid density and x is the horizontal dimension. The conservation of mass for an incompressible fluid, when applied within the basal crack, requires:

$$\frac{\partial wU}{\partial t} + \frac{\partial w}{\partial t} = 0 \quad (5.2)$$

For the growth of our mode I crack, we assume the fracture criterion to be:

$$K_I = K_{IC} = 0 \quad (5.3)$$

Justification for setting the critical fracture intensity equal to zero is provided in Tsai and Rice (2010; 2012).

For our rheological law, we use the effective stress formulation for linear viscoelasticity (Kojic and Bathe, 1987; and Aagaard et al., 2011; see Appendix 5A) to modify the elasticity equations of Erdogan et al. (1973). This new viscoelastic rheological relationship is:

$$0 = -\sigma_{XZ} = \int_{-L}^L \left[\left(\frac{1}{s-x} + k_{11} \right) \frac{\partial u}{\partial s} + k_{12} \frac{\partial w}{\partial s} \right] ds \quad (5.4A)$$

And

$$-4\pi p(x)S_{VE} = \int_{-L}^L \left[k_{21} \frac{\partial u}{\partial s} + \left(\frac{1}{s-x} + k_{22} \right) \frac{\partial w}{\partial s} \right] ds \quad (5.4B)$$

where σ_{XZ} is the two-dimensional shear stress, S_{VE} is the vertical normal component of the consistent viscoelastic tangent compliance modulus (fully defined in appendix 5A), and the k_{ij} 's are coefficients taken from Erdogan et al. (1973).

The initial and boundary conditions used to close these four equations are:

$$\begin{aligned} p(0, t) &= p_I \\ w(L, t) &= 0 \end{aligned} \quad (5.5)$$

$$U(L, t) = U_{tip} = \frac{dL}{dt}$$

where p_I is the inlet pressure at the conduit base and U_{tip} is the fluid velocity at the crack tip. These three conditions ensure that the pressure at the center of the crack is held constant (and is assumed to be equal to the weight of the water in the conduit minus the ice overburden pressure), the crack is closed at and beyond the crack tip, and that the fluid motion at the crack tip is the same as the propagation velocity of the crack tip itself, such that there is always fluid in the crack tip region. Later in this chapter, the value of the pressure at the crack center will be modified to reflect the variability of the inlet pressure as a function of conduit size and fluid height.

5.2.2 Solution Method

To solve the conservation equations, we use the hybrid Chebyshev/series-minimization scheme detailed in Tsai and Rice (2012). First, the conservation equations are non-dimensionalized using the relations shown in Table 5.1. We then take $\hat{p}(\hat{x}, \hat{t})$ and $\hat{w}(\hat{x}, \hat{t})$ as:

$$\begin{aligned} \frac{\hat{p}(\hat{x}, \hat{t})}{D} = & \sum_{k=0}^{2N} a_k p_k(\hat{x}) = a_0 p_0(\hat{x}) + \sum_{k=1}^N a_{2k-1} [c_{2k-1} - |\hat{x}|^{2k-1}] \\ & + \sum_{k=1}^N a_{2k} [c_{2k} - U_{2k}(\hat{x})] \end{aligned} \quad (5.6)$$

and

$$\frac{\hat{w}(\hat{x}, \hat{t})}{D} = \sum_{k=0}^{2N} a_k w_k(\hat{x}) = a_0 \left(\frac{1 - \hat{x}}{2} \right)^{6/7} + \sum_{k=1}^{2N} a_k w_k(\hat{x}) \quad (5.7)$$

where U_{2k} are Chebyshev polynomials of the second kind; c_k and D are fitted parameters such that w_k and p_k satisfy equations 5.3 and 5.4; and a_k will be solved for later. Note

that our formulation of viscoelasticity requires a modification to Tsai and Rice's fitting method for the parameters c_k and D . To account for the time-variable effective Young's modulus introduced by our viscoelasticity model, the force component F_{21} of equation 7.100 in Erdogan et al. (1973) is set equal:

$$\begin{aligned} F_{21} &= -\frac{\pi}{2} p_I S_{VE} && \text{dimensional} \\ \hat{F}_{21} &= -\frac{\pi}{2} \hat{S}_{VE} && \text{non-dimensional} \end{aligned} \quad (5.8)$$

Propagating this change through all our equations, we now solve for the coefficients c_k and D and then combine equations 5.1 and 5.2 using an implicit (backwards Euler) scheme to approximate the time derivative of w , such that :

$$\left. \frac{-(\sum_k a_k w_k)^{10/3}}{a_0^{4/3}/7} \frac{\partial(\sum_k a_k p_k)}{\partial \hat{x}} \right|_{t_1} = \left[\int_{\hat{x}}^1 \frac{\sum_k a_k w_k|_{t_1} - \sum_k a_k w_k|_{t_0}}{\hat{t}_1 - \hat{t}_0} \right] \quad (5.9)$$

where t_0 is the current timestep and t_1 is the next timestep. Note that the initial solution is found using the self-similar solution of Tsai and Rice (2010). Equation 5.9 satisfies the fluid flow requirements within the crack as the crack lengthens as a function of time. This equation closes the system of equations necessary to solve for the coefficients a_k that minimize the error between the two sides of this equation, under the added constrain that $\hat{w}(\hat{x}, \hat{t})$ must remain nonnegative. A variable timestep is chosen to be equal to the time required for the crack length to change by 5%.

To determine the impact of viscoelasticity on our model's solution, we compare our viscoelastic results to those found using the purely elastic rheology of Tsai and Rice (2012). We note that at each timestep, the value of S_{VE} changes and thus the ratio of viscous to elastic deformation changes. The variability in S_{VE} implies that the final result

must be found by iteratively changing the crack length. The derivation of S_{VE} and its physical interpretation are discussed in appendix 5A.

5.2.3 Nonlinear Viscoelasticity and Finite Element Implementation

Ice is traditionally modeled using the nonlinear Glen flow equation (Glen, 1955; 1958) for viscous deformation, rather than the Newtonian fluid equation discussed and implemented above. Unfortunately, though an equivalent stress form of a nonlinear viscoelastic material exists (e.g., Kojic and Bathe, 1987; Aagaard et al., 2011), such a formulation cannot be used to represent ice in our semi-analytic model as S_{VE} would be a function of $p(x)$ and thus x . The field equations from which we derive our equation 4 require the separation of the material moduli from the spatial derivatives of the displacements (see Erdogan and Gupta, 1971), such that a problem with spatial variable moduli cannot be solved explicitly in our current framework. Thus, we use to a finite element version of our analytic models to explore the impact of using a more physically representative nonlinear viscoelastic rheology for ice.

We use the program *PyLith* for our finite element analysis (Williams et al., 2005; Williams, 2006; Aagaard et al., 2007; 2008). Figure 5.1B shows a schematic of our finite element version of the lake drainage problem. Only half of the crack (length-wise) is modeled due to the symmetry across the crack's central axis. The ice body has a domain above the crack of thickness $H=1\text{ km}$, a domain below the crack with a thickness much greater than H to approximate a half-space, and a region of uncracked ice at least $5L$ long. To define unique upper and lower surfaces of our crack, an offset Δh separates the two edges, where $\Delta h \ll w$. These models use a three-dimensional "pseudo-plane-strain"

mesh, where there is a finite thickness in the third dimension but the displacements in this direction are set equal to zero. This approach is equivalent to assuming the problem is infinite in the third dimension.

In our finite element analysis, we do not iteratively lengthen our crack, but instead use a crack of known length and a pressure distribution taken from our linear viscoelastic results to determine what the expected nonlinear viscoelastic crack opening would be. Thus, the fluid equations (equations 5.1 and 5.2) are not satisfied for this static finite element formulation of the viscoelastic model, as the value of w increases with time. However, where the viscous crack opening is small compared to the elastic crack opening, the effect on the overall surface deformation of not accounting for the time-dependent viscous opening on the pressure distribution is negligible.

The total model time is equal to the timestep in the linear viscoelastic model at the same crack length. Note that while the timestep varies slightly with varying viscosity in the linear model, all timesteps are chosen from the model with $\eta = 1e11 \text{ Pa} \cdot \text{s}$. For the models shown here, the model-averaged error in the speed of crack propagation introduced by using the timestep calibrated to a single linear rheology can be as high as 5%, with increasing errors for models with viscosities increasingly different from our reference model. Such an error is deemed acceptable, as an iterative scheme coupling the fluid flow, mass conservation, and fracture equations to the finite element model output for a nonlinear rheological model is beyond the scope of this work.

The applied boundary conditions in the finite element model are equivalent to those used in the analytic model with a few extra conditions where required by the finite element method. Along the crack of length L , the pressure distribution $p(x \geq 0)$ from

the linear viscoelastic model of the same crack length is applied to both sides of our crack as a normal traction. The nodes at (and beyond) the crack tip are held to have zero displacements in all directions. We ensure the symmetry of our solution by fixing u along the nodes above and below the center of the crack. The base of the half-space domain is held fixed, with zero displacements in all directions.

5.3 Model Solutions

In this section, we present solutions from our semi-analytic linear viscoelastic models and from our finite element nonlinear viscoelastic models. The first subsection summarizes the linear viscoelastic model results, focusing on the relative importance of the viscous component of deformation over the evolution of the drainage crack. The second portion of this section discusses the results of our nonlinear models, comparing these nonlinear results to the linear model output. Lastly, the final subsection describes a method for approximating the nonlinear viscoelastic behavior of ice using a time-variable viscosity in our linear semi-analytic model.

5.3.1 Linear Viscoelastic Results

The motivation behind implementing a linear viscoelastic rheology is to quantify the variation between the viscoelastic and elastic solutions to our lake drainage model, and to determine if using a viscoelastic model is necessary to reproduce the Greenland observations. Our model explored a range of viscosities between $\eta = 1e12 \text{ Pa} \cdot \text{s}$ and $1e11 \text{ Pa} \cdot \text{s}$, as these bracket the magnitude of the nonlinear crack openings discussed in the next section (5.3.2). For comparison, such viscosities also match the range of

published linear viscosities for ice under similar strain-rates and stresses (e.g., Jellinek and Brill, 1956; Reeh et al., 2003). Note that only the most representative model results are plotted here and that the figures discussed in this section also have results for our “pseudo-nonlinear” model, which will be discussed later in section 5.3.3.

Figure 5.2A shows the dimensionless pressure and crack opening at several crack lengths for the elastic and end-member viscoelastic models. Only at the longest crack length ($L/H=5$) do any noticeable variations in pressure exist between the models, though even at $L/H=5$ the difference between models is modest. For the dimensionless crack opening (figure 5.2B), there are substantial deviations between the elastic and viscoelastic solutions starting at a crack lengths of $L/H>1$, with even a slight variation as early as a crack length of $L/H=0.5$.

These snapshots of \hat{w} suggest that the viscous deformation becomes more important as the crack length increases. To further explore this effect, figure 5.3A compares the time rate of change of the crack opening for a viscoelastic ($\eta = 1e12 Pa \cdot s$) and an elastic model and figure 5.3B shows the elastic and viscoelastic deformation for these models as functions of crack length. Both the elastic and viscoelastic models predict increasing deformation rates with increasing crack length, but the viscoelastic model predicts a higher rate of deformation than is seen in the elastic model. Thus, as the basal crack grows, there should be an increase in the relative amount of viscous crack opening.

Lastly, the scaled velocity $\phi = \frac{U_{TIP}}{U_S}$ increases at longer crack lengths compared to the expected rate from the $L^{1/6}$ dependence of U_S alone (see Figure 5.4). At a crack

length of $L/H=5$, the value of the scaled velocity is about 6 times the scaled velocity at a crack length of $L/H=0.02$. This strong dependence of ϕ on crack length was first reported by Tsai and Rice (2012). Our results demonstrate that viscoelasticity further increases the dependence of the scaled velocity on the crack length. Additionally, decreasing the viscosity in the viscoelastic model increases the value of ϕ at a given crack length. The inset portion of figure 5.4 shows the expected variation between the viscoelastic and elastic solutions to longer crack lengths. As with the crack opening, the relative difference between solutions increases over crack lengths of interest, though the relative crack velocity does asymptotically approach a constant value at very long and very short crack lengths.

In summary, our linear viscoelastic models predict increased crack opening, crack opening rates, and crack propagation speeds than the elastic model. The differences between the two rheologies become important at a crack length roughly equivalent to the ice sheet thickness, with viscoelasticity becoming increasingly important at longer cracks.

5.3.2 Nonlinear Viscoelastic Results

Having demonstrated that the viscoelastic solution deviates from the elastic solution, especially for crack lengths that approach and surpass the thickness of the upper ice layer, we now explore the importance of using a more physically representative stress-dependent viscosity as the viscous portion of our ice rheology. We compare the linear viscoelastic solutions just discussed to the solutions from our nonlinear viscoelastic finite element models, using a reference viscosity coefficient for our glacier corresponding to a uniform temperature of -5°C (taken from Cuffey and Paterson, 2010). Recall our

nonlinear models do not change the pressure or crack length, but rather model a single chosen crack length and timespan equivalent to the linear viscoelastic model. Thus, the greater the variation between the nonlinear and linear models, the more important using nonlinear viscoelasticity is to correctly model the ice deformation.

Figure 5.5 shows the nonlinear viscous crack opening at four different crack lengths (20 meters, 1 kilometer, 2 kilometers, and 3.333 kilometers) plotted against the linear viscous crack openings for a range of linear viscosities. Two features are immediately apparent: the relative magnitude of the nonlinear model compared to the linear models varies in time, and the character of the nonlinear crack opening changes with increasing crack length. This second feature is confirmed in the upper panels of figure 5.6, which show the normalized linear and nonlinear crack openings and the normalized pressure. The lower panels in figure 5.6 plot the effective viscosity of the upper and lower crack surfaces. The effective viscosity is defined in appendix 5C.

As the crack grows longer, the magnitude of viscous deformation increases in relation to the magnitude of the elastic deformation, as is expected from our linear viscous elastic modeling. Such a trend is shown in figure 5.7A. Note that while the viscous deformation monotonically increases, the trend in the exact value is not constant. The relative viscous deformation grows very rapidly around $L/H=0.02$, slows at $L/H\approx 0.025$ and then speeds up after $L/H\approx 1$. Figure 5.7B shows the relative viscous deformation in the upper crack edge compared to the lower crack edge. With increasing crack length, the viscous deformation of the upper crack edge rapidly grows large enough to dominate the overall viscous crack opening signal. The upward partitioning of the

viscous deformation is especially pronounced beyond $L/H \approx 0.5$, and is caused by the reduced effective viscosity in the upper body at longer crack lengths (see appendix 5C).

From these features, the nonlinear crack growth is divided into three regimes as a function of L/H : a half-space regime for short cracks ($L \ll H$), a beam-like regime for long cracks ($L > H$), and a transitional regime in between ($L \approx H$). The remainder of this section discusses each of these regimes in turn. The transitional region is defined on the lower end by the location where the trend in $\frac{w_V}{w_E}$ changes slope (figure 5.7A) and on the upper end by the region where the normalized viscous deformation coincides with the normalized linear deformation (figure 5.6). The domain of each regime is shown in figure 5.7.

5.3.2.1 Half-Space Regime

At the shortest crack length, the deformation within the finite-thickness upper ice layer and the lower half-space are effectively indistinguishable. Using figure 5.6A as a representative model within this crack regime (appropriate as L is 20 times smaller than H), the nonlinear solution clearly deviates greatly from the linear solution. The nonlinear model predicts that the viscous deformation should be more uniform along the crack length than in the linear model. This is equally evident in figure 5.5A, where near the crack tip, the nonlinear solution predicts a deformation of similar magnitude to the linear model with a viscosity of $1e11 \text{ Pa} \cdot \text{s}$, while near the crack center, the solution approaches that of a linear model with a viscosity of $1e12 \text{ Pa} \cdot \text{s}$. Additionally, a region of increased deformation exists at the crack tip, unlike the linear viscoelastic trend of monotonically reduced crack opening along the crack length.

As seen in figure 5.6A, the effective viscosities in the upper and lower halves of the models are essentially the same. As the effective viscosity is stress dependent, an equal effective viscosity implies that the stress induced by the fluid pressure in the crack is evenly partitioned between the upper and lower model regions. As expected, the changes in effective viscosity along the length of the crack mirror the value of the fluid pressure in the crack, and the region of highest effective viscosity corresponds to the zero crossing of the relative pressure. Near the crack tip, the large negative pressures (i.e., excess ice overburden pressure) cause a drop in the effective viscosity. This reduced viscosity creates the region of increased deformation seen at the crack tip.

Finally, while the crack opening is equal in the upper and lower portions of the crack, the overall magnitude of the crack deformation at this short crack length is very small compared to the elastic deformation (figure 5.7). In this half-space regime of crack growth, the relative viscous deformation is substantially less than 1% of the elastic opening. Thus, for cracks short enough to be in the half-space regime, modeling viscoelasticity is unnecessary as the viscous deformation is trivial.

5.3.2.2 Transitional Regime

As the basal crack increases in length, the profile of the crack opening changes. When the crack length approaches the ice thickness, the free surface begins to impact the deformation of the top edge of the crack. Eventually, the nature of the crack opening transitions from the half-space regime discussed above to the beam-like regime that will be discussed in section 5.3.2.3. Within the transitional regime between the half-space and beam-like regimes, the crack opening near the center of the crack ($\hat{x} \approx 0$) increases

relative to the crack opening near the crack tip. In the normalized crack opening figures (upper panels of figure 5.6), such a trend manifests itself as a convergence towards the linear viscoelastic solution as the crack lengthens. The solution completely transitions into the beam-like regime when the normalized difference (R^2 value) between the linear and nonlinear crack openings drops below 10%.

The explanation for the nonlinear model's trend towards the linear solution with increased crack length, is tied to both the increasingly beam-like nature of the upper ice body and the larger magnitude of the crack opening for longer cracks. The combined effect of these factors is that the effective viscosity within the upper body steadily decreases as the flexural (bending) stresses within the upper body become more pronounced. This understanding is built upon five modeling results:

- 1) As demonstrated in appendix 5B, the normalized bending shape of a beam is somewhat insensitive to the nature of an applied pressure distribution as long as the pressure is roughly the same near the free edge of the beam.
- 2) In our nonlinear models with $L/H > \sim 1$, the flexural stress (i.e., the stress proportional to $\frac{\partial^2 w}{\partial x^2}$) in the upper ice body is larger than the stress induced in the body by the applied pressure. Furthermore, the opening increases faster than linearly with increasing crack length (figure 5.3), implying that this flexural stress becomes increasingly more dominant than the (roughly constant) applied pressure at larger crack lengths.

- 3) As the stress in the upper ice body is dominated by the flexural stress, the effective viscosity can be approximated by the flexural stresses independent of the applied pressure. Such a result is seen in the bottom panels of figure 5.6, where the effective viscosity of the upper body (blue) diverges from the effective viscosity of the lower body (red) at increasing crack length.
- 4) For $L/H > \sim 1$, the flexural stress is close to uniform save near the middle of the beam, where the stress is low. Therefore, the effective viscosity only changes significantly near the middle of the upper ice body, where the effective viscosity is high.
- 5) As demonstrated in appendix 5B, the normalized bending profile of a beam is insensitive to changes in the material parameters near the middle of the beam. Thus, the nonlinear crack model begins to behave more like the linear crack model as the crack grows longer.

However, within the entire transitional regime, the viscous crack opening is less than 10% of the elastic opening, suggesting that viscoelasticity is still somewhat negligible even as the upper ice body begins to act more beam-like.

5.3.2.3 Beam-Like Regime

Once the crack grows to $L/H \approx 2$, the normalized nonlinear viscous deformation is only slightly different from the linear viscoelastic deformation for the reasons discussed above. However, while the normalized solution may be well approximated using a linear effective viscosity, the value of the nonlinear crack opening increases such that the

viscosity of an equivalent linear model drops with increasing crack length. An appropriate equivalent effective viscosity, $\tilde{\eta}_{eff}$, for the nonlinear model at a given crack length is found by fitting the nonlinear solution to a series of linear viscoelastic models over a range of viscosities. Figure 5.8 shows the trend in these equivalent effective viscosities, $\tilde{\eta}_{eff}$, as a function of crack length, for cracks within the beam-like regime.

As in the transitional regime, the reason for the decrease in $\tilde{\eta}_{eff}$ with crack length is the increased crack opening at longer crack lengths. The larger crack opening leads to larger flexural stresses that in turn result in the reduced equivalent effective viscosity around the crack center and tip. While the fitted value of $\tilde{\eta}_{eff}$ falls between the maximum and minimum values of effective viscosity in the material immediately above the crack, $\tilde{\eta}_{eff}$ does not correspond to any standard statistical measure of the effective viscosity. Both the median and mean values of the effective viscosity overestimate the value of $\tilde{\eta}_{eff}$ for the corresponding linear viscoelastic model. Thus, we rely on an empirical relationship for $\tilde{\eta}_{eff}$, finding that the evolution of $\tilde{\eta}_{eff}$ with crack length can be well fit using:

$$\log_{10}(\tilde{\eta}_{eff}) = 12.72 - 0.37L \quad (5.10)$$

Lastly, the magnitude of the viscous deformation becomes a substantial fraction of the elastic deformation in the beam-like regime, reaching a 1:1 ratio between the viscous and elastic deformation at a crack length just over $L/H \approx 5$. Thus, once the crack has grown to several times the ice thickness, the viscous deformation becomes as important as the elastic deformation. For cracks of the length predicted by Tsai and Rice

(2010; 2012), the viscous deformation should surpasses the elastic deformation late in the crack evolution.

5.3.3 “Pseudo-Nonlinear” Viscoelastic Results

From the nonlinear results presented above, the nonlinear viscoelastic solution only varies significantly from the linear solution when the overall viscous deformation is negligible. As such, the nonlinear viscoelastic deformation can be approximated by using the linear viscoelastic semi-analytic model with a time-varying (i.e., crack length dependent) equivalent effective viscosity. The evolution of the equivalent effective viscosity is fit empirically using equation 5.10. We call this model our “pseudo-nonlinear” (PNL) model.

Returning to figures 5.2 to 5.4, the PNL solution is the black curve in all three figures. As with the linear viscoelastic model, the PNL pressure solution, shown in figure 5.2A, only differs slightly from the other model pressure distributions, even at a crack length of $L/H=5$. The total crack opening of the PNL model is smaller than that of the linear viscoelastic model with a viscosity of $1e11 \text{ Pa} \cdot \text{s}$ at crack lengths up to and including $L/H=1$ (figure 5.2B). This result is expected as the equivalent effective viscosity in the PNL model is greater than that of the shown linear viscoelastic model at these crack lengths. At $L/H=5$, the crack opening in the PNL model surpasses that of the linear model with a viscosity of $1e11 \text{ Pa} \cdot \text{s}$, despite only having a lower effective viscosity at crack lengths greater than $L/H \sim 4.7$. Such behavior is easily explained by the rapid change in $\frac{d\hat{w}_v}{dt}$ in figure 5.3A, as the decreasing effective viscosity at larger crack lengths further enhances the viscous opening rate beyond that seen in the linear

model. Similarly, in figure 5.4, the scaled fluid velocity increases faster in the PNL model than in either the elastic or linear viscoelastic models.

Given the well-established nonlinearity of the viscous deformation of ice, our PNL model is the most physically representative model for crack propagation considered here. However, a major assumption of the PNL approach is that the input pressure remains constant, as our empirical fit of the nonlinear effective viscosity (equation 5.10) holds only for a constant inlet pressure. Calibrating an empirical fit that allows for variable pressure would necessitate knowing the pressure history, which would require a full crack evolution model to determine consistent values of crack opening, crack propagation velocity, and inlet pressure. Such modeling is well beyond the scope of this work. Thus, the PNL solution is presented as an indication of the expected results for a nonlinear viscoelastic model, but as will be discussed in the next section, the need for a variable inlet pressure when modeling the Greenland observations dictates our decision to directly compare only the observations to our the linear model results.

5.4 Comparison to Observations

The model results discussed in the previous sections demonstrate that viscoelasticity becomes increasingly important as the basal crack grows longer. We now compare the linear model results to the observations of Das et al. (2008) to determine if viscoelasticity is an important consideration for realistic lake drainage problems. First, we use our models to predict the drainage rate and volume of a theoretical supraglacial lake, comparing the drainage times of our models to observations of lake level height during the Greenland lake drainage event. Second, we create a finite element model to

determine the expected surface deformation during and immediately following a lake drainage event, comparing our model results to a GPS station placed by Das et al. (2008) 1.7 kilometers away from the drainage conduit during the Greenland event.

5.4.1 Lake Drainage

Das et al. (2008) observed a lake of volume 0.044 km^3 of water drained from the surface completely in less than two hours. We create a simple model for the volume in the lake, conduit, and crack system by assuming that the surface lake has a constant cross-sectional area of 5.6 km^2 (as reported by Das et al. 2008), the basal crack volume is approximated as a cylinder of with height equal to an average crack opening, and the drainage conduit is an oblong cylinder of semi-major axes a and $u_0 = a \frac{p_I}{2E}$, and height H . The resulting drained volume is:

$$V_d = V_b + V_c \approx \pi L^2 w_{ave} + \frac{\pi a^2 H p_I}{2E} \quad (5.11)$$

This geometry is shown schematically in figure 5.9. Two implicit assumptions of this model are that while the lake is draining, no water leaves the crack system and that there is a constant input pressure at the intersection of the drainage conduit and the basal crack during the initial drainage phase. However, once the finite volume of the lake drains ($V_d = V_0$), the water level in the conduit will begin to drop due to the conservation of volume in the conduit/crack system. The height of the water level in the conduit system, H_W , during the post-drainage phase is defined to be (after Tsai and Rice, 2010):

$$H_W = H \left(\frac{\rho_{ice}}{\rho} + \frac{\rho_{ice} - \rho}{\rho} \chi_w \right) \quad (5.12)$$

where χ_w is a constant between 0 and 1. As the inlet pressure is linear with water level, we make the substitution:

$$p_I = \chi_w p_{static} \quad (5.13)$$

where p_{static} is the overburden pressure of a static water column of height H . The value of χ_w can now be found by substituting $w_{ave} = \frac{\hat{w}_{ave} p_I L}{E}$, $V_d = V_0$, and equation 5.13 into equation 5.11, resulting in:

$$\chi_w = \frac{L\hat{w}_{ave} - \frac{H\rho_{ice}}{\rho} \left(\frac{a}{L}\right)^2 \pm \sqrt{\left(\frac{H\rho_{ice}}{\rho} \left(\frac{a}{L}\right)^2 - L\hat{w}_{ave}\right)^2 - 2\frac{\rho_{ice}-\rho}{\rho} \left(\frac{a}{L}\right)^2 \frac{V_0 E}{\pi L^2 p_{static}}}}{\frac{H\rho_{ice}}{\rho} \left(\frac{a}{L}\right)^2} \quad (5.14)$$

In this form, the only quantity other than χ_w that is unknown is $\left(\frac{a}{L}\right)$, the ratio of the conduit's long axis to the length of the basal crack. As discussed in Tsai and Rice (2010; 2012), we expect $\left(\frac{a}{L}\right)$ to be between ~ 0.1 and 1.0 . As our bias is towards larger values of $\left(\frac{a}{L}\right)$ due to the sizable crack observed by Das et al. (2008), we impose a range of values for $\left(\frac{a}{L}\right)$ equal to 0.7, 0.8, 0.9, and 1.0, allowing us to solve explicitly for the drainage volume.

Figure 5.10 shows the drainage volume, drainage rate, and crack opening for these four models. The elastic model solution is shown in blue, while the solution to the linear viscoelastic model with a viscosity of $\eta = 1e11 \text{ Pa} \cdot \text{s}$ is in red. As will be discussed later, this viscosity provides an overestimate of the viscous deformation for an equivalent PNL version of this analysis (see subsection 5.5.2).

From figure 5.10, our model predicts more rapid drainage than the Greenland observations suggest, with the total lake volume draining into the conduit in only ~ 0.32

hours. As expected from this exceedingly short duration, the drainage rates are about 20 times larger than the peak observed drainage rate of $\sim 14,300 \text{ m}^3/\text{s}$. Note that this drainage rate is the linear drainage rate between the final two undrained lake level measurements of Das et al. (2008), assuming a constant lake area. Additionally, varying the values of $\left(\frac{a}{L}\right)$ makes essentially no difference for the model's solutions. For example, the largest difference in drainage time is about 0.2% and the greatest difference in peak crack opening is about 2% between all values of $\left(\frac{a}{L}\right)$. This near-independence of the solution on $\left(\frac{a}{L}\right)$ implies that the basal crack volume, rather than the conduit's volume, controls the total drainage volume, and that the dependence of χ_w on $\left(\frac{a}{L}\right)$ is minimal.

Comparing our elastic (blue lines) and viscoelastic models (red lines), the viscoelastic solution completely drains the supraglacial lake faster than the elastic solution, as expected from the added viscous component of deformation. The difference in drainage time between the solutions is 0.0065 hours (23.4 seconds), a difference of about 2%. However, the difference in the modeled crack opening is more pronounced, with the viscoelastic solution predicting a crack opening about 9% larger than the elastic model. Additionally, after the lake has finished draining, the difference in the modeled crack openings grows, reaching a difference of about 17% between rheologies two hours after the lake drainage began. The exception to this trend is the brief period of time where elastic crack is growing while the viscoelastic crack is shrinking. Thus, the viscoelastic model predicts slightly faster lake drainage, a larger peak crack opening value, and larger crack openings during the post-drainage phase.

To address our exceedingly rapid lake drainage, we now apply a correction for the fluid drag on the water falling through the vertical conduit. Following appendix D of Tsai and Rice (2010), the conduit size dictates the turbulent loss of fluid pressure. This effect is added to our models by introducing a correction factor χ to the pressure term, where χ is constant between 0 and 1 representing the fraction of total fluid overburden pressure transmitted to the basal crack. The relationship between χ , L , and a , taken from equation D12 of Tsai and Rice (2010), is:

$$\chi = \left(\frac{\left(\frac{a}{L}\right)^{16/3} \left(\frac{L}{H}\right)}{0.456 + \left(\frac{a}{L}\right)^{16/3} \left(\frac{L}{H}\right)} \right) \quad (5.15)$$

Note that this formulation of χ assumes only elastic deformation of the conduit, clearly a very relevant simplification given our interest in viscoelasticity. The implications for viscoelastic deformation of the conduit are discussed later in section 5.5.

This correction is applied to the linear viscoelastic model by replacing p_I with $\chi\chi_w p_{static}$ and adding the constraint shown in equation 5.11. As with the models without the fluid drag correction, we assume a value for $\left(\frac{a}{L}\right)$, exploring a range of $\left(\frac{a}{L}\right)$ to find the value that best-fit the observed lake level data. With the added fluid drag correction, the choice of $\left(\frac{a}{L}\right)$ now has a substantial effect on the model results. Appendix 5D discusses the importance of $\left(\frac{a}{L}\right)$ to greater detail. Figure 5.11 shows the approximate lake levels, drainage rates, and crack openings for the elastic and linear viscoelastic ($\eta = 1e11 \text{ Pa} \cdot \text{s}$) models for our best-fit value of $\left(\frac{a}{L}\right) = 0.51$.

The first impact of conduit size is that the value of $\left(\frac{a}{L}\right)$ has a strong impact on the timing of the lake drainage event, unlike the model without a fluid drag correction. These models predict a much longer total drainage time than Das et al. (2008) observed, as the models do not completely drain the surface lake until about 40.5 hours after the crack begins forming. However, recall that the drainage time estimated from the Greenland drainage event is based on the timing of the peak horizontal surface displacement (e.g., figure 2C of Das et al.). Thus, while our best-fit model predicts the full drainage time to be just over 40 hours, the duration of the observable lake level change fits the lake level data of Das et al. (2008) closely (figure 5.11A). The threshold for an observable change in lake level is five centimeters.

Our modeling suggests there are three phases in the lake drainage process: a long initialization period of little to no observable lake level change, a rapid acceleration in the lake drainage rate until the lake drainage is complete, and then a decelerating phase of post-drainage crack growth. The few lake level data points from the Greenland lake during the rapid drainage phase suggest that there may be an acceleration in the drainage rate until the drainage finishes. However, our models predict a longer period of acceleration and a more rapid final drainage rate than are seen observationally. The net result is that our best-fit model has observable rapid drainage for 1.8 hours, which falls into the range of potential drainage time seen by Das et al. (2008), as seen in figure 5.14.

Turning now to figure 5.11B, our drainage rates are about a factor of five larger than the rate estimated by linear interpolation between the data points of Das et al. (2008). While our modeled rate is fast, the drainage rates are within an order of

magnitude of the observations, which is reasonably close considering the number of approximations going into our two-dimensional model and the sparsity of the lake level data from Das et al. (2008) during the rapid drainage phase. However, our model does predict a constant acceleration of the drainage rate up until the lake has completely drained. The observations are sparse enough to allow for either constant drainage acceleration throughout the entire drainage or a drop in the drainage rate near the end of the drainage process.

Lastly, the addition of fluid drag slightly reduces the maximum crack opening values. The smaller crack openings result in longer drainage times before the complete drainage of the surface lake. An increase in the total drainage time results in a longer basal crack. The viscoelastic models systematically predict a larger deformation than the corresponding elastic model, with the difference in peak crack opening of about 10%. However, during the post-drainage phase, the difference between the elastic and viscoelastic crack openings increases to about 15%. Such a drop in the relative crack opening in the post-drainage phase is opposite the trend seen in the models without fluid drag.

5.4.2 Surface Deformation

We now use our preferred model from figure 5.11 to estimate the expected surface motion at a point 1.7 kilometers away from the main drainage conduit—the location of the GPS station used by Das et al. (2008). We model the surface uplift using an elastic finite element model rather than the analytic estimate for uplift used by Tsai and Rice (2010), as discussed in more detail in appendix 5E. As will be shown, a basal crack can

create a substantial amount of horizontal motion at the theoretical GPS location. As Tsai and Rice (2010) used the approximation that all the horizontal motion comes from the pressure within the conduit, such an analytic approximation is not valid.

Figure 5.12 shows the model results, plotted against the surface motion data of Das et al. (2008). To standardize the timing of our model results to the observations, we adopt the convention of Das et al. (2008) and assume that the surface lake finishes draining synchronously with the peak horizontal displacement. The elastic crack model is shown with dashed lines, the viscoelastic model with solid lines, and the observations with bolded lines. The blue, green, and black lines correspond to the horizontal displacement, vertical displacement, and crack opening, respectively.

Table 5.2 summarizes many of the important model and observational quantities shown in figure 5.12. The model under-predicts the value of the surface deformation at the GPS station by factors of 1.7 and 2.5 (vertical and horizontal) but predicts that the horizontal deformation should be a smaller percentage of the vertical deformation than is seen observationally. Additionally, the models suggest that the peak ground motions are contemporaneous with the peak crack opening. In the Greenland observations, there is a noticeable lag in the peak vertical motion after the peak horizontal motion. For the decay of the displacements following peak ground motion, our models do a good job fitting the relative amplitude of the vertical displacement, but predict a stronger decay of the horizontal signal than in the observations. Finally, from a qualitative perspective, our results are more peaked than the GPS observations, which have a more gradual evolution of the surface displacements.

We now consider the role that the crack length has in determining the relative horizontal and vertical displacements. Figure 5.13A shows the model results normalized by the maximum magnitude of the crack opening, thus removing any influence of the changing inlet pressure on the displacement results. The horizontal displacement has a natural high in the relative displacement amplitude, peaking when the crack is slightly longer than the distance from the conduit to the GPS location (~ 2.2 kilometers versus the GPS location at 1.7 kilometers). This behavior is unlike that of the relative vertical displacement, which grows continuously with increasing crack length. Thus, if the basal crack was allowed to grow with an infinite reservoir of water, there would be a drop in the horizontal displacement at any given point due to the geometric effect of the crack growing beneath and beyond that location. In appendix 5E, the peak horizontal displacement clearly follows the crack tip, travelling laterally away from the crack's center as the crack grows longer.

The only reason this effect is not found in our model results is because the lake drains completely before the crack length grows long enough to express this trend in the horizontal displacements at the GPS location. As shown in figure 5.13B, the value of the relative horizontal deformation coincidentally begins to drop around the same time that the surface lake finishes draining, masking most of this geometrically-controlled signal. However, the slight reduction in the slope near the peak of the horizontal deformation is due to the movement of the crack tip away from the GPS station.

5.5 Discussion

We are now equipped to discuss two different consequences of our supraglacial lake drainage modeling. First, our model results suggest a reinterpretation of the estimated duration of the lake drainage event from the observations of Das et al. (2008). This discussion highlights two major discrepancies between our model results and the Greenland observations: the potential deceleration of the drainage rate just before the surface lake finishes draining, and the time delay between the observed vertical and horizontal displacement peaks. Second, the general importance of viscoelasticity in correctly modeling the drainage of a supraglacial lake is addressed, with some of the remaining limitations of our model discussed.

5.5.1 Re-Evaluating Lake Drainage Timing

In Das et al. (2008), the authors estimate the total lake drainage duration based on the observed peak surface horizontal motion of their GPS station, which approximately matches a linear extrapolation of the final half-dozen lake level observations. However, as discussed in subsection 5.4.2, the peak horizontal surface displacement is controlled by the crack length in addition to the crack opening (figure 5.13). Such a relationship means that the horizontal displacement may be reflective of the crack's geometry rather than the total crack opening (and thus lake level), and that the peak value may not correspond to the end of the surface lake drainage. As the vertical surface displacements monotonically grow with crack length, we propose that using the peak vertical motion is a better estimate for the duration of the lake drainage event.

Applying this new estimate of the rapid drainage duration to the data of Das et al. (2008), the duration of the rapid lake drainage would be closer to 1.6-1.8 hours rather than the suggested 1.4 (as shown in figure 5.14). This new drainage time suggests that the lake is still draining when the monitoring station Hobo 1 is grounded. As Hobo 1 was farther away from the drainage conduit and came to rest at a higher elevation than station Hobo 2, such a result could be explained by bathymetry (i.e., after about 17:15, the lake has drained below the level of ~ 5 meters, leaving Hobo 2 stranded on the ice's surface while the lake is still draining elsewhere).

However, the two major discrepancies remain between our model results and the observations: first, our models suggest that the drainage rate accelerates until the supraglacial lake is fully drained while a constant or even reduced drainage rate is necessary to match the observed drainage duration; second, our models do not show a delay between the peak horizontal and vertical surface displacements, as is seen in the observations from Greenland.

5.5.1.1 Drainage Deceleration

Our models predict a continuous acceleration in the drainage rates until the surficial lake finishes draining, while the observations of Das et al. (2008), in conjunction with our drainage timing, do not support such a trend in drainage rate. The simplest explanation for this discrepancy is that our models are systematically missing an important process near the end of the rapid lake drainage phase that reduces the final drainage rate. As all the observational data shows, the rate of displacement slows before reaching the peak value for both the horizontal and vertical components, while our models only show this

behavior in the horizontal component (and is attributable to the geometry of the crack relative to the GPS station, see section 5.4.2).

One potential process that our models miss is that the drainage conduit may act less like a drain (i.e., a completely submerged crack) and more like a moulin (i.e., water flowing into the crack from the side) as the lake level drops (shown conceptually in figure 5.15). The net result of such a transformation would be a reduction in the drainage rate late in the rapid lake drainage phase. Another possibility is that, for the observed lake drainage event, one of the two main drainage conduits stopped contributing to the lake drainage due to the falling lake level, resulting in a drop in the lake drainage rate. To test either hypothesis, a more detailed mapping of the supraglacial lake bed and/or knowing the spatial extent of the lake's surface through the drainage event would be necessary.

5.5.1.2 Displacement Peak Timing

Our models fail to reproduce the offset in the timing of the vertical and horizontal displacement peaks seen by Das et al. (2008). One potential cause is that the draining surface lake is assumed to have a constant surface area. Such an assumption is unlikely to be a good approximation for the geometry of a supraglacial lake. A change in the lake's cross-sectional area could be the cause of an apparent increased drainage rate as interpreted from the lake level data.

In our models, the net result of assuming a shrinking cross-sectional area of the lake with depth will be an increased rate of change in surface elevation due solely to bathymetry, even with a constant change in lake volume. As we fit our ideal model by

changing $\left(\frac{a}{L}\right)$ until the water level of the constant-surface-area lake matched the trend in the observed lake level, having a narrowing lake would cause us to select a value of $\left(\frac{a}{L}\right)$ that is too large. Overestimating the size of the drainage conduit would lead to an elevated drainage rate and thus a shorter duration of the rapid drainage phase. Figure 5.16 shows schematically the effect of having a variable bathymetry on the observed lake level.

Having a bathymetrically variable lake does not address the need for a constant or reduced drainage rate late in the drainage process, and actually makes this issue worse, if the lake's surface area decreases as a function of depth. Needing a reduced $\left(\frac{a}{L}\right)$ to explain the surface observations would increase the crack length at complete drainage. As seen in figure 5.13, a longer crack length would cause the horizontal deformation at the GPS station to peak earlier than the vertical deformation as is seen in Das et al.'s (2008) GPS observations. However, as with the absolute drainage rates, a more detailed understanding of the bathymetry and drainage history of the supraglacial lake is necessary to test this hypothesis.

5.5.2 Influence of Viscoelasticity

A major goal of this research is to quantify the importance of using a viscoelastic rheology for ice to model the process of supraglacial lake drainage. From our modeling, viscoelasticity has three major effects on our solutions to the lake drainage problem: predicting the secession of surface drainage sooner, a larger peak crack opening, and a larger post-drainage deformation than in an equivalent elastic model.

Unfortunately, the total drainage timing is not measurable from surface observations, as the surface deformation only reaches an observable level late in the drainage process when the drainage rates rapidly accelerate. The duration of the rapid drainage phase, an easily measured time, is not strongly affected by the choice of rheology. Similarly, the peak crack opening is not currently a measurable quantity. Thus, only the relative amplitude of the post-drainage deformation provides information that can constrain the importance of viscoelasticity. However, as the difference between the viscoelastic and elastic models is expected to be about 10% for our model, this information alone is not sufficient to conclusively determine if viscoelasticity is necessary to match the observations.

Of course, the model results presented in section 5.4 are for a single linear viscosity and do not explore the full range of possible viscosities. From the definition of the consistent tangent viscoelastic compliance modulus S_{VE} (equation 5A.4), reducing the model viscosity will likewise reduce S_{VE} , resulting in increased crack opening at a given pressure. A larger crack opening increases the crack propagation speed and drainage rate, reducing the crack length at, and thus the time until, the complete drainage of the surface lake. The net result is that reducing the viscosity causes the viscoelastic solution to diverge more strongly from the elastic solution both in terms of drainage duration and deformation magnitude. The opposite is true for increasing the viscosity, which causes the solution to behave more like the elastic solution.

However, as we previously stated, the viscous deformation is demonstrably nonlinear (e.g., Glen, 1955; 1958). As shown by our constant inlet pressure PNL model (subsection 5.3.3), a nontrivial amount of viscous deformation will occur only when the

effective viscosity of the nonlinear model drops substantially during the beam-like phase (when the crack length is longer than the glacier thickness). However, if the viscous crack opening becomes large, the lake will completely drain more rapidly than in the corresponding elastic model. After this point, the crack deflates, reducing the flexural stresses that control the value of the effective viscosity, resulting in a larger viscosity and a smaller proportion of viscous deformation. Thus, the nonlinear model should only vary significantly from the linear viscoelastic model during the period of rapid lake drainage, and only if the lake volume is sufficiently large to grow the basal crack longer than the glacier's thickness.

Additionally, as our cracks only grow elastically to between two and three kilometers before the surface lake finishes draining, using equation 5.10, the effective viscosity in the PNL model should not drop below about $1e11 \text{ Pa} \cdot \text{s}$, suggesting that the linear results from section 5.4 represent a maximum result for any possible nonlinear viscous deformation. Thus, we must conclude that the effects of viscoelasticity on the drainage of a supraglacial lake are fairly minor (about 10% at most). While such a difference is not trivial, the effects of the conduit size on the solution are demonstrably larger (see section 5.4 and appendix 5D). We suggest that creating a physically-consistent model for the drainage conduit's evolution during the drainage process is more important to correctly model the lake drainage phenomenon than using either a linear or nonlinear viscoelastic rheology. That being said, if there is an appreciable viscoelastic effect on the growth and size of the drainage conduit, then viscoelasticity could be necessary to correctly model supraglacial lake drainage, but such modeling is beyond the scope of this project.

5.6 Summary and Conclusions

In this chapter, we presented a methodology for incorporating linear viscoelasticity into the semi-analytic model of Tsai and Rice (2010; 2012) for the growth of a subglacial crack filled with a turbulent fluid during the drainage of a supraglacial meltwater lake. From using finite element analysis to model an ice-appropriate nonlinear viscoelastic rheology, we found that we can approximate the behavior of the nonlinear model using a linear model with a time-varying effective viscosity, assuming that the inlet pressure is held constant.

Next, we applied two correction factors taken from Tsai and Rice (2010) to estimate the drainage history in our models, incorporating the effects of the finite volume of the surface lake and the reduction in inlet pressure due to drag on the fluid falling through the drainage conduit to better match the observations of a real supraglacial drainage event from Greenland (Das et al., 2008). Our modeling suggests that the estimated drainage time from Das et al. (2008) may be too short. More generally, our model results suggest that a viscoelastic rheology does not match the observations of Das et al. (2008) to a significantly greater extent than a linear elastic model does. Using our general model results for linear and nonlinear viscosity, we propose that exploring the full range of reasonable viscous parameters will not increase the divergence of the viscoelastic model from the elastic model beyond what is shown here.

Another important result of this work is that the opening of a basal crack alone is sufficient to cause horizontal as well as vertical surface deformation. This horizontal motion of a given point on the glacier's surface is dependent on the relative positions of

the surface observation to the crack tip, with the horizontal displacement peaking when the crack tip is beneath the observation. Thus, unlike the vertical deformation, which necessarily increases with increasing crack opening, the horizontal deformation at a single location can peak and decay even as the crack continues to grow. This result provides a possible mechanism for explaining the observed difference in peak horizontal and vertical surface deformation seen by Das et al. (2008) during the Jakobshavn Isbrae lake drainage event.

Thus, we conclude that both using linear and nonlinear viscoelasticity has, at best, a second-order effect on the modeling of the lake drainage process. While the viscous component of deformation is not negligible (even reaching about 10% at times), our work suggests that several of the modeling assumptions have a larger impact on our model results. Such factors include the lack a physically based evolution law for the drainage conduit, not knowing the bathymetry of the draining lake, and not having a good understanding of any possible changes to the drainage process when the surface lake drains to low water levels. We suggest that the next step in better understanding and mathematically modeling the phenomenon of supraglacial lake drainage is to model the dynamic growth of the (vertical) drainage conduit, especially late in the lake drainage process.

| | Variable Names | Units |
|--|--|---------------------|
| | A Conduit radius | m |
| | a_k Fitted coefficient | -- |
| | \mathcal{C}_{VE} Consistent viscoelastic tangent matrix | Pa |
| | c_k Fitted coefficient | -- |
| | D Fitted coefficient | -- |
| | E Young's modulus | Pa |
| | F_{21} Force in the 21 component | N |
| | f Darcy-Wesibach friction factor | -- |
| | f_i Force vector | N |
| | f_0 Reference friction factor | -- |
| | H Ice sheet thickness | m |
| | Δh FEM crack edge separation | mm |
| | K_I Mode 1 fracture intensity | Pa m ^{1/2} |
| | K_{IC} Critical mode 1 fracture intensity | Pa m ^{1/2} |
| | K Nikuradse roughness height | cm |
| | L Crack half-length | km |
| | n_i Normal vector | -- |
| | p Net fluid pressure | Pa |
| | p_I Inlet pressure | Pa |
| | Re Reynold's number | -- |
| | S_T Traction boundary surface | -- |
| | S_U Displacement boundary surface | -- |
| | S_{VE} Consistent viscoelastic tangent compliance matrix | Pa ⁻¹ |
| | T_i Applied traction | Pa |
| | t Time | s |
| | t_0 Current timestep | s |
| | t_1 Next timestep | s |
| | U Fluid velocity | m/s |
| | U_{2k} Chebyshev polynomial of the second kind | -- |
| | U_{TIP} Crack tip velocity | m/s |
| | u Displacement (horizontal) | m |
| | u_i Displacement vector | m |
| | u_i^0 Applied displacement | m |
| | V Model volume | m ³ |
| | V_b Basal crack volume | m ³ |
| | V_c Drainage conduit volume | m ³ |
| | V_d Volume of fluid drained | m ³ |
| | V_0 Total lake volume | m ³ |
| | w Crack opening (deflection) | m |
| | w_{AVE} Average crack opening | m |
| | w_E Elastic crack opening | m |
| | w_V Viscous crack opening | m |

| | | |
|----------------------|---------------------------------------|--------------------|
| x | Horizontal coordinate | km |
| α | Timestepping coefficient | -- |
| ε | Strain | -- |
| η | Linear viscosity | Pa s |
| η_{eff} | Effective viscosity | Pa s |
| $\tilde{\eta}_{eff}$ | Equivalent effective linear viscosity | Pa s |
| ν | Poisson's ratio | -- |
| ξ | Bimaterial interface coefficient | -- |
| ρ | Fluid density | kg m ⁻³ |
| σ | Stress | Pa |
| σ_{flex} | Flexural stress | Pa |
| σ_{ij} | Stress tensor | Pa |
| σ_{xz} | Two-dimensional shear stress | Pa |
| τ_{max} | Maxwell relaxation time | s |
| ϕ | Scaled velocity | -- |
| χ | Input pressure coefficient | -- |
| χ_w | Fluid drag correction factor | -- |
| \wedge | Indicates dimensionless variable | |

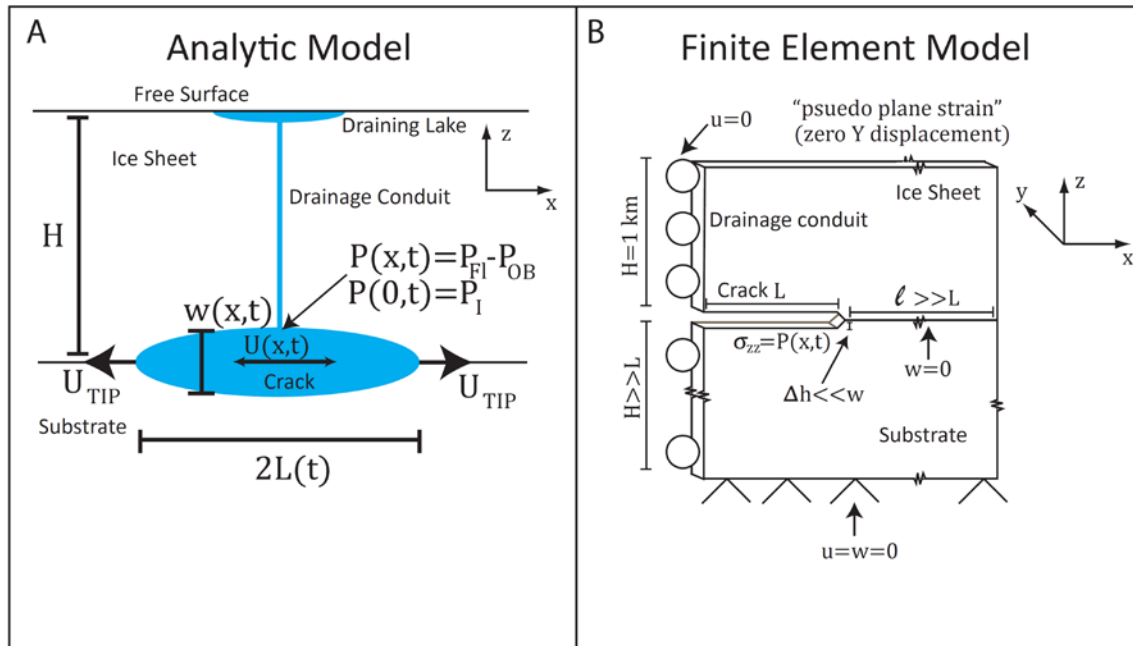


Figure 5.1: Diagrams of the lake drainage models discussed in this paper. Panel A is a schematic of the fluid-filled basal crack model used for our linear viscoelastic modeling. Panel B shows a schematic for the finite element modeling used for modeling nonlinear viscoelasticity. The details of these models are discussed in the methodology section of the main text.

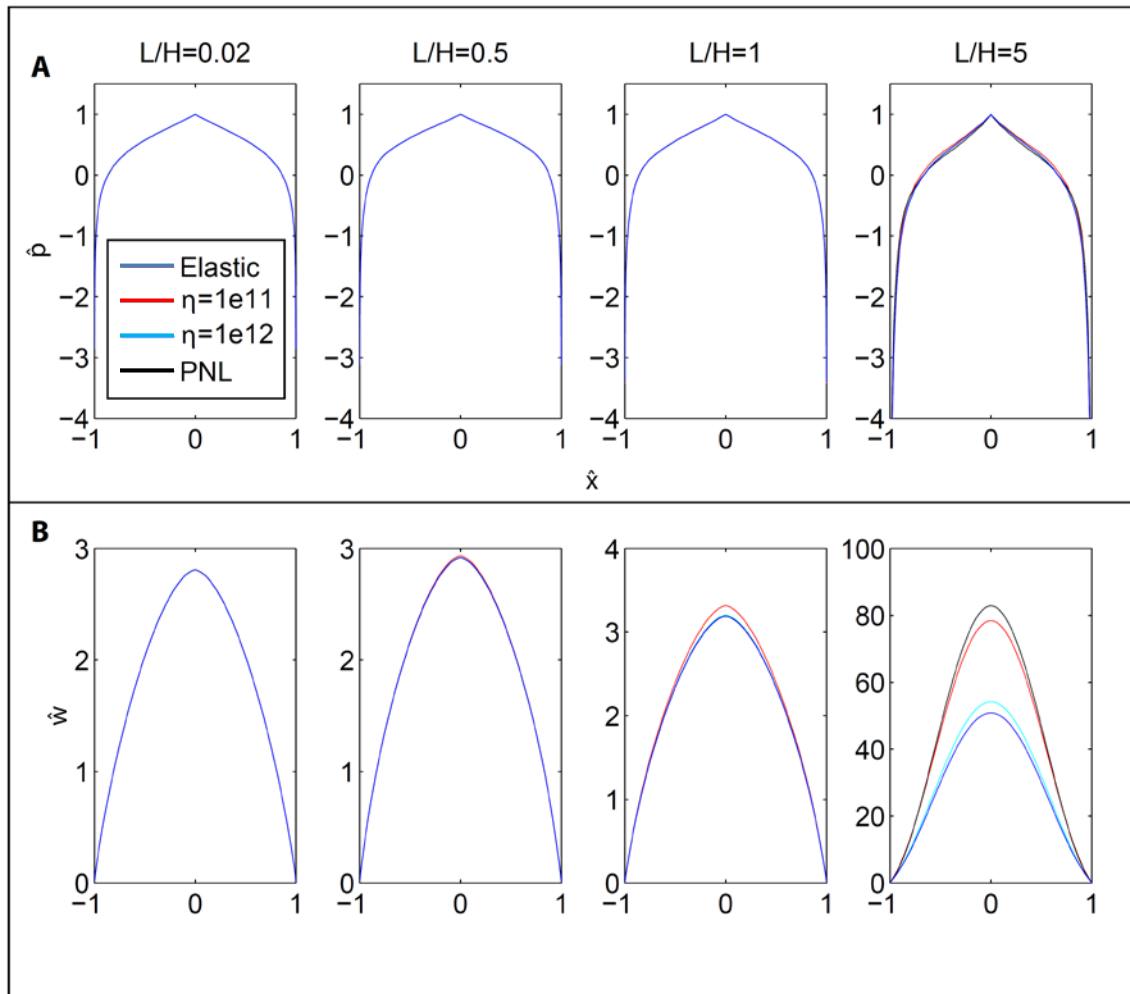


Figure 5.2: Snapshots of dimensionless pressure (panel A) and crack opening (panel B) for cracks with length $L/H=0.02, 0.5, 1$, and 5 . In all plots, there are curves representing the elastic solution, two linear viscoelastic solutions ($\eta = 10^{11}, 10^{12}$ Pa), and the pseudo-nonlinear (PNL) solution. In most of these plots, the four models have indistinguishable solutions.

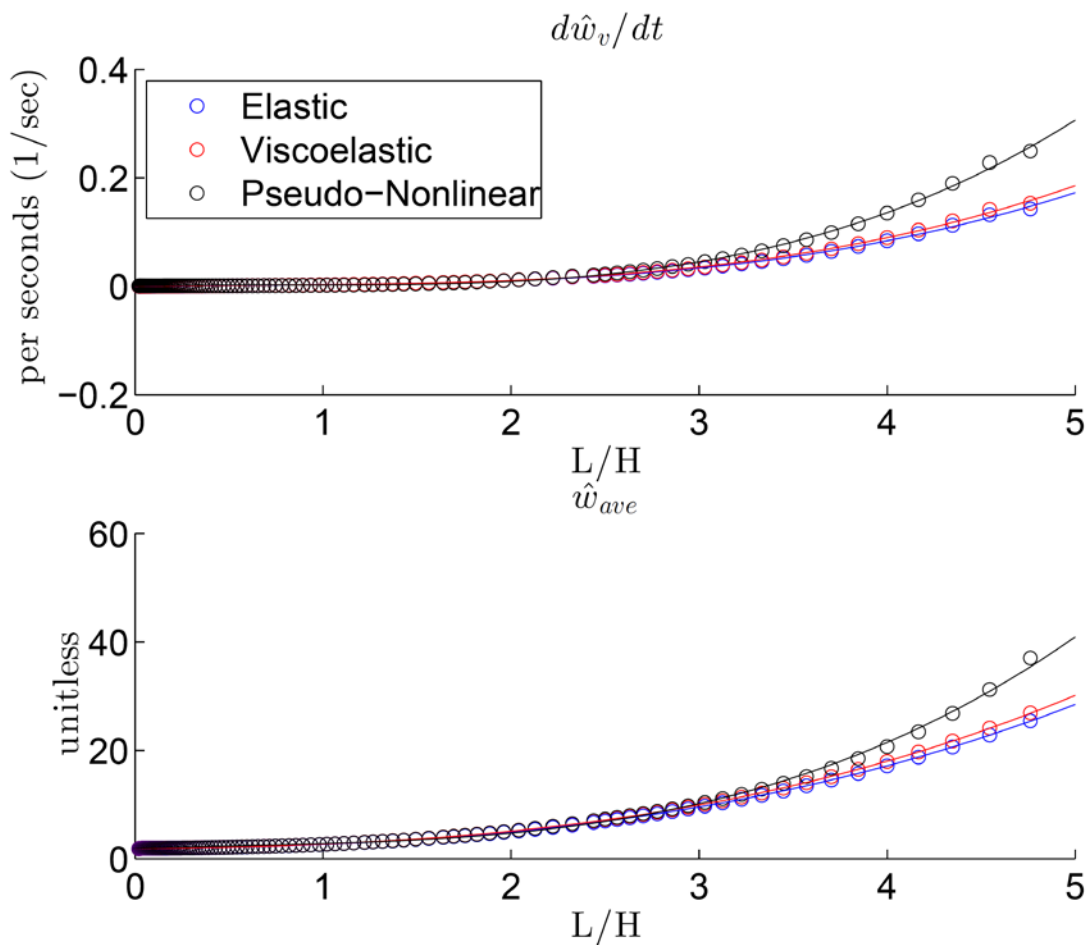


Figure 5.3: Plots showing the evolution of dimensionless crack opening as a function of crack length. The three curves plotted are the elastic solution, linear viscoelastic solution for $10^{12} Pa$, and the pseudo-nonlinear solution. Panel A shows the rate of change of the dimensionless crack opening, while Panel B shows the value of the dimensionless crack opening. The circles represent the model output values, while the curves are polynomial fits to these data.

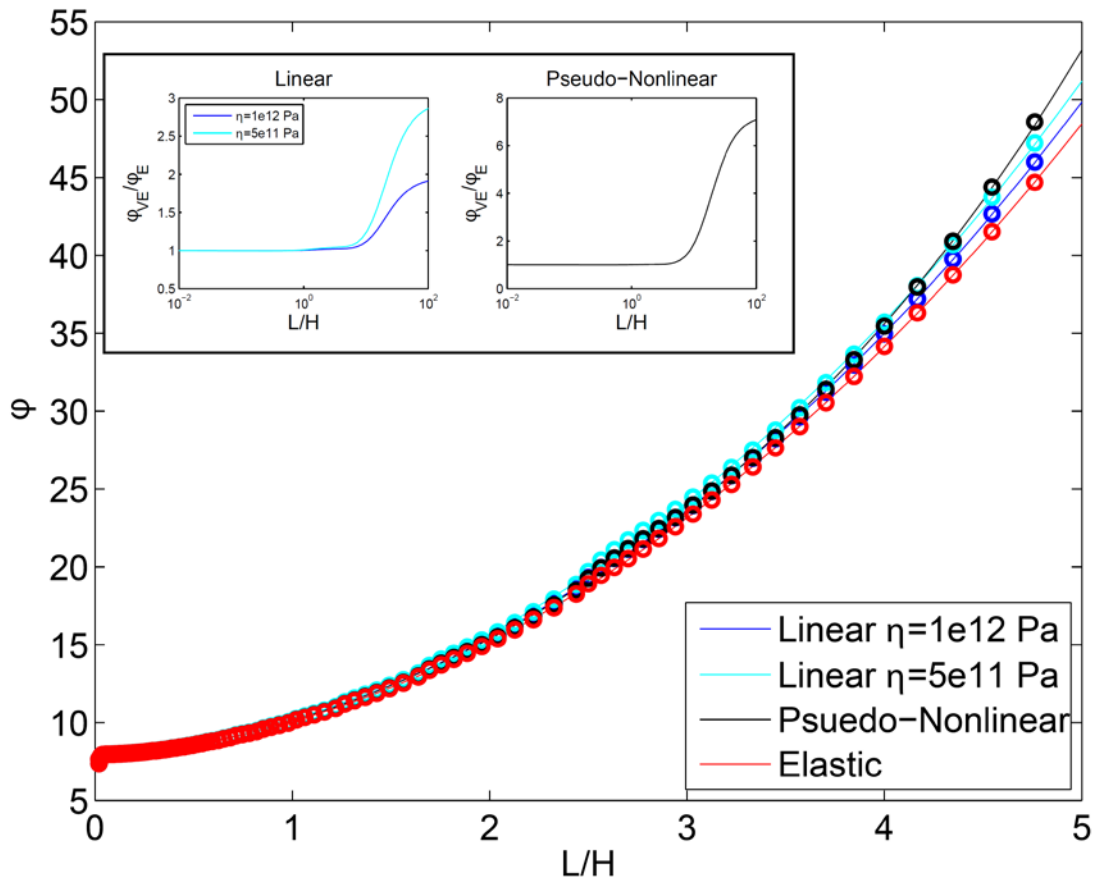


Figure 5.4: Plot of the scaled fluid velocity ϕ as a function of crack length for our elastic model, two linear viscoelastic models ($\eta = 1 \cdot 10^{11}, 5 \cdot 10^{11}$ Pa) and the pseudo-nonlinear model. The circles represent the model output values, while the curves are polynomial fits to these data. The inset figure shows the extrapolation to large and small crack lengths for the phi values of the viscoelastic models relative to the elastic model. Note that the results for the elastic model differ in magnitude from those of Tsai and Rice (2012) as we choose to neglect the bimaterial interface coefficient ξ in determining the value of ϕ , unlike Tsai and Rice (2012).

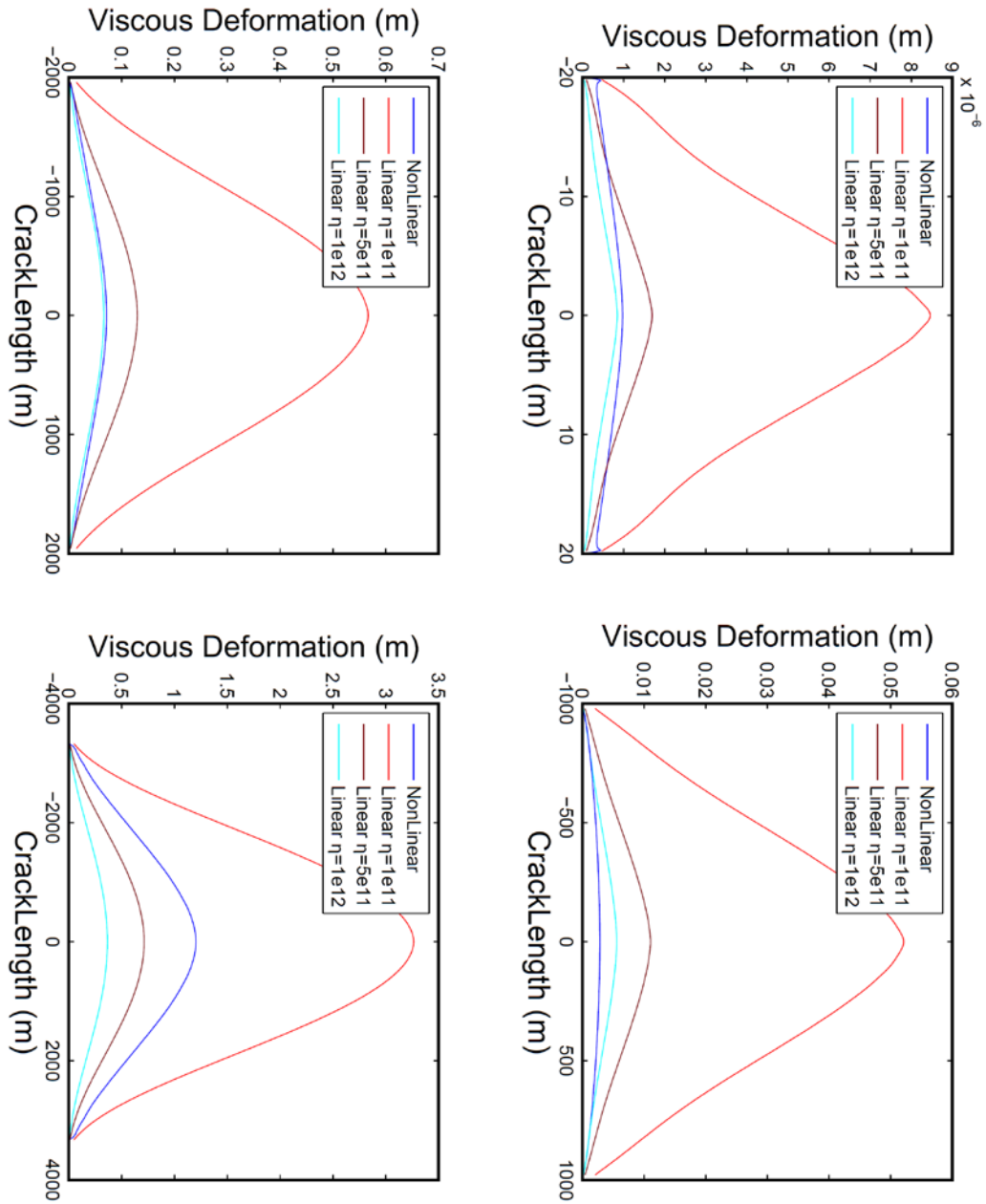


Figure 5.5: Viscous deformation at four crack lengths (20 meters, 1 kilometer, 2 kilometers, and 3.333 kilometers). The four models plotted are the nonlinear finite element model results and 3 linear viscoelastic models for a range of viscosities (1e11, 5e11, and 1e12 Pa·s).

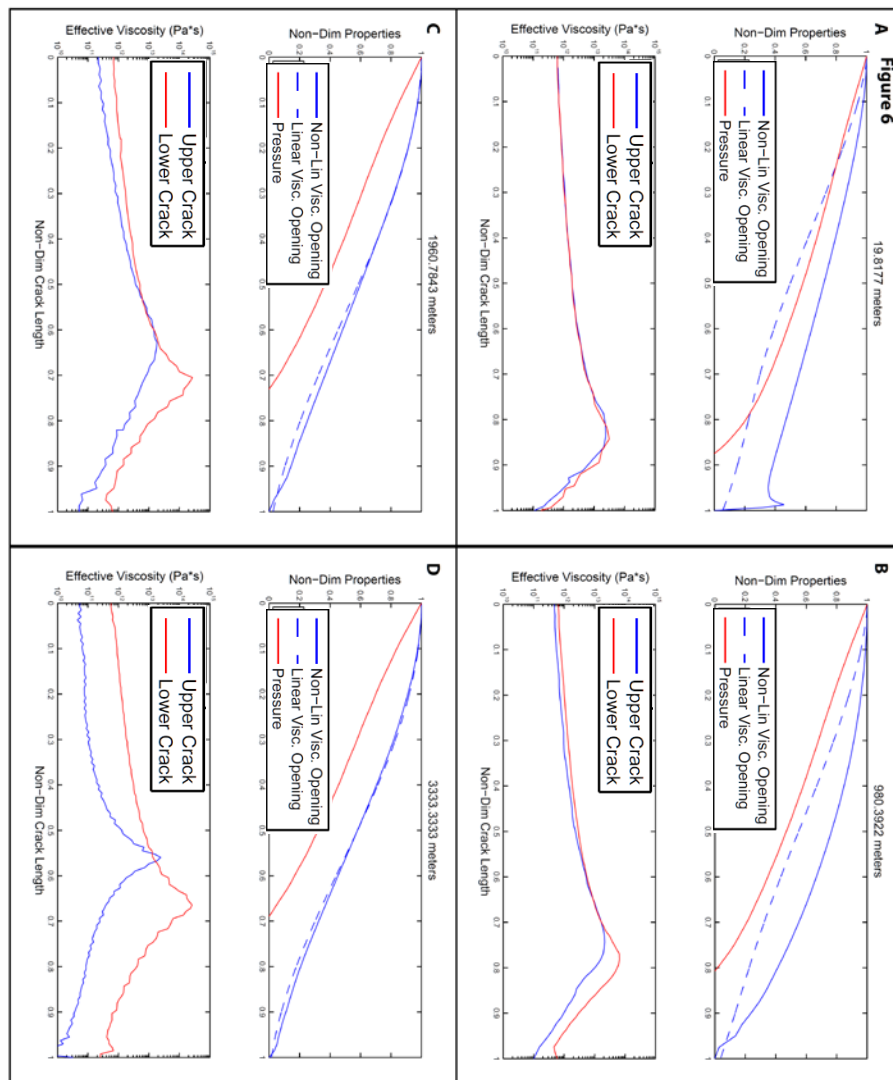


Figure 5.6: Plots showing the relationship between the normalized crack opening, normalized pressure, and effective viscosity. Panels A to D correspond to the four crack lengths shown in figure 5. In each panel, the upper plot has the normalized pressure (red) and crack opening for a linear viscoelastic (dashed blue) and nonlinear viscoelastic model (solid blue). In the lower plot, the effective viscosities for the upper (blue) and lower (red) edges of the crack are shown for the nonlinear viscoelastic model. The effective viscosity is calculated from the stress output of the finite element models.

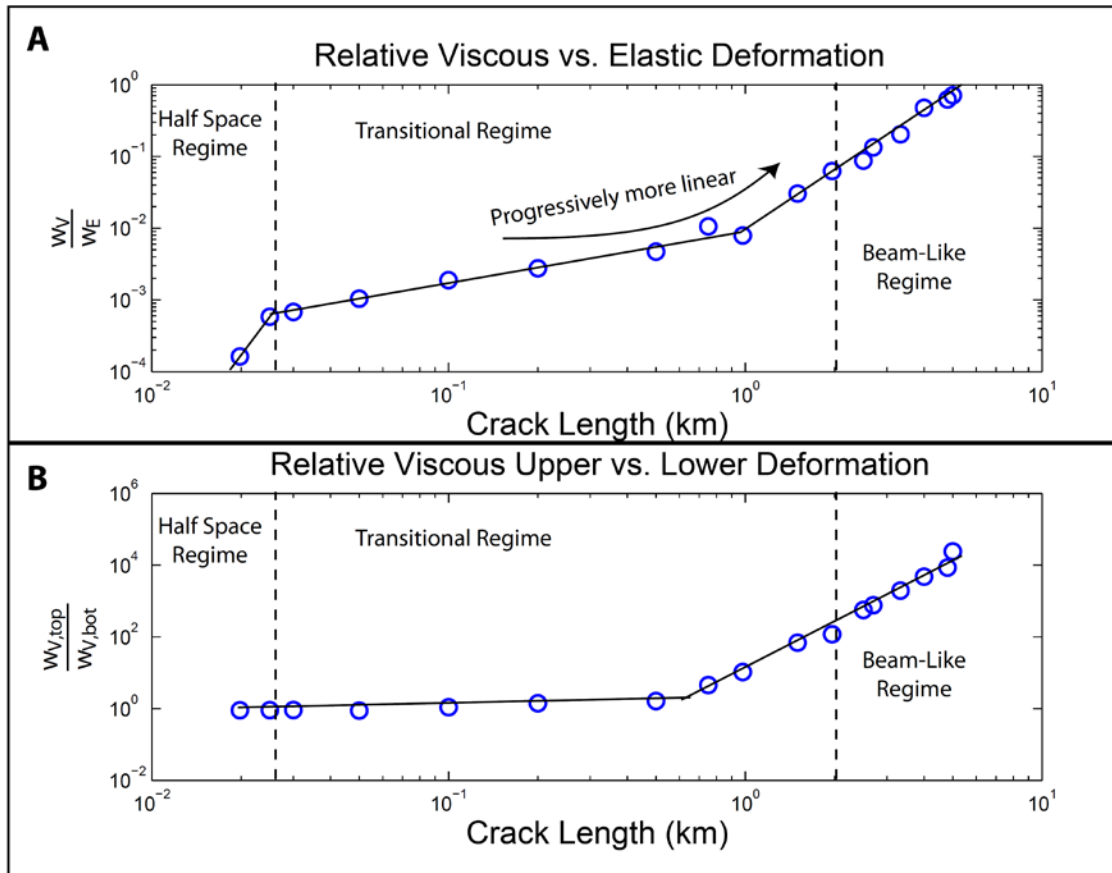


Figure 5.7: Summary figure for our nonlinear viscoelastic finite element modeling, where each point represents a separate model result. Panel A shows the relative magnitude of the viscous to elastic deformation, while Panel B shows the relative magnitude of the viscous deformation in the upper body compared to that of the lower body. The lines connecting the points are added to aid in visualizing the trend in the data. The three regimes defined in the background of each panel are defined and discussed in the main body of the text.

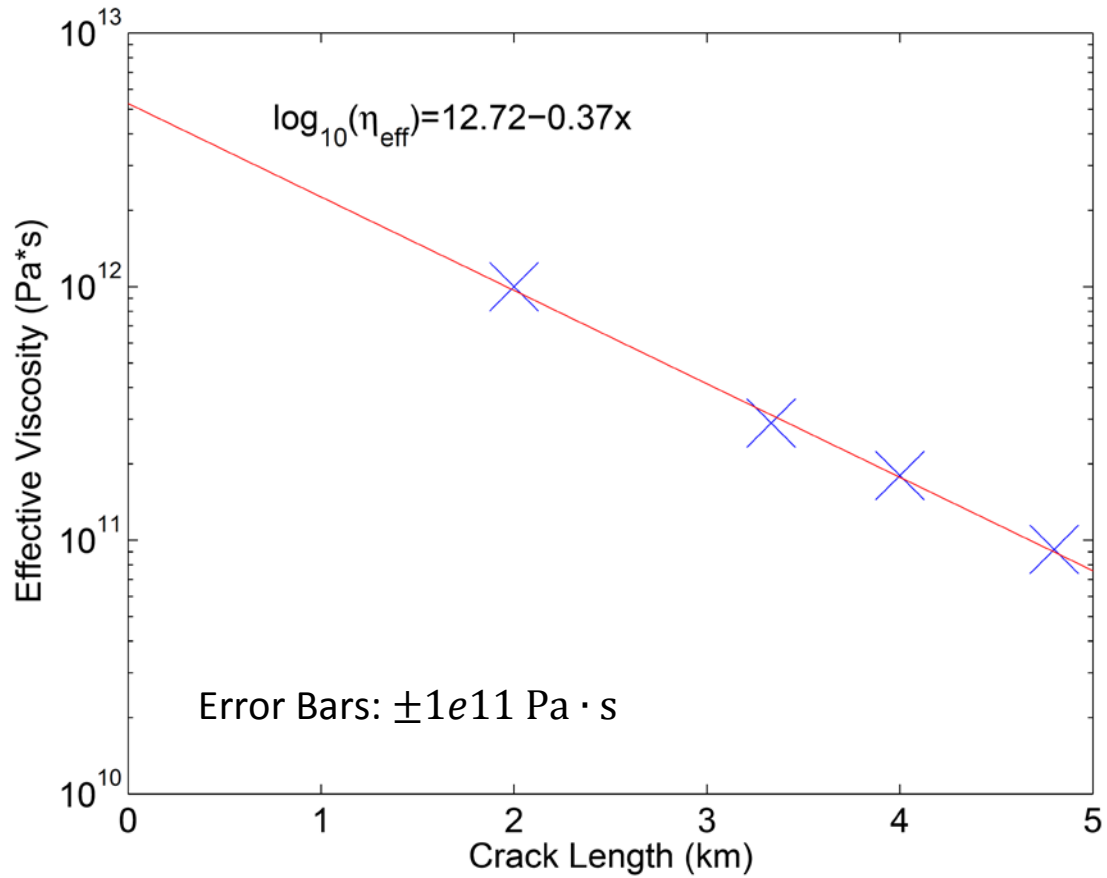


Figure 5.8: Fit of the (linear) effective viscosities approximating the nonlinear solutions as a function of crack length. See discussion in text for justification for fitting nonlinear model results with linear models. The fitted line defines the trend in effective viscosity values used to create our pseudo-nonlinear viscoelastic model.

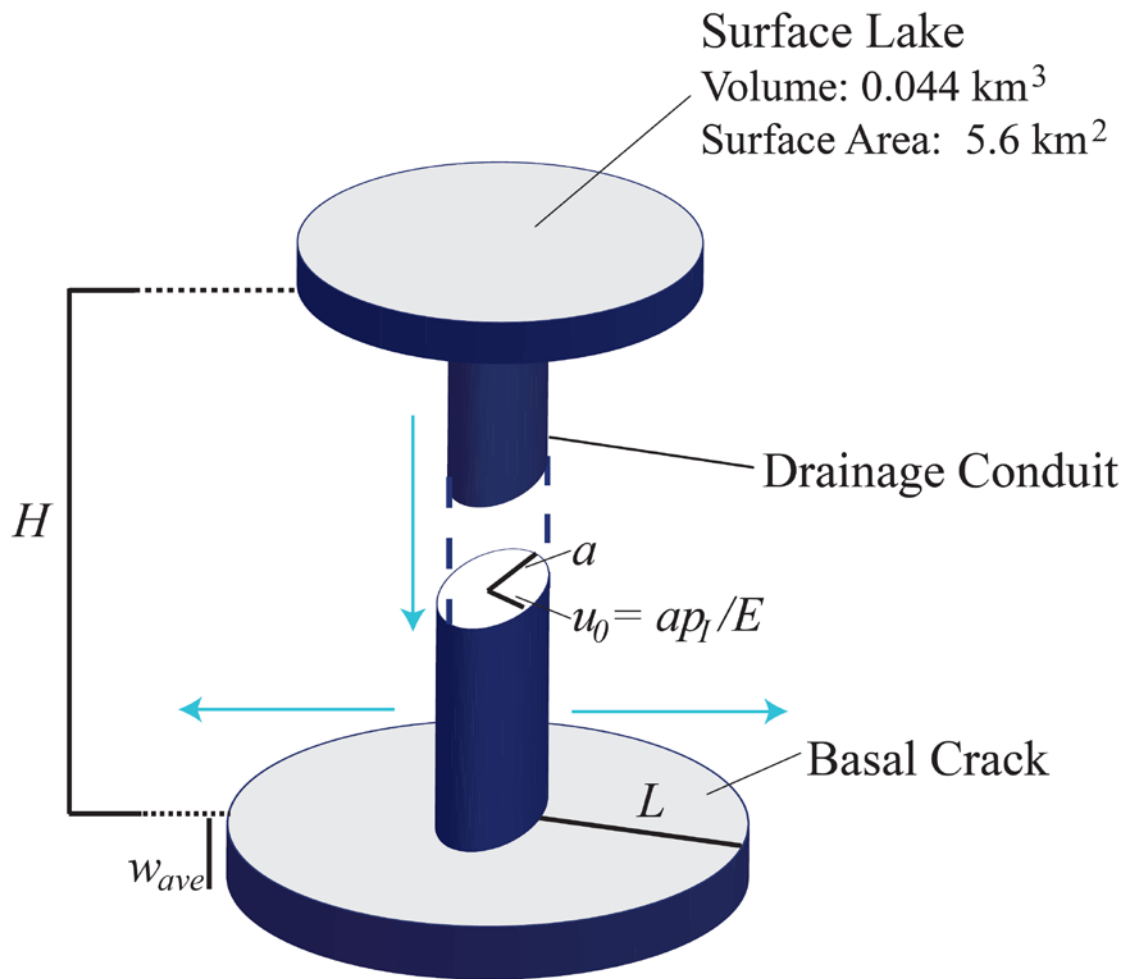


Figure 5.9: Schematic diagram of the fluid volume system used in section 5.4 to approximate the total drained fluid volume. The surface lake is assumed to have a constant surface area of 5.6 km², meaning that the depth is assumed to be 7.9 meter. The drainage conduit has is an ellipsoidal cylinder, with semi-major axes a and u_0 . Before drainage is complete, the height of the water level in the conduit is H , the thickness of the ice. Once drainage finishes, the water level becomes H_w , as defined in equation 5.12. Finally, the basal crack is assumed to extend radially and to have a thickness of w_{ave} , the average crack opening.

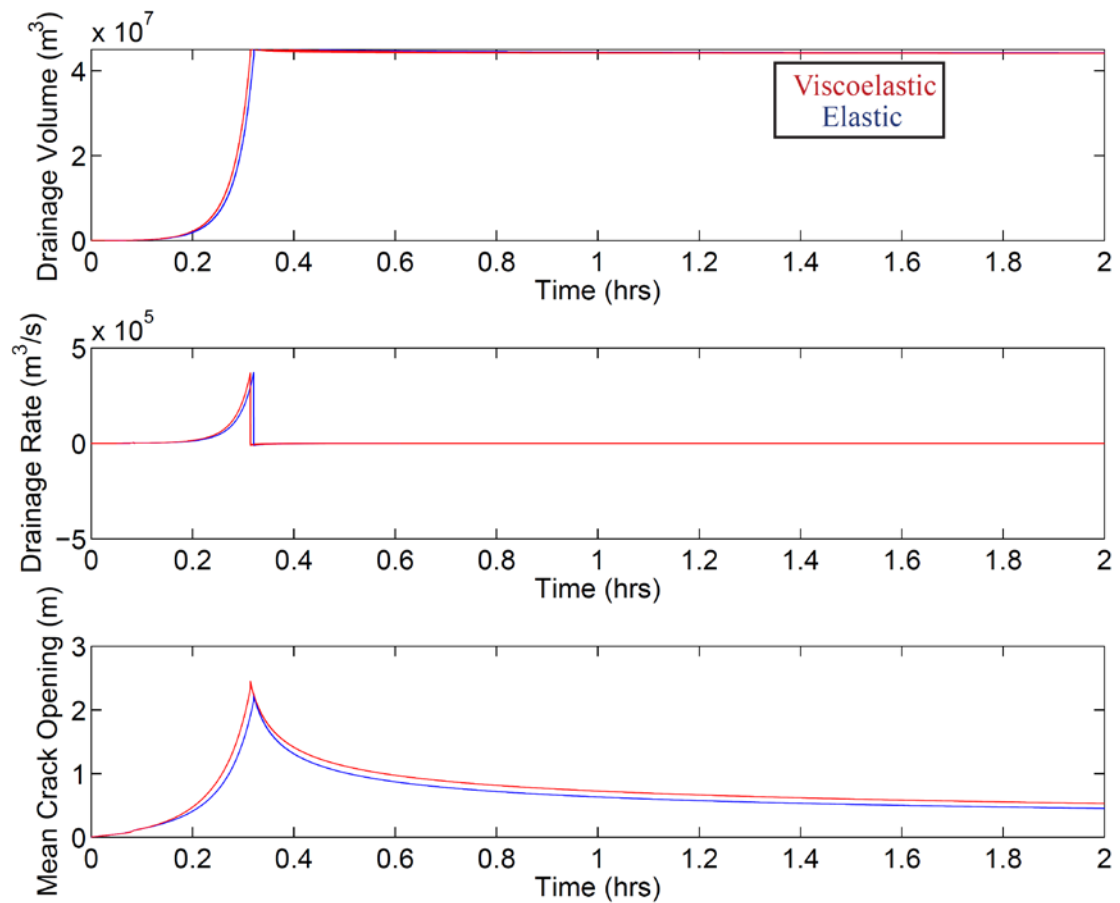


Figure 5.10: Plots of the drainage volume (A), drainage rate (B) and the average crack opening (C) for four models over a range of a/L values. The drainage volume and crack openings are found explicitly from our models, while the drainage rate is the time derivative of the drainage volume. The four model results are close enough to be indistinguishable from one another at the shown scale. The red lines show the results for the viscoelastic models, while the blue lines show the elastic model outputs. Note that while the models with different rheologies are not identical, the values all three parameters are similar between the two models.

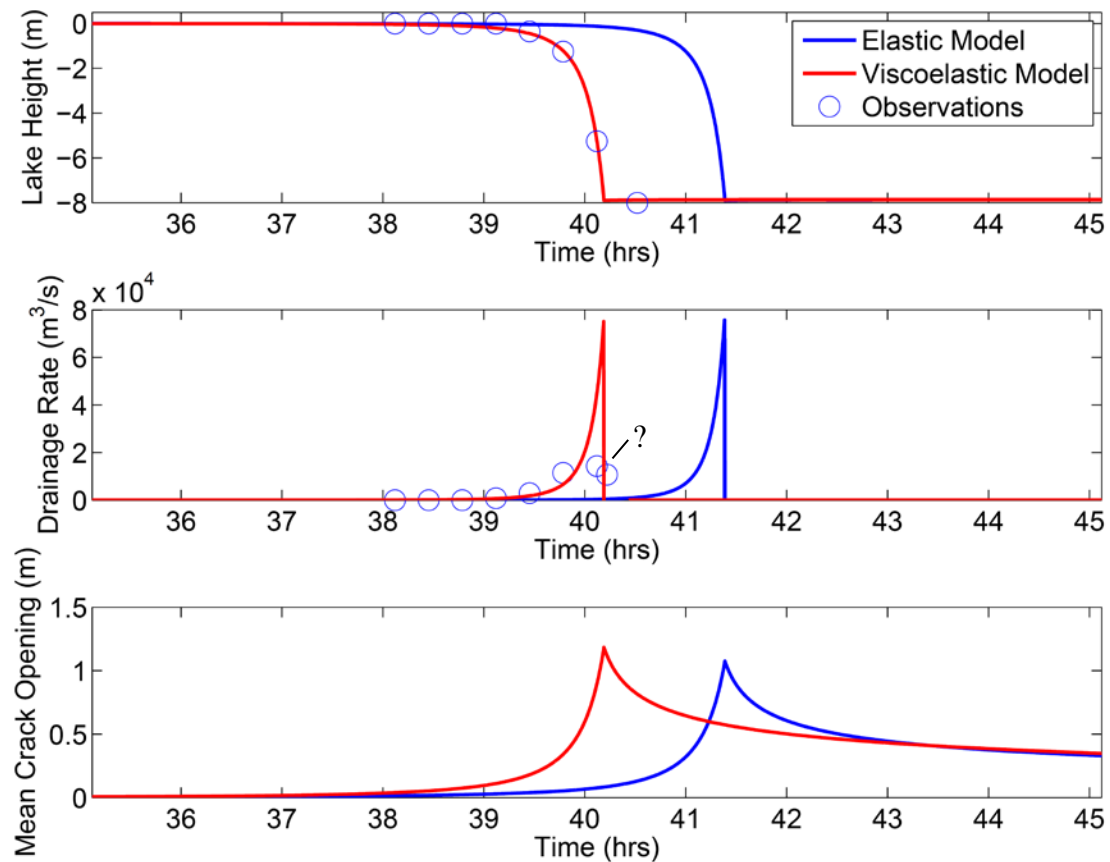


Figure 5.11: Plots of the surface lake level (A), drainage rate (B) and the average crack opening (C) for our fluid drag model with a best-fit of $a/L=0.51$. The crack openings are found explicitly from our models, while the surface lake level is calculated from the drainage volume assuming a constant lake surface area and the drainage rate is the time derivative of the drainage volume. The red lines show the results for the viscoelastic models, while the blue lines show the elastic model outputs. The circles are the lake level values taken from Das et al. (2008). The observational drainage rates are calculated from the time derivative of these values, with the peak observation drainage rate being 14,300 m^3/s . Note that the observational data have been shifted in time to overlie the model results.

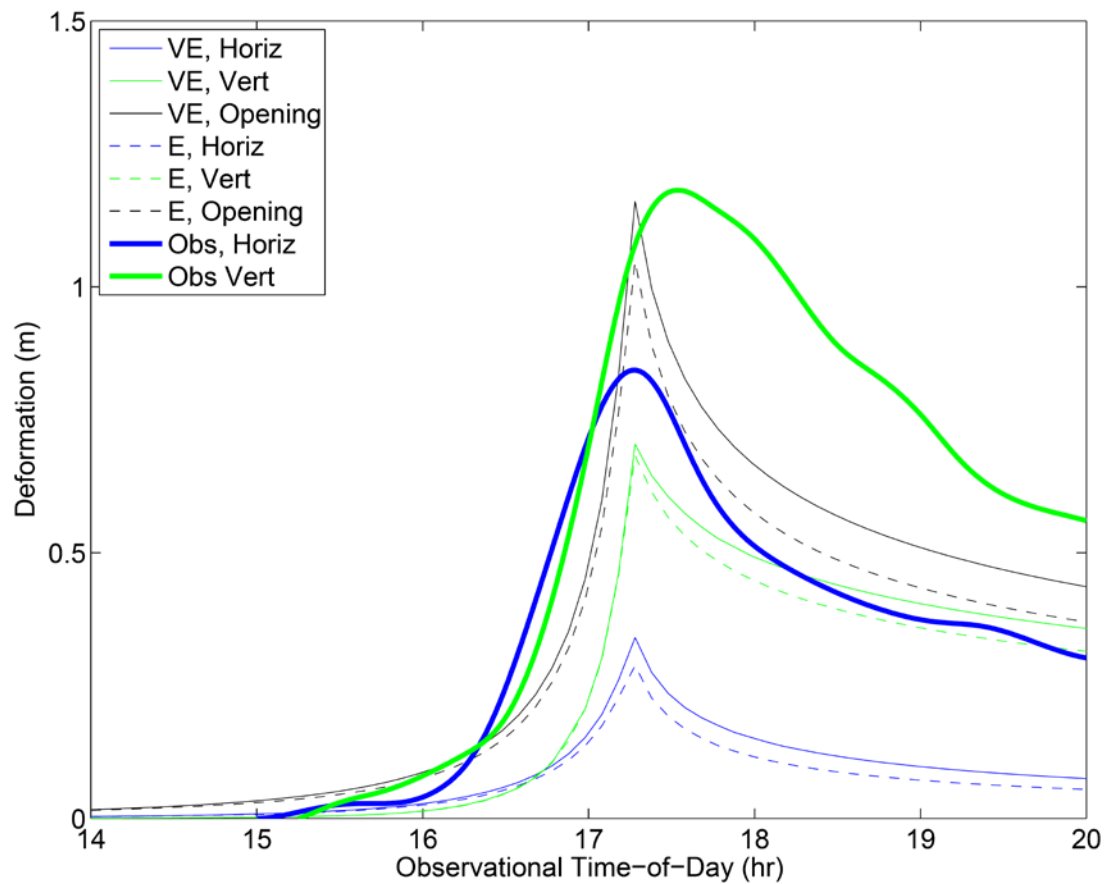


Figure 5.12: Observational and modeled surface deformation at a location 1.7 kilometers away from the main drainage conduit. Fine lines represent the viscoelastic model results, dashed lines the elastic model results, and bolded lines the observations. The line color corresponds to: blue, horizontal surface displacement; green, vertical surface displacement; black, crack opening (model only). Note that the model results are shifted in time such that the peak in horizontal deformation is the common reference time between the observations and the model results (see discussion in the main text for a justification of this reference point).

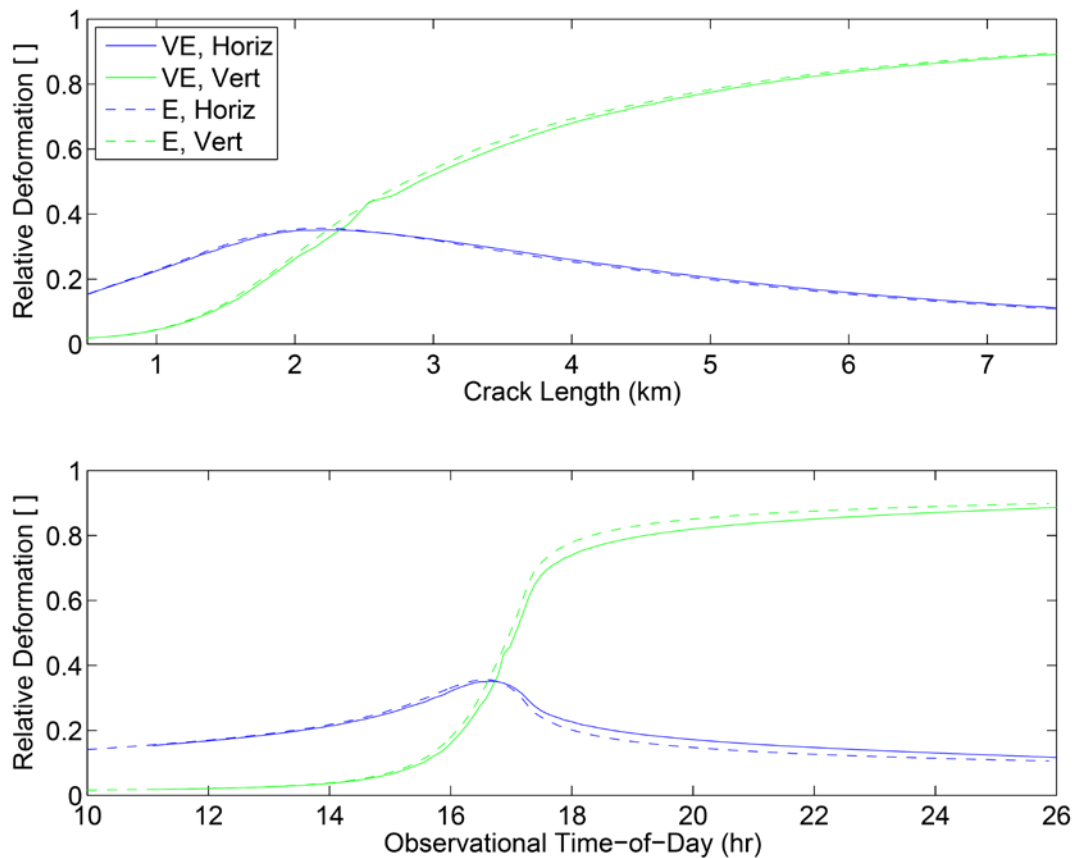


Figure 5.13: Plots of the relative surface horizontal (blue) and vertical (green) surface displacements for our elastic (dashed) and viscoelastic (solid) models, with respect to crack length (A) and time of day (B, the same horizontal scale as in figure 5.12). The relative surface displacement is the modeled surface displacement at a location 1.7 kilometers away from the main drainage conduit, divided by the maximum basal crack opening value, thus removing influence of the changing pressure from the output. The horizontal component shows a peak at about 2.2 kilometers/16.7 hours that is related only to the geometrical effect of the crack growing beneath the observational location. Such a feature is not seen in the vertical component of the relative surface deformation.

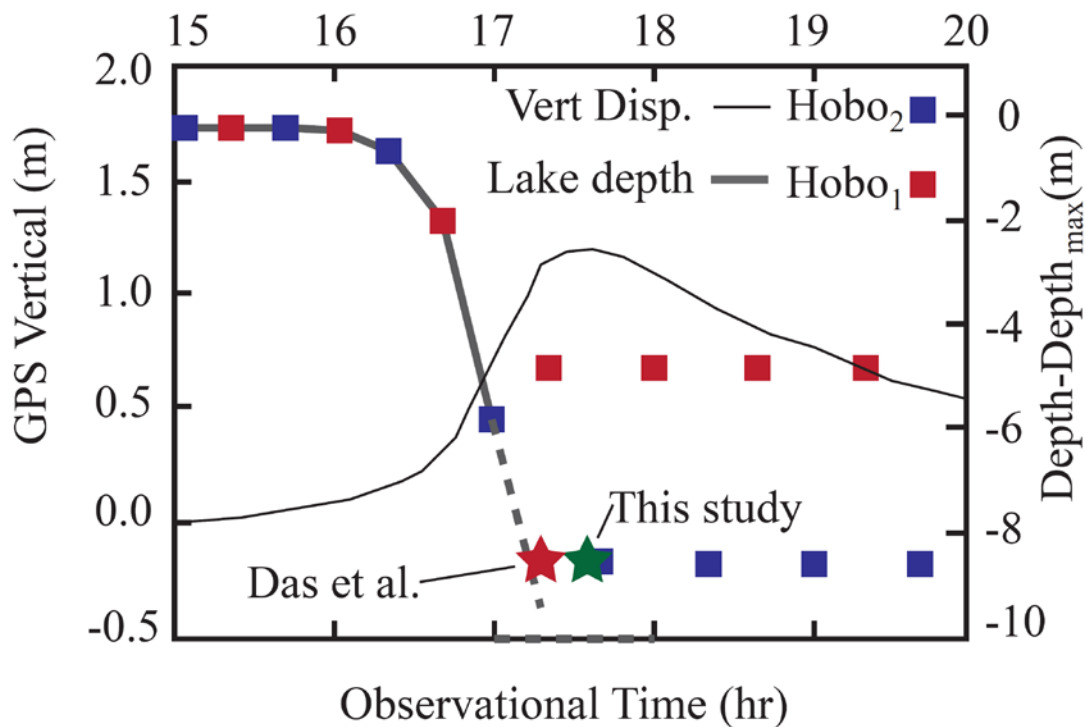


Figure 5.14: Lake level and vertical GPS data reproduced from figure 2B of Das et al. (2008). The red and blue squares are the observations of lake level from the two stations Hobo1 and Hobo2, while the thin black line is the vertical component of the GPS displacement, shifted to have a zero relative vertical offset at the start of the observational window shown in this figure. The red star shows the timing of the drainage, as estimated by Das et al. (2008), while the green star shows our estimate of the drainage timing, which is coincident with the peak in the vertical GPS displacements.

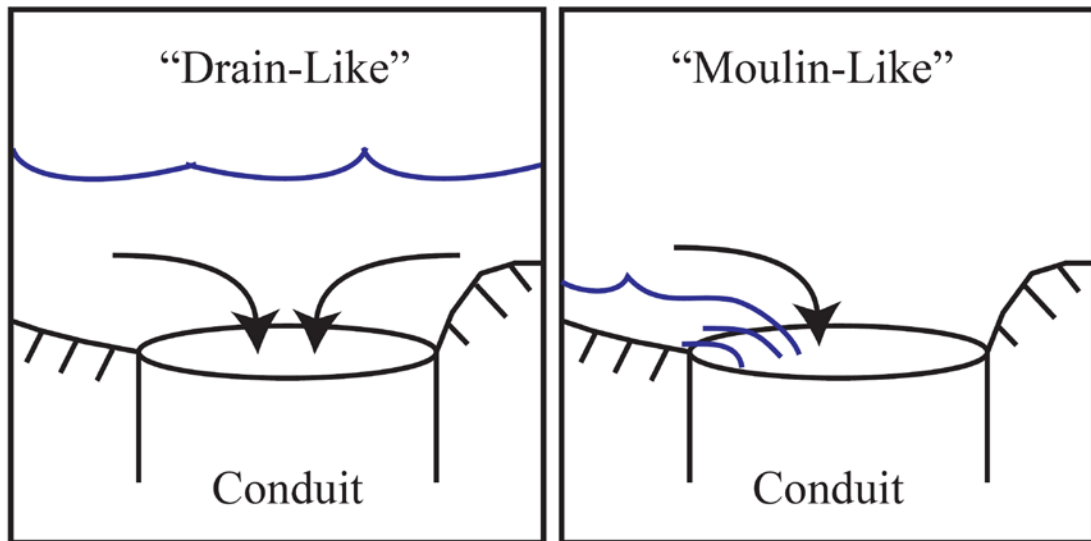


Figure 5.15: Conceptual images of the two different drainage styles described in section 5.5.1.1. The “drain-like” mode, on the left, is assumed to be the major drainage regime while the lake is at a high level. The “moulin-like” mode, on the right, is a potential style of low lake level drainage that would have a significantly reduced drainage rate, as is seen observationally when the lake is nearly completely drained.

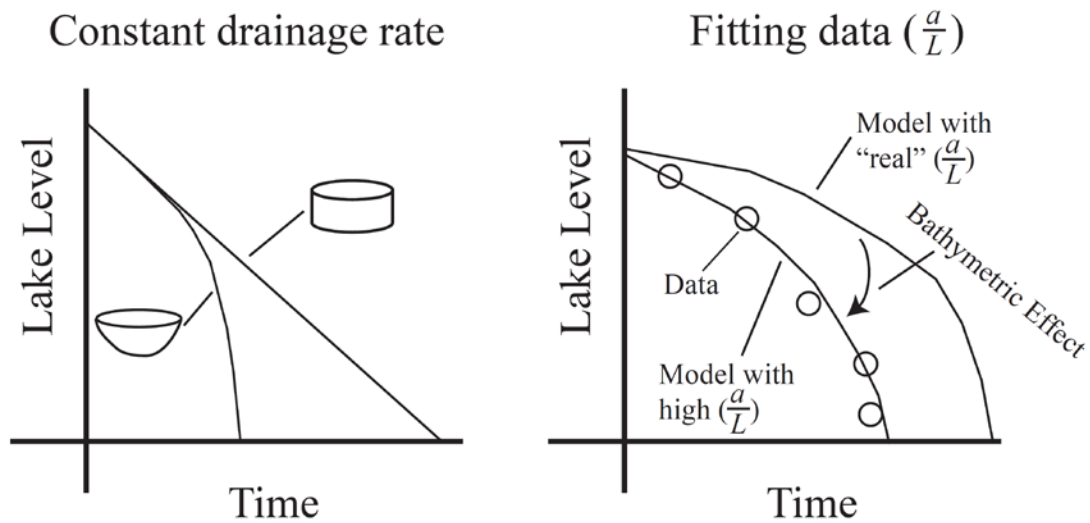


Figure 5.16: Schematic diagrams of the effects that a variable cross-sectional area of the surface lake will have on lake level observations and the problems introduced in using these data as a model constraint. The plot on the left assumes that there is a constant drainage rate of fluid into a conduit at the bottom the model lake. For a constant area lake, the lake level falls linearly; however, if the lake's area decreases with depth, the lake level fall seemingly accelerates late in the drainage process. In the plot on the right, a theoretical assemblage of lake level data is shown, with two of our model curves shown schematically. The model run with the "real" conduit size does not fit the lake level data, due to the possibility of a bathymetric effect on the lake level that is independent of the real drainage rate and conduit geometry.

| Variable Name | Dimensional | Non-dimensional |
|-----------------|-------------|----------------------------|
| Position | x | $\hat{x} = x/L$ |
| Pressure | p | $\hat{p} = p/p_I$ |
| Displacement | u | $\hat{u} = uE' / (p_I L)$ |
| | w | $\hat{w} = wE' / (p_I L)$ |
| Fluid Velocity | U | $\hat{U} = U_{tip}$ |
| Time | t | $\hat{t} = tU_{tip}/L$ |
| Tangent Modulus | S_{VE} | $\hat{S}_{VE} = S_{VE}/E'$ |

Table 5.1: List of variables with dimensional and non-dimensional versions. The

constants used in the non-dimensionalization are L , crack length; p_I , input pressure;

$E' = E/(1 - \nu^2)$, the plane-strain Young's modulus; $U_{tip} = \phi U_s = \phi \sqrt{\frac{p_I}{\rho}} \left(\frac{p_I}{E'}\right)^{2/3} \left(\frac{L}{k}\right)^{1/6}$,

the fluid velocity at the crack tip; ϕ , the velocity scale constant; ρ , the fluid density; and

k , the Nikuradse roughness height

| | Relative Peak Timing (hrs) | Peak Timing Difference (%) | Peak Magnitude (m) | Tail Magnitude at 20:00 (m) | Relative Tail to Peak (%) | Vertical to Horizontal Disp. (%) | Crack Length at Peak (km) |
|--------------|-------------------------------------|-------------------------------------|--------------------------|--------------------------------------|------------------------------------|--|------------------------------------|
| E, Horiz | 0 | 0 | 0.29 | 0.055 | 19 | 234 | 3.661 |
| E, Vert. | 0 | 0 | 0.68 | 0.32 | 47 | | |
| VE, Horiz | 0 | 0 | 0.34 | 0.076 | 22 | 206 | 3.476 |
| VE, Vert | 0 | 0 | 0.70 | 0.36 | 51 | | |
| Obs Horiz | 0 | 0 | 0.84 | 0.30 | 35 | 140 | ? |
| Obs Vert | 0.26 | 11.4 | 1.18 | 0.56 | 47 | | |
| E, Crack | 0 | 0 | 1.05 | 0.37 | 35 | n/a | n/a |
| VE, Crack | 0 | 0 | 1.16 | 0.44 | 38 | | |

Table 5.2: Quantities of interest shown in figure 5.12. E refers to the elastic models,

while VE refers to the viscoelastic models. The relative peak timing is with respect to the observation and modeled horizontal displacement peak. The tail value is taken at 20:00 (20 hours), and is chosen to give a quantitative comparison of the drop in surface displacement at a time after the peak displacement. The vertical to horizontal displacement percentage is the percentage of the peak vertical displacement compared the peak horizontal displacement. Finally, the crack length at the peak is the length of the basal crack at the time of the peak displacement in that model. The crack length for the observed lake drainage event is not known. The crack rows at the bottom refer to the modeled crack opening for the elastic and viscoelastic models.

Appendix 5A: Effective Stress Formulation for Linear

Viscoelasticity

Here we summarize the effective stress formulation for the deformation of a linear viscoelastic model. To begin, imagine the stress-strain relationship for a theoretical linear Maxwell viscoelastic medium, with constant moduli, under the action of a constant stress σ that is, at some time t , removed. From using the definition of a Maxwell material, we see immediately that the strain just before the stress is removed is:

$$\varepsilon = \frac{\sigma}{E} + \frac{t\sigma}{\eta} \quad (5A.1)$$

In equation 5A.1, the first term represents the recoverable elastic strain, while the second term is the irrecoverable viscous strain. Figure 5A.1 plots the trajectory of this relationship in stress-strain space through the entire stressing cycle. At any given time, the change in strain as a function of stress for the entire cycle up can be represented by a line connecting the origin to the current location in stress-strain space. We call the slope of this line \mathcal{C}_{VE} , the consistent viscoelastic tangent modulus. We define \mathcal{C}_{VE} to be:

$$\mathcal{C}_{VE} = \frac{d\sigma}{d\varepsilon} \quad (5A.2)$$

Note that \mathcal{C}_{VE} is dependent on the value of t and η , and at time $t = 0$ it is equivalent to the Young's modulus. This approach is equivalent to using the viscoelastic correspondence principle (e.g., Findley et al., 2011).

A brief summary of the derivation of \mathcal{C}_{VE} from Aagaard et al. (2009) and Kojic and Bathe (1987) follows. Next, we define the deviatoric stress and strain tensors in the following fashion:

$$S_{ij} = \sigma_{ij} - P\delta_{ij} \quad (5A.3)$$

$$e_{ij} = \varepsilon_{ij} - \theta\delta_{ij} \quad (5A.4)$$

Where S is the deviatoric stress tensor, σ is the stress tensor, P is the hydrostatic pressure, δ is the Kronecker Delta function, e is the deviatoric strain tensor, ε is the strain tensor, and θ is the dilatation. We make the assumption that the volumetric strain is inelastic (i.e., that viscous body is incompressible), so that we can make the assertion that:

$${}^{t+\Delta t}\bar{S} = \frac{{}^{t+\Delta t}E}{1+{}^{t+\Delta t}\nu} ({}^{t+\Delta t}\bar{e} - {}^{t+\Delta t}\bar{e}^P - {}^{t+\Delta t}\bar{e}^C) \quad (5A.5)$$

$${}^{t+\Delta t}\sigma_m = \frac{{}^{t+\Delta t}E}{1-2{}^{t+\Delta t}\nu} ({}^{t+\Delta t}e_m - {}^{t+\Delta t}e^{th}) \quad (5A.6)$$

Where:

${}^{t+\Delta t}\bar{S}$ is the deviatoric stress tensor defined by ${}^{t+\Delta t}\bar{S} = {}^{t+\Delta t}\sigma_{ij} - {}^{t+\Delta t}\sigma_m\delta_{ij}$

${}^{t+\Delta t}\bar{e}$ is the deviatoric strain tensor defined by ${}^{t+\Delta t}\bar{e} = {}^{t+\Delta t}\varepsilon_{ij} - {}^{t+\Delta t}\varepsilon_m\delta_{ij}$

${}^{t+\Delta t}\bar{e}^P$ is the plastic deviatoric strain tensor

${}^{t+\Delta t}\bar{e}^C$ is the creep deviatoric strain tensor

${}^{t+\Delta t}\sigma_m$ is the mean stress tensor defined by ${}^{t+\Delta t}\sigma_m = {}^{t+\Delta t}\sigma_{ii}/3$

${}^{t+\Delta t}\varepsilon_m$ is the mean strain tensor defined by ${}^{t+\Delta t}\varepsilon_m = {}^{t+\Delta t}\varepsilon_{ii}/3$

${}^{t+\Delta t}E$ is the Young's modulus corresponding to temperature ${}^{t+\Delta t}T$

${}^{t+\Delta t}\nu$ is the Poisson's ratio corresponding to temperature ${}^{t+\Delta t}T$

${}^{t+\Delta t}\varepsilon^{th}$ is the thermal strain

$t + \Delta t$ means corresponding to time $t + \Delta t$

Removing any thermal contribution from this problem and adding in the initial stress and strain states, we can rewrite (5A.5) and (5A.6) to:

$${}^{t+\Delta t}\bar{S} = \frac{E}{1+\nu} ({}^{t+\Delta t}\bar{e} - {}^{t+\Delta t}\bar{e}^P - {}^{t+\Delta t}\bar{e}^C - \bar{e}^I) + \bar{S}^I \quad (5A.7)$$

$${}^{t+\Delta t}\sigma_m = \frac{E}{1-2\nu} ({}^{t+\Delta t}e_m - e^I) + \sigma_m^I \quad (5A.8)$$

As ε_m is zero for creep and plasticity, σ_m can be found directly from equation (5A.8).

Using a discrete timestep of Δt , equation (5A.7) can be rewritten as:

$${}^{t+\Delta t}\bar{S} = \frac{E}{1+\nu} ({}^{t+\Delta t}\bar{e}' - \Delta\bar{e}^P - \Delta\bar{e}^C) + \bar{S}^I \quad (5A.9)$$

Where:

$${}^{t+\Delta t}\bar{e}' = {}^{t+\Delta t}\bar{e} - {}^t\bar{e}^P - {}^t\bar{e}^C - \bar{e}^I \quad (5A.10)$$

Thus, the problem has been reduced to determining the values of ${}^{t+\Delta t}\bar{S}$, Δe^P , and Δe^C . We now apply the implicit α -method of Bathe (1995). First, the effective creep strain is written:

$$\Delta\bar{e}^C \equiv \sqrt{\frac{2}{3}\Delta\bar{e}^C \cdot \Delta\bar{e}^C} \quad (5A.11)$$

And the effective creep stress:

$${}^{t+\Delta t}\bar{\sigma} \equiv \sqrt{\frac{3}{2}{}^{t+\Delta t}\bar{S} \cdot {}^{t+\Delta t}\bar{S}} \quad (5A.12)$$

The weighted effective stress is then defined to be:

$$\begin{aligned} {}^\tau\bar{\sigma} &= (1 - \alpha) {}^t\bar{\sigma} + \alpha {}^{t+\Delta t}\bar{\sigma} \\ &= (1 - \alpha) \sqrt{\frac{3}{2} {}^t\bar{S} \cdot {}^t\bar{S}} + \alpha \sqrt{\frac{3}{2} {}^{t+\Delta t}\bar{S} \cdot {}^{t+\Delta t}\bar{S}} \end{aligned} \quad (5A.13)$$

Where α , a weighing factor, is between 0 and 1. Note that if α is equal to 0, this implicit formulation reverts to an explicit formulation. The α -method then allows us to write:

$$\Delta \bar{e}^C = \Delta t \tau \gamma \tau \bar{S} \quad (5A.14)$$

Where:

$$\tau \gamma = \frac{3 \Delta \bar{e}^C}{2 \bar{\sigma} \tau} \quad (5A.15)$$

$$\tau \bar{S} = (1 - \alpha) \bar{S} + \alpha^{t+\Delta t} \bar{S} \quad (5A.16)$$

The next step is to consider the creep rheology, which has the general form:

$$\bar{e}^C = f_1(\bar{\sigma}) f_2(t) f_3(T) \quad (5A.17)$$

Converting the power law rheology into the effective stress formulation, we get:

$$\bar{e}^C = a_0(\bar{\sigma})^{a_1} (t)^{a_2} f(T) \quad (5A.18)$$

To solve this material model, first equation (5A.17) is changed into a function of incremental creep strain:

$$\Delta \bar{e}^C = \Delta t f_1(\tau \bar{\sigma}) \dot{f}_2(\tau) f_3(\tau T) \quad (5A.19)$$

where $\dot{f}_2(\tau)$ is the time derivative of f_2 at weighted time τ and τT is the weighted temperature:

$$\tau = t + \alpha \Delta t \quad (5A.20)$$

$$\tau T = (1 - \alpha) T + \alpha^{t+\Delta t} T \quad (5A.21)$$

Now it behooves us to reformulate our creep laws into more usable forms. First, the invariants of the creep strain tensor and deviatoric stress tensors will be used in place of \bar{e}^C and $\bar{\sigma}$, respectively. Using the example of a triaxial creep experiment with a general nonlinear viscoelastic rheology, we get:

$$\dot{e}_{11}^C = A_E e^{\frac{-Q}{RT}} (\sigma_1 - \sigma_3)^n = A_E e^{\frac{-Q}{RT}} \sigma_d^n \quad (5A.22)$$

In a triaxial experiment, the main stress components are $\sigma_2 = \sigma_3 = \sigma_c$ which is the confining pressure of the experiment. Assuming that σ_1 is the applied stress in the main

axial direction, the hydrostatic pressure can be defined to be:

$$P = \frac{\sigma_1 + 2\sigma_c}{3} \quad (5A.23)$$

And thus the deviatoric stresses are:

$$\begin{aligned} S_1 &= \frac{2}{3}(\sigma_1 - \sigma_c) \\ S_2 = S_3 &= -\frac{1}{3}(\sigma_1 - \sigma_c) \end{aligned} \quad (5A.24)$$

As $\sigma_c = \sigma_3$, we get:

$$\begin{aligned} S_1 &= \frac{2}{3}\sigma_d \\ S_2 = S_3 &= -\frac{1}{3}\sigma_d \end{aligned} \quad (5A.25)$$

Assuming the material is incompressible and isotropic, the strain rates are:

$$\begin{aligned} \dot{\epsilon}_{11}^C &= \dot{\epsilon}_{11} \\ \dot{\epsilon}_{22}^C = \dot{\epsilon}_{33}^C &= -\frac{1}{2}\dot{\epsilon}_{11} \end{aligned} \quad (5A.26)$$

Thus the second deviatoric stress and strain-rate invariants are, respectively:

$$\sqrt{J'_2} = \sqrt{-S_1S_2 - S_2S_3 - S_1S_3} = \frac{\sigma_d}{\sqrt{3}} \quad (5A.27)$$

Applying the definition 5A.27 to equation 5A.22, we get:

$$\sqrt{\dot{L}'_2^C} = A_E \frac{\sqrt{3}^{n+1}}{2} e^{-\frac{Q}{RT}} \sqrt{J'_2}^{-n} \quad (5A.28)$$

We can compact the constants, for example:

$$A_T = A_M e^{-\frac{Q}{RT}} = A_E \frac{\sqrt{3}^{n+1}}{2} e^{-\frac{Q}{RT}} \quad (5A.29)$$

However, the formulation of A_T shown in 5A.29 is not, strictly speaking, constant as it depends of the value of the stress exponent n . This can be avoided by introducing a reference stress and strain-rate σ_0 and $\dot{\epsilon}_0$ such that the flow law, in terms of the second

invariants, becomes:

$$\frac{\sqrt{\dot{I}'_2}}{\dot{e}_0} = \frac{\sqrt{J'_2}^{-n}}{S_0} \quad (5A.30)$$

where

$$A_T = \frac{\dot{e}_0}{S_0^n} \quad (5A.31)$$

Thus the component form of 5A.27 can be rewritten, using 5A.29-5A.31, as:

$$\dot{e}_{ij}^c = \frac{\dot{e}_0 \sqrt{J'_2}^{-n-1} S_{ij}}{S_0^n} \quad (5A.32)$$

Now, using equation (5A.19), we can find the incremental strain of each rheological model:

$$\begin{aligned} \Delta \bar{e}^c &\approx \frac{\Delta t \dot{e}_0 \sqrt{\tau J'_2}^{-n-1} \bar{S}}{S_0^n} \\ &= \frac{\Delta t \dot{e}_0 \bar{\tau} \sigma^{n-1} \bar{S}}{\sqrt{3}^{n-1} S_0^n} \end{aligned} \quad (5A.33)$$

From equation (5A.14) we can find the value of τ_γ and from equation (5A.15) the value of $\Delta \bar{e}^c$ in the following manner:

$$\tau_\gamma = \frac{\dot{e}_0 \sqrt{\tau J'_2}^{-n-1}}{S_0^n} \quad (5A.34)$$

$$\Delta \bar{e}^c \approx \frac{2 \Delta t \dot{e}_0 \tau \bar{\sigma}^n}{\sqrt{3}^{n+1} S_0^n} \quad (5A.35)$$

Plugging 5A.34, 5A.35, and 5A.16 into 5A.9 results in the following forms, assuming that the condition of ${}^{t+\Delta t} \bar{e}^P = 0$ (no plasticity) is enforced:

$${}^{t+\Delta t} \bar{S} = \frac{1}{\alpha_E} \{ \bar{e}' - \Delta t \tau_\gamma [(1 - \alpha) {}^t \bar{S} + \alpha {}^{t+\Delta t} \bar{S}] \} + \bar{S}^I \quad (5A.36)$$

Where

$$a_E = \frac{1 + \nu}{E} \quad (5A.37)$$

Equation (5A.36) can be rewritten as:

$${}^{t+\Delta t}\bar{S}(a_E + \alpha\Delta t \tau\gamma) = \bar{e}'' - \Delta t \tau\gamma(1 - \alpha) {}^t\bar{S} + \alpha {}^{t+\Delta t}\bar{S} + a_E \bar{S}^I \quad (5A.38)$$

Taking the scalar inner product of 5A.38 results in the form:

$${}^{t+\Delta t}J'_2 a^2 - b + c \tau\gamma - d^2 \tau\gamma^2 = F = 0 \quad (5A.39)$$

Where

$$\begin{aligned} a &= a_E + \alpha\Delta t \tau\gamma \\ b &= \frac{1}{2} {}^{t+\Delta t}\bar{e}' \cdot {}^{t+\Delta t}\bar{e}' + a_E {}^{t+\Delta t}\bar{e}' \cdot \bar{S}^I + a_E^2 J_2^I \\ c &= \Delta t(1 - \alpha) {}^{t+\Delta t}\bar{e}' \cdot {}^t\bar{S} + \Delta t(1 - \alpha) a_E {}^t\bar{S} \cdot \bar{S}^I \\ d &= \Delta t(1 - \alpha) \sqrt{{}^tJ'_2} \end{aligned} \quad (5A.40)$$

5A.39 is solved by taking the derivative of 5A.39 with respect to $\sqrt{{}^{t+\Delta t}J'_2}$. This results

in a general answer, shown below as equations 5A.41 and 5A.42:

$$\frac{\delta F}{\delta \sqrt{{}^{t+\Delta t}J'_2}} = 2a^2 \sqrt{{}^{t+\Delta t}J'_2} + \frac{\delta \tau\gamma}{\delta \sqrt{{}^{t+\Delta t}J'_2}} (2\alpha\Delta t {}^{t+\Delta t}J'_2 + c + d^2) \quad (5A.41)$$

$$\frac{\delta \tau\gamma}{\delta \sqrt{{}^{t+\Delta t}J'_2}} = \frac{\dot{e}_0 \alpha (n-1) \sqrt{{}^tJ'_2}^{n-2}}{S_0^n} \quad (5A.42)$$

Lastly, we need to compute the viscoelastic tangent material matrix, which relates stress to strain. It is:

$$\mathbf{C}_{VE} = \frac{\delta {}^{t+\Delta t}\bar{\sigma}}{\delta {}^{t+\Delta t}\bar{\epsilon}} \quad (5A.43)$$

The stress vector is:

$$\begin{aligned} {}^{t+\Delta t}\bar{\sigma}_i &= {}^{t+\Delta t}S_i + {}^{t+\Delta t}P_i \text{ for } i = 1,2,3 \\ {}^{t+\Delta t}\bar{\sigma}_i &= {}^{t+\Delta t}S_i \text{ for } i = 4,5,6 \end{aligned} \quad (5A.44)$$

And thus:

$$\begin{aligned} C_{ij}^{VE} &= C_{ij}^{Dev} + \frac{1}{3} \frac{E}{1-2\nu} \quad i \leq 3, j \leq 3 \\ C_{ij}^{VE} &= C_{ij}^{Dev} \text{ otherwise} \end{aligned} \quad (5A.45)$$

To solve for C_{ij}^{Dev} :

$$C_{ij}^{Dev} = \frac{{}^{t+\Delta t}S_i}{{}^{t+\Delta t}\varepsilon_j} = \frac{\delta^{t+\Delta t}S_i}{\delta^{t+\Delta t}e'_{l_k}} \frac{\delta^{t+\Delta t}e'_{l_k}}{\delta^{t+\Delta t}e_l} \frac{\delta^{t+\Delta t}e_l}{\delta^{t+\Delta t}\varepsilon_j} \quad (5A.46)$$

We now solve each derivative term in 5A.46 separately, saving $\frac{\delta^{t+\Delta t}S_i}{\delta^{t+\Delta t}e'_{l_k}}$ for last. By taking the derivative of equation 5A.10 with respect to ${}^{t+\Delta t}e_l$ we find directly:

$$\frac{\delta^{t+\Delta t}e'_{l_k}}{\delta^{t+\Delta t}e_l} = \delta_{kl} \quad (5A.47)$$

And from equation 5A.4 we find:

$$\begin{aligned} \frac{\delta^{t+\Delta t}e'_{l_k}}{\delta^{t+\Delta t}e_l} &= \frac{1}{3} \begin{bmatrix} 2 & -1 & -1 \\ -1 & 2 & -1 \\ -1 & -1 & 2 \end{bmatrix} \quad i \leq l, j \leq 3 \\ &= \delta_{ij} \text{ otherwise} \end{aligned} \quad (5A.48)$$

To solve for $\frac{\delta^{t+\Delta t}S_i}{\delta^{t+\Delta t}e'_{l_k}}$ it first becomes necessary to solve several other differentiations.

First, rewrite equation 5A.38 as:

$$\begin{aligned} F &= {}^{t+\Delta t}\bar{S}(a_E + \alpha \Delta t \tau \gamma) - {}^{t+\Delta t}\bar{e}'' + \Delta t \tau \gamma (1 - \alpha) {}^t\bar{S} - \alpha {}^{t+\Delta t}\bar{S} \\ &+ a_E \bar{S}^I = 0 \end{aligned} \quad (5A.49)$$

It follows directly that:

$$\frac{\delta F}{\delta^{t+\Delta t}e'_{l_k}} = -\delta_{ik} \quad (5A.50)$$

And:

$$\frac{\delta F}{\delta^{t+\Delta t} S_i} = a_E + \alpha \Delta t \tau_\gamma + \frac{\delta \tau_\gamma}{\delta^{t+\Delta t} S_i} \Delta t [\alpha^{t+\Delta t} S_i + (1 - \alpha) {}^t S_i] \quad (5A.51)$$

To find $\frac{\delta \tau_\gamma}{\delta^{t+\Delta t} S_i}$ first we α -expand τ_γ using equation 5A.34

$$\tau_\gamma = \frac{\dot{e}_0}{S_0^n} [\alpha \sqrt{{}^{t+\Delta t} J'_2} + \sqrt{{}^t J'_2}]^{n-1} \quad (5A.52)$$

Now product-rule expand $\frac{\delta \tau_\gamma}{\delta^{t+\Delta t} S_i}$:

$$\frac{\delta \sqrt{{}^{t+\Delta t} J'_2}}{\delta^{t+\Delta t} S_i} = \frac{\delta \tau_\gamma}{\delta \sqrt{{}^{t+\Delta t} J'_2}} \frac{\delta \sqrt{{}^{t+\Delta t} J'_2}}{\delta^{t+\Delta t} S_i} \quad (5A.53)$$

We know one set of derivatives from equation 5A.41. The other derivative is:

$$\frac{\delta \sqrt{{}^{t+\Delta t} J'_2}}{\delta^{t+\Delta t} S_i} = \frac{{}^{t+\Delta t} W_i}{2 \sqrt{{}^{t+\Delta t} J'_2}} \quad (5A.54)$$

Where

$$\begin{aligned} {}^{t+\Delta t} W_i &= {}^{t+\Delta t} S_i \text{ if } 1 \leq i \leq 3 \\ &= 2 {}^{t+\Delta t} S_i \text{ otherwise} \end{aligned} \quad (5A.56)$$

Thus the solutions to $\frac{\delta \tau_\gamma}{\delta^{t+\Delta t} S_i}$ are:

$$\frac{\delta \tau_\gamma}{\delta^{t+\Delta t} S_i} = \frac{\dot{e}_0 \alpha (n-1) \sqrt{{}^t J'_2}^{n-2} {}^{t+\Delta t} W_i}{2 \sqrt{{}^{t+\Delta t} J'_2} S_0^n} \quad (5A.57)$$

Now combining 5A.51 with 5A.57 and 5A.50, and recalling the Euler chain rule shown below:

$$\frac{\delta x}{\delta y} = - \frac{\frac{\delta z}{\delta y}}{\frac{\delta z}{\delta x}} \quad (5A.58)$$

results in the following, using $\tau S_i = \alpha^{t+\Delta t} S_i + (1 - \alpha) {}^t S_i$:

$$\frac{\delta^{t+\Delta t} S_i}{\delta^{t+\Delta t} e'_k} = \frac{\delta_{ik}}{\alpha_E + \alpha \Delta t \left[\tau_\gamma + \frac{\dot{e}_0 \tau S_i (n-1) \sqrt{\tau J'_2}^{n-2} t + \Delta t W_i}{2 \sqrt{t + \delta t J'_2 S_0^n}} \right]} \quad (5A.59)$$

Now C_{ij}^{VE} can be solved for:

$$C_{ij}^{VE} = \frac{1}{3} \frac{E}{1 - \nu} \begin{bmatrix} 1 & 1 & 1 & 0 & 0 & 0 \\ 1 & 1 & 1 & 0 & 0 & 0 \\ 1 & 1 & 1 & 0 & 0 & 0 \\ 0 & 0 & 0 & 0 & 0 & 0 \\ 0 & 0 & 0 & 0 & 0 & 0 \\ 0 & 0 & 0 & 0 & 0 & 0 \end{bmatrix} \quad (5A.60)$$

$$+ \frac{1}{3} \frac{\delta^{t+\Delta t} S_i}{\delta^{t+\Delta t} e'_k} \begin{bmatrix} 2 & -1 & -1 & 0 & 0 & 0 \\ -1 & 2 & -1 & 0 & 0 & 0 \\ -1 & -1 & 2 & 0 & 0 & 0 \\ 0 & 0 & 0 & 3 & 0 & 0 \\ 0 & 0 & 0 & 0 & 3 & 0 \\ 0 & 0 & 0 & 0 & 0 & 3 \end{bmatrix}$$

Modifying equation 5A.60 to represent a plane-strain condition for two-dimensions, we find that the consistent viscoelastic tangent modulus is:

$$\mathbf{C}_{VE} = \frac{1}{3} \left(\frac{E}{1 - 2\nu} \right) \begin{bmatrix} 1 & 1 & 0 \\ 1 & 1 & 0 \\ 0 & 0 & 1 \end{bmatrix} \quad (5A.61)$$

$$+ \frac{1}{3} \left(\frac{1 + \nu}{E} + \frac{\alpha \Delta t}{2\eta} \right)^{-1} \begin{bmatrix} 2 & -1 & 0 \\ -1 & 2 & 0 \\ 0 & 0 & 3 \end{bmatrix}$$

This definition of \mathbf{C}_{VE} relies on the definition of the parameter α , which comes from the alpha-method of time discretization (Bathe, 1995). For our purposes, α will always be set to 1; this ensures that we are advancing the time step implicitly (such an α value is consistent with the timestepping presented in equation 9).

To match the rheological formulation shown in equation 5.4, we then convert \mathbf{C}_{VE} into the consistent viscoelastic tangent compliance modulus S_{VE} by taking the inverse of \mathbf{C}_{VE} . Thus we get:

$$S_{VE} = \begin{bmatrix} \frac{\left(\frac{\alpha\Delta t}{2\eta} + 3\left(\frac{1-\nu}{E}\right)\right)\left(\frac{\alpha\Delta t}{2\eta} + \frac{1+\nu}{E}\right)}{\frac{\alpha\Delta t}{\eta} + \frac{3}{E}} & -\frac{\left(\frac{3\nu}{E} + \frac{\alpha\Delta t}{2\eta}\right)\left(\frac{\alpha\Delta t}{2\eta} + \frac{1+\nu}{E}\right)}{\frac{\alpha\Delta t}{\eta} + \frac{3}{E}} & 0 \\ -\frac{\left(\frac{3\nu}{E} + \frac{\alpha\Delta t}{2\eta}\right)\left(\frac{\alpha\Delta t}{2\eta} + \frac{1+\nu}{E}\right)}{\frac{\alpha\Delta t}{\eta} + \frac{3}{E}} & \frac{\left(\frac{\alpha\Delta t}{2\eta} + 3\left(\frac{1-\nu}{E}\right)\right)\left(\frac{\alpha\Delta t}{2\eta} + \frac{1+\nu}{E}\right)}{\frac{\alpha\Delta t}{\eta} + \frac{3}{E}} & 0 \\ 0 & 0 & \frac{1+\nu}{E} + \frac{\alpha\Delta t}{2\eta} \end{bmatrix} \quad (5A.62)$$

For cases where the viscous deformation is negligible, S_{VE} simplifies to the standard elastic compliance matrix in two-dimensions.

| | Variable Names (Appendix 5A) | Units |
|--------------------|---|-----------------------------------|
| A_E | Viscosity coefficient | $\text{Pa}^{-n} \text{s}^{-1}$ |
| A_M | Triaxial viscosity coefficient | $\text{Pa}^{-n} \text{s}^{-1}$ |
| A_T | Temperature-variable triaxial viscosity coefficient | $\text{Pa}^{-n} \text{s}^{-1}$ |
| a | Placeholder variable, see 5A.40 | Pa^{-1} |
| a_E | Placeholder variable, see 5A.37 | Pa^{-1} |
| b | Placeholder variable, see 5A.40 | -- |
| \mathbf{C}_{VE} | Consistent viscoelastic tangent matrix | Pa |
| \mathbf{C}^{Dev} | Deviatoric consistent viscoelastic tangent matrix | Pa |
| c | Placeholder variable, see 5A.40 | Pa s |
| d | Placeholder variable, see 5A.40 | $\text{Pa}^2 \text{s}^2$ |
| e_{ij} | Deviatoric strain tensor (component form) | -- |
| \bar{e} | Deviatoric strain tensor | -- |
| \bar{e}' | Deviatoric strain (elastic) | -- |
| \bar{e}^C | Deviatoric creep strain | -- |
| \bar{e}^P | Deviatoric plastic strain | -- |
| F | Inner product of 5A.38 | -- |
| J_2' | Second deviatoric stress invariant | Pa |
| \dot{L}_2^C | Second deviatoric strain-rate invariant | s^{-1} |
| n | Power law exponent | -- |
| P | Hydrostatic pressure | Pa |
| Q | Activation energy | J |
| R | Universal gas constant | $\text{J mol}^{-1} \text{K}^{-1}$ |
| \bar{S} | Deviatoric stress tensor | Pa |
| S_{ij} | Deviatoric stress tensor (component form) | Pa |
| S_{VE} | Consistent viscoelastic compliance tangent matrix | Pa^{-1} |
| T | Temperature | $^{\circ}\text{C}$ |
| t | Current time | s |
| W_i | Placeholder variable, see 5A.56 | Pa |
| α | Time-weighting factor | -- |
| γ | Creep strain increment | $\text{Pa}^{-1} \text{s}^{-1}$ |
| Δt | Timestep | s |
| $\Delta \bar{e}^C$ | Discrete deviatoric creep strain increment | -- |
| $\Delta \bar{e}^C$ | Effective creep strain | -- |
| $\Delta \bar{e}^P$ | Discrete deviatoric plastic strain increment | -- |
| δ | Kronecker delta function | -- |
| $\dot{\epsilon}_0$ | Reference strain rate (material) | s^{-1} |

| | | |
|--------------------|---------------------------------|------|
| ε_{ij} | Strain tensor (component form) | -- |
| ε_m | Mean strain tensor | -- |
| ε^{th} | Thermal strain tensor | -- |
| η | Linear viscosity | Pa s |
| θ | Dilatation | -- |
| $\bar{\sigma}$ | Effective creep stress | -- |
| σ_c | Triaxial confining stress | Pa |
| σ_d | Triaxial deviatoric stress | Pa |
| σ_{ij} | Stress tensor (component form) | Pa |
| σ_m | Mean stress tensor | Pa |
| " $\dot{\quad}$ " | Indicates time derivative | |
| " I " | Indicates initial condition | |
| " t " | Indicates current timestep | |
| " $t+\Delta t$ " | Indicates next timestep | |
| " τ " | Indicates time-weighted version | |

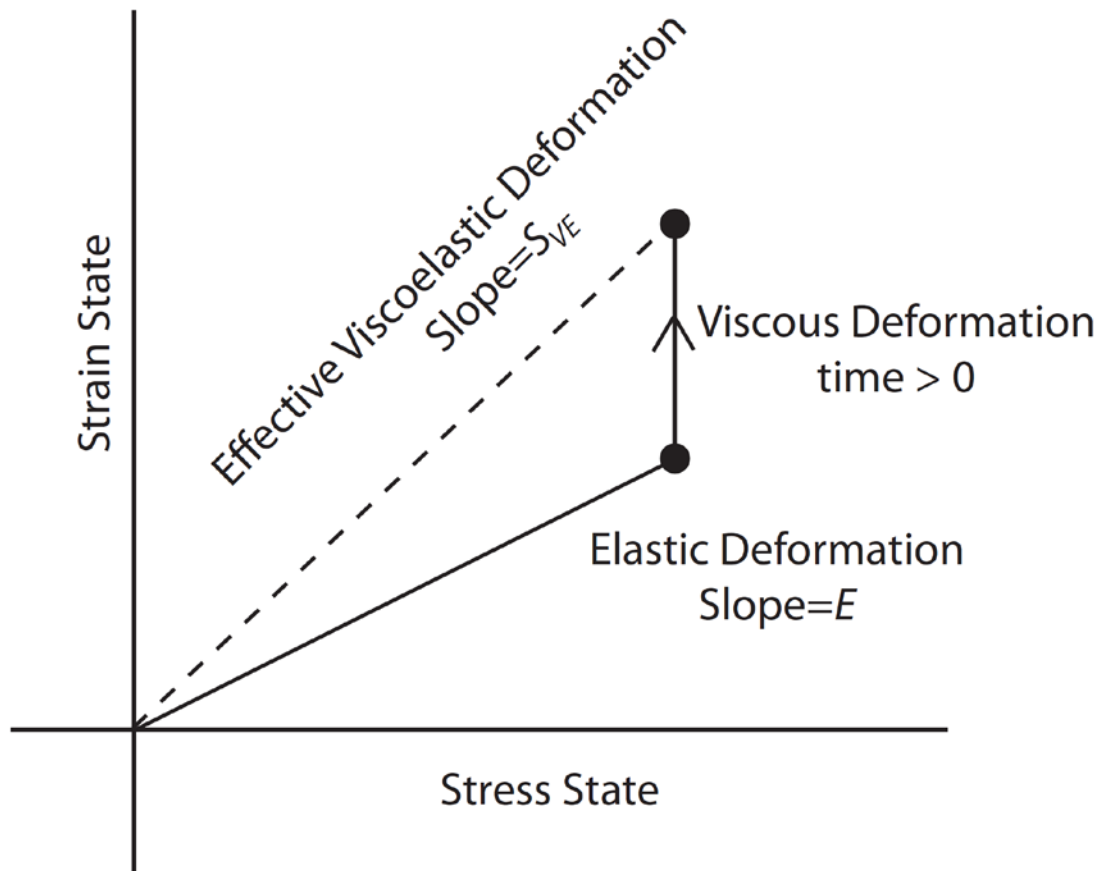


Figure 5A.1: Schematic view demonstrating the effective stress formulation. For a given (constant) stress state, the strain state moves instantaneously to an elastic configuration. Over time, the material evolves viscously to a new strain state. The slope to this a given point along the viscous deformation path is the consistent tangent modulus discussed in Appendix A.

Appendix 5B: Expected Deformation of a 1D Inhomogeneous Bernoulli-Euler Beam

To gain an understanding of the result of a stress-dependent viscosity within the beam-like deformation regime, we model a one-dimensional Bernoulli-Euler beam with a raised Young's modulus near the center of the beam. We are justified in using the linear elastic solution to infer the behavior of the nonlinear viscoelastic solution as: 1) the nonlinear case converges to the linear solution in the beam-like regime; 2) a linear elastic solution can be connected to the appropriate linear viscoelastic solution through the correspondence principle (e.g., Findley et al., 2011).

The governing equation for a Bernoulli-Euler beam with inhomogeneous elasticity under the action of a distributed pressure is:

$$\frac{\partial^2}{\partial x^2} \left(E(x)I \frac{\partial^2 w}{\partial x^2} \right) = p(x) \quad (5B.1)$$

We impose a fixed ($w = \frac{\partial w}{\partial x} = 0$) condition on one end of the beam, and impose a sliding ($\frac{\partial w}{\partial x} = \frac{\partial^3 w}{\partial x^3} = 0$) condition on the other side.

We begin by applying a constant pressure distribution to the series of elastic models summarized in table 5B.1, exploring the impact of the following three moduli profiles: 1) changes in the magnitude of the “peaked” modulus in the center of the beam; 2) changes in the width of the this modulus peak; 3) changes in the modulus at the edge of the beam. Figure 5B1.A shows the results for these models with a constant pressure, with the upper panel showing absolute deflection w , and the lower pattern showing the normalized value of deflection w/w_{max} . We see that while many of the models with

raised central Young's modulus have reduced absolute deflection compared to the homogenous model, the value of the moduli at the ends of the beam have a much stronger impact on the overall deflection value. To quantify the "closeness" of the two normalized profiles, we plot the R^2 value of the normalized models compared to the linear model in figure B2. The red circles correspond to the constant edges, while the blue circles correspond to models with linearly varying moduli in the edge of the beam. We see clearly that the variation from the homogeneous model is larger with edge variable elasticity, though we note that all the values fall beneath an R^2 of 0.994, suggesting that the all models are very close to a linear solution with an appropriately chosen effective Young's modulus.

Of course, our pressure distribution is not constant in our problem, but changes along the crack profile. To investigate the impact of a variable pressure distribution on the beam model results, we now run the same 18 models with a pressure distribution that varies linearly from $-p_l$ to $+p_l$ over the length of the beam. These model results are shown in figure B1B and the R^2 values are shown as X's in figure B2. We see immediately that the models with the variable pressure profile are closer to linear than those with the constant pressure distribution.

Thus, we can use these linear elastic model results to approximate the expected linear viscoelastic response by replacing the Young's modulus with the linear viscosity profile multiplied by the time over which the pressure is applied ($E(x) \rightarrow \eta(x)\Delta t$). As a nonlinear viscoelastic model is equivalent to a linear model with a stress-dependent effective viscosity (e.g., see appendix 5A), we can use these one-dimensional models to predict the impact of having a centralized region of increased effective viscosity, as is

seen in the beam-like regime for our nonlinear viscoelastic models. While we never expect the nonlinear solution to converge to the linear solution as long as there is a variation in the effective modulus, these results demonstrate that we can approximate our nonlinear model with a linear model with varying viscosity with a high degree of certainty.

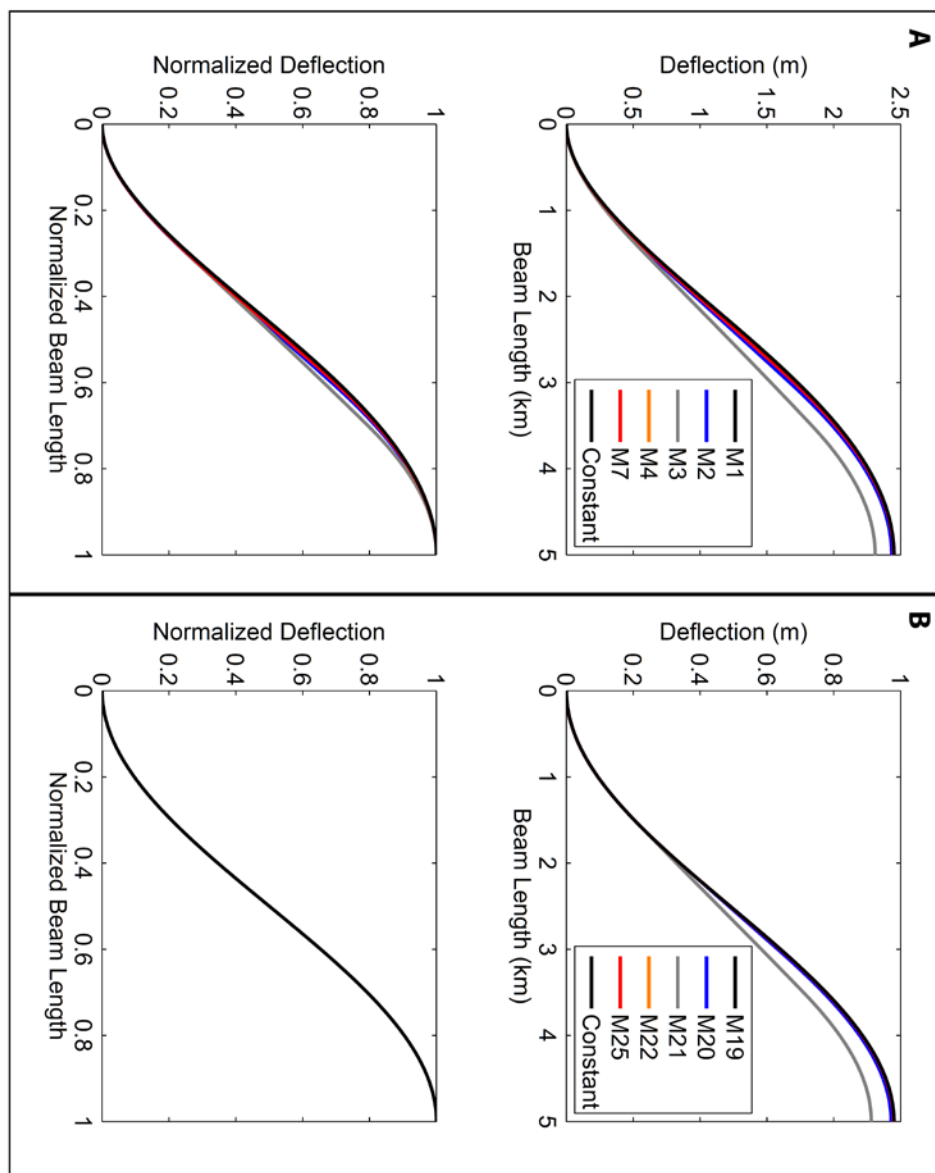


Figure 5B.1: Figures showing the modeled beam deflection for a representative set of moduli profiles. Panel A shows the results for a constant pressure distribution, while panel B shows the results for a linearly varying pressure distribution. The upper plot in each panel is the absolute deflection, while the lower plot is the normalized deflection. In all figures, the black line is the value for a homogenous model. Model numbers correspond to the model names in table B1.

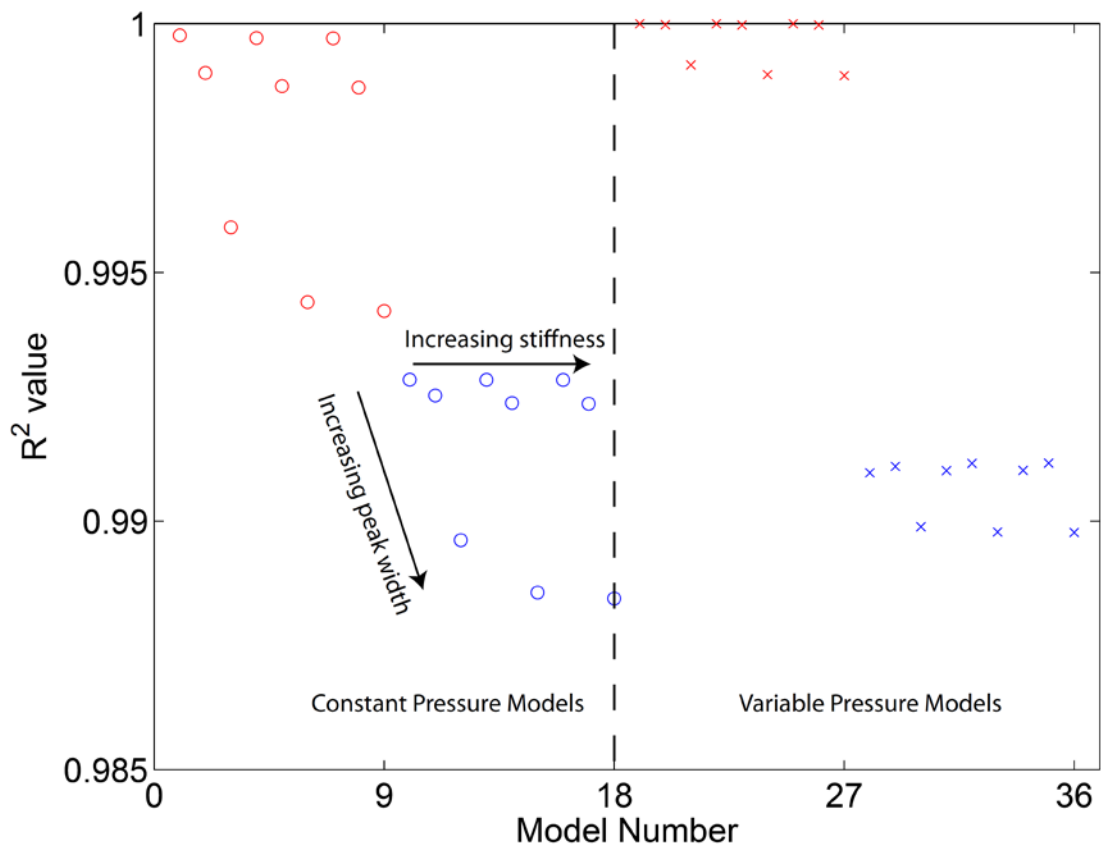


Figure 5B.2: R^2 values comparing the normalized beam deflections for our 36 variable elasticity models to the homogeneous model. The vertical axis is the R^2 value, while the horizontal axis is the model number. Symbols correspond to the loading condition (circles=constant, x's=varying pressure), while the color corresponds to the edge condition (red=constant, blue=varying). All values are very close to an R^2 value of 1.

| Name | Peak Width % | Peak Magnitude | Edge Moduli | R ² (1-18) | R ² (19-36) |
|----------|-----------------|-------------------|-------------|-----------------------|------------------------|
| Constant | 0 | Same | Constant | 1 | 1 |
| M1 | 10 | 1 order | Constant | 0.9998 | 1 |
| M2 | 20 | 1 order | Constant | 0.9990 | 1 |
| M3 | 40 | 1 order | Constant | 0.9959 | 0.9992 |
| M4 | 10 | 2 orders | Constant | 0.9997 | 1 |
| M5 | 20 | 2 orders | Constant | 0.9987 | 1 |
| M6 | 40 | 2 orders | Constant | 0.9944 | 0.9990 |
| M7 | 10 | 3 orders | Constant | 0.9997 | 1 |
| M8 | 20 | 3 orders | Constant | 0.9987 | 1 |
| M9 | 40 | 3 orders | Constant | 0.9942 | 0.9990 |
| M10 | 10 | 1 order | Linear | 0.9928 | 0.9910 |
| M11 | 20 | 1 order | Linear | 0.9925 | 0.9911 |
| M12 | 40 | 1 order | Linear | 0.9896 | 0.9899 |
| M13 | 10 | 2 orders | Linear | 0.9928 | 0.9910 |
| M14 | 20 | 2 orders | Linear | 0.9924 | 0.9912 |
| M15 | 40 | 2 orders | Linear | 0.9886 | 0.9898 |
| M16 | 10 | 3 orders | Linear | 0.9928 | 0.9910 |
| M17 | 20 | 3 orders | Linear | 0.9924 | 0.9912 |
| M18 | 40 | 3 orders | Linear | 0.9884 | 0.9898 |

Models M19-M36 are the same as the above models with a variable applied pressure.

Table 5B.1: Beam model elasticity profile parameters and R² values for the 37 models

run as part of Appendix B. The peak width defines the percent of the overall peak length that has a raised moduli. The peak magnitude column corresponds to the magnitude of the central modulus relative to the modulus at the edge of the beam. The edge modulus describes the nature of the moduli near the beam edges. The R² value is defined in the text of Appendix B. Note the models M19-M36 have the same values as the corresponding models M1-M18, but have a variable applied pressure profile rather than a constant pressure, as described in the main text of Appendix B.

Appendix 5C: Finite Element Output: Spatial Variability of Effective Viscosity

In this appendix, we present figures of the full two-dimensional effective viscosity field for the nonlinear viscoelastic finite element models used to analyze the effect of nonlinearity (subsection 5.3.2). We define the effective viscosity to be a stress-dependent modulus that linearized the viscous component of the material model, as shown below:

$$\eta_{eff} = \frac{1}{A\sigma_{eff}^{n-1}} \quad (5C.1)$$

The five figures correspond to crack lengths of twenty meters, one kilometer, two kilometers, three and a third kilometers, and five kilometers. The twenty meter crack falls into the half-space deformation regime, the one kilometer crack is in the transitional regime, and the remaining models lie within the beam-like regime. In all models, the black line indicates the location and length of the basal crack.

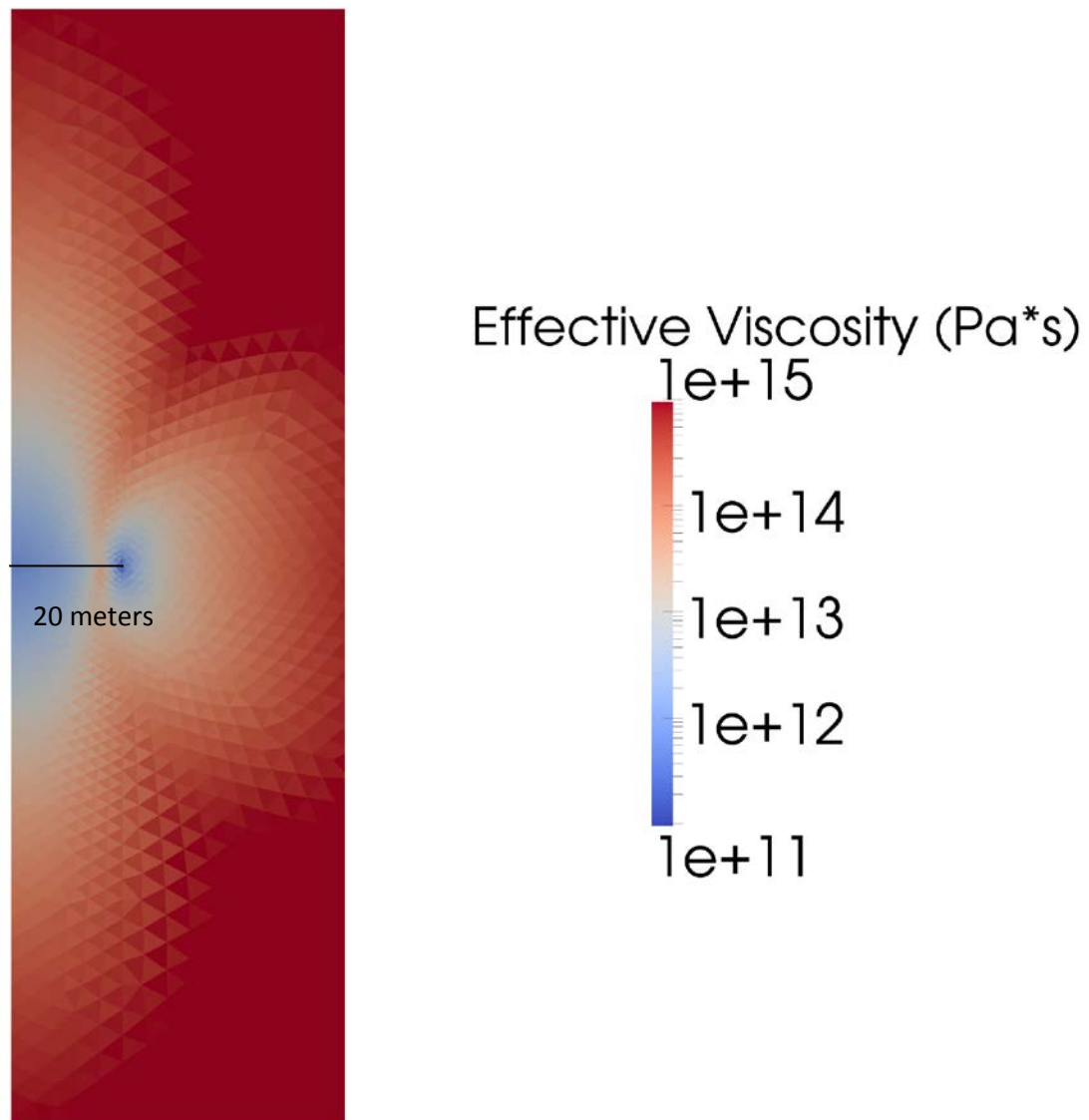


Figure 5C.1: Effective viscosity distribution for a crack 20 meters long. Note that the upper and lower edges of this figure do not correspond to the free surface and bottom of the mesh, respectively. The boundaries are chosen arbitrarily to aid in view of the effective viscosity distribution. This crack length is in the half-space regime.

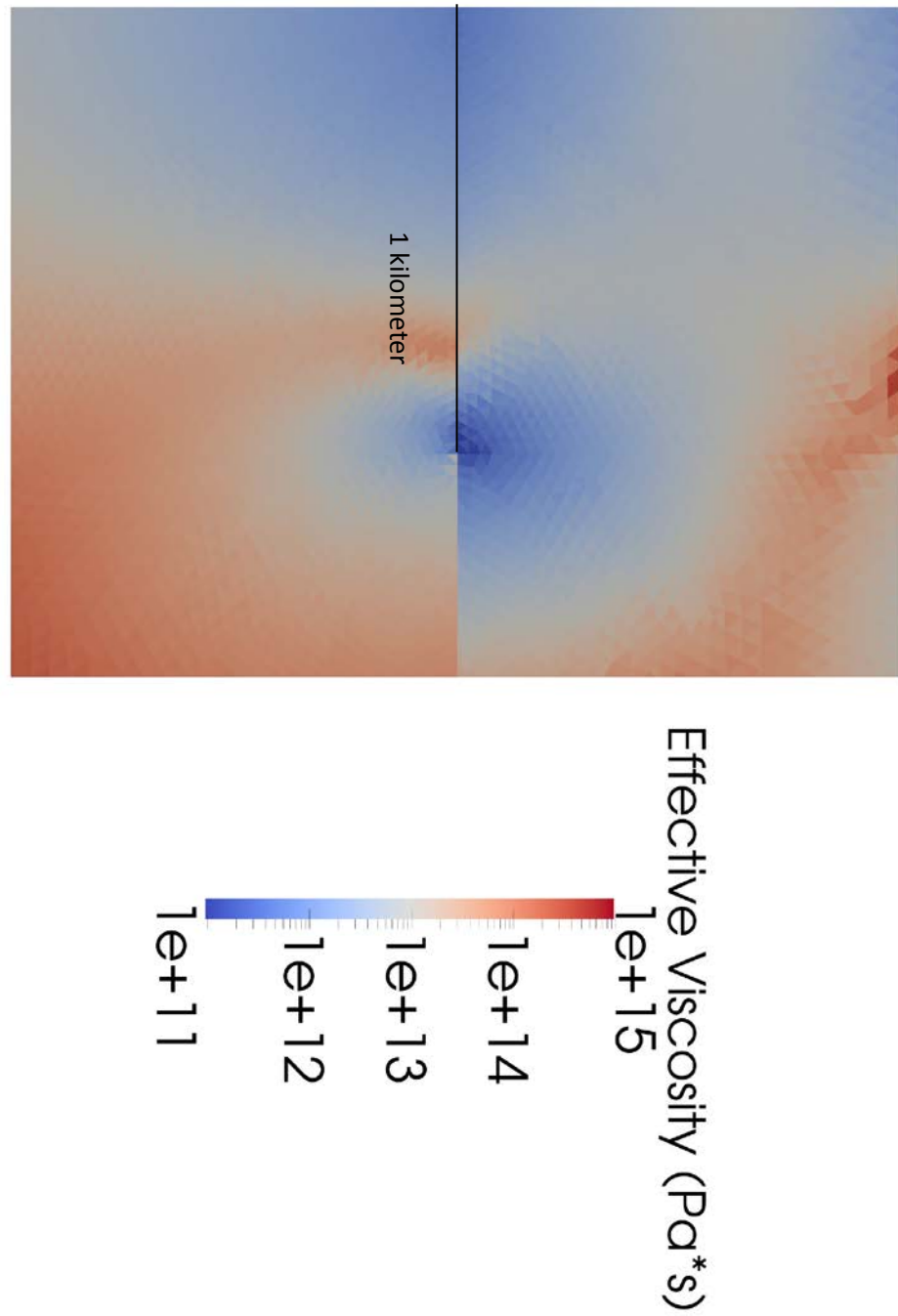


Figure 5C.2: Effective viscosity distribution for a crack one kilometer long. This crack falls within the transitional regime. Note the figure is rotated 90 degrees.

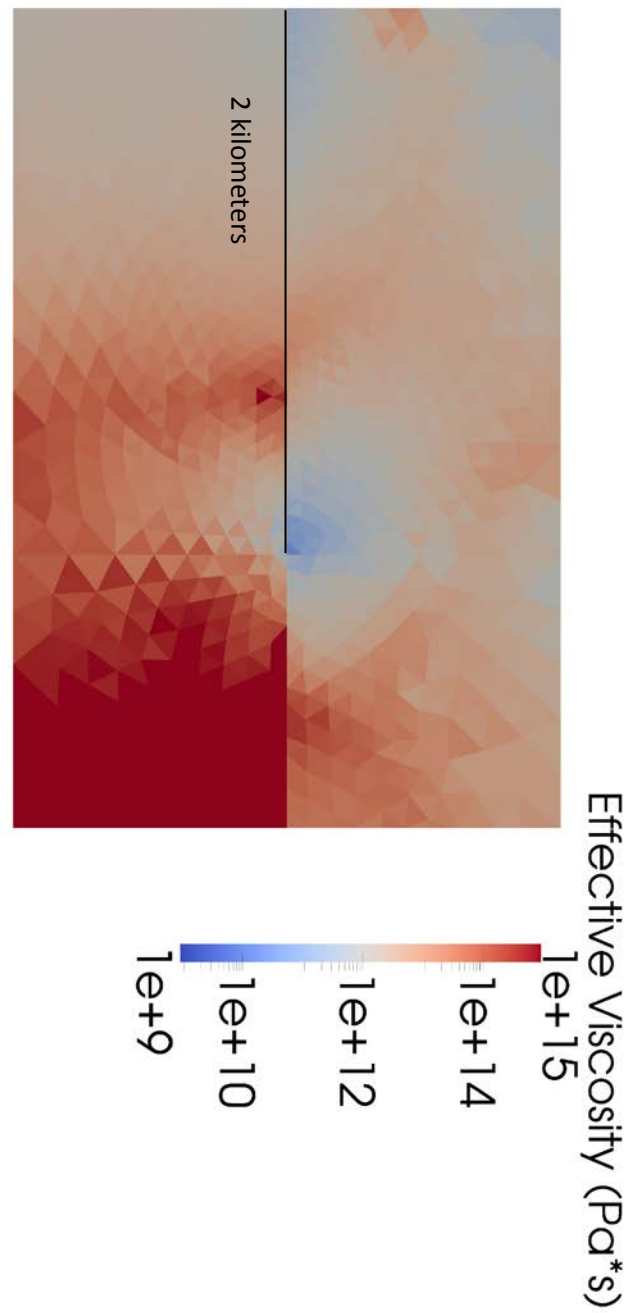


Figure 5C.3: Effective viscosity distribution for a crack two kilometers long. This crack length lies right within the beam-like regime. Note the figure is rotated 90 degrees.

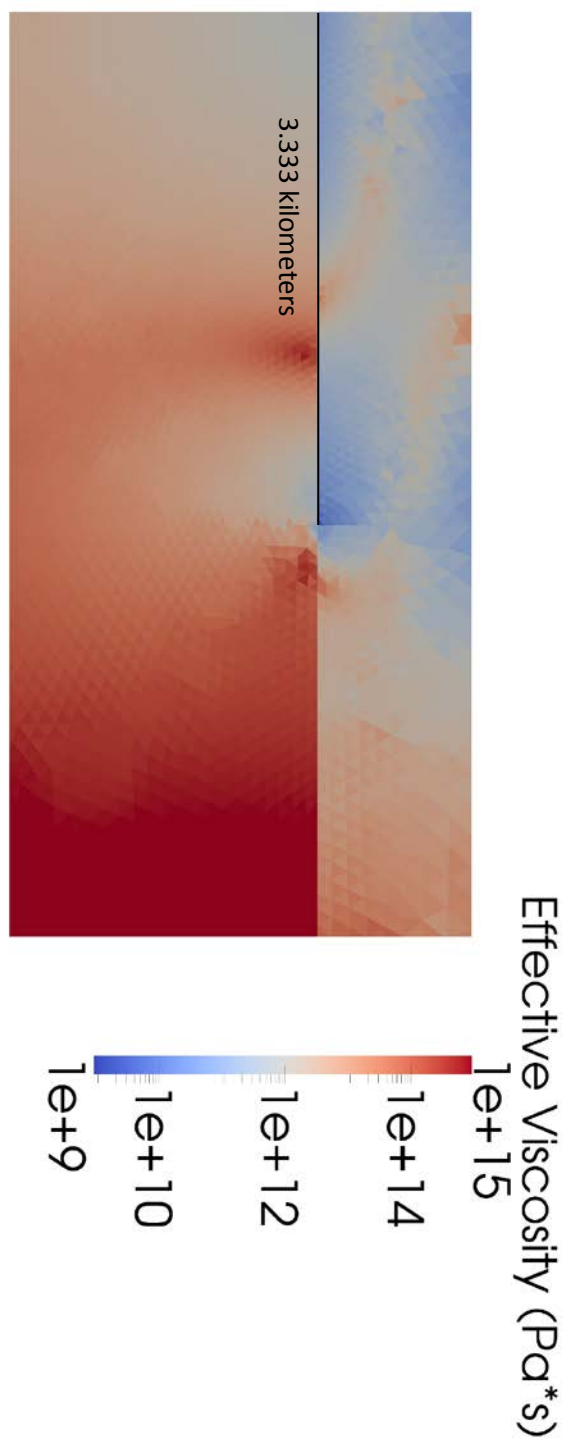


Figure 5C.4: Effective viscosity distribution for a crack 3.333 kilometers long. This crack length lies within the beam-like regime. Note the figure is rotated 90 degrees.



Figure 5C.5: Effective viscosity distribution for a crack five kilometers long. This crack length lies within the beam-like regime. Note the figure is rotated 90 degrees.

Appendix 5D: Conduit Size

In section 5.4, we demonstrate that we can fit the observations of Das et al. (2008) to within a factor of two of the observations; however, as part of this analysis, we need to make an assumption of the value of $\left(\frac{a}{L}\right)$, the ratio of the conduit's long axis to the basal crack length. In this appendix, we discuss the impact of the choice of $\left(\frac{a}{L}\right)$ on our overall solution, and look how well our models predict the observed surficial crack.

We start by looking at the relationship of $\left(\frac{a}{L}\right)$ to the two correction factors χ and χ_w , as defined in equations 5.14 and 5.15. Figure 5D.1 plots the value of these correction factors, as well as the total correction to pressure, $\chi * \chi_w$, as functions of crack length for several assumed values of $\left(\frac{a}{L}\right)$. In this figure, we take the result from our elastic model for the value of crack opening and drainage volume used to determine these parameters; our choice here is arbitrary and the correction factors follow the same general trends independent of the model rheology. As the crack length increases, the value of χ increases asymptotically towards 1. For χ_w , the value is fixed at 1 until the lake completely drains into the conduit. For some of the models, χ_w will jump above 1 at the onset of the post-drainage phase; this behavior is due to the model over-shooting the total drainage volume, which is then corrected at the next timestep. After the lake completely drains, χ_w rapidly drops and asymptotically approaches 0. From the $\chi * \chi_w$ curve, we see that χ_w dominates the total value of the correction factor once in the post-drainage phase. For the varying values of $\left(\frac{a}{L}\right)$, we see that decreasing the relative conduit

size delays the complete lake drainage. The net result is that a smaller overall conduit will result for models with a smaller value of $\left(\frac{a}{L}\right)$, despite the longer crack size L at drainage.

Furthermore, reducing $\left(\frac{a}{L}\right)$ results in a reduced correction factor over the entire crack length. Reducing the correction factor results in a smaller peak value of inlet pressure, p_I , for a given model, which in turn reduces the value of the crack velocity, U_{tip} , as seen in figure 5D.2. In this figure, we see that reducing the size of the conduit has the effect of reducing the overall crack propagation speed until the lake completely drains and the correction factor χ_w “turns on.” Once χ_w is a non-one value, the crack velocities all follow the same evolution curve, essentially independent of the conduit size (the velocities vary by less than 1/10% between values of $\left(\frac{a}{L}\right)$). From this relationship, we can make the somewhat surprising statement that once the lake has completely drained, the geometry of the conduit does not influence the further evolution of the basal crack, even though the excess fluid pressure in the conduit is the driver of post-drainage crack growth.

The net results of the variation of the correction factors and the crack propagation velocity with the selection of $\left(\frac{a}{L}\right)$ is summarized in figure 5D.3. As with figure 5.10, this figure shows the drainage volume, drainage rate, and crack opening values as a function of time, though the models shown here have the fluid drag correction added. As expected, we see that reducing the value of $\left(\frac{a}{L}\right)$ causes the duration of the total drainage cycle to increase and the drainage rate to drop due to the reduced crack propagation

velocity. Furthermore, the total crack opening drops as the relative conduit size is reduced, due to the reduced magnitude of the correction factors. Following this trend and running models at progressive smaller values of $\left(\frac{a}{L}\right)$ allowed us to find the best-fit model presented in figure 5.11, which has a value of $\left(\frac{a}{L}\right) = 0.51$.

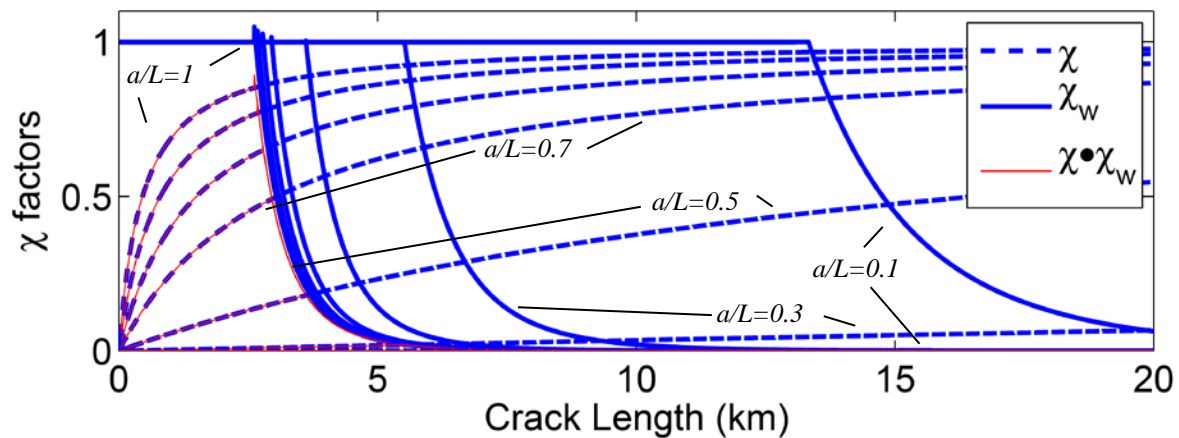


Figure 5D.1: Variation of the corrections factors χ and χ_w with the relative conduit size $\left(\frac{a}{L}\right)$. The dashed line shows χ , the solid line χ_w , and the red line the total correction factor $\chi \cdot \chi_w$. Curves for relative conduit lengths of 1.0, 0.9, 0.8, 0.7, 0.5, 0.3, and 0.1 are shown.

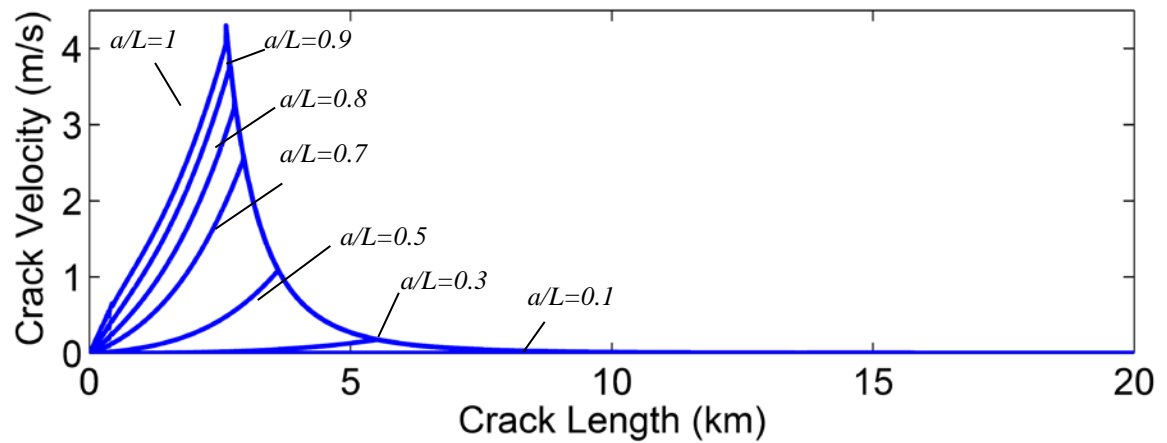


Figure 5D.2: Variation of the crack propagation speed, U_{tip} , as a function of crack length, for a series of relative conduit lengths of $\left(\frac{a}{L}\right)$ equal to 1.0, 0.9, 0.8, 0.7, 0.5, 0.3, and 0.1. Note that the curves all fall on the same line, controlled by the value of χ_w when the surficial lake has completely drained.

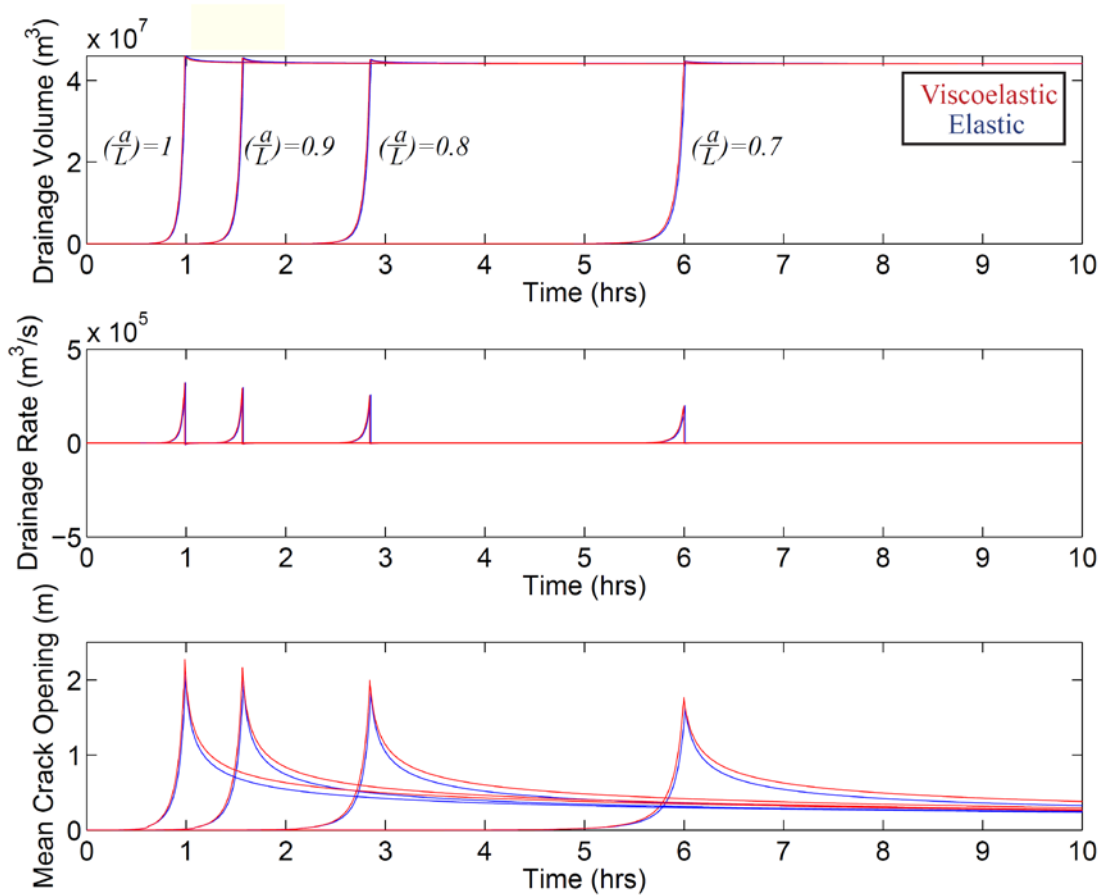


Figure 5D.3: Drainage volumes, drainage rates, and average crack openings for models with a range of $(\frac{a}{L})$ values equal to 1.0, 0.9, 0.8, 0.7, for models with the fluid drag correction, as functions of times. The red curves show the viscoelastic results, while the blue curves show the elastic results.

Appendix 5E: Finite Element Output: Surface Deformation Caused by Crack Opening

In subsection 5.4.2, we found the surface deformation that occurs at a location equivalent to the GPS station of Das et al. (2008) by using a finite element model. For these finite element models, we used the two-dimensional mesh geometry shown in figure 5E.1, which models only the glacier above the basal crack. In this model, we only consider the surface deformation due to the presence of the basal crack, and neglect any surface deformation caused by the opening of the drainage conduit. To represent the crack, the displacement profile from our analytic model (either the elastic or linear viscoelastic) is applied to the base of the model, with any displacement beyond the length of the crack set to zero. In these models, the crack is stationary and the crack length does not evolve.

As our assumption is that the vertical drainage conduit is a long, oblate cylinder (see figure 5.9), there must be three-dimensional effects that limit the horizontal motion of the ice at the conduit that are neglected in a two-dimensional model. To bracket this three-dimensional effect, we ran models with two end-member conditions at the conduit. The first condition represents ice near the lateral ends of the conduit. For this condition, we force the horizontal displacement to always be equal to zero (i.e., there is symmetry across the conduit). The second condition represents ice near the lateral center of the conduit, where the ice on either side of the conduit is horizontally decoupled. For this location, we allow the mesh at the conduit to deform freely. The resulting difference in the displacements at the GPS location 1.7 kilometers away is small, with the peak horizontal and vertical deformations being less than a factor of two different for these

models, as demonstrated by the displacement profiles for the models shown in figures 5E.2 and 5E.3. The figures in the main paper (i.e., figures 5.12 and 5.13) show results from models assuming the GPS station is along the centerline of the conduit, as is the case in the survey of Das et al. (2008).

Lastly, the ice in this model is assumed to be elastic. For the models using the elastic crack opening to calculate surface displacement, such an assumption is consistent. However, this approach is clearly not self-consistent when the linear viscoelastic crack opening is used, as in this formulation the viscous and elastic crack opening are assumed to only act elastically on the deformation of the glacier (i.e., there is no time-dependent deformation in the glacier). The assumption of elastic deformation is a necessary simplification, as to fully capture the viscous deformation of the glacier, the crack would have to be iteratively lengthened, an approach beyond the scope of this chapter. Thus, the surface displacements for the viscoelastic model (such as are shown in figures 5.12 and 5.13) are only approximately correct, and are underestimate of the total surface deformation. However, using the relative magnitudes of the viscous and elastic crack openings as a guide (figure 5.7A), the expected error is about 10% at most, with shorter cracks having smaller errors than the longer cracks.

Lastly, as we are using finite element analysis, we have the full displacement field over the entirety of our mesh, not just at the location of the GPS station. Figures 5E.4 and 5E.5 show snapshots of the deformation of the glacier at a series of timesteps used in subsection 5.4.2. These figures provide a picture of the full deformation pattern due to the growth of a basal ice crack.

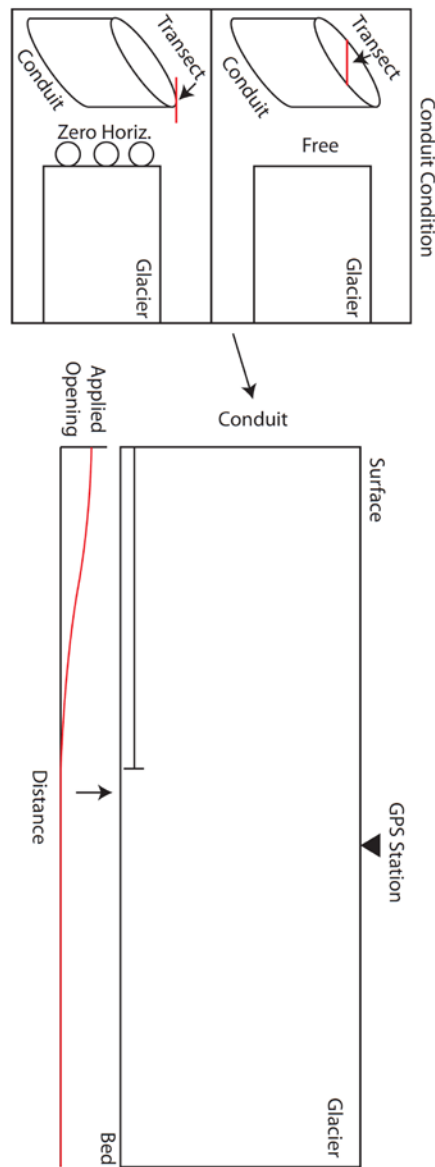


Figure 5E.1: Finite element model setup discussed in appendix 5E. The right portion of the figure shows the mesh, with a defined crack length of L , the vertical conduit, and the GPS station location. The two conduit conditions are shown in the left portion of the figure. In each panel, the left portion shows the theoretical two-dimensional transect of the drainage conduit the finite element boundary condition shown on the right of the panel corresponds to.

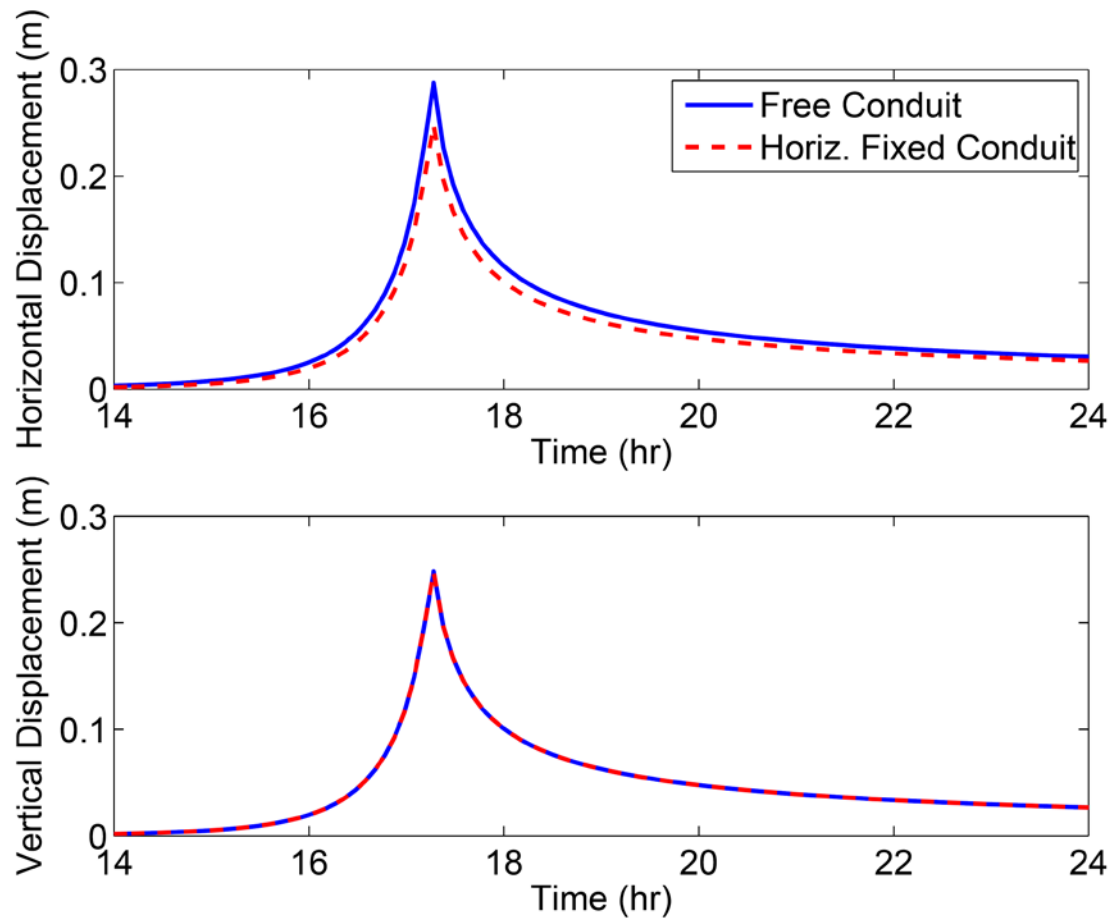


Figure 5E.2: Horizontal and vertical surface deformation for models using the free conduit condition (blue) and the horizontally fixed conduit condition (dashed red). The model shown here is for the elastic crack opening.

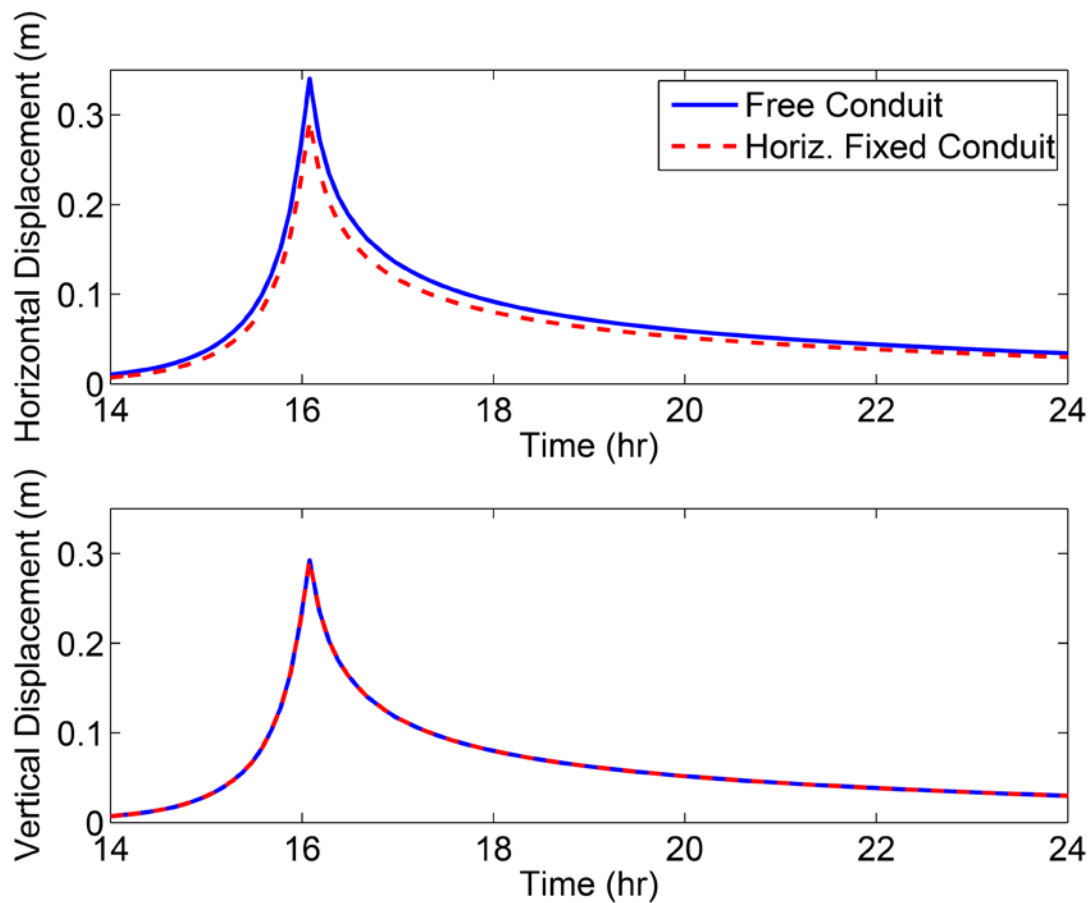


Figure 5E.3: Horizontal and vertical surface deformation for models using the free conduit condition (blue) and the horizontally fixed conduit condition (dashed red). The model shown here is for the viscoelastic crack opening.

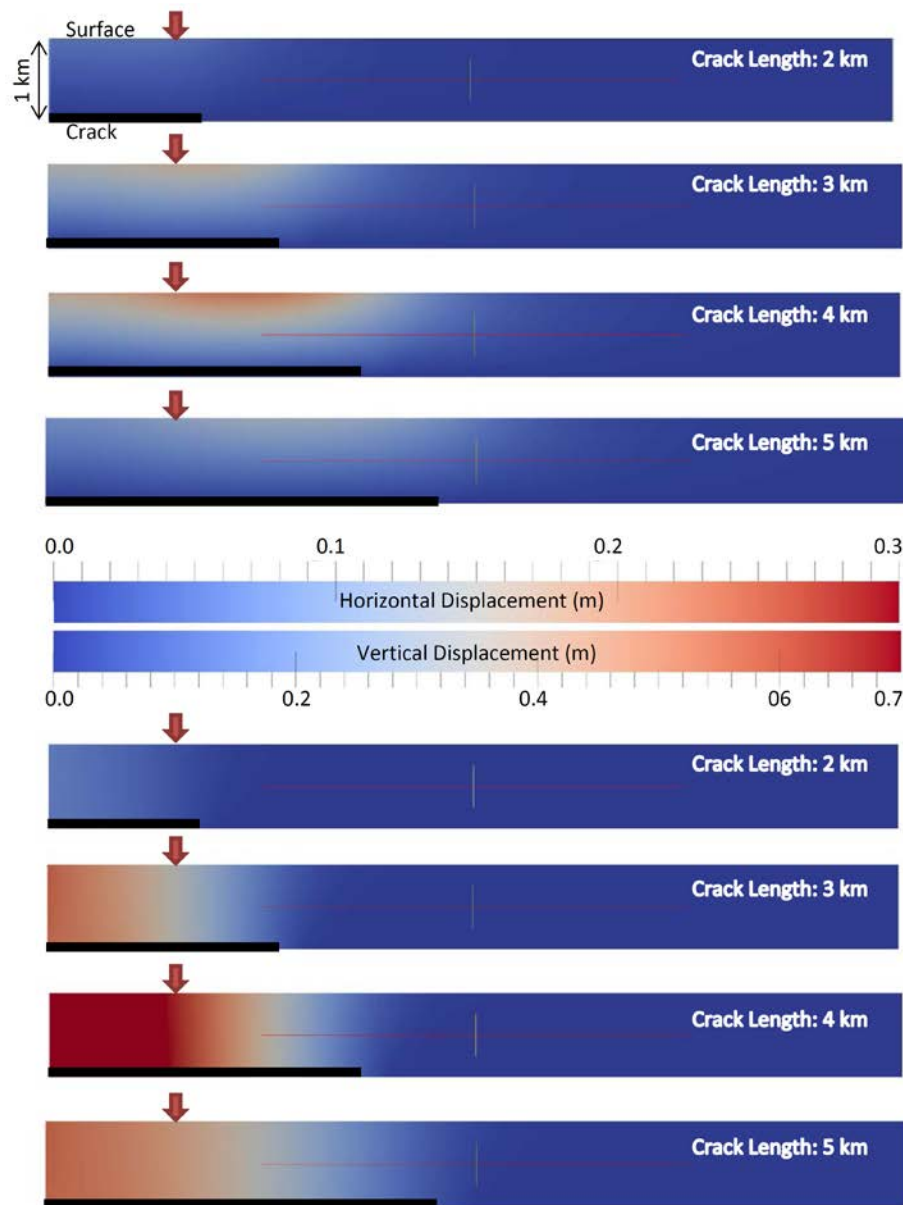


Figure 5E.4: Displacement fields with crack lengths of 2, 3, 4, and 5 kilometers for the finite element models described in subsection 5.4.2 with the elastic value of crack opening. The upper figures are the horizontal displacements, while the lower figures are the vertical displacements. The arrow shows the location of the point approximating the GPS station at 1.7 kilometers away from the crack center (left edge of the domain).

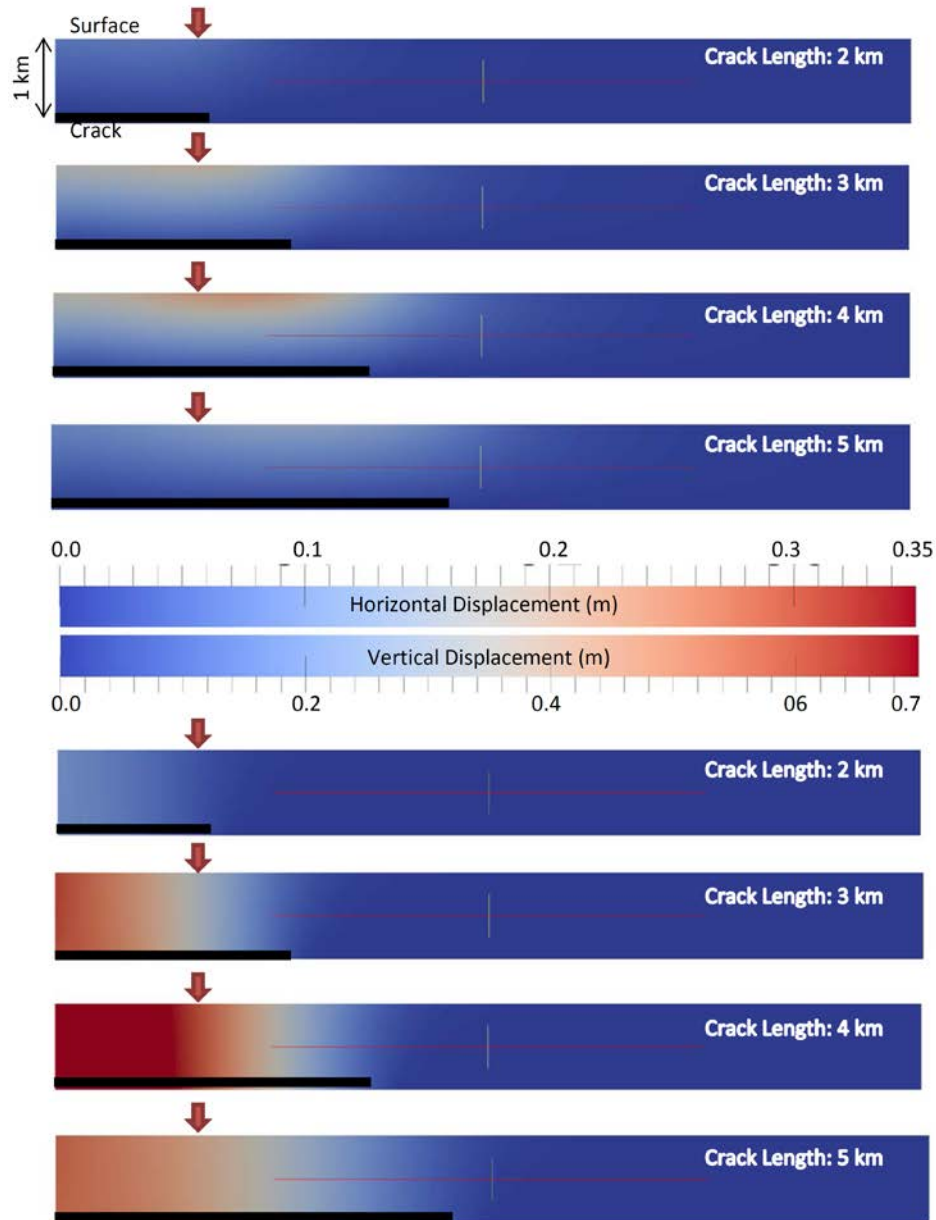


Figure 5E.5: Displacement fields with crack lengths of 2, 3, 4, and 5 kilometers for the finite element models described in subsection 5.4.2 with the viscoelastic value of crack opening. The upper figures are the horizontal displacements, while the lower figures are the vertical displacements. The arrow shows the location of the point approximating the GPS station at 1.7 kilometers away from the crack center (left edge of the domain).

Chapter 6

Synopsis and Implications

This final chapter provides a brief recapitulation of the findings detailed in chapters 2 through 5. While the conclusions of each chapter largely stand alone, we then close with a prospective on viscoelasticity in the context of the short-timescale behavior of ice.

6.1 Synopsis

In chapter 2, we used two-dimensional and three-dimensional models of elastic ice streams to quantify the spatial extent of an ice stream's response to a tidal load. Our results demonstrated that the geometry of the ice stream—specifically the dimension constrained by the choice of the boundary conditions—imposes a fundamental limit on inland transmission of tidal stresses. For models approximating real ice streams, only in the singular case of Whillans Ice Plain does traction applied at the grounding line maintain sufficient amplitude over an inland distance large enough to match observations of tidal influence. In all our models of more channelized ice streams, lateral margins limit the distance of stress transmission. Thus, the inland propagation of a tidal signal is controlled primarily by the ice stream width. In such cases, the modeled extent of the response to tidal forcing fails to match observations of tidal perturbations in ice motion.

In chapter 3, we explored two potential phenomena for decoupling an ice stream from its lateral margins: damage-related compliance of the shear margins, and a nonlinear viscoelastic constitutive law for glacier ice. Using linear continuum damage mechanics to parameterize the influence of cracks, fractures, and crevasses on the effective ice elasticity, our modeling results demonstrated that spatially variable elasticity can increase

the length-scale for the transmission of a tidal load relative to a homogeneous elastic model. We used our results to map the possible parameter space in terms of damage magnitude and margin size for a model with discrete “weakened” shear margins. We found that the amount of damage necessary to increase the transmission length-scale in channelized ice streams to an extent large enough to match observations would effectively pulverize the ice margins completely. Our nonlinear viscoelastic models showed a sizable decrease in the effective viscosity along the margins of the modeled ice stream relative to the central portions of the ice controlled by the gravitational stress acting on the ice. However, the timescales and magnitudes of the tidal forcing were such that the ocean tide neither perturbs the ice’s viscosity profile substantially nor does the material shift into a viscously-dominated deformation regime. A large discrepancy remains between the Antarctic observations and our model results even when the ice is modeled with a nonlinear, temperature-dependent viscoelastic rheology.

In chapter 4, we outlined a methodology to use the observed phase delay between the tidal forcing of an outlet glacier and that glacier’s displacement response to infer *in situ* viscoelastic material properties for ice. Using the general *arctangent* form of the phase shift for a Maxwell viscoelastic material, we demonstrated the bounds that such simple two-dimensional models can provide using the GPS data of de Juan-Verger (2011) for Helheim glacier in Greenland as a sample dataset. Additionally, we discussed the best ice streams and the potential survey requirements to collect ideal data for constraining rheological parameters for *in situ* glacial ice.

In chapter 5, we explored the importance of viscoelasticity during the rapid drainage of supraglacial lakes. Our modeling demonstrated that there is a nontrivial, yet

second-order, effect of viscoelasticity during the opening of a subglacial drainage crack. Our model solutions allowed us to reinterpret some of the details of an earlier set of field observations for a supraglacial lake drainage event on Jakobshavn Isbrae. However, we suggest that viscoelasticity is less important to understanding the physics of supraglacial lake drainage than the accurate observation of the surface lake bathymetry and a better understanding of the evolution of the vertical drainage conduit.

6.2 The Importance of Ice Viscoelasticity

A recurring theme throughout this thesis is the extent to which it is important to consider viscoelastic effects during ice deformation to correctly model short-timescale glacier processes. A consideration of viscoelastic effects is relevant because the material properties of ice are such that the stress relaxation timescale of ice is similar to the timescale of the glacial phenomena explored here. While our work is not the first to model the viscoelastic deformation of ice streams, our models do provide a test for determining the relative importance of ice viscoelasticity over hourly to weekly timescales.

In our tidally-loaded models, viscoelasticity has a negligible effect on the stress state, perturbing the transmission length-scale by about 1% and 2% for the semidiurnal and diurnal tidal frequencies, respectively. For the fortnightly tide, incorporating viscoelasticity does increase the stress-transmission length-scale by about 45%, but even this increase is about an order of magnitude smaller than is necessary to match our model results to observations. In all cases, however, viscoelastic models exhibit a noticeable time delay between the ocean tide and the ice stream's response. This delay grows with increasing distance inland of the grounding line. For the lake drainage problem,

viscoelasticity increases the total crack opening value by about 10% late in the crack evolution, resulting in a difference in the total drainage time of about an hour (though the observable drainage duration is not strongly affected by using a viscoelastic model). Thus, at least for the problems investigated here, viscoelasticity expresses itself primarily as a change in the timing of the various forcing processes on our model glaciers relative to elastic models, rather than as a large change in the amplitude of the ice's response to these external forces.

A practical concern is that the computational modeling of a nonlinear viscoelastic material is inherently difficult, especially when compared to an equivalent linear elastic version of the same problem. Conceptually, external and internal forces and stresses due to processes other than the one of interest must be considered due to the nonlinearity, and can only be neglected after careful study. Furthermore, there is practical concern that viscous problems take more computational time than elastic problems due to the time-dependence of the solution. When combined with the “convergence loop within a convergence loop” style of iterative solver standard in many nonlinear finite element solvers, the large computation demand for a nonlinear viscoelastic problem will necessarily limit the total number of models that can be run in given span of time. For perspective, every elastic model from chapters 2 and 3 could have been run in the same period of time as a single nonlinear viscoelastic model forced at a fortnightly tidal period. Clearly, if viscoelasticity is not critical to the problem being investigated, using a linear elastic model is a powerful approximation to significantly reduce the computational time necessary to model a system.

We have demonstrated that understanding both the stress transmission of a tidal load and of the drainage process of supraglacial lakes is incomplete. While our modeling demonstrates that effects of viscoelasticity are not negligible for either phenomenon, more important questions remain to be answered before the second-order nature of viscoelasticity becomes a necessary addition to improving the accuracy of glacier models. The lack of a general mechanism for explaining the long-distance transmission of a tidal load severely hampers the believability of the current published models investigating the interactions between an ocean tide and ice stream motion.

In the lake drainage problem, the evolution of the input pressure at the base of the drainage conduit is the most critical factor determining the growth size and duration of the basal drainage crack. Modeling the formation and growth of the drainage conduit, as well as the inflow rates into such a conduit, are more important to determining the inlet pressure, and thus the overall crack evolution, than is viscoelasticity. Thus, implementing viscoelasticity at the current stage of understanding in each of the glacial processes studied here is essentially fine-tuning an inherently oversimplified model missing physics essential to the problem.

Lastly, our introduction to this thesis framed this work in the larger context of using glaciological constraints on ice stream motion as input into climate models. While the work presented here is clearly far removed from any sort of global climate model, the general conclusion from chapters 2 and 3 that the ice stream margins are critical to determining the spatial extent of tidal forcing on an ice stream is relevant. That the shear margins impose a fixed length-scale on the transmission of a tidal load demonstrates that including the shear margins in a model is at least as important as correctly modeling the

basal sliding relationship. Such a requirement implies the need to use three-dimensional models of ice streams. However, our work demonstrates that, for short-timescale perturbations of ice stream motion, the magnitude of the tidal response is primarily elastic, though the timing of the ice response is controlled by viscoelasticity.

6.3 Closing Thoughts

This thesis represents an effort to quantify the short-timescale behavior of glacial ice in the context of tidal forcing and supraglacial lake drainage. More generally, this work helps elucidate the important processes—both those constrained by geophysical modeling and those still conceptual—acting during the short-timescale deformation of ice. Much of the work presented here involves determining if ice viscoelasticity is important to correctly modeling the physics of these processes. Viscoelasticity is commonly cited as the “next step” in ice modeling; however the work here suggests that viscoelastic effects are of second order, and that there are still fundamental physical processes that are missing from the collective understanding of ice stream motion before viscoelasticity become truly necessary in glaciological models.

References

- Aagaard, B., C. Williams, M. Knepley (2008), PyLith: A finite-element code for modeling quasi-static and dynamic crustal deformation, *Eos Trans. AGU*, 89, Fall Meet. Suppl., Abstract T41A-1925.
- Aagaard, B., C. Williams, M. Knepley (2007), PyLith: A finite-element code for modeling quasi-static and dynamic crustal deformation, *Eos Trans. AGU*, 88, Fall Meet. Suppl., Abstract T21B-0592.
- Aagaard, B., S. Kientz, M. Knepley, S. Somala, L. Strand, and C. Williams (2011), PyLith User Manual, Version 1.6.0, Davis, CA: Computational Infrastructure of Geodynamics, URL: geodynamics.org/cig/software/pylith/pylith_manual-1.6.pdf.
- Adalgeirsdottir, G., A.M. Smith, T. Murray, M.A. King, K. Makinson, K.W. Nicholls, and A.E. Behar (2008), Tidal influence on Rutford Ice Stream, West Antarctica: observations of surface flow and basal processes from closely spaced GPS and passive seismic stations, *J. Glaciol.*, 54, 187, 715–724.
- Alley, R.B., D.D. Blankenship, C.R. Bentley, and S.T. Rooney (1986), Deformation of till beneath Ice Stream B, West Antarctica, *Nature*, 322, 57–59.
- Alley, R.B., and I.M. Whillans (1991), Changes in the West Antarctic Ice Sheet, *Science*, 254, 959–963.
- Alley, R.B., S. Anandakrishnan, C.R. Bentley, and N. Lord (1994), A water-piracy hypothesis for the stagnation of Ice Stream C, Antarctica, *Ann. Glaciol.*, 20, 187–194.

- Alley, R.B., T.K. Dupont, B.R. Parizek, and S. Anandakrishnan (2005), Access of surface meltwater to beds of sub-freezing glaciers: preliminary insights, *Ann. Glaciol.*, *40*, 8–14.
- Anandakrishnan, S., and C.R. Bentley (1993), Micro-earthquakes beneath ice stream-B and ice stream-C, West Antarctica—Observations and implications, *J. Glaciol.*, *39*, 455–462.
- Anandakrishnan, S., and R.B. Alley (1997), Tidal forcing of basal seismicity of ice stream C, West Antarctica, observed far inland, *J. Geophys. Res.*, *102*, 183–196.
- Anandakrishnan, S., D. E. Voigt, R. B. Alley, and M. A. King (2003), Ice stream D flow speed is strongly modulated by the tide beneath the Ross Ice Shelf, *Geophys. Res. Lett.*, *30*, 1361, doi:10.1029/2002GL016329.
- Balay, S., W.D. Gropp, L.C. McInnes, and B.F. Smith (1997), Efficient Management of Parallelism in Object Oriented Numerical Software Libraries, in *Modern Software Tools in Scientific Computing*, ed. E. Arge, A.M. Bruaset, and H.P. Langtangen, Birkhauser Press, pp. 163-202.
- Balay, S., J. Brown, K. Buschelman, W.D. Gropp, D. Kaushik, M.G. Knepley, L.C. McInnes, B.F. Smith, and H. Zhang (2012a), PETSc Webpage, URL: mcs.anl.gov/petsc.
- Balay, S., J. Brown, K. Buschelman, V. Eijkhout, W.D. Gropp, D. Kaushik, M.G. Knepley, L.C. McInnes, B. F. Smith, and H. Zhang (2012b), PETSc Users Manual, ANL-95/11—Revision 3.3, Argonne National Laboratory.

- Bamber, J.L., R.L. Layberry, and S.P. Gogineni (2001), A new ice thickness and bed data set for the Greenland Ice Sheet, 1. Measurement, data reduction, and errors, *J. Geophys. Res.*, *106*, 33733–33780.
- Bartholomew, I., P. Nienow, A. Sole, D. Mair, T. Cowton, S. Palmer, and J. Wadham (2011), Supraglacial forcing of subglacial drainage in the ablation zone of the Greenland ice sheet, *Geophys. Res. Lett.*, *38*, L08502, doi:10.1029/2011GL047063.
- Bathe, K.-J. (1995), *Finite-Element Procedures*, Prentice Hall, Upper Saddle River, N. J., 1037 pp.
- Bauer, A. (1961), Influence de la dynamique des fleuves de glace sur cell de l'Islandsis du Groenland, *Int. Assoc. Hydrol. Sci.*, *54*, 578–584.
- Bindschadler, R.A., S.N. Stephenson, D.R. MacAyeal, and S. Shabtaie (1987), Ice dynamics at the mouth of Ice Stream B, Antarctica, *J. Geophys. Res.*, *92*, 8885–8894.
- Bindschadler, R. A., P. L. Vornberger, M. A. King, and L. Padman (2003), Tidally driven stick-slip motion in the mouth of Whillans Ice Stream, Antarctica, *Ann. Glaciol.*, *36*, 263–272.
- Blankenship, D.D. and C.R. Bentley (1987), The crystalline fabric of polar ice sheets inferred from seismic anisotropy. *Int. Assoc. Hydrol. Sci.*, *170*, 17–28.
- Blankenship, D.D., C.R. Bentley, S.T. Rooney, and R.B. Alley (1986), Seismic measurements reveal a saturated porous layer beneath an active Antarctic Ice Stream, *Nature*, *322*, 54–57.

- Borstad, C.P., A. Khazendar, E. Larour, M. Morlighem, E. Rignot, M.P. Schodlock, and H. Seroussi (2012), A damage mechanics assessment of the Larsen B ice shelf prior to collapse: Towards a physically-based calving law. *Geophys. Res. Lett.*, *39*, L18502, doi:10.1029/2012GL053317.
- Box, J.E., D.H. Bromwich, B.A. Veenhuis, L.-S. Bai, J.C. Stroeve, J.C. Rogers, K. Steffen, T. Haran, and S.-H. Wang (2006), Greenland Ice Sheet Surface Mass Balance Variability (1988–2004) from Calibrated Polar MM5 Output, *J. Clim.*, *19*, 2783–2800.
- Box, J.E., and K. Ski (2007), Remote sounding of Greenland supraglacial melt lakes: implications for subglacial hydraulics, *J. Glaciol.*, *53*, 257–265.
- Brunt, K. M., H. A. Fricker, L. Padman, T. A. Scambos, and S. O'Neel (2010), Mapping the grounding zone of the Ross Ice Shelf, Antarctica, using ICESat laser altimetry, *Ann. Glaciol.*, *51*, 71–79.
- Budd, W.F., and T.H. Jacka (1989), A review of ice rheology for ice sheet modeling, *Cold Reg. Sci. and Tech.*, *16*, 107–144.
- Chaboche, J.L. (1977), Viscoplastic constitutive equations for description of cyclic and anisotropic behavior of metals, *Bulletin De L'Academie Polonaise Des Science-Serie Des Sciences Techniques*, *25*, 39–48.
- Clarke, T.S., and K. Echelmeyer (1996), Seismic-reflection evidence for a deep subglacial trough beneath Jakobshavn Isbrae, West Greenland, *J. Glaciol.*, *43*, 219–232,

- Clarke, T.S., C. Liu, N.E. Lord, and C.R. Bentley (2000), Evidence for a recently abandoned shear margin adjacent to ice stream B2, Antarctica, from ice-penetrating radar measurements, *J. Geophys. Res.*, 105 (B6), 13409–13422.
- Conway, H., G. Catania, C. Raymond, T. Scambos, H. Engelhardt, and A. Gades (2002), Switch of flow direction in an Antarctic Ice Stream, *Nature*, 419, 465–467.
- Cuffey, K. M., and W. S. B. Paterson (2010), *The Physics of Glaciers*, 4th ed., Elsevier, San Diego, C.A., 693 pp.
- Dahl-Jensen, D., and N. S. Gundestrup (1987). Constitutive properties of ice at Dye 3, Greenland. *Int. Assoc. Hydrol. Sci.*, 170, 31–43.
- Das S., I. Joughin, M.D. Behn, I.M. Howat, M.A. King, D. Lizarralde, and M.P. Bhatia (2008), Fraction propagation to the base of the Greenland Ice Sheet during supraglacial lake drainage, *Science*, 320, doi:10.1126/science.1153360.
- Davis, J.L., P. Elósegui, G. Hamilton, L. Stearns, M. Langer, M.K. Nettles, and T.B. Larsen (2007), Mechanisms for Tidally Induced Glacier Deformation and Flow Variations, East Greenland, *Eos Trans. AGU*, 88(52), Fall Meet. Suppl., Abstract G33B-1234.
- De Angelis, H., and P. Skvarca (2003), Glacier surge after ice shelf collapse, *Sci.* 299, 1560–1562.
- Deichmann, N., J. Ansorge, F. Scherbaum, A. Aschwanden, F. Bernardi, and G.H. Gudmundsson (2000), Evidence for deep icequakes in an Alpine glacier, *Ann. Glaciol.*, 31, 85–90, doi:10.3189/172756400781820462.
- de Juan, J., P. Elósegui, M. Nettles, J.L. Davis, T. Larsen, A. Ahlstrøm, M.L. Andersen, G. Ekström, R. Forsberg, G.S. Hamilton, S.A. Khan, K.M. Schild, L.A. Stearns,

and L. Stenseng (2009), Ocean tides modulation of flow at Helheim Glacier, East Greenland, observed by GPS, Abstract C11A-01 presented at Fall Meeting, AGU, San Francisco, Calif., 14–18 Dec.

de Juan, J., P. Elósegui, M. Nettles, J.L. Davis, T. Larsen, G.S. Hamilton, and L.A. Stearns (2010a), GPS measurements of flow variations at a large Greenland outlet glacier due to ocean tidal forcing, Abstract C21A-0516 presented at Fall Meeting, AGU, San Francisco, Calif., 13–17 Dec.

de Juan, J., P. Elósegui, M. Nettles, T.B. Larsen, J.L. Davis, G.S. Hamilton, L.A. Stearns, M.L. Andersen, G. Ekström, A.P. Ahlstrøm, L. Stenseng, S.A. Khan, and R. Forsberg (2010b), Sudden increase in tidal response linked to calving and acceleration at a large Greenland outlet glacier, *Geophys. Res. Lett.*, 37, L12501, doi:10.1029/2010GL043286.

de Juan Verger, J. (2011), *Tidewater Glacier Flow of Helheim Glacier, Greenland, 2006-2008, Using High-Rate GPS*, PhD Dissertation, Geodynamics and Geophysics Department, University of Barcelona.

Duddu, R., and H. Waisman (2012), A temperature dependent creep damage model for polycrystalline ice, *Mech. Mat.*, 46, 23–41.

Dyrgerov., M., and M.F. Meier (2005), Glaciers and the Changing Earth System: a 2004 Snapshot, Occasional Paper 58, *Inst. Art. and Alp. Res.*, Univ. of Col., Boulder, CO, 118.

Echelmeyer, K., and Z. Wang (1987). Direct observations of basal sliding and deformation of basal drift at sub-freezing temperatures. *J. Glaciol.*, 33, 83–98.

- Echelmeyer, K., and W.D. Harrison (1990), Jakobshavn Isbrae, West Greenland: Seasonal Variations in Velocity—Or Lack Thereof, *J. Glaciol.*, 36, 122, 82–88.
- Echelmeyer, K., T.S. Clarke, and W.D. Harrison (1991), Surficial glaciology of Jakobshavn Isbrae, West Greenland: Part I. Surface morphology, *J. Glaciol.*, 37, 127, 368–382.
- Echelmeyer, K., W.D. Harrison, T.S. Clarke, and C. Benson (1992), Surficial glaciology of Jakobshavn Isbrae, West Greenland: Part 2, Ablation, accumulation and temperature, *J. Glaciol.*, 38, 169–181.
- Echelmeyer, K.A., W.D. Harrison, C. Larson, and J.E. Mitchell (1994), The role of the margins in the dynamics of an active ice stream. *J. Glaciol.*, 40, 527–538.
- Ekström, G., M. Nettles, and G.A. Abers (2003), Glacial earthquakes, *Sci.*, 302, 622–624, doi:10.1126/science.1088057.
- Engelhardt, H. (2004a), Thermal regime and dynamics of the West Antarctic ice sheet, *Ann. Glaciol.*, 39, 85–92.
- Engelhardt, H. (2004b), Ice temperature and high geothermal flux at Siple Dome, West Antarctica, from borehole measurements, *J. Glaciol.*, 50, 251–256.
- Engelhardt, H., N. Humphrey, B. Kamb, and M. Fahnestock (1990), Physical conditions at the base of a fast moving Antarctic ice stream, *Science*, 248, 57–79.
- Engelhardt, H. and W.B. Kamb (1993), Vertical temperature profile of Ice Stream B, *Antarctic Journal, Review 1993*, 63–66.
- Engelhardt, H., and W.B. Kamb (1998), Basal sliding of Ice Stream B, West Antarctica, *J. Glaciol.*, 44, 223–230.

- Erdogan, F., G.D Gupta (1971), Layered composites with an interface flaw, *Int. J. Solids and Struct.*, Vol. 7, Iss. 8, 1089–1107, doi:10.1016/0020-7683(71)90082-5.
- Erdogan, F., G.D. Gupta , and T.S. Cook (1973), “Numerical Solution of Singular Integral Equations,” *Methods of Analysis and Solution of Crack Problems. Recent Developments in Fraction Mechanics*, G.C. Sih, ed., Leyden, Noordhoff Int. Pub., San Diego, CA, 368–425.
- Fahnestock, M.A., T.A. Scambos, R.A. Bindschadler, and G. Kvaran (2000), A millennium of variable ice flow recorded by the Ross Ice Shelf, Antarctica, *J. Glaciol.*, 46, 652–664.
- Findley, W., J.S. Lai, and K. Onaran (2011), *Creep and Relaxation of Nonlinear Viscoelastic Materials*, Dover Civil and Mechanical Engineering ed., North-Holland Pub. Co., United States, 371 pp.
- Funk, M., K. Echelmeyer, and A. Iken (1994), Mechanisms of fast flow in Jakobshavn Isbrae, West Greenland: Part II. Modeling of englacial temperatures, *J. Glaciol.*, 40, 569–585.
- Gades, A.M., C.F. Raymond, H. Conway, and R. Jacobel (2000), Bed properties of Siple Dome and adjacent ice streams, West Antarctica, inferred from radio echo-sounding measurements, *J. Glaciol.*, 46, 88–94.
- Gammon, P. H., H. Kiefte, and M. J. Clouter (1983), Elastic-constants of ice samples by Brillouin spectroscopy, *J. Phys. Chem.*, 87, 4025–4029, doi:10.1021/j100244a004.

- Gammon, P. H., H. Kieffe, M. J. Clouter, and W. W. Denner (1983), Elastic-constants of artificial and natural ice samples by Brillouin Spectroscopy, *J. Glaciol.*, 29, 433–460.
- Gioia, G., and P. Chakraborty (2006), Turbulent Friction in Rough Pipes and the Energy Spectrum of the Phenomenological Theory, *Phys. Rev. Lett.*, 96, 1–4.
- Glen, J.W. (1955), The creep of polycrystalline ice, *Proc. Roy. Soc. London, Ser. A.* 228, 519–538;
- Glen J.W. (1958), The flow law of ice. A discussion of the assumptions made in glacier theory, their experimental foundations and consequences, *Int. Assoc. Sci. Hydrol.*, 47, 171–183.
- Goldberg, D., D.M. Holland and C. Schoof (2009), Grounding line movement and ice shelf buttressing in marine ice sheets, *J. Geophys. Res.*, 114, F04026, doi:10.1029/2008JF001227.
- Goldsby, D.L., and D.L. Kohlstedt (1997), Grain boundary sliding in fine-grained ice I, *Scripta Mater.*, 37, 1399–1406.
- Goldsby, D.L., and D.L. Kohlstedt (2001), Superplastic deformation of ice: experimental observations, *J. Geophys. Res.*, 106B6, 11017–11030.
- Goodier, J. N. (1942), An extension of Saint-Venant's Principle, with applications, *J. App. Physics*, vol. 13, 167–171.
- Gow, A.J. (1968), Deep core studies of the accumulation and densification of snow at Byrd Station, Antarctica, *Int. Assoc. Sci. Hydrol.*, 86, 78–90.
- Gudmundsson, G. H. (2006), Fortnightly variations in the flow velocity of Rutford Ice Stream, West Antarctica, *Nature*, 444, doi:10.1038/nature05430.

- Gudmundsson, G. H. (2007), Tides and the flow of Rutford Ice Stream, West Antarctica, *J. Geophys. Res.*, *112*, F04007, doi:10.1029/2006JF000731.
- Gudmundsson, G. H. (2011), Ice-Stream response to ocean tides and the form of the basal sliding law, *Cryo.*, vol. 5, iss. 1, doi:10.5194/tc-5-259-2011, 259–270.
- Hamilton, G.S., L.A. Stearns, P. Elósegui, J.L. Davis, M. Nettles, A.P. Ahlstrøm, S.A. Khan, M. Langer, L. Stenseng, G. Ekström, R. Forsberg, T.M. Jørgensen, and T.B. Larsen (2006), Tidal Modulation of Ice Flow on Kangerdlugssuaq and Helheim Glaciers, East Greenland, from High-Rate GPS Measurements, *Eos Trans. AGU*, *87*(52), Fall Meet. Suppl., Abstract C51C-02.
- Hanna, E., P. Huybrechts, I. Janssens, J. Cappelen, K. Steffen, and A. Stephens (2005), Runoff and mass balance of the Greenland ice sheet: 1958–2003, *J. Geophys. Res.*, *110*, D13108.
- Harrison, W. D., K. A., Echelmeyer, and H. Engelhardt (1993), Short-period observations of speed, strain and seismicity on Ice Stream B, Antarctica, *J. Glaciol.*, *39*, 463–470.
- Heinert, M, and B. Riedel (2007), Parametric modelling of the geometrical ice-ocean interaction in the Ekstroemisen grounding zone based on short time-series, *Geophys. J. Int.*, *169*, 407–420, doi:10.1111/j.1365-246X.2007.03364.x.
- Hoffman, M.J., G.A. Catania, T.A. Neumann, L.C. Andrews, and J.A. Rumrill (2011), Links between acceleration, melting, and supraglacial lake drainage of the western Greenland Ice Sheet, *J. Geophys. Res.*, *116*, F04035, doi: 10.1029/2010JF001934.
- Holdsworth, G. (1969), Flexure of a floating ice tongue, *J. Glaciol.*, *8*, 358–397.
- Holdsworth, G. (1977), Tidal interaction with ice shelves, *Ann. Glaciol.*, *33*, 133–146.

- Hooke, R.L., and B. Hanson (1986), Borehole deformation experiments, Barnes Ice Cap, Canada, *Cold Reg. Sci. Tech.*, 12, 261–276.
- Howat, I.M., I. Joughin, S. Tulaczyk, and S. Gogineni (2005), Rapid retreat and acceleration of Helheim Glacier, east Greenland, *Geophys. Res. Lett.*, 32, L22502.
- Hughes, T.J. (1998), *Ice Sheets*, Oxford University Press, New York, N.Y., 343 pp.
- Humphrey, N., B., Kamb, M. Fahnestock, and H. Engelhardt (1993), Characteristics of the Bed of Lower Columbia Glacier, Alaska, *J. Geophys. Res.*, 98, 837–846.
- Iken, A., K. Echelmeyer, W. Harrison, and M. Funk (1993), Mechanisms of fast flow in Jakobshavn Isbrae, West Greenland: part 1. Measurements of temperature and water level in deep boreholes, *J. Glaciol.*, 39, 15–25.
- IPCC (1990), *Climate change: the IPCC scientific assessment*, Houghton, J.T., G.J. Jenkins, and J.J. Ephraums, eds. Cambridge University Press, Cambridge, United Kingdom, 365 pp.
- IPCC (1996), *Climate change 1995, the science of climate change*. Houghton, J.T., L.G. Meira Filho, B.A. Callander, N. Harris, A. Kattenberg, and K. Maskell, eds. Cambridge University Press, Cambridge, United Kingdom, 572 pp.
- IPCC (2007), *Climate Change 2007: The Physical Science Basis. Contribution of Working Group I to the Fourth Assessment Report of the Intergovernmental Panel on Climate Change*, Solomon S., D. Qin, M. Manning, Z. Chen, M. Marquis, K.B. Averyt, M. Tignor, and H.L. Miller, eds. Cambridge University Press, Cambridge, United Kingdom and New York, N.Y., U.S.A.
- Jacobs, S.S., H.H. Hellmer, and A. Jenkins (1996), Antarctic ice sheet melting in the Southeast Pacific, *Geophys. Res. Lett.*, 23 (9), 957–960.

- Jacobson, H.P., and C.F. Raymond (1998), Thermal effects on the location of ice stream margins, *J. Geophys. Res.*, 103 (B6), 12111–12122.
- Jellinek, H. H. G. and R. Brill (1956), Viscoelastic properties of ice, *J. App. Physics*, vol. 27, no. 10, 1198–1209.
- Jezek, K.C., R.B. Alley, and R.H. Thomas (1985), Rheology of glacial ice, *Science*, 227, 1335–1337.
- Joughin I., M. Fahnestock, D. MacAyeal, J. Bamber, and P. Gogineni (2001), Observation and analysis of ice flow in the largest Greenland ice stream, *J. Geophys. Res.*, 106 (D24), 34021–34034.
- Joughin, I., D. R. MacAyeal, and S. Tulaczyk (2004a), Basal shear stress of the Ross ice streams from control method inversions, *J. Geophys. Res.*, 109, B09405.
- Joughin I., W. Abdalati, and M. Fahnestock (2004b), Large fluctuations in speed on Greenland's Jakobshavn Isbrae glacier, *Nature*, 432, 608–610.
- Joughin, I., S. Tulaczyk, D.R. MacAyeal, and H. Engelhardt (2004c), Melting and freezing beneath the Ross ice streams, Antarctica, *J. Glaciol.*, 50, 96–108.
- Joughin, I., R.A. Bindschadler, M.A. King, D. Voigt, R.B. Alley, S. Anandakrishnan, H. Horgan, L. Peters, P. Winberry, S.B. Das, and G. Catania (2005), Continued deceleration of Whillans Ice Stream, West Antarctica, *Geophys. Res. Lett.*, 32, L22501.
- Joughin, I., S.B. Das, M.A. King, B.E. Smith, I.M. Howat, and T. Moon (2008), Seasonal Speedup Along the Western Flank of the Greenland Ice Sheet, *Sci.*, 320, 781783.
- Kachanov, L.M. (1958), Time to failure under creep conditions, *Izv. Akad. Nauk SSSR, Otd. Tekh. Nauk*, 8, 26–31.

- Kachanov, L.M. (1986), *Introduction to Continuum Damage Mechanics*, Martinus Nijhoff Publishers, Dordrecht, the Netherlands, 135 pp.
- Kamb, B. (1991), Rheological nonlinearity and flow instability in the deforming bed mechanism of ice stream motion, *J. Geophys. Res.*, 92 (B9), 9083–9100.
- Kamb, B. (2001), Basal zone of the West Antarctic ice streams and its role in the lubrication of their motion, *J. Geophys. Res.*, 96, 16585–16595.
- King, M.A., K. Makinson, and G.H. Gudmundsson (2011), Nonlinear interaction between ocean tides and the Larsen C Ice Shelf system, *Geophys. Res. Lett.*, 38, L08501, doi:10.1029/2011GL046680.
- Kojic, M. and K-J. Bathe (1987), The ‘Effective Stress-Function’ Algorithm for Thermo-Elasto-Plasticity and Creep, *Int. J. Num. Meth. Eng.*, 24, 1509–1532.
- Krawczynski, M.J., M.D. Behn, S.B. Das, and I. Joughin (2009), Constraints on the lake volume required for hydro-fracture through ice sheets, *Geo. Res. Lett.*, 36, L10501, doi:10.1029/2008GL036765.
- Krimmel, R.M. and B.H. Vaughn (1987), Columbia Glacier, Alaska: Changes in Velocity 1977-1986, *J. Geophys. Res.*, 92, 8961–8968.
- Krinner, G., O. Magand, I. Simmonds, C. Genthon, and J.-L. Dufresene (2006), Simulated Antarctic precipitation and surface mass balance at the end of the twentieth and twenty-first centuries, *Clim. Dyn.*, 28, 215–230.
- Lemaitre, J., and J.L. Chaboche (1978), Phenomenological approach to damage rupture, *Journal de Mecanique Appliquee*, 2, 317–365.
- Lingle, C.S., T.J. Hughes, and R.C. Kollmeyer (1981), Tidal flexure of Jakobshavns glacier, West Greenland, *J. Geophys. Res.*, 86 (B5), 3960–3968.

- Lüthi, D., M. Funk, A. Iken, S. Gogineni, and M. Truffer (2002), Mechanisms of fast flow in Jakobshavn Isbrae, West Greenland: part III. Measurements of ice deformation, temperature and cross-borehole conductivity in boreholes to the bedrock, *J. Glaciol.*, 28, 369–385.
- Lythe, M.B., D.G Vaughan, and the BEDMAP Consortium (2001), BEDMAP: a new ice thickness and subglacial topographic model of Antarctica, *J. Geophys. Res.*, 106 (B6), 11335–11351.
- L’vovich, M.I. (1979), *World water resources and their future*, American Geophysical Union, Washington, D.C., United States, 415 pp.
- MacAyeal, D.R., E. Rignot, and C.L. Hulbe (1998), Ice-shelf dynamics near the front of the Filchner-Ronne Ice Shelf, Antarctica, revealed by SAR interferometry: model/interferogram comparison, *J. Glaciol.*, 44, 419–428.
- MacAyeal, D.R., V. Rommelaere, P. Huybrechts, C.L. Hulbe, J. Betermann, and C. Ritz (1996), An ice-shelf model test based on the Ross Ice Shelf, *Ann. Glaciol.*, 23, 46–51.
- Manning, R. (1891), On the Flow of Water in Open Channels and Pipes, *Trans. Inst. Civil Eng.*, 20. 161–207.
- Meier, M.F., M.B. Dyurgerov, U.K. Rick, S. O’Neel, W.T. Pfeffer, R.S. Anderson, S.P. Anderson, and A.F. Glazovsky (2007), Glaciers dominate Eustatic sea-level rise in the 21st century, *Sci.*, 317, 14–16, doi:10.1126/science.1143906.
- Meier, M., S. Lundstrom, D. Stone, B. Kam, H. Engelhardt, N. Humphrey, W.W. Dunlap, M. Fahnestock, R.M. Krimmel and R. Walters (1994), Mechanical and

- hydrologic basis for the rapid motion of a large tidewater glacier, 1. Observations, *J. Geophys. Res.*, 99, 15219–15229.
- Morgan, V.I., T.H. Jacka, G.J. Ackerman, and A.L. Clarke (1982), Outlet glacier and mass-budget studies in Enderby, Kemp, and Mac. Robertson Lands, Antarctica, *Ann. Glaciol.*, 3, 204–210.
- Morland, L.W. (2009), Primary, secondary and tertiary creep of ice modeled as a viscoelastic fluid, *J. Glaciol.*, 55, 170–178.
- Mote, T.L. (2003), Estimation of runoff rates, mass balance, and elevation changes on the Greenland ice sheet from passive microwave observations, *J. Geophys. Res.*, 108 (D2), ACL13.1-ACL13.7.
- Murakami, S. (2012), *Continuum damage mechanics: a continuum mechanics approach to the analysis of damage and fracture*, Springer Science+Business Media, London, 402 pp.
- Nanthikensan, S. and S. S. Sunder (1994), Anisotropic elasticity of polycrystalline ice I_h , *Cold Reg. Sci. and Tech.*, 22, 149–169.
- Neave, K.G., and J.C. Savage (1970), Icequakes on Athabasca Glacier, *J. Geophys. Res.*, 75, 1351–1362, doi:10.1029/JB075i008p01351.
- Nye, J.F. (1953), The flow law of ice from measurements in glacier tunnels, laboratory experiments, and the Jungfraufirn borehold experiment, *Proc. R. Soc. Lond. Ser. A.*, 219, 477–489.
- O’Neel, S., K.A. Echelmeyer and R.J. Motyka (2001), Short-term flow dynamics of a retreating tidewater glacier: LeConte Glacier, Alaska, U.S.A., *J. Glaciol.*, 47, 567–578.

- O'Neel., K.A. Echelmeyer and R.J. Motyka (2001), Short-term variations in calving of a tidewater glacier: LeConte Glacier, Alaska, U.S.A., *J. Glaciol.*, 49, 587–598.
- O'Neel, S., H.P. Marshall, D.E. McNamara, and W.T. Pfeffer (2007), Seismic detection and analysis of icequakes at Columbia Glacier, Alaska, *J. Geophys. Res.*, 112, F03S23, doi:10.1029/2006JF000595.
- Palmer, S. A. Shepherd, P. Nienow, and I. Joughin (2011), Seasonal speedup of the Greenland Ice Sheet linked to routing of surface water, *Earth and Plan. Sci. Lett.*, 302, 423–428.
- Parizek, B.R. and R.B. Alley (2004), Implications of increased Greenland surface melt under global-warming scenarios: ice-sheet simulations, *J. Glaciol.*, 49(164), 22–36.
- Paterson, W. S. B. (1991). Why ice-age ice is sometimes soft, *Cold Reg. Sci. and Tech.*, 20, 75–98.
- Paterson, W. S. B. (1994). *The Physics of Glaciers*, 3rd ed., Pergamon, pp 480.
- Pawlowicz, R., B. Beardsley, and S. Lentz (2002), Classical tidal harmonic analysis including error estimates in MATLAB using T_TIDE, *Comp. & Geosci.*, 28, 929–937.
- Petrenko, V. F. and R. W. Whitford (2002), *Physics of Ice*, 2nd ed., Oxford University Press, Oxford, England.
- Podrasky, D.B., M. Trugger, M.A. Fahnestock, M.P. Luethi (2010), Short Period Velocity Response to Tides and Calving Near the Terminus of Jakobshavn Isbrae, Abstract C23C-0636 presented at Fall Meeting, AGU, San Francisco, Calif., 13–17 Dec.

- Podrasky D., M. Truffer, M. Fahnestock, J.M. Amundson, R. Cassotto, and L. Joughin (2012), Outlet glacier response to forcing over hourly to interannual timescales, Jakobshavn Isbrae, Greenland, *J. Glaciol.*, 58, 212, 1212–1226, doi:10.3186/2012JoG12J065.
- Pralong, A., and M. Funk (2005), Dynamic damage model of crevasse opening and application to glacier calving, *J. Geophys. Res.-Solid Earth*, 110B1, B1309, doi:10.1029/2004JB003104.
- Qamar, A. (1988), Calving icebergs: A source of low-frequency seismic signals from Columbia Glacier, Alaska, *J. Geophys. Res.*, 93, 6615–6623, doi:10.1029/JB093iB06p06615.
- Rabotnov, Y.U.N. (1968), Creep rupture, Proceedings of the XII International Congress of Applied Mechanics, Stanford-Springer, pp. 342–349.
- Raymond, C.F. (2000), Energy balance of ice streams, *J. Glaciol.*, 46, 665–674.
- Raymond, C.F., and M. Nolan (2000), Drainage of a glacial lake through an ice spillway, *Int. Assoc. Hydrol. Sci.*, Publ. 264, 199–207.
- Raymond, C.F., K.A. Echelmeyer, I.M. Whillans, and C.S.M. Doake (2001), Ice stream shear margins, in: Alley, R.B., and R.A. Bindschadler (eds.), *The West Antarctic Ice Sheet, Behavior and Environment*, American Geophysical Union, *Antarctic Res. Series*, 77, 137–155.
- Raymond Pralong, M., and G.H. Gudmundsson (2011), Bayesian estimation of basal conditions on Rutford Ice Stream, West Antarctica, from surface data, *J. Glaciol.*, 57, 202, 315–324.

- Reeh, N., C. Mayer, H. Miller, H.H. Thomson, and A. Weidick (1999), Present and past climate control on fjord glaciations in Greenland: Implications for IRD-deposition in the sea, *Geophys. Res. Lett.*, *26*, 1036–1042.
- Reeh, N., C. Mayer, O. B. Olesen, E. L. Christensen, and H. H. Thomsen (2000), Tidal movement of Nioghalvfjerd fjorden glacier, northeast Greenland: observations and modelling, *Ann. Glaciol.*, *31*, 111–117.
- Reeh, N., E.L. Christensen, C. Mayer, and O.B. Olesen (2003), Tidal bending of glaciers: a linear viscoelastic approach, *Ann. Glaciol.*, *37*, 83–89.
- Riedel, B. and M. Heinert (1998), First results of GPS array observations in the grounding zone of Ekstroem Ice Shelf, in Oerter, H., comp. *Filcher-Ronne Ice Shelf Programme (FRISP). Report No. 12*, Bremerhave, Alfred Wegener Institute for Polar and Marine Research, 74–76.
- Riedel, B., U. Nixdorf, M. Heinert, A. Eckstaller, and C. Mayer (1999), The response of the Ekstromisen (Antarctica) grounding zone to tidal forcing, *Ann. Glaciol.*, *29*, 239–242.
- Riesen, P., K. Hutter, and M. Funk (2010), A viscoelastic Rivlin-Ericksen material model applicable to glacier ice, *Nonlin. Proc. Geophys.*, *17*, 673–384, doi:10.5194/npg-147-673-2010.
- Rignot, E. (1996), Tidal motion, ice velocity and melt rate of Petermann Gletscher, Greenland, measured from radar interferometry, *J. Glaciol.*, *42*, 476–485.
- Rignot, E.J. (1998a), Fast Recession of a West Antarctic Glacier, *Science*, *281*, 549, doi:10.1126/science.281.5376.549.

- Rignot, E. (1998b), Hinge-line migration of Petermann Gletscher, north Greenland, detected using satellite-radar interferometry, *J. Glaciol.*, *21*, 469-476.
- Rignot, E., G. Casassa, P. Gogineni, W. Krabill, A Rivera, and R. Thomas (2004), Accelerated discharge from the Antarctic Peninsula following the collapse of Larsen B ice shelf, *Geophys. Res. Lett.*, *31*, L18401.
- Rignot, E., and P. Kanagaratnam (2006), Changes in the velocity structure of Greenland Ice Sheet, *Sci.*, *331*, 986–990.
- Rignot, E., J.E. Box, E. Burgess, and E. Hanna (2008), Mass balance of the Greenland ice sheet from 1958 to 2007, *Geophys. Res. Lett.*, *35*, L20502.
- Rott, H., P. Skvarca, and T. Nagler (1996), Rapid collapse of Northern Larsen Ice Shelf, Antarctica, *Sci.*, *271*, 788–792.
- Rubin, H. and J. Atkinson (2001), *Environmental Fluid Mechanics*, Macel Dekker, Inc., New York.
- Scambos, T.A., J.A. Bohlander, C.A. Shuman, and P. Skvarca (2004), Glacier acceleration and thinning after ice shelf collapse in the Larsen B embayment, Antarctica, *Geophys. Res. Lett.*, *31*, L18402.
- Salamatin, A.N., E.A., Tsyganova, S.V. Popov, and V.Y. Lipenkov (2008), Ice flow line modeling and ice core data interpretation: Vostok Station (East Antarctica). In: Hondoh, T. (Ed.), *Physics of Ice Core Records*, vol. 2, Hokkaido Univerity Press.
- Schoof, C. (2007a), Ice sheet grounding line dynamics: Steady states, stability, and hysteresis, *J. Geophys. Res.*, *112*, F03S38, doi:10.1029/2006JF000664.
- Schoof, C. (2007b), Marine ice-sheet dynamics. Part 1. The case of rapid sliding, *J. Fluid Mech.*, *573*, 27–55, doi:10.1017/S0022112006003570.

- Scott, J. B. T., G. H. Gudmundsson, A. M. Smith, R. G. Bingham, H. D. Pritchard, and D. G. Vaughan (2009), Increased rate of acceleration on Pin Island Glacier strongly coupled to changes in gravitational driving stress, *The Cryosphere*, 3, 125–131.
- Selmes, N., T. Murray, and T.D. James (2011), Fast draining lakes on the Greenland Ice Sheet, *Geophys. Res. Lett.*, 38, L15501, doi:10.1029/2011GL047872.
- Sergienko, O. V., D. R. MacAyeal, and R. A. Bindschadler (2009), Stick-slip behavior of ice streams: modeling investigations, *Ann. Glaciol.*, 50, 87–94.
- Shabtaie, S., and C.R. Bentley (1987), West Antarctic ice streams draining into the Ross Ice Shelf: configuration and mass balance, *J. Geophys. Res.*, 92, 1311–1336.
- Shabtaie, S., and C.R. Bentley (1988), Ice-thickness map of the West Antarctic ice streams by radar sounding, *Ann. Glaciol.*, 11, 126–136.
- Shoji, H., and C.C. Langway Jr. (1988), Flow-law parameters of the Dye 3, Greenland, deep ice core, *Ann. Glaciol.*, 10, 146–150.
- SMIC Report (1971), Inadvertent climate modification: report of the study of man's impact on climate, MIT Press, Cambridge, MA., 308 pp.
- Smith, A.M. (1997), Basal conditions on Rutford Ice Stream, West Antarctica, from seismic observations, *J. Geophys. Res.*, 102, 543–552.
- Smith, A.M. (2006), Microearthquakes and subglacial conditions, *Geophys. Res. Lett.*, 33, L24501, doi:10.1029/2006GL028207.
- Sohn, H.-G., K.C. Jezek, and C.J. van der Veen (1998), Jakobshavn Glacier, West Greenland: 30 years of spaceborne observations, *Geophys. Res. Lett.*, 25, 2699–2702.

- Stuart, G., T. Murray, A. Brisbourne, P. Styles, and S. Toon (2005), Seismic emissions from a surging glacier: Bakaninbreen, Svalbard, *Ann. Glaciol.*, 42, 151–157, doi:10.3189/172756405781812538.
- Stephenson, S. N. (1984), Glacier flexure and the position of grounding lines: measurements by tiltmeter on Rutford Ice Stream, Antarctica, *Ann. Glaciol.*, 5, 165–169.
- Strickler, A. (1923), Beitrage zur frage der geschwindigkeitsformel und der rauhigkeitszahlen fur stome, kanale und geshlossene leitungen, Technical report, *Mitteilungen des Eidgenossischen Amtes fur Wasserwirtschaft*, 16, Bern, Switzerland.
- Strickler, A. (1981), *Contributions to the Question of a Velocity Formula and Roughness Data for Streams, Channels, and Closed Pipelines*, T. Roesgen and W.R. Brownlie, translators, W.M. Keck Lab of Hydraulics and Water Resources, California Institute of Technology, Pasadena, CA.
- Tedesco, M., M. Lüthje, K. Steffen, N. Steiner, X. Fettweis, I. Willis, N. Bayou, and A. Banwell (2012), Measurement and modeling of ablation of the bottom of supraglacial lakes in western Greenland, *Geophys. Res. Lett.*, 39, L02502, doi:10.1029/2011GL049882.
- Thiel, E., A.P. Crary, R.A. Haubrich, and J.C. Behrendt (1960), Gravimetric Determination of Ocean Tide, Weddell and Ross Seas, Antarctica, *J. Geophys. Res.*, 65, 629–636.

- Thomas, R.H., W. Abdalati, T.L. Akins, B.M. Csatho, E.B. Frederick, S. P. Gogeneni, W.B. Krabill, S.S. Manizade, E.J. Rignot (2000), *Geophys. Res. Lett.*, 9, 1291–1294, doi:10.1029/1999GL008473.
- Thomas, R.H., W. Abdalati, E. Frederick, W.B. Krabill, S. Manizade, and K. Steffen (2003), Investigation of surface melting and dynamic thinning on Jakobshavn Isbrae, Greenland, *J. Glaciol.*, 49, 231–239.
- Thomas, R.H. (2004), Force-perturbation analysis of recent thinning and acceleration of Jakobshavn Isbrae, Greenland, *J. Glaciol.*, 50, 57–66.
- Timoshenko, S. P. and J. N. Goodier (1982), *Theory of Elasticity*, 3rd. ed., McGraw-Hill Book Company, San Fransisco, C.A., 567 pp.
- Tsai, V.C., and G. Ekström (2007), Analysis of glacial earthquakes, *J. Geophys. Res.* 112, F03S22, doi:10.1029/2066JF000596.
- Tsai, V.C., J.R. Rice, and M. Fahnestock (2008), Possible mechanisms for glacial earthquakes, *J. Geophys. Res.*, 113, F03014, doi:10.1029/2007JF000944.
- Tsai, V.C., and J.R. Rice (2010), A Model for Turbulent Hydraulic Fracture and Application to Crack Propagation at Glacier Beds, *J. Geophys. Res.*, 115, F03007, doi:10.1029/2009JF001474.
- Tsai, V.C., and J.R. Rice (2012), Modeling Turbulent Hydraulic Fracture Near a Free Surface, *J. Appl. Mech.*, 79, 031003, doi:1115/1.4005879.
- Tulaczyk, S., B. Kamb, and H.F. Engelhardt (2000a), Basal mechanics of Ice Stream B, West Antarctica. 1. Till mechanics, *J. Geophys. Res.*, 105 (B1), 463–481.

- Tulaczyk S., B. Kamb, and H.F. Engelhardt (2000b), Basal mechanics of Ice Stream B, West Antarctica. II. Undrained-plastic-bed model, *J. Geophys. Res.*, *105* (B1), 483–490.
- Tulaczyk, S., B. Kamb, R.P., Scherer, and H.F. Engelhardt (1998), Sedimentary processes beneath a West Antarctic ice stream; constraints from textural and compositional properties of subglacial debris, *J. Sediment. Res.*, *68*, 487–496.
- Turcotte, D.L., and G. Schubert (2002), *Geodynamics*, 2nd ed., Cambridge University Press, Cambridge, United Kingdom, 456 pp.
- Van der Veen, C.J. (1999), *Fundamentals of Glacier Dynamics*, A.A.Balkema Publishers, Rotterdam, Netherlands, 462 pp.
- VanWormer, D., and E. Berg (1973), Seismic evidence for glacier motion, *J. Glaciol.*, *12*, 259–265.
- Vaughan D.G. (1994), Investigating tidal flexure on an ice shelf using kinematic GPS, *Ann. Glaciol.*, *20*, 372–376.
- Vaughan D.G. (1995), Tidal flexure at ice shelf margins, *J. Geophys. Res.*, *100* (B4), 6213–6224.
- Vaughan, D.G., and C.S.M. Doake (1996), Recent atmospheric warming and retreat of ice shelves on the Antarctica Peninsula, *Nature*, *379*, 328–331.
- Walker, R.T., K. Christianson, B.P. Parizek, S. Anandakrishnan, and R.B. Alley (2012), A viscoelastic flowline model applied to tidal forcing of Bindschadler Ice Stream, West Antarctica, *Earth and Planet. Sci. Lett.*, *319–320*, 128–132.
- Walsh, J.B. (1965), The Effect of Cracks on the Uniaxial Elastic Compression of Rocks, *J. Geophys. Res.*, *70*, 399–411.

- Walter, J. I., E. E. Brodsky, W. Tulaczyk, S. Y. Schwartz, and R. Pettersson (2011), -
Transient slip events from near-field seismic and geodetic data on a glacier fault,
Whillans Ice Plain, West Antarctica, *J. Geophys. Res.*, *116*, F01021,
doi:10.1029/2010JF001754.
- Walters, R.A. (1989), Small-amplitude, short-period variations in the speed of a tide-
water glacier in south-central Alaska, U.S.A., *Ann. Glaciol.*, *12*, 187–191.
- Walters, R.A. and W.W. Dunlap (1987), Analysis of Time Series of Glacier Speed:
Columbia Glacier, Alaska, *J. Geophys. Res.*, *92*, 8969–8975.
- Weaver, C.S., and S.D. Malone (1979), Seismic evidence for discrete glacier motion at
the rock-ice interface, *J. Glaciol.*, *23*, 171–184.
- Weertman, J. (1957), On the sliding of glaciers, *J. Glaciol.*, *3*, 33–38.
- Weertman, J. (1964), The theory of glacier sliding, *J. Glaciol.*, *5*, 287–303.
- Weertman, J. (1983), Creep deformation of ice, *Ann. Rev. Earth Planet. Sci.*, *11*, 215–
240.
- Whillans, I.M., and C.J. van der Veen (1993a), New and improved determinations of
velocity of Ice Stream-B and Ice Stream-C, West Antarctica, *J. Glaciol.*, *39*, 483–
490.
- Whillans, I.M., and C.J. van der Veen (1993b), Patterns of calculated basal drag on Ice
Stream-B and Ice Stream-C, Antarctica, *J. Glaciol.*, *39*, 437–446.
- Whillans, I.M. and C.J. van der Veen (1997), The role of lateral drag in the dynamics of
Ice Stream B, Antarctica, *J. Glaciol.*, *43*, 231–237.

- Whillans, I.M., J. Bolzan, and S. Shabtaie (1987), Velocity of Ice Streams B and C, Antarctica, *J. Geophys. Res.*, 92 (B2), 8895-8902, doi:10.1029/JB092iB09p08895.
- Whillans, I.M, M. Jackson, and Y.H. Tseng (1993), Velocity pattern in a transect across Ice Stream B-Antarctica, *J. Glaciol.*, 39, 562–572.
- Wiens, D. A., S. Anandakrishnan, J. P. Winberry, and M. A. King (2008), Simultaneous teleseismic and geodetic observations of the stick-slip motion of an Antarctic ice stream, *Nature*, 453, 770–775, doi:10.1038/nature06990.
- Wild, M., P. Calanca, S.C. Scherrer, and A. Ohmura (2003), Effect of polar ice sheets on global sea-level in high resolution greenhouse scenarios, *J. Geophys. Res.*, 108 (D5), 4165.
- Williams, C.A. (2006), Development of a package for modeling stress in the lithosphere, *Eos Trans. AGU*, 87, Jt. Assem. Suppl., Abstract T24A-01 Invited.
- Williams, C.A., B. Aagaard, M.G. Knepley (2005), Development of software for studying earthquakes across multiple spatial and temporal scales by coupling quasi-static and dynamic simulations, *Eos Trans. AGU*, 86, Fall Meet. Suppl., Abstract S53A-1072.
- Winberry, J. P., S. Anandakrishnan, R. B. Alley, R. A. Bindschadler, and M. A. King (2009), Basal mechanics of ice streams: Insights from the stick-slip motion of Whillans Ice Stream, West Antarctica, *J. Geophys. Res.*, 114, F01016, doi:10.1029/2008JF001035.

- Winberry, J.P., S. Anandakrishnan, D.A. Wiens, R.B. Alley, and K. Christianson (2011), Dynamics of stick-slip motion, Whillans Ice Stream, Antarctica, *Earth and Plan. Sci. Lett.*, 305, 283–289, doi:10.1016/j.epsl.2011.02.052.
- Wolf, L.W., and J.N. Davies (1986), Glacier-generated earthquakes from Prince William Sound, Alaska, *Bull. Seismol. Soc. Am.*, 76, 367–379.
- Zwally, H.J., W. Abdalati, T. Herring, K. Larson, J. Saba, and K. Steffen (2002), Surface melt-induced acceleration of Greenland ice-sheet flow, *Sci.*, 297, 218–222.
- Zwally, H.J., R.A. Bindschadler, A.C. Brenner, T.V. Martin, and R.H. Thomas (1983), Surface Elevation Contours of Greenland and Antarctic Ice Sheets, *J. Geophys. Res.*, 88, 1589–1596.